A Multiorbital DMFT Analysis of the Dynamic Hubbard Model

by

Christopher John Arthur Polachic

A thesis submitted in partial fulfillment of the requirements for the degree of

Doctor of Philosophy

Department of Physics

University of Alberta

Abstract

The conventional, single band Hubbard model captures the dynamics that arise in strongly correlated electron systems in the competition between electron transport and local Coulomb interactions. However, some of the important physics of real lattices is overlooked by its simplicity. The dynamic Hubbard model (DHM) provides additional degrees of freedom for electron states in a lattice by including a higher energy orbital and hybridization parameters for electrons to take advantage of a reduced Coulomb repulsion in the upper orbital when the lattice is at half-filling.

This "relaxation" of the electronic state is accompanied by an asymmetry between electron and hole quasiparticles in the model. In this thesis we employ the computational tool of multiorbital dynamical mean field theory (MODMFT) to study electron-hole asymmetry in the DHM as evidenced in the behaviour of the quasiparticle weight and optical conductivity of electrons. In agreement with previous exact diagonalization work on the DHM, we find that the relaxation of electronic states is associated with quasiparticle dressing in the hole regime of the lower orbital, and a transfer of optical conductivity spectral weight from low to high frequencies. These observations are evidences of the electron-hole asymmetry in the two-orbital system.

In this context, we evaluate the role of two critical variables in the DHM: the local and nonlocal hybridizations which parameterize interorbital electron transitions in the Hamiltonian. We demonstrate that the electron-hole asymmetry of the model has a more complex relationship to these hybridization parameters than previously identified. Mott physics plays an essential role in the quasiparticle dressing due to the local hybridization, while the nonlocal hybridization promotes electron-hole asymmetry by providing a separate channel for electron transport which serves to reduce the quasiparticle weight of holes in the lower band.

We also briefly examine the phenomenon of orbital selective Mott transitions in the DHM within the parameter regime of electron state relaxation, and evaluate the role played

by the hybridization parameters in this context.

Acknowledgements

The first step in a graduate research program is to identify and investigate potential supervising faculty, across a variety of institutions, working within the appropriate, perhaps narrowly defined, field of study. My first meeting with Dr. Frank Marsiglio, in his crowded office with back-to-back overflowing bookshelves, confirmed for me that in my own backyard at the University of Alberta I would have a terrific opportunity to work with a creative, thoughtful and kindhearted supervisor with many years of experience in the field. After meeting with Frank it was not hard to turn down other offers at good schools. I am grateful for Frank's patience, insight and good humour. My family, especially my sons, have appreciated the hospitality shown by Frank and his wife, Mary, in their faith-filled home. I have learned a great deal from Frank's enthusiasm as a teacher, his ability to reveal the human and approachable side of abstract physics through storytelling, and his conviction that confluent hypergeometric functions of the second kind are the key to many of life's most important integrals.

The friendship of Burkhard Ritter, my office-mate over four years, was of tremendous moral and technical support. It is important to share one's victories and misery with someone walking the same journey, and more than anyone Burkhard has done that with me over the course our parallel PhD experiences. I am also mindful of helpful early discussions about the basics of DMFT with Giang Bach and Reza Nourafkan.

I appreciate the time taken by Professors Richard Sydora and John Beamish as members of my supervisory committee, along with Frank Hegmann and Charles Lucy who were involved in my candidacy meeting; and Joseph Maciejko and Mark Jarrell who took part in the final oral examination.

With much gratitude I mention the support and freedom provided my professional colleagues at Power to Change Ministries, who have made room for my long PhD journey - especially Melanie Dreger and Sean Cullen whose lives might have been easier had I never applied to the program.

I am amazed at the resilience and unwavering encouragement that my wife, Gretchen, has shown over this very busy multi-year project. There have been no obvious limits to her sacrificial flexibility and optimism. Thank you, my love, for a full and unrestrained commitment from beginning to end, with five years of no real vacations and little input into a process that at times had tremendous personal impact on you.

Together as a family we are most grateful to God for providing every good thing for us, exceedingly and abundantly beyond what we could ask or imagine.

Contents

List of Tables

List of Figures

Chapter 1

Strongly Correlated Electron Systems

1.1 Band Theory of Solids

In 1894 George Johnstone Stoney suggested the word "electron" to describe the fundamental unit of electricity in matter [1]. It would be two decades before Tolman and Stewart [2,3] provided experimental evidence that the electric current in metals such as copper, silver and aluminum is carried by negative charges with a mass very similar to that of the free electrons observed in cathode ray experiments such as J. J. Thomson's [4].

This electric current had been described in a classical theory of metallic conduction by Paul Drude in 1900 [5, 6] and later by Lorentz [7]. Drude's theory envisions a gas of electrons flowing through the crystalline environment of a metal's ionic constituents. The electrons move without restriction except for occasional collisions with the heavy atomic nuclei. Interactions between the electrons are neglected. Among its deficiencies, including a grossly imperfect estimate of specific heat, this free electron model offers no microscopic explanation of the difference between conductors and insulators, a distinction requiring a quantum mechanical wave-like extension of electrons throughout the periodic lattice of ionic potentials within a solid.

Early developments in quantum theory provided qualitative improvements to the classical free electron picture. A quantum theory of solids was formulated more accurately describing electronic energetics and transport properties in solid crystalline material [8]. Two key developments were Sommerfeld's incorporation of the Pauli exclusion principle and Fermi-Dirac statistics [9], and the interaction between the periodic lattice and electronic wave nature described by Felix Bloch [10], giving rise to the band theory of solids.

Assuming non- or weakly-interacting electrons in the ionic lattice, band theory provides a simple theoretical description of the metallic and insulating material states in terms of the concentration of electrons occupying energy bands arising from the bulk nature of the lattice. An atomic crystal lattice is formed by the lower energy state available to individual atoms via geometrically-arranged group binding, mediated by the electromagnetic attraction of the positively charged nuclei with the negatively charged electrons localized to other nearby nuclei. This reduction in energy from interactions yields the binding energy of the solid. The interatomic binding is classified in various types: van der Waals, ionic, covalent, metallic and hydrogen bonds, emphasizing different expressions of this attraction between positive ions and negative electrons as described by the application of the Schrödinger equation for the ionic system applied to the electronic wavefunctions.

In the limit of isolated atoms, electrons form shells related to their *in situ* angular momentum state, restricted by the Pauli exclusion principle to occupy different available states in the shell. As atoms are brought into spatial proximity to form a solid, the overall wavefunction of the atomic system realizes an energetically more favourable ground state through the sharing of electrons in incomplete shells.

Metallic binding involves the covalent sharing of electrons between atoms with incomplete electronic shells, yielding a crystal wavefunction that is a superposition of the various angular momentum states available to a localized electron, interacting with its environment of nuclei. The sharing of local electron states is an effective delocalization emphasizing the wave-like character of the otherwise particle-like, localized electrons. The resulting "fluid" of itinerant negative charge carriers acts as a binding agent for the ions which form the structure of the metallic solid. The stability of the metallic crystal associated with its binding energy is obtained by the lowering of electron kinetic energy through their spatial extension in the crystal.

Free electrons unaffected by an electric potential have a de Broglie wavelength,

$$\lambda = \frac{\hbar}{mv}\,, \tag{1.1}$$

with energy

$$E = \frac{\hbar^2 k^2}{2m}\,. \tag{1.2}$$

Within the constrained environment of the periodic crystal lattice, however, the momentum, $\hbar k$, and wavelength of single, non-interacting electrons become intertwined with the lattice periodicity and are redefined in terms of "crystal momentum" states which differ from the free electron states. These are ordered into energy bands.

Pauli exclusion demands that in any quantum system no two electrons can occupy the same quantum state as defined uniquely by a complete set of quantum numbers such as momentum along an axis of coordinate space. In a finite-sized crystal lattice with N sites, the number of possible momentum states available to electrons is limited by the dimensionality of the space, and the values of allowed momenta, k_n, are discretized accordingly, so that,

$$k_n = \frac{2\pi n}{Na} \tag{1.3}$$

where $n \in \mathbb{Z}$, $-\frac{N}{2} < n \leq \frac{N}{2}$, and a is the lattice spacing.

The consequence of the exclusion principle is that the electrons must be distributed throughout this allowed momentum-space, or Brillouin zone, across a wide range of values. Since each electron can have either intrinsic spin up or down, only two electrons can simultaneously hold a given momentum. Under the fictitious condition of zero temperature (free from thermal excitations), the electrons can be imagined to "fill" the momentum states of the lattice in twos up to the highest energy, labeled the "Fermi energy", ϵ_F, corresponding to a Fermi momentum, k_F. All states above the Fermi energy remain unoccupied, unless the electrons gain energy from their environment and become excited.

While electron drift is an inherent feature of a perfect lattice, including quantum mechanics in the theory of metals establishes the presence of forbidden states in the energy landscape of a crystalline material inhibiting uni-directional charge carrier conductance. These states arise at energies equivalent to the edges of the Brillouin zone and give rise to bands of allowed electron states separated by "gaps" of energy states that are forbidden to electron occupation. Electrical conduction involves the net transport of electrons in a direction selected by (and opposite to) some applied electric field. Under the condition of a full band, the situation of an insulator, the total current will necessarily be zero since every electron traveling in one direction will have a pair moving with opposite momentum according to 1.3. If, however, the band is partially filled then the application of an electric field will induce a net current since nearby electron states remain available to create a net flow of charge.

Thus, coordinate space electron transport within a crystalline material involves the transition of electrons between available energy states and band gaps act as energy barriers to electron transport under the condition that the average number of electrons per lattice site filling a volume of material is sufficient to completely fill the momentum-space Brillouin zone up to the top of a band. In the simplest case, this condition is expected to be satisfied for a volume of material containing some even number of electrons per lattice site, since under Pauli exclusion two electrons of opposite spin orientation are allowed per energy

state of the Brillouin zone. Excepting the case where a complicated lattice structure allows an overlap of energy bands, conduction can arise only through a partially occupied energy band, or the input of energy into the system sufficient to excite an electron near a band edge across a forbidden gap zone and into a higher and mostly unoccupied band, as in the case of semiconductors.

1.2 Mott Physics

The scenario of electrons crossing a band gap through thermal excitation was suggested by Wilson [11, 12] to explain the behaviour of semiconducting materials with a narrow forbidden region. With an increased environmental temperature, the electrons would experience an emptying of a few states in the lower band and the subsequent occupation of a few excited electrons in the lowest energy states of the band immediately above the gap, resulting in thermally-mediated conduction within both bands.

It was noted, however, by DeBoer and Verwey [13] that Wilson's simple and elegant band theory was insufficient to properly explain the behaviour of a large class of transition metal oxides like NiO which do not exhibit full electron bands, having on average an odd number of electrons per lattice site, but are nonetheless not metallic. In response came Peierls' proposal that "a rather drastic modification of the present electron theory of metals" was required by accounting for the effects of electron-electron interactions on generating insulating behaviour [14]. This avenue was explored by Mott in the context of crystalline arrays of atoms under pressure or with variable lattice spacing at zero temperature [15–17].

Mott argued that a change in atomic volume would result in a sharp phase transition between metallic and non-metallic behaviour caused by the splitting of a band into two subbands when there is only a small overlap of electron wavefunctions between neighbouring atomic orbitals. A lower energy band is formed from electrons residing alone on lattice sites, and a higher band from doubly-occupying electrons which are unable to avoid the high cost of their mutual Coulomb repulsion.

This band splitting involves the evolution of a metal-insulator gap, illustrated in figure 1.1, due to the strong Coulomb repulsion between electrons in a half-filled lattice. The transition between metallic and insulating behaviour for half-filled bands has been a voraciously studied phenomenon in condensed matter physics which has become known as the Mott (or Mott-Hubbard) metal-insulator transition (MIT). It arises from the competition between the wave and particle natures of the electrons in the lattice, as the delocalization of their wave property is constrained by the repulsion of multiple negative charge carriers

occupying the spatially confined environment of a single lattice site [18]. Electron delocalization tends toward occasional double occupancy of lattice ions and thus a repulsive interaction between the charge carriers. For systems in which the Coulomb repulsion is large compared to the overlap of electron orbitals between neighbouring lattice sites, the likelihood of double occupancy becomes energetically unfavourable. In the case of a lattice that is exactly half-filled by electrons, the lower Mott sub-band will be exactly filled and the upper band empty with an energy gap between localizing the otherwise itinerant electrons.

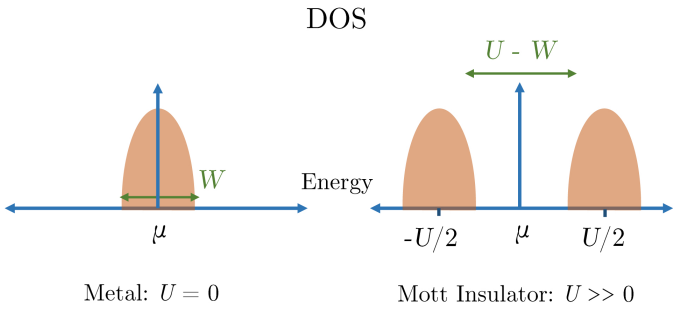

Figure 1.1: Electron density of states (DOS) at half-filling, illustrated for the metallic case and that of the Mott insulator. The bandwidth, W, is associated with the kinetic energy (or more specifically, the hopping parameter, t, of the Hubbard Hamiltonian [1.4]). Electron filling in both cases is from low energy up to the chemical potential μ. The metallic electrons form a Drude peak around energy states equal to the chemical potential, with available states energetically congruent to filled states, thus allowing small excitations to generate conductance. For the insulator, when the Coulomb repulsion U is large, the electron states split into two bands separated by a gap. The lower band, associated with electrons individually occupying lattice sites, is filled. The higher energy band is associated with (unfilled) electron states of doubly-occupied sites. Only an increase in the chemical potential or large excitations (*e.g.* thermal) will cause electron transitions into these states, allowing conduction.

The Mott-Hubbard MIT is a central and illustrative problem in modeling strong correlation effects resulting from the spatial confinement of narrow electron orbitals in many condensed matter materials. Where band theory predicts metallic behaviour for partially filled bands, strong interactions between electrons lead to observable MITs in transition metal oxides such as vanadium sesquioxide (V_2O_3) [19]. These materials, along with rare earth metals, have partially filled narrow $3d$ and $4f$ bands, respectively, where the strong correlation between spatially confined electrons becomes a critical driver of interesting physics including high temperature superconductivity, colossal magnetoresistance and the

MIT [20].

1.3 Fermi Liquid Theory

The complex behaviours of strongly correlated electron systems provide a challenge for theoretical descriptions which take into account the multiparticle relationships of the materials in which they occur. Capturing the effects of Coulomb interactions between many electrons in a lattice is a daunting task in theoretical modeling that is greatly simplified by the tenets of Fermi liquid theory [21, 22].

Fermi liquid theory describes the excitations of electrons in an interacting many-body system at finite temperature through effective "quasiparticles." The states of the quasiparticles are assumed to be in adiabatic continuity with those of a non-interacting electron system and can therefore be labeled with the same quantum numbers as the non-interacting states. As well, one assumes that while the unique states of electrons subject to Coulomb interactions may be short-lived in the material, the quasiparticle states have a long lifetime and behave as essentially free particles with a rescaled effective mass, m^*, which is dependent on the self energy of the quasiparticles (and thus their mutual interactions) and their lifetime as measured by the weight of the coherent part of the single-particle Green's function [23].

In this thesis, the quasiparticle picture of Fermi liquid theory is assumed to be a correct description of the metallic states of the systems investigated, breaking down in the transition to insulating behaviour in the MIT. In section 5.3 we will define the quasiparticle weight as a measure of the quasiparticle coherence, an important tool in evaluating our model of strongly correlated electrons.

1.4 Hubbard Model

One very important theoretical approach to describing strong correlations between electrons in spatially confined systems is the Hubbard model [24–27], a straightforward mathematical description of the microscopic energy state of these materials. Grounded in the tight-binding approximation of electron-ion wave function overlap in a crystalline solid [28], the Hubbard model provides a simple but remarkably effective encapsulation of the real material energetics arising from Coulomb repulsion between spatially proximate electrons and the propensity of these charge-carriers to travel among the ions of a lattice, as governed by the overlap of electron wave functions.

In the formalism of second quantization, the Hamiltonian for the Hubbard model is given as,

$$H = -\sum_{i,j,\sigma} t_{ij}(c^{\dagger}_{i\sigma}c_{j\sigma} + c^{\dagger}_{j\sigma}c_{i\sigma}) + U\sum_{i} c^{\dagger}_{i\uparrow}c_{i\uparrow}c^{\dagger}_{i\downarrow}c_{i\downarrow}, \tag{1.4}$$

where i and j indicate particular lattice sites on which electrons with spin σ are localized in Wannier orbitals. The operators, $c^{\dagger}_{i\sigma}$ and $c_{i\sigma}$, respectively create and annihilate an electron at site i with spin σ. In the second term, the Coulomb repulsion, U, acts only locally between electrons occupying the same lattice site, with their spin state denoted by $\uparrow$ and $\downarrow$. The first term gives the kinetic energy contribution from electron transport through the lattice, which is modeled as tunneling or "hopping" of charge-carriers between sites due to the overlap between electron orbitals and the attractive potential well of neighbouring ionic centres. t_{ij} is the hopping integral of electrons moving between the labeled sites, and is normally restricted to nearest neighbouring atoms so that

$$t_{ij} \to t\sum_{\hat{\alpha}} \delta_{i+\hat{\alpha},j} = t \tag{1.5}$$

where $\hat{\alpha}$ denotes all vectors pointing to a nearest neighbour.

In the interests of simplicity, (1.4) ignores many characteristics of real lattices including spin-spin interactions, the motion of the lattice ions, asymmetry in electron propagation, extended hopping of electrons beyond nearest-neighbour sites (with [1.5]), and long range Coulomb interactions of the form $U(\mathbf{R}_{ij}) = e^2/\mathbf{R}_{ij}$. Thus the present model captures the essential physics contained in the competition between the strongest (local) electron-electron interactions and their kinetic energy.

Although developed with narrow d and f band phenomena in mind [24], the Hubbard model (1.4) describes a single s-band with spatial symmetry [26]. The band is comprised of N discrete electron energy states, where N is the number of lattice sites in the crystal (becoming a continuous distribution of levels in the thermodynamic limit of $N \to \infty$). Each site, and thus each energy level can be occupied by at most two electrons of opposite spin ("up" and "down"), in keeping with the uncertainty principle as discussed in section 1.1. Thus, a Hubbard lattice is "filled" with $2N$ electrons. A filling operator, $\hat{n}$, is defined for the average number of electrons per lattice site,

$$\hat{n} = \frac{1}{N}\sum_{i\sigma} c^{\dagger}_{i\sigma}c_{i\sigma}\,, \tag{1.6}$$

and returns the expectation value $n = 1$ for half-filling and $n = 2$ when the lattice is completely full.

The filling of the model can be affected by considering the Hamiltonian (1.4) in the so-called "grand canonical ensemble" with a third term defining the chemical potential μ so that,

$$H = -\sum_{i,j,\sigma} t_{ij}(c^\dagger_{i\sigma}c_{j\sigma} + c^\dagger_{j\sigma}c_{i\sigma}) + U\sum_i c^\dagger_{i\uparrow}c_{i\uparrow}c^\dagger_{i\downarrow}c_{i\downarrow} - \mu\sum_{i\sigma} c^\dagger_{i\sigma}c_{i\sigma}\,. \tag{1.7}$$

A basis for the overall state of the lattice is given by the direct product of the states of all of the site configurations. Each site, j, has four possible states [where the arrows represent the spin of the occupying electron(s)]: $|\emptyset\rangle_j$ (unoccupied site), $|\uparrow\rangle_j$, $|\downarrow\rangle_j$ and the doubly-occupied site, $|\uparrow\downarrow\rangle_j$. The Hilbert space of the entire N-site Hubbard state is therefore of size 4^N.

In the non-interacting limit, $U = 0$, the Hubbard model contains only the initial nearest-neighbour hopping term. Under Fourier transformation the momentum eigenvalues are,

$$\epsilon_{k_n} = -2t\cos k_n \tag{1.8}$$

where k_n is the free electron momentum in (1.3).

In the more general case of non-zero electron-electron interactions ($U \neq 0$) the solution to the Hubbard model is challenging, and has only been found exactly for the one-dimensional lattice [29].

An important characteristic of (1.4) is particle-hole symmetry; that is, that any phase diagram generated from solutions to the model is symmetric about $n = 1$ [30]. Thus the physics of systems that are *accurately* described by the Hubbard model should be the same for the charge carriers being particles or holes. Within Fermi liquid theory the quasiparticles of the Hubbard lattice can be identified in adiabatic continuity with either electrons or holes and will be referred to in this thesis as such with the quasiparticle picture implicitly understood. In the limit of low filling ($n \approx 0$) the quasiparticles are understood to be electron-like, whereas for a nearly full band ($n \approx 2$) they are hole-like. This distinction becomes important for the two-band dynamic Hubbard model introduced in chapter 2, where electron-hole *asymmetry* predominates under certain conditions.

1.5 Thesis Overview

In this thesis we perform a computational study of the Dynamic Hubbard model (DHM), a two-orbital extension of the single band Hubbard model (1.4). The DHM is motivated and defined in chapter 2, and a survey is made of previous work on Hamiltonians similar to the DHM. This model has been extensively studied by Hirsch [31] using four-site exact

diagonalization, focusing on the electron-hole asymmetry. The primary focus of our thesis is to explore the same model as Hirsch using more sophisticated tools.

Our computational tool for studying the DHM is a multiorbital extension of Dynamical Mean Field Theory (DMFT). The conventional, or single orbital DMFT formalism and method will be outlined in chapter 3, with a particular focus on its application to the Hubbard model (1.4) and the MIT.

Chapter 4 provides the necessary extension of single orbital DMFT to the two-orbital context of the DHM, through multiorbital DMFT (MODMFT). The MODMFT formalism used in our work will be defined and the workflow specified for solving DHM Hamiltonians with arbitrary parameter sets. We have developed an original implementation of MODMFT in the C++ programming language. The most important characteristic of our algorithm is the inclusion of both local and nonlocal hybridization parameters in the Hamiltonian, a requirement for a proper comparison with the results of Hirsch's DHM formulation. The nonlocal hybridization of multiorbital systems has received very little attention in the literature of MODMFT and our implementation provides original insight into its role in strongly correlated multiorbital models.

Results from the MODMFT method are dependent on the selection of particular outputs. These tools of our analysis are laid out in chapter 5, defining observables which give us insight into the DHM physics. In particular, Hirsch's examination of electron-hole asymmetry focuses on the behaviour of the quasiparticle weight and optical conductivity in response to dressing of quasiparticles. We have developed the analytical and computational tools to measure these outputs in the context of our method, and our specific definitions provide an original contribution to the study of multiorbital systems.

In chapter 6 we present a number of checks and limits on our MODMFT study of the DHM. We include a demonstration of consistency with the single band results of DMFT and the non-interacting limit, as well as justification of some analysis choices which provide necessary efficiencies in the computational regimen.

The results of our study are finally presented in chapter 7, where we compare our MODMFT calculations with previous work on the DHM. In particular we explore the phenomenon of electron-hole asymmetry through the quasiparticle weight and optical conductivity, and evaluate the influence of the orbital hybridizations on these properties. We emphasize the role of the as-yet poorly understood nonlocal hybridization which parameterizes interorbital electron transport through the lattice. At the end of chapter 7 we briefly address the appearance of orbital selective Mott transitions which arise from the energetically dissimilar orbitals of the DHM, and are sensitive to the hybridization parameters. These transitions are not directly relevant to our examination of electron-hole

asymmetry in the DHM, but are nonetheless a feature of the DHM which apparently has not been previously explored.

Our results and outlook are summarized in the conclusion, chapter 8.

Chapter 2

Dynamic Hubbard Model

2.1 Limitations of the Single Band Hubbard Model

The conventional Hubbard model (1.4) is a simple description of electronic behaviour in a many-particle lattice system, incorporating competition between electronic transport and Coulomb repulsion in determining the system's dynamics. The simplicity of the model is due in large part to the assumption of a single band with s-wave symmetry, so that electron transport through the lattice is isotropic [26].

The Coulomb repulsion term in the Hubbard model assumes an on-site interaction, U, between electrons in a doubly-occupied configuration of a single atomic orbital. This interaction energy can be derived from the single electron wavefunctions supposing that at each site both electrons are in a hydrogenic ground state ($1s$ orbital),

$$\psi_{1s}(Z,r) = \left(\frac{Z^3}{\pi a_0^3}\right)^{1/2} e^{-Zr/a_0}, \tag{2.1}$$

with atomic number Z, Bohr radius a_0, and r the distance from the ionic centre. The Coulomb repulsion, $U(r)$, is then calculated to be,

$$\begin{aligned} U(Z) &= \int d^3r d^3r' \left|\psi_{1s}(r)\right|^2 V_{\text{coulomb}}(r,r') \left|\psi_{1s}(r')\right|^2 \\ &= \int d^3r d^3r' \left|\psi_{1s}(r)\right|^2 \frac{e^2}{|\vec{r}-\vec{r}'|} \left|\psi_{1s}(r')\right|^2 = \frac{5}{4}(13.606\,\text{eV})Z. \end{aligned} \tag{2.2}$$

Hirsch [32] used experimental data [33] to show that the measured *effective* Coulomb energy of a doubly-occupied site is consistently different from the value calculated above under the Hubbard model's single s-band simplification. This effective energy, from mea-

sured values, is simply,

$$U_{\text{eff}} = 2E_1 - E_2 \tag{2.3}$$

where E_1 is the energy of a lone electron bound to the positive nucleus, and E_2 is the energy of two electrons bound to the nucleus. The doubling of the first term immediately assumes non-interacting electrons, and thus the difference of the terms is the net effect of including Coulomb repulsion on a doubly-occupied site.

For hydrogen ($Z = 1$), one uses the ionization energy, $E_1^{\text{H}} = 13.606\,\text{eV}$ and the electron affinity, $A^{\text{H}} = 0.754\,\text{eV} = E_2^{\text{H}} - E_1^{\text{H}}$ to find,

$$U_{\text{eff}}^{\text{H}} = 12.844\,\text{eV} = U(1) - 4.154\,\text{eV}, \tag{2.4}$$

where $U(1)$ is the expected value from hydrogenic orbitals defined in (2.2).

For helium ($Z = 2$) and further up the periodic table, 2.3 is the difference in the two upper ionization energies, $I_Z^Z - I_{Z-1}^Z$. Thus,

$$U_{\text{eff}}^{\text{He}} = I_{II}^{\text{He}} - I_I^{\text{He}} = 54.418\,\text{eV} - 24.587\,\text{eV} = U(2) - 4.164\,\text{eV}. \tag{2.5}$$

The difference in energy of about 4 eV between measurements and the theoretical values of (2.2) is obvious for $Z < 8$, and is plotted in figure 2.1 using the limit of currently available data [33]. The overall offset of the data points suggests that the electron interactions have a strong effect on the state of the two-electron atom across all values of Z.

Atomic electron orbitals are therefore not rigidly hydrogenic, as assumed in the single-band Hubbard picture. This reality motivates alternative approaches to providing a more realistic picture of the electronic wave function in a many-particle system.

One such approach has been the development of more sophisticated wave functions to describe the two-electron atom, taking into account the electron-electron correlations. The most straightforward example [34] is a variational solution first developed by Frenkel [35] from the trial Hartree wave function,

$$\Psi_{\text{Fre}}(r_1, r_2) = \psi_{\tilde{Z}}(r_1)\psi_{\tilde{Z}}(r_2) \tag{2.6}$$

where r_1 and r_2 are the electron spatial coordinates of hydrogenic wavefunctions from (2.1). The effective atomic number,

$$\tilde{Z} = Z - \frac{5}{16}, \tag{2.7}$$

is determined by minimizing the energy, and suggests shielding of the nucleus from one electron by the other [36].

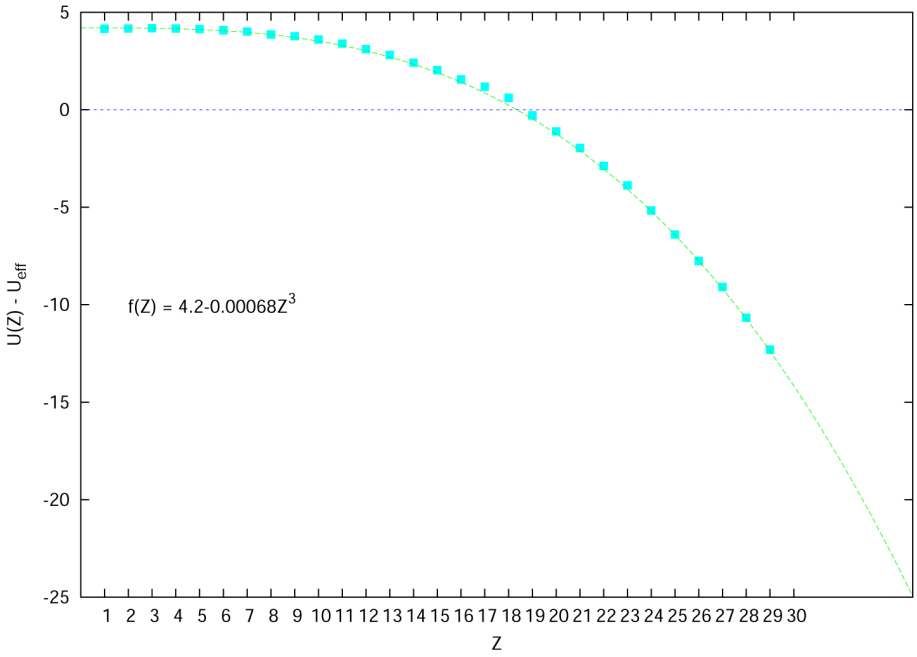

Figure 2.1: Energy difference between the Coulomb repulsion U^Z, calculated for two electrons in hydrogenic $1s$ orbitals around a nucleus of atomic number Z and the experimental values [33] for the effective Coulomb interaction of doubly-occupied ionized nuclei. A fit (solid line), $f(Z)$, to the data (points) is also shown.

Eckart [37] improved on this with a more sophisticated variational wave function including radial correlations between electrons:

$$\Psi_{\mathrm{Eck}}(r_1, r_2) = \frac{\psi_{Z_1}(r_1)\psi_{Z_2}(r_2) + \psi_{Z_2}(r_1)\psi_{Z_1}(r_2)}{2\left(\int \psi_{Z_1}(r)\psi_{Z_2}(r)dr\right)}. \tag{2.8}$$

finding effective values of $Z_1 \approx 2.14$ and $Z_2 \approx 1.19$ for helium. More recently these have been reevaluated in a more general form by Hirsch [36] as $Z_1 \approx 1.14Z - 0.105$ and $Z_2 \approx 0.905Z - 0.622$.

Still more reliable is the approach taken by Hylleraas [38] who allowed for radial and angular correlations between electrons in a trial wavefunction, $\Psi_{\mathrm{Hyl}}(\vec{r}_1, \vec{r}_2)$, by including the spatial separation $r_{12} = |\vec{r}_1 - \vec{r}_2|$ as a parameter [36].

Table 2.1 compares the energy of the two-electron atom arrived at through the three approaches, alongside the experimental value for $Z = 1$ and $Z = 2$ nuclei. It is clear that the inclusion of the angular information in Ψ_{Hyl} provides an important contribution to procuring a physically improved result which provides a better approximation of the true Helium eigenspectrum than does the $1s$ and $2s$ orbitals of a radial central potential

solution [39]. In all three approaches, as illustrated in figure 2.2, there is a qualitative distinction between the eigenstate of a single electron orbiting its nucleus and that of the electron orbiting along with a second electron. This distinction captures the essential change the electron must undergo because of the strong correlations in the system.

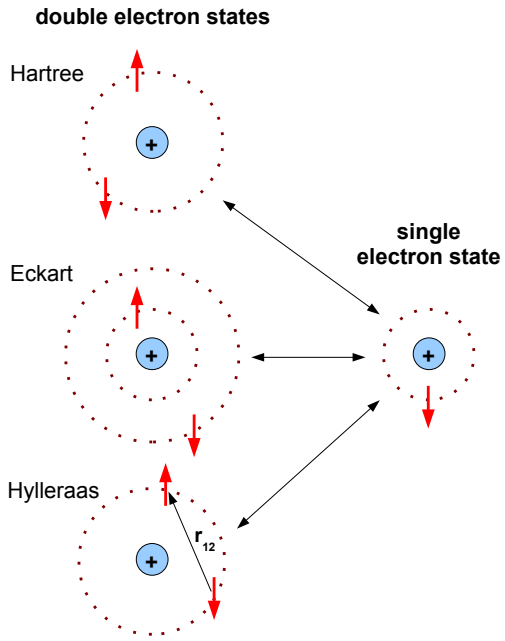

Figure 2.2: Illustration of electron orbital reorganization under various double occupancy wavefunctions. A single electron occupies its own orbital around the nucleus. Joined by a second electron (of opposite spin), the electron orbital much adjust. The Hartree variational wavefunction places both electrons in the same expanded orbital. In the Eckart picture, the electrons occupy separate orbitals. In the Hylleraas picture, the electrons share an orbital but the two-electron wavefunction is sensitive to their relative separation.

Table 2.1: Energies (in eV) found from the variational wave functions Ψ_{Fre}, Ψ_{Eck} and Ψ_{Hyl}, compared with the experimental value, E_{exp}, for nuclei of $Z = 1$ and $Z = 2$ (data adapted from [36]).

Z	E_{Fre}	E_{Eck}	E_{Hyl}	E_{exp}
1	-12.86	-13.97	-14.30	-14.36
2	-77.49	-78.25	-78.98	-79.02

2.2 The Many-Particle Case

While successful in approximating the state of a single interacting two-electron ion, it is not difficult to see that a different approach is required with respect to the Hubbard Hamiltonian which models a many-body lattice. In that context it is necessary (and expedient) to imagine highly localized hydrogen-like Wannier orbitals in keeping with the tight-binding model [30], but still somehow capture the qualitative distinction in the electronic states of singly-occupied and doubly-occupied atoms.

The dynamic Hubbard model (DHM) provides just such an approach, extending the single-orbital Hubbard model to a two-orbital characterization of the strongly-correlated system. In the DHM, the electron eigenstates are allowed to change in response to occupation and the accompanying energetic adjustments of local interactions. The intra-atomic Coulomb repulsion between doubly-occupying electrons will cause their wavefunctions to hybridize among higher energy single particle states which allow greater spatial separation of the electron densities under the Coulomb integral (2.2), thus reducing the overall energy of the total eigenstate [40].

The importance of including a second orbital at higher energy into the Hubbard description can be illustrated with the relatively simple case of the helium atom. It serves as a practical example of the complexity of real systems. The helium Hamiltonian, in the Born-Oppenheimer approximation and neglecting spin-orbit coupling, is,

$$H_{\mathrm{He}} = -\frac{\hbar^2}{2m}\left(\nabla_1^2 + \nabla_2^2\right) - Ze^2\left(\frac{1}{r_1} + \frac{1}{r_2}\right) + \frac{e^2}{|\vec{r_1} - \vec{r_2}|} \tag{2.9}$$

where $Z = 2$ for the helium nucleus. The two-particle Coulomb repulsion is encapsulated in the last term of (2.9), and is the complicating factor in determining the exact ground state of the system. The ground state solution, the form of which is known through variational calculations to a high degree of accuracy [41], spans a specialized set of basis functions which are substantially different from the usual hydrogenic orbitals, as discussed in section 2.1.

In terms of explicitly hydrogenic orbitals, a complete solution of (2.9) has been shown [42] to include a superposition of all the bound and continuum states of the helium system. Compared to an accurate variational Hylleraas wave function [38], the spin singlet ground state,

$$\Psi_{\mathrm{singlet}}(r_1, r_2) = \frac{1}{\sqrt{2}}\left[\phi_\uparrow(r_1)\phi_\downarrow(r_2) - \phi_\downarrow(r_1)\phi_\uparrow(r_2)\right], \tag{2.10}$$

a product of spin-up $\phi_\uparrow$ and spin-down $\phi_\downarrow$ hydrogenic $1s$ orbitals, contributes only 92.6%

of the proper helium ground state. An additional 4.6% of the variational ground state is recovered by inclusion of the excited state where one electron occupies the 1s orbital and the other populates the $2s$ orbital [42].

From this analysis, it is clear that a two-orbital hybridization model of a many-particle system will provide an important physical degree of freedom to capture the physics of real lattices. The DHM Hamiltonian is designed with this improvement in mind.

2.3 Varieties of Dynamic Hubbard Models

Three classes of Hamiltonian have been proposed by Hirsch [36,43] which extend the Hubbard model to include the necessary physics of a DHM. In any such model, the orbital hybridization of doubly-occupied sites must appear within the local part of the Hamiltonian, H_i, as a component of the full Hamiltonian,

$$H_{\mathrm{DHM}} = -\sum_{\langle ij\rangle} t_{ij}\left(c^{\dagger}_{i\sigma}c_{j\sigma} + c^{\dagger}_{j\sigma}c_{i\sigma}\right) + \sum_{i} H_i\,. \tag{2.11}$$

where $\langle ij\rangle$ indicates that electrons only travel between nearest neighbours. Two of these models capture this "orbital relaxation" in an effective mechanism, while the third contains the $2s$ orbital explicitly.

The first case [32] is a variant of the Holstein Hamiltonian [44], coupling a boson oscillator having creation and annihilation operators, $a^{\dagger}_i$ and a_i, to double occupancy of a single orbital. The oscillator has mass M, spring constant K, and frequency $\omega_0 = \sqrt{K/M}$. In this case, the local part of (2.11) might have the form,

$$H_i = H_{\mathrm{DHMo}} = \omega_0 a^{\dagger}_i a_i + \left[U + g\omega_0\left(a^{\dagger}_i + a_i\right)\right] n_{i\uparrow}n_{i\downarrow}\,, \tag{2.12}$$

where g is a coupling constant giving an effective on-site repulsion $U_{\mathrm{eff}} = U - \omega_0 g^2$ when a second electron is added to the single orbital. The on-site repulsion is transformed into a dynamical variable dependent on the displacement of the oscillator,

$$x_i = \frac{a + a^{\dagger}}{\sqrt{2M\omega_0/\hbar}}\,, \tag{2.13}$$

which effectively models the change in electron orbital occupancy driven by Coulomb repulsion.

The boson oscillator model (2.12) has been studied using a generalized Lang Firsov transformation [32,45,46].

Similarly, the DHM physics can be captured through a Hamiltonian with an auxiliary spin degree of freedom [36, 47, 48], where, for instance,

$$H_i = H_{\text{DHMs}} = \omega_0 \sigma_i^x + g\omega_0 \sigma_i^z + [U - 2g\omega_0 \sigma_i^z]\, n_{i\uparrow} n_{i\downarrow}. \tag{2.14}$$

Here, σ_i^x and σ_i^z are spin-$\frac{1}{2}$ Pauli matrices providing a dynamic local degree of freedom coupled to electronic double-occupancy. Again, the effective Coulomb repulsion depends on the form of the auxiliary parameter, in this case, a local spin, whose energy levels have a spacing ω_0. On double occupancy, the local electronic orbitals are effectively adjusted in reaction to the new energy conditions.

The auxiliary spin scenario (2.14) has been studied by exact diagonalization of a four-site one-dimensional chain [48, 49], larger chains (up to 20 sites) using quantum Monte Carlo in one [49] and two [50] dimensions, two-site dynamical mean field theory [51] and exactly solving a simple dimer model [52].

A third and more direct approach [31, 40] to the orbital relaxation of double-occupancy augments the Hubbard Hamiltonian (1.4) with additional electronic degrees of freedom only. In this scenario, each lattice site allows electron occupation of a lower (0) or upper (1) energy level. As illustrated in figure 2.3 the lattice is characterized by two electron bands centered on different energies, ϵ_0 and ϵ_1, with intraband hopping t_0 and t_1 between nearest-neighbour sites, and interband intersite hopping $t_{01} = t_{10}$. There are three Coulomb interactions among localized electrons: U_0 for a doubly-occupied lower orbital, U_1 for the upper excited orbital, and U_{01} acting between electrons occupying separate orbitals. In addition, an intra-atomic hybridization parameter t' mixes the onsite identity of electrons between the upper and lower orbitals[1]. We will refer to the hybridization variables t' and t_{01}, respectively, as "local" and "nonlocal".

The full Hamiltonian for this "electronic" DHM including both the local (H_i) and

[1]Recalling the identification of the single band Hubbard (1.4) orbital as $1s$, we note that in a strict sense, we must be cautious about similarly considering these orbitals of the DHM as $1s$ and $2s$ states of the hydrogen atom, since the essential dynamic of this model assumes single-electron transitions between the orbitals in response to the presence or absence of a second electron. Quantum mechanical selection rules forbid the direct transition of an electron between states where the change in angular momentum quantum number, l, would be $\Delta l = 0$, as would apply in a transition between 1s and 2s orbitals of the hydrogen atom. The physical meaning of these orbitals can be taken as signaling the creation of a set of new, hybridized orbitals of energy E_- and E_+ (clearly defined in the non-interacting limit of section 6.6), which might taken as approximations of the Hylleraas states discussed above.

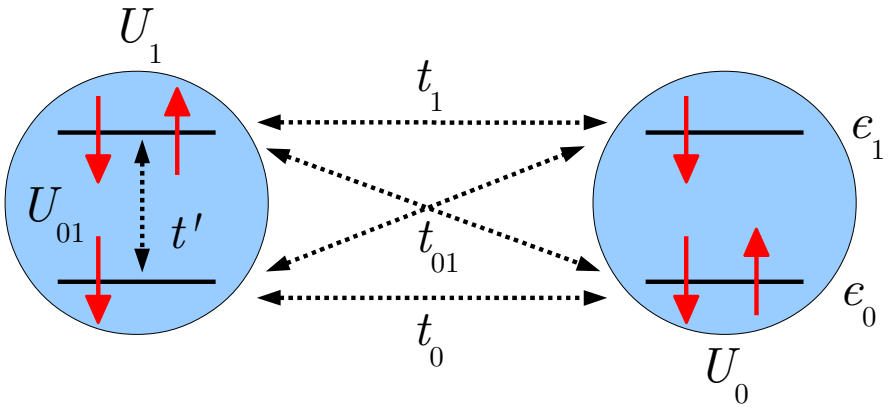

Figure 2.3: Two nearest-neighbour lattice sites illustrating the parameters in the electronic DHM Hamiltonian (2.15). The bare energy of electrons occupying the lower orbital is ϵ_0, and the upper orbital ϵ_1. The dotted arrows indicate electron tunneling between sites parameterized by overlap integrals t_0 and t_1, as well as a nonlocal hybridization t_{01}. This, along with the local hybridization factor t', provides a degree of freedom for electrons to transition between orbitals to lower the energy of double occupancy. The Coulomb repulsions U_0 and U_1 apply to doubly-occupied lower and upper orbitals, respectively. U_{01} is the energy penalty for an electron-electron interaction between the orbitals.

non-local parts of (2.11), in the grand canonical ensemble, is now,

$$
\begin{aligned}
H_{\mathrm{DHMe}} &= H_{\mathrm{KE}} + H_{\mathrm{local}} + H_{\mathrm{hyb}} \qquad (2.15)\\
H_{\mathrm{KE}} &= -\sum_{\langle ij\rangle\sigma}\Big[t_0(c^\dagger_{0i\sigma}c_{0j\sigma} + c^\dagger_{0j\sigma}c_{0i\sigma}) + t_1(c^\dagger_{1i\sigma}c_{1j\sigma} + c^\dagger_{1j\sigma}c_{1i\sigma})\\
&\quad + t_{01}(c^\dagger_{1i\sigma}c_{0j\sigma} + c^\dagger_{0j\sigma}c_{1i\sigma})\Big]\\
H_{\mathrm{local}} &= U_0\sum_i n_{0i\uparrow}n_{0i\downarrow} + U_1\sum_i n_{1i\uparrow}n_{1i\downarrow} + U_{01}\sum_{i\sigma\sigma'} n_{0i\sigma}n_{1i\sigma'} + (\epsilon_0-\mu)\sum_{i\sigma} n_{0\sigma}\\
&\quad + (\epsilon_1-\mu)\sum_{i\sigma} n_{1\sigma}\\
H_{\mathrm{hyb}} &= -t'\sum_{i\sigma}(c^\dagger_{0i\sigma}c_{1i\sigma} + c^\dagger_{1i\sigma}c_{0i\sigma})
\end{aligned}
$$

In principle, the generality of (2.15) through the variability of its coefficient parameters permits overlap of the electronic DHM with other, similar double band Hubbard models which nonetheless do not capture the fundamental physics associated with the characteristic adjustment of electronic orbitals particular to the premise of the DHM. For example, a

periodic Anderson model (PAM) [53] with one or two[2] conduction bands (having electron operators d and f) and local hybridization t' is characterized by the general Hamiltonian,

$$\begin{aligned} H_{PAM} &= \sum_{k\sigma}\left(\epsilon_k^d d_{k\sigma}^\dagger d_{k\sigma} + \epsilon_k^f f_{k\sigma}^\dagger f_{k\sigma}\right) + \sum_{i\sigma}\left(\epsilon_d d_{i\sigma}^\dagger d_{i\sigma} + \epsilon_f f_{i\sigma}^\dagger f_{i\sigma}\right) \\ &+ U\sum_i n_{fi\uparrow} n_{fi\downarrow} + t'\sum_{i\sigma}\left(d_{i\sigma}^\dagger f_{i\sigma} + f_{i\sigma}^\dagger d_{i\sigma}\right). \end{aligned} \tag{2.16}$$

In the single-band PAM (for instance [54]), associating the f-orbital with the lower interacting electrons in (2.15) implies $U_0 = U$ and $t_0 = t_{01} = 0$; associating the f electrons with the upper orbital defines $U_0 = 0$ and $t_1 = t_{01} = 0$, with the lower orbital electrons being itinerant. In the two-band PAM, both hopping parameters are simultaneously non-zero allowing the possibility of two conducting bands.

In either case, (2.16) is formally equivalent to a special variety of (2.15), but further consideration is required to identify whether specific incarnations of (2.15) (and [2.16]) can provide the necessary physics of a DHM.

With this in mind, for the present purpose a set of minimal restrictions on (2.15) to evaluate the fundamental physics of orbital relaxation would include,

Condition 1: A non-zero Coulomb repulsion, $U_0 > 0$, in the lower orbital, *motivating* a reflexive dynamic in electronic double occupancy.

Condition 2: A non-zero local or nonlocal hybridization, t' or t_{01}, thus *allowing* the reorganization of electrons in the orbitals on double occupancy.

Condition 3: A non-zero hopping parameter, t_0, for the lower band, associated with the itinerant electrons described in the single band Hubbard model which experience the adjustment of their wavefunction on double occupancy.

Condition 4: An energy gap between the two orbitals so that $\epsilon_1 > \epsilon_0$, avoiding the case of orbital degeneracy.

The two-band PAM (2.16) has been studied by Kogoutiouk and Terletska [55] for $t_0 = t_{01} = 0$ and $U_1 = 0$, which parameters do not meet condition 3 in (2.3). Similarly, the use of an attractive U_0 in the two-band PAM studied by Sarasua and Continentino [56] violates the requirement of repulsion in Condition 1. By contrast, Continentino *et al.* ([57]) and Tovar Costa *et al.* ([58], [59]) examined the MIT and the effect of t' in (2.16) with two conduction bands and $U_1 = 0$. Their quite general analysis allows for agreement with all

[2]Essentially a double-band Hubbard model with on-site hybridization.

the conditions in (2.3), although the motivation of orbital relaxation physics appears not to have been explicit.

A two-band Hubbard model with intra-orbital hybridization t_{01} (and including an exchange interaction) has been studied with quantum Monte Carlo dynamical mean field theory by Koga *et al.* [60], providing interesting results relating to the effect of hybridization on the orbital-selective Mott transition (see section 7.6). However, this particular realization of (2.15) employs degenerate electron bands, thus violating condition 4 as a necessary characteristic of a dynamic Hubbard model.

Hirsch [40] identified two further restrictions on the relative values of parameters in the electronic Hamiltonian (2.15):

$$U_1 + 2\epsilon_1 < U_{01} + \epsilon_0 + \epsilon_1 < U_0 + 2\epsilon_0 \tag{2.17}$$

$$U_0, U_{01} >> \epsilon_1 >> t_0 \,. \tag{2.18}$$

These restrictions in (2.17) involve the energy ordering of two-particle states of the lattice sites, ensuring that electrons on doubly-occupied sites will tend to favour the upper orbital over the lower due to the reduced cost of Coulomb repulsion from U_1. This ordering is illustrated in figure 2.4 and reflects the underlying classical intuition that electron pairs in the $2s$ orbital have less spatial overlap of their densities due to a larger orbital size than $1s$ electron states [40].

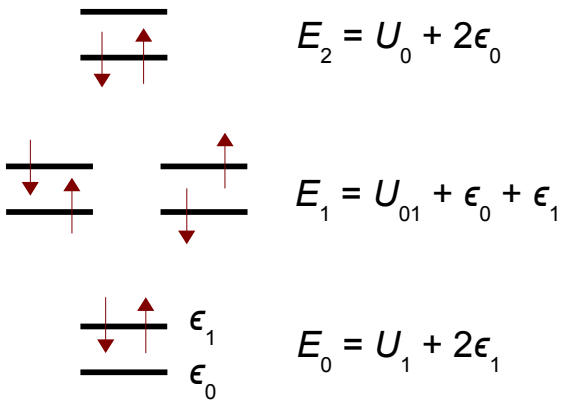

Figure 2.4: The non-hybridized two-electron energy states of the dynamic Hubbard model Hamiltonian (2.15), when the energy scaling condition (2.17) is applied. The lowest energy state, E_0, obtains with double-occupancy in the upper orbital. The highest energy double-occupancy state, E_2, has the electrons both populating the lower orbital.

Parameter relationships expressed in (2.18) are intended to reflect the length scales of real lattices: due to spatial proximity, electrons interact more strongly with one another via Coulomb repulsion than they do with the attractive nucleus they orbit ($U_0, U_{01} >> \epsilon_1$); and interatomic distances are larger than intra-atomic distances ($\epsilon_1 >> t_0$). This second inequality on atomic length scales also encapsulates an important aspect of the DHM that makes it essentially *dynamic*: that intra-atomic states tend to respond quickly to the local electron occupancy conditions, remaking the site orbital on a shorter time scale than applies to hopping [40].

The electronic DHM Hamiltonian (2.15) differs from the other two DHM realizations, (2.12) and (2.14), by allowing a full occupancy of a lattice with four electrons. Pauli exclusion restricts each site orbital to hold only one up and one down electron. In the naive comparison to hydrogenic states, the orbitals comprise different states of the quantum number n, and can thus be simultaneously occupied by electrons having the same spin configuration with reference to some geometrical axis. In the electronic DHM, a full lattice site is quadruply occupied, and there are $2^4 = 16$ possible electronic occupations available to the atom, illustrated in figure 2.5. These are the 2^4 basis states for the single-site Hamiltonian.

Meeting the critical four conditions given in (2.3) (but perhaps not those specified by Hirsch in [2.17] and [2.18]), the electronic DHM has been studied in a handful of cases using different methods, and with a variety of motivations.

The first explicit investigation was by Hirsch in 1991 [40] for $t_1 = 0$, with localized electrons in the upper band, mapping to an effective single band model. This early paper was followed by a more comprehensive evaluation of the DHM by Hirsch in 2003 [31] using exact diagonalization of a four-site chain. It appears that these papers constitute the only specific evaluations of the electronic dynamic Hubbard model (2.15) with the critical physics of orbital relaxation as the focal point. They are, therefore, the important context for comparing the results of our work as discussed in chapter 7.

A handful of other researchers have studied a version of the DHM without emphasizing the specific physics relevant to our work. Shortly after Hirsch's 1991 paper [40], Georges *et al.* [61] employed QMDMFT in the restricted case of a bipartite lattice where the hybridization occurs only in t_{01} and $t_0 = t_1 = 0$ to model electron transport in a "CuO-type" system.

The study of CuO lattices motivated further interest in DHM-type Hamiltonians in the work of Si *et al.* [62] who restricted hopping to the lower orbital, and the previously mentioned work of Continentino *et al.* [57] and Tovar Costa *et al.* [58, 59] focusing on the orbital selective Mott metal-insulator transition (OSMT) and t'.

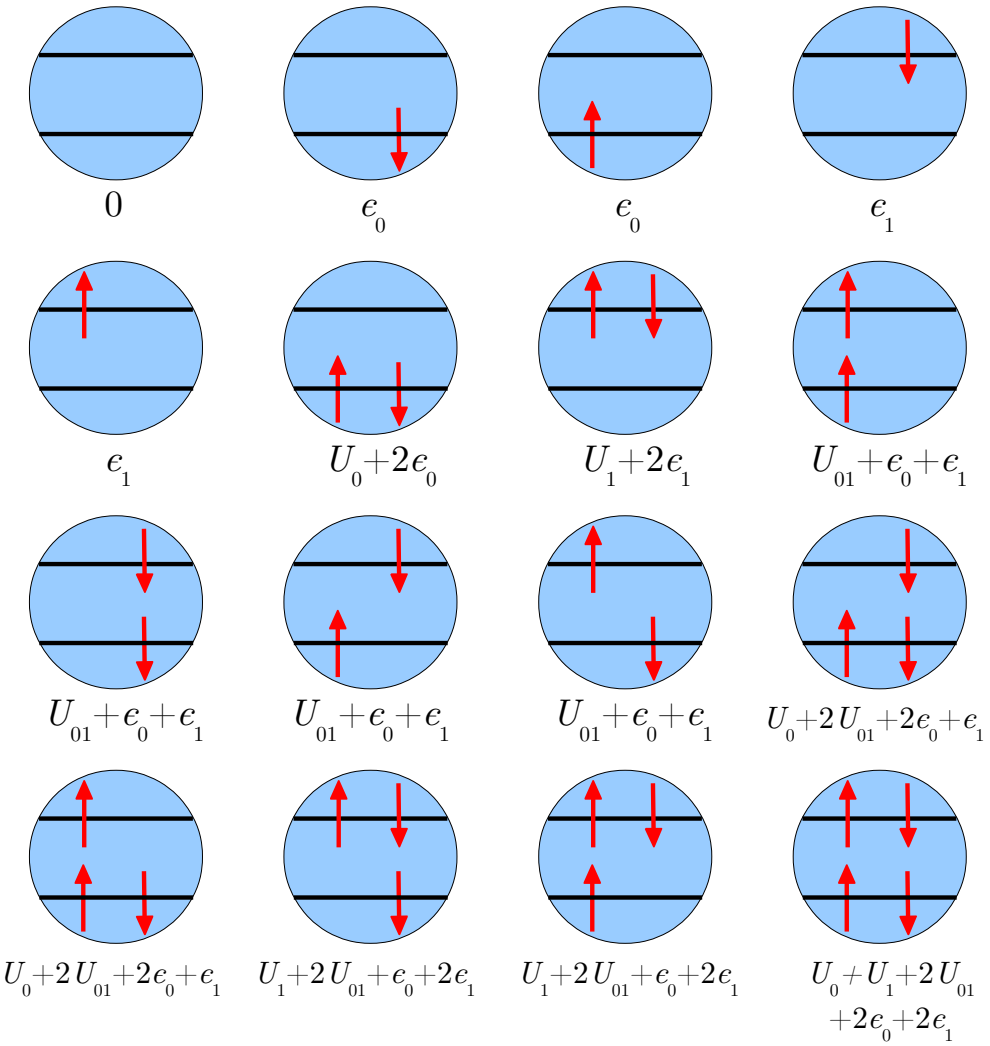

Figure 2.5: Sixteen possible electron basis states of the electronic DHM (2.15), along with the total local energy of each state, with parameters illustrated in figure 2.3.

More recently, interest in the OSMT (see section 7.6) has motivated Song and Zou [63] and Song [64] to employ two-site DMFT in exploring a DHM with only t_{01} hybridization, not t', and $U_0 = U_1$, and the inclusion of Hund's coupling terms. In a similar vein, Winograd and de'Medici [65] have published a zero-temperature study of the OSMT using a DHM with Hund's coupling and interorbital Coulomb repulsion restricted as $U_0 = U_1$, $t_{01} = 0$ and degenerate bands.

2.4 Four-Site Solution of the Electronic DHM

In 1991 Hirsch [40] introduced a simple version of the electronic DHM (2.15) restricting electron hopping to the lower orbital so that $t_1 = t_{01} = 0$, with the Hamiltonian,

$$\begin{aligned} H &= -t_0 \sum_{\langle ij\rangle\sigma} \left[c^\dagger_{0i\sigma} c_{0j\sigma} + c^\dagger_{0j\sigma} c_{0i\sigma} \right] + U_0 \sum_i n_{0i\uparrow} n_{0i\downarrow} + U_1 \sum_i n_{1i\uparrow} n_{1i\downarrow} \\ &\quad + U_{01} \sum_{i\sigma\sigma'} n_{0i\sigma} n_{1i\sigma'} + \epsilon_0 \sum_{i\sigma} n_{0\sigma} + \epsilon_1 \sum_{i\sigma} n_{1\sigma} \\ &\quad - t' \sum_{i\sigma} (c^\dagger_{0i\sigma} c_{1i\sigma} + c^\dagger_{1i\sigma} c_{0i\sigma}) \,. \end{aligned} \tag{2.19}$$

Assuming the energy condition (2.17) and that $U_{01} - U_1 - (\epsilon_1 - \epsilon_0) >> t' << 1$, Hirsch employed a perturbation approximation to lowest order in t' to map the two-band Hamiltonian to a single-band system of effective fermions, whose spin states respectively capture the single-occupancy of electrons on the lower orbital (with some small weight in the upper orbital), and the doubly-occupied site weighted primarily with both electrons in the upper orbital and some minor contribution from the electrons in different orbitals of the site. With this approximation, Hirsch demonstrated an increased hopping rate for holes moving onto lattice sites occupied by few electrons, or equivalently, many other holes. This provided evidence for pairing of holes in the electronic DHM, in agreement with hole-pairing evidence from other versions of the model [47, 66].

In 2003 Hirsch returned to the electronic DHM, extending the analysis to a more general case with a thorough exact diagonalization study [31] of the full Hamiltonian (2.15). In that work, the focus was on ground state properties of a linear chain of four sites using free-end boundary conditions (to avoid finite-size effects related to degenerate eigenstates). For simplicity, Hirsch defined the three hopping parameters as equal, so that,

$$t_0 = t_1 = t_{01} = t \,, \tag{2.20}$$

with the justification that the essential physics is unchanged by this constraint, according to his previous study [40] and work by others on the periodic Anderson model [54].

For the sake of computational efficiency, Hirsch additionally constrained the Hilbert space of the exact diagonalization problem, eliminating all states containing three or more electrons at any of the four sites, as well as states where a site is occupied by two electrons of the same spin.

The main focus of the paper was the change in quasiparticle properties in the interacting system as a function of band filling. Four key results emerged from the exact diagonalization study [31]:

1. Quasiparticles are found to be less coherent as holes (high filling) than as electrons (low filling), as measured by changes in the quasiparticle weight.

2. Optical conductivity spectral weight is transferred from low to high frequency as band filling increases toward the hole regime ($n \approx 2$).

3. For certain parameter regimes, an attractive effective interaction is found between charge carriers, and associated with pairing of holes. The same parameters are also associated with an increase in the coherence of the quasiparticles and their hopping between sites.

4. Pairing of holes is correlated with lowering of the system's kinetic energy.

These results issue from the fundamental asymmetry between holes and electrons in the DHM, arising from the orbital relaxation that occurs at high band filling. According to Hirsch, this asymmetry creates the conditions for superconductivity to obtain through the mechanism of hole pairing, as explained in section 2.5. The particular physics of electron-hole asymmetry does not arise in standard treatments of the single-band Hubbard model, which is symmetric on electron-hole transformation of the creation and annihilation operators.

An important advantage of the finite system size of [31] is the countability of electrons occupying the lattice sites. A full band is composed of eight occupying electrons, two per site. In this finite-size limit, Hirsch was able to directly evaluate the differences in key indicators of hole-pairing and the onset of the superconducting transition by examining the physics with one hole (seven electrons) or two holes (six electrons) occupying the linear chain. Band-filling with two holes permits pairing, and under these circumstances Hirsch observed some important effects when system parameters were properly tuned ($t' = 0.2, U_0 = 10, U_{01} = 6, \epsilon_0 = 0, t_{01} = t_0 = t_1 = 1$), as illustrated in figure 2.6. In particular,

for the case where U_1 and ϵ_1 are both small, the quasiparticle weight for two holes (six electrons) is larger than for a single hole (seven electrons) and thus hole pairing is associated with "re-coherence"; paired holes experience an effective attraction seen in the negative value of U_{eff} at $N_e = 8$, defined as,

$$U_{\text{eff}}(N_e) = E_0(N_e) + E_0(N_e - 2) - 2E_0(N_e - 1) \tag{2.21}$$

where N_e is the number of electrons in the system and E_0 the ground state energy at that filling; and the effective hopping, t_{eff}, of hole pairs between lattice sites is larger than for single holes (in agreement with other DHM studies on correlated hopping Hubbard Hamiltonians [40, 67, 68]).

The exact diagonalization results are in qualitative agreement with those found from studies of the auxiliary spin DHM (2.14), particularly in a four-site exact diagonalization of that model by Hirsch [48], and a two-site dynamical mean field zero temperature study by Bach [51] who saw the same shift of spectral weight and decoherence of charge carriers as band filling is increased, and was also able to investigate the Mott physics of the auxiliary spin DHM.

Our study of the electronic DHM (2.15) explores the electron-hole asymmetry in the same parameter space as Hirsch's four-site exact diagonalization analysis. The DMFT method allows full generality in the hybridization parameters t_{01} and t', as well as the Hilbert space size (permitting the full quadruple electron occupation of a lattice site). These advancements on the four-site chain allow for a more sophisticated analysis of the physics behind the electronic DHM, including realization of Mott physics, unavailable to Hirsch in consequence of the computationally restricted Hilbert space. The results of our DMFT analysis are given in chapter 7, where comparisons are made to those of Hirsch [31].

2.5 Superconductivity through Hole Pairing

The conventional understanding of superconductivity, BCS theory [69], identifies the interaction between electrons and ions as the driving agency behind the phenomenon. The strong Coulomb interactions acting directly between the electrons are confined to the background state in which the displacement of ions from their equilibrium positions mediate an effective interaction between the otherwise mutually repulsive charge carriers, forming a condensate of low energy Cooper pairs. This coupling of electrons to phonons drives the superconducting phase transition by providing a more favourable (lower) potential energy state for the system [70].

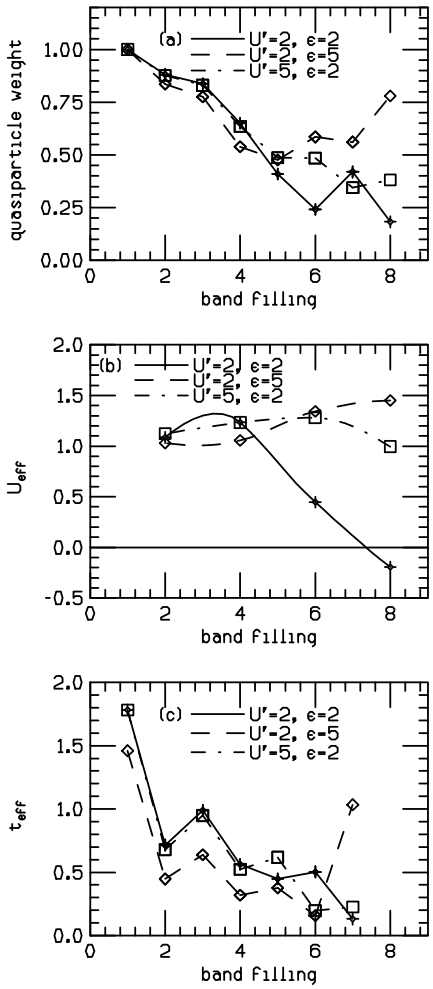

Figure 2.6: Effects of hole pairing in the four-site exact diagonalization of (2.15), with system parameters specially chosen for the proper physics to occur ($t' = 0.2, U_0 = 10, U_{01} = 6, \epsilon_0 = 0, t_{01} = t_0 = t_1 = 1$). Here, ϵ corresponds to our $\epsilon_1 - \epsilon_0$ and U' to our U_1. The solid line is the specific regime where hole-pairing is seen to promote superconductivity: a) the quasiparticle weight for two holes (six electrons) is higher than for one hole (seven electrons); b) $U_{\rm eff}$ is the effective Coulomb repulsion defined in (2.21) which becomes attractive (negative) at the top of the band; c) the effective hopping for two holes is higher than for a single hole. From [31].

Alternatively, Hirsch developed [39] a theory of hole superconductivity [47, 66, 71] on the basis of hole-pairing near the top of a band (*i.e.* when the band is nearly filled with electrons). As previously discussed, the high density of electrons will result in electronic wavefunctions adjusting to minimize the energy cost of the Coulomb repulsion, the central feature of the dynamic Hubbard model. In this regime, electron-electron repulsion is of competitive size in the system with the electron-phonon interaction, and in fact dominates the physics. As electron states reorganize to minimize their mutual repulsion energy at the lesser cost of increasing the electron-ion energy, new states of paired holes emerge with high electron-electron energy but low electron-ion energy. These paired-hole states condense to the bottom of the energy band leading to hole superconductivity [39].

The Hirsch model of hole superconductivity appeals to the fundamental asymmetry between electrons and holes in condensed matter systems described by orbital relaxation in the dynamic Hubbard model. This asymmetry is absent from the single-band Hubbard Hamiltonian, where electrons and holes are treated on the same footing, but appears in Hubbard models with a correlated hopping term [67] and in the DHM (2.15).

The higher electron density of the nearly full band therefore results in holes as charge-carriers moving around the lattice in a background of negative electron charge, which becomes deformed in response to the changing overall wavefunction. The holes, then, are highly "dressed" quasiparticles with low coherence or high effective mass (corresponding to a low quasiparticle weight). They are essentially followed through the lattice by a cloud of disturbed electron background, much like polarons in the Holstein model [30, 44] of electron-ion coupling [72].

In this highly dressed state, it has been shown [40, 67, 68] that *paired* holes (of opposite spin) tend to propagate more easily through the lattice: the effective hopping amplitude of charge carriers becomes dependent on the electronic occupation of the sites involved in the electron tunneling. The first hole to hop onto a lattice site causes a significant reformation in the electronic background, while the second hole in a pair makes the hop with a reduced disruption to the background and this transition becomes easier [39]. The hopping, t_{hole}, is enhanced for pairs of holes moving together as,

$$t_{\text{pair}} = t_{\text{hole}}\sqrt{z_h} \tag{2.22}$$

where z_h is the hole quasiparticle weight [73]. This enhanced, correlated hopping provides an effective attractive interaction between nearest neighbour holes with opposite spin, which is indicative of a superconducting transition [74, 75].

Consequently, paired or correlated holes are somewhat undressed and thus have a re-

duced effective mass compared to isolated and highly dressed holes moving about the lattice. The lower effective mass from pairing of holes implies a higher mobility allowing for a reduction in kinetic energy and a corresponding lowering of the system's free energy. This energy reduction provides the condensation energy for the superconducting transition as the undressed holes form the condensate. This contrasts with the potential energy reduction that explains the condensate of Cooper pairs in BCS theory [68].

One may equivalently understand the onset of the superconducting state from the perspective of electron charge carriers. As the *local* density of holes increases (through pairing), the density of electrons necessarily decreases and the quasiparticles undress, becoming more free-particle-like [76].

The London penetration depth, λ, related to the screening of magnetic fields from the interior of a superconductor, is,

$$\lambda = \sqrt{\frac{mc^2}{4\pi ne^2}} \tag{2.23}$$

where m, n and e are the mass, density and charge of the superconducting carriers [77]. This relationship between λ and m suggests that this lowering in quasiparticle effective mass will also reduce the London penetration depth, leading to transfer of optical spectral weight from high frequencies to the low frequency Drude peak which is directly related to the value of λ [76]. This effect has been observed experimentally [78,79] in the hole-pairing regime of the electronic DHM exact diagonalization study [31].

The underlying physics of the Hirsch theory of hole-pairing-driven superconductivity rests on the validity of orbital relaxation in nearly full electron bands. This theoretical framework is robustly described in the general form of the Hamiltonian (2.15), an expression more complex than that of the single-band Hubbard model whose exact "solution" has proven understandably elusive throughout the history of condensed matter physics. The computational method of dynamical mean field theory, however, has proven to be an important tool to gain insight into the physics of both the single-band Hubbard model and multiorbital Hubbard models such as (2.15).

Chapter 3

Dynamical Mean Field Theory

3.1 Motivation Behind DMFT

A change to the parameters defining a material can result in important and dramatic physical responses when the electrons experience significant repulsive Coulomb interactions. These interesting phenomena of strongly correlated systems find their simplest microscopic description in the single band Hubbard model of spin-$\frac{1}{2}$ fermions on a lattice. This model captures the essential physics at work due to the competition between kinetic energy and Coulomb repulsion in the many-body system. Especially at low energies, these materials demonstrate exotic and complex responses to small changes in their properties [80].

Despite its formal compactness, however, the Hubbard Hamiltonian (1.4) cannot be solved analytically except for very small systems (which cannot be relied upon to capture the dynamics of a true many-body "bulk" lattice environment), and in the special case of one-dimensional chains of atoms with nearest-neighbour hopping [29]. This special case remains the only Hubbard model with an exact ground state solution, and has at least some practical application such as modeling finite dimensional systems such as aromatic benzene rings [81]. In higher dimensional systems an exact solution of the Hubbard model remains outstanding and has been the subject of concerted theoretical effort [30].

The essential difficulty of solving the Hubbard model is that the two terms of its Hamiltonian cannot be made diagonal in the same formal quantum basis space. The kinetic energy term is diagonal in the momentum representation of the operators while the interaction term becomes diagonal when the Hamiltonian is Fourier transformed to coordination space. The operators of the two spaces are governed by the position-momentum uncertainty relation thus rendering an exact analytical diagonalization of the entire Hubbard Hamiltonian out of reach for large, realistic systems.

The quantum mechanical basis for a single-band Hubbard many-body system of N lattice sites spans a Hilbert space of size 4^N, determined by the four possible electron occupations on each site, as permitted by the Pauli exclusion principle:

1. an empty site occupied by no electrons;
2. a single up-electron;
3. a single down-electron;
4. a doubly-occupied site of one up and one down electron.

Since the size of the Hilbert space grows exponentially with N, for even a small lattice a Hamiltonian matrix cannot in practice be diagonalized (hence solved) analytically with current computer technology, for reasons pertaining not only to processor speeds but more importantly to dynamic storage limitations. Diagonalizing a matrix of size $N \times N$ requires computational operations on the order of N^3 [82] and sufficient dynamic memory capacity for storage of $N \times N$ floating-point values[1]. Exact and complete eigenspectrum solutions of the Hubbard model Hilbert space are therefore computationally limited to extremely small lattice sizes. This constitutes a fundamental restriction on the exploration of various aspects of the system that arise in the thermodynamic limit such as spatially ordered phases [84].

The computational difficulty of obtaining the complete eigenspectrum can be limited by utilizing symmetries of the system where the Hamiltonian commutes with an operator. Useful symmetries would be particle number conservation and commutation of the Hamiltonian with the Pauli spin matrices (when neglecting spin-flip as a mechanism of the lattice system). With these symmetries, the Hamiltonian matrix can be divided into independent blocks which can be diagonalized separately.

Where the electron population of the Hamiltonian block is fixed with $n_\uparrow$ spin-up and $n_\downarrow$ spin-down indistinguishable electrons, in the absence of spin flips the result is both conservation of total spin angular momentum $S_z = \frac{1}{2}n_\uparrow + \frac{-1}{2}n_\downarrow$ and particle number $N = n_\uparrow + n_\downarrow$. In this way the Hilbert space of the larger Hubbard Hamiltonian can be divided into an analysis of smaller Hilbert spaces.

The size of the reduced Hilbert space problem involves the combinatorial solution of distributing these $n_\uparrow$ and $n_\downarrow$ fermions on the available sites without violating the Pauli

[1] At the time of writing, a typical high-end desktop computer might have the capacity to churn out the exactly calculated complete eigenspectrum for an eight-site lattice requiring dynamic storage in the tens of gigabytes. The record 1.6 PB of storage available to users of the IBM Sequoia supercomputer [83], the third fastest in the world, would "nearly" permit the exact solution of a lattice of twelve sites. A thirteen-site lattice awaits the future development of a computer harnessing 36 PB of dynamic memory.

exclusion principle which forbids two fermions of identical quantum state from populating the lattice. The total number of ways of assigning the up and down electrons is $\binom{N}{n_\uparrow}\binom{N}{n_\downarrow}$, and the largest of the Hubbard Hilbert spaces will correspond to the block with $n_\uparrow = n_\downarrow = \frac{N}{2}$ and total block matrix size of $\binom{N}{\lfloor N/2 \rfloor}\binom{N}{N-\lfloor N/2 \rfloor}$.

Assuming parallelization of the diagonalization algorithm across independent blocks, the dimension of this largest block will be the effective constraint on computational efficiency in solving the complete eigenspectrum. Within the limits of current desktop technology one might solve the spectrum for a system of 18 or 19 lattice sites, while the available global limits on supercomputer dynamic memory would permit a solution for the full eigenspectrum of a 26 site system [83].[2]

It is clear that in the absence of exact solutions for large realistic systems of correlated electrons an important area of research relates to approximation techniques which reduce the computational expense of solving the Hubbard model, while providing insight into the model's characteristic competition between the kinetic energy and double-occupancy penalization of the Hamiltonian's two terms. Any lattice site, at any time, may be found to be in a variety of electron occupation states and the dynamics of how these many-body states evolve requires a sufficiently sensitive approximation scheme. A static mean-field approximation such as Hartree-Fock is insufficient to capture the important physics expected to obtain for the interesting case where the on-site Coulomb repulsion U is of similar size to (or larger than) the electron hopping parameter t [20]. In the same physically interesting region perturbation methods, requiring one term to dominate the other, are also ruled out.

For a quarter century following the development of Hubbard's model of strong correlations [24, 26], physicists tried to develop a broad approach to analyzing this important Hamiltonian. In particular, a microscopic description of the metal-insulator transition proved elusive, since any effective technique must simultaneously capture the renormalized quasiparticle behaviour at the Fermi energy and the localization effects embodied in the Hubbard bands of the single electron density of states.

Hubbard's own analysis [26] provided good insight into the development of the insulating gap in the transition, but failed to demonstrate a well-defined quasiparticle peak in the metallic phase [85]. From the metallic side of the metal-insulator transition, as the Coulomb repulsion is increased, Brinkman and Rice [86] used a variational calculation to determine the critical value U_c, but were unable to provide insight into the insulating behaviour which should be anticipated by the formation of higher energy excitations that

[2] This estimate conveniently ignores the processing time and associated patience required to perform the required calculations.

eventually form the Hubbard bands [87]. The two methods provided differing critical values for the Coulomb parameter at which the MIT transition occurs and the relationship between the Hubbard and Brinkman Rice predictions was unclear. Of critical interest was the question of whether the insulating gap opens continuously or through a sharp transition, and the way in which this transition illuminates a breakdown in Fermi liquid theory as the quasiparticle character of the electrons disappears [88].

A breakthrough in 1989 by Metzner and Vollhardt [89] and Müller-Hartmann [90] provided the framework for a robust solution of the dynamics of this strongly correlated problem, relying on a simplification of the interaction dynamics that occurs in the limit of infinite lattice coordination number.

3.2 The Simplification of Infinite Dimensionality

In the study of spin systems, especially classical ones, the use of an infinite limit to some system parameter—such as spatial dimension, spin degeneracy or coordination number—has provided a simplification toward an exact solution of many problems. The properties in this limit yield insight into the physical system that is finite, but similarly "large" in the space of that parameter [20].

The Weiss molecular field [91] of localized atomic spins, an approximation to the Ising model (itself a reduction of a general extended Hubbard model [30] for $U >> t$), is an example which becomes exact in just such a limit—that of infinite dimensionality, $d \to \infty$. The Ising Hamiltonian H^{Ising} describes the interaction with its n neighbours of a central atom, j, of spin component S_{jz} along the z-axis, subjected to an applied magnetic field H_z, such that,

$$H_j^{\text{Ising}} = -g\mu_0 H_z S_{jz} - 2J S_{jz} \sum_{k=1}^{n} S_{kz} \tag{3.1}$$

where g is the Landé factor, μ_0 the Bohr magneton, and J the exchange interaction strength (which depends on the atomic separation but for simplicity is assumed constant for all k, which denotes the neighbouring spins). The final term describes the interaction between the (z component) spins of the neighbouring electrons and the central atom. It can be approximated with a mean interaction value,

$$H_{\text{mean}} \equiv \frac{2J}{g\mu_0} \sum_{k=1}^{n} \langle S_{kz} \rangle \,. \tag{3.2}$$

The effective "molecular" or "Weiss" magnetic field H_{mean} is incorporated into (3.1) to

give a simplified problem of a single atom within an average magnetic field:

$$H_j^{\text{Ising}} = -g\mu_0(H_0 + H_{\text{mean}})S_{jz}\,. \tag{3.3}$$

This Weiss mean-field approximation gives a qualitatively correct result for the magnetic phases of the Ising model in three dimensions but is unreliable at lower dimensionality [84]. It becomes exact, however, in the limit of infinite dimensions ($d \to \infty \Rightarrow n \to \infty$), under the strict condition that the interaction J is scaled inversely with dimensionality as $J \equiv \frac{J^*}{n}$ (where J^* is a constant parameter). Under that condition, the energy density of (3.2) remains finite and non-zero, and the sum over the mean of the neighbouring spins is asymptotically equivalent to the sum over the actual spins, since,

$$\lim_{n\to\infty} \frac{J^*}{n} \sum_{k=1}^{n} \langle S_{kz}\rangle = \lim_{n\to\infty} \frac{J^*}{n} \sum_{k=1}^{n} S_{kz} \tag{3.4}$$

because,

$$\lim_{n\to\infty} \frac{J^*}{n} \sum_{k=1}^{n} (S_{kz} - \langle S_{kz}\rangle) \approx 0\,. \tag{3.5}$$

Here, the positive and negative fluctuations $S_{kz} - \langle S_{kz}\rangle$ will cancel around the mean value to within a remainder of $\mathcal{O}(\frac{1}{n})$.

The mean field approximation of the Ising model is thus a meaningful solution of a system of localized spins in the limit of infinite dimensionality. With this relationship in mind, Metzner and Vollhardt [89] showed that the same limit leads to a dramatic simplification for the investigation of quantum many-body systems described by the Hubbard model.

As with the Ising model (3.1), it is necessary to perform a scaling on the Hubbard Hamiltonian to ensure that in the $d \to \infty$ limit the energy per lattice site does not diverge. In this case, the interaction term,

$$H_{\text{int}} = U \sum_i n_{i\uparrow} n_{i\downarrow} \tag{3.6}$$

proves insensitive to the dimensionality, being localized to one site only.[3]

The Hubbard kinetic energy term in the mean field approximation with nearest-neigh-

[3] In the case of an extended Hubbard model with nearest-neighbour Couloumb interactions, scaling is required for the interaction parameter.

bour hopping t is,

$$\frac{1}{n}\langle H_{\mathrm{KE}}\rangle = \frac{-t}{n}\sum_{\langle ij\rangle}\langle c_i^\dagger c_j\rangle. \tag{3.7}$$

and must be scaled appropriately to ensure the kinetic energy does not explode relative to the interaction energy. The proper scaling is determined from the density of states for large dimensions. From the central limit theorem, for the hyper-cubic lattice this is a Gaussian density of states [89],

$$D_{hc}(\epsilon) \overset{d\to\infty}{\longrightarrow} \frac{1}{2t\sqrt{\pi d}}\exp\left[-\left(\frac{\omega}{2t\sqrt{d}}\right)^2\right]. \tag{3.8}$$

For $d \to \infty$ this density of states remains non-trivial when the hopping amplitude is redefined as,

$$t = \frac{t^*}{\sqrt{d}} \tag{3.9}$$

for constant t^* [20].

With this scaling, the self-energy perturbation expansion becomes entirely diagonal in coordination space, as all non-local terms involving electron-electron interactions between different lattice sites are proportional to $\frac{1}{\sqrt{d}}$ [84]. This result has been explicitly shown to hold for a variety of lattice geometries extended to infinite dimensionality including cubic [90], honeycomb/diamond [92] and the Bethe lattice [87], which has a semi-circular density of states [93, 94],

$$D_{\mathrm{Bethe}}(\epsilon) = \frac{1}{\pi}\sqrt{1-\frac{\epsilon^2}{4t^{*2}}}. \tag{3.10}$$

Only the local (or on-site) term is retained, so that,

$$\lim_{d\to\infty}\Sigma_{ij,\sigma}(z) = \Sigma_{ij,\sigma}(z)\delta_{ij}. \tag{3.11}$$

Site-diagonal self energy was an important assumption made by Hubbard in his work [26] on solving the insulating side of the metal-insulator transition. The variational wave function used by Brinkman and Rice [86] in tackling the problem from the metallic side of the transition becomes exact in the limit of $d \to \infty$. Therefore, the limit explored by Metzner and Vollhardt has the *a priori* appearance of connecting the results found by these different methods, and this has been borne out in actual calculations [88].

The coordinate localization of the self energy (3.11) translates in momentum space into a momentum-independent self energy. With this important simplification, the k-dependence of the single-particle Green's function $G_\sigma(k,z)$ for the many-body interacting

system is contained exclusively in the free-electron dispersion ϵ_k as,

$$G_\sigma(k,z) = \frac{1}{z + \mu - \epsilon_k - \Sigma_\sigma(z)}\,. \tag{3.12}$$

The momentum-independence of the self energy provides the necessary simplification for the development of dynamical mean field theory (DMFT), a computational tool which can provide an exact solution to the Hubbard model in infinite dimensions. The solution is realized by mapping the interacting lattice problem onto that of an impurity embedded in a mean-field medium.

The DMFT technique emphasizes two essential characteristics arising from the mean field approximation of the strongly-interacting system. First, in common with all mean field theories, there is a loss of the spatial fluctuations of the electrons between unique sites of the lattice. All properties of the system are in the context of onsite behaviour, an obvious consequence of the lack of momentum resolution in the problem. On the other hand, the on-site behaviour of the system is dynamical with respect to electron occupancy, offering information about the lattice problem that would be unavailable to a static mean-field solution. A dynamical solution is essential to capturing the competition in the Hubbard model between the on-site Coulomb repulsion and the general tendency for itinerant charge-carriers to remove themselves from the local site into the lattice environment. The consequence of this competition is nicely captured by the properties of a momentum-independent single-particle Green's function and self-energy that will be the ultimate result of the DMFT approximation.

3.3 Anderson Impurity Model

In the limit of infinite dimensionality, the equivalence of the fully interacting lattice and a single site interacting with a mean field environment suggested [88,95] that the onsite single particle Green's function $G_{ii}(z)$ for a system modeled by the Hubbard Hamiltonian is comparable to the Green's function G^{imp} for the single-impurity Anderson model (SIAM) [96]. The SIAM is an appropriate intermediate step in generating a mean field approximation to the fully interacting lattice Hubbard problem.

The general Anderson impurity model envisions a localized magnetic impurity occupied by a N_f-degenerate d or f shell of interacting electrons coupled to a non-interacting effective medium (often called the "bath") which represents the mean-field influence of a conduction band in the surrounding lattice. In principle, the conduction band states form a continuum of Bloch states $\phi_l(\mathbf{r})$ of the crystal, but in practice the band is parameterized by a finite

value of N_l pseudo-sites of occupation energy ε_l. Electrons occupying the local impurity site with energy ϵ_f are "hybridized" with the band electrons through a coupling constant V_{lf}, an effective hopping between the impurity and the surrounding crystal environment.

For a system with chemical potential μ, the Hamiltonian of the Anderson model is,

$$\begin{aligned} H_{\mathrm{AM}} =& \sum_{f\sigma}^{N_f} (\epsilon_f - \mu) c^\dagger_{f\sigma} c_{f\sigma} + \sum_{l\sigma}^{N_l} \sum_{f}^{N_f} (\varepsilon_l - \mu) C^\dagger_{lf\sigma} C_{lf\sigma} + U \sum_{f>f'}^{N_f} c^\dagger_{f\uparrow} c_{f\uparrow} c^\dagger_{f'\downarrow} c_{f'\downarrow} \\ &+ \sum_{\sigma} \sum_{l}^{N_l} \sum_{f}^{N_f} V_{lf} (C^\dagger_{l\sigma} c_{f\sigma} + C^{f\dagger}_{\sigma} c_{l\sigma}) \,, \end{aligned} \tag{3.13}$$

where the operators $C^\dagger$ (C) create (destroy) a bath electron, and $c^\dagger$ (c) create (destroy) an f-shell electron on the impurity site. Similarly to the Hubbard model, in the absence of the interaction term, $U \sum_f^{N_f} c^\dagger_{f\uparrow} c_{f\uparrow} c^\dagger_{f\downarrow} c_{f\downarrow}$, (3.13) (known in that limit as the Fano-Anderson model [96, 97]) is exactly solvable [30].

The final term of (3.13) describes the hybridization between the f-shell electrons and the conduction band. The bath pseudo-sites couple selectively to individual impurity electrons so that each f orbital has, in practice, its own bath. It is important to note that the bath energies ε_l do not represent actual states in the physical lattice, but are representative of these in a mean-field way. Even in the thermodynamic limit of $k \to \infty$ the connectivity of the pseudo-sites does not map one-to-one to a physical lattice geometry, since the hybridization constants, V_{lf}, couple *every* bath site to the single impurity site.

A specific case of (3.13) is employed in developing the DMFT method, where the impurity site is restricted to a single orbital, yielding a simplified Hamiltonian for the single-impurity Anderson Model (SIAM):

$$\begin{aligned} H_{\mathrm{SIAM}} =& (\epsilon_c - \mu) \sum_{\sigma} c^\dagger_{\sigma} c_{\sigma} + \sum_{l\sigma} (\varepsilon_l - \mu) C^\dagger_{l\sigma} C_{l\sigma} + U c^\dagger_{\uparrow} c_{\uparrow} c^\dagger_{\downarrow} c_{\downarrow} \\ &+ \sum_{l\sigma} V_l (C^\dagger_{l\sigma} c_{\sigma} + c^\dagger_{\sigma} C_{l\sigma}), \end{aligned} \tag{3.14}$$

visualized in figure 3.1.

Anderson [96] employed the Hartree-Fock approximation to derive a mean-field Green's function,

$$g^{\mathrm{imp}}(z)^{-1} = z - (\epsilon_c - \mu) - \sum_l \frac{V_l^2}{z - (\varepsilon_l - \mu)} \,, \tag{3.15}$$

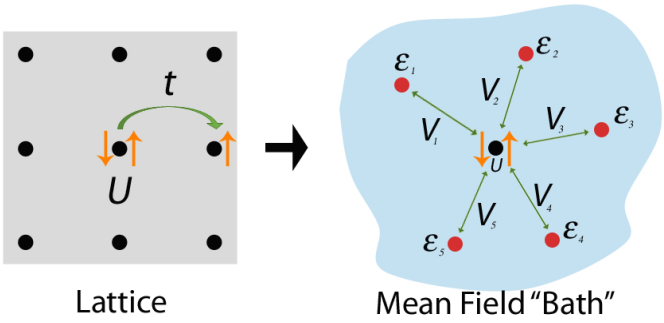

Figure 3.1: The single impurity Anderson model (SIAM) maps the physics of interacting electrons on a lattice onto a mean field approximation. In the lattice problem, the electrons repel one another via the on-site Coulomb repulsion U, and move about the geometry of the physical lattice sites according to the hopping parameter t, related to the overlap of tight-binding orbitals which form electronic bands in the lattice. In the mean field picture, a single site is considered as an impurity in a non-interacting "bath" represented by l pseudo-sites of energy ε_1, ε_2, ..., ε_l. Electrons on the impurity site continue to interact locally via U, the Coulomb repulsion, and hop to and from the bath via hybridization parameters V_1, V_2, ..., V_l.

which is the dynamic equivalent of the static Weiss field in the Ising model problem discussed in section 3.2. Referred to as the "Weiss field" in the DMFT literature [84], g^{imp} describes the dynamical mean field to which the local problem of electrons on an impurity site are coupled to their (effective) environment, and is the basis for designating the approximation method as "dynamical mean field theory".

3.4 Hubbard Model Dynamical Mean Field Solution

Physically, the effective quantity (3.15) captures the processes taking place in the rest of the lattice, independent of the impurity. It can be thought of as describing the behaviour of all others lattice sites, i, with the site of interest, o, physically removed, leaving a "cavity" among the otherwise connected sites [95]. The Hubbard model for these remaining sites would be described by a local (or onsite) Green's function $G^o_{ii}(z)$, for each of the remaining lattice sites, where the superscript indicates the removal of site o.

In the case of a translationally invariant Bethe lattice (figure 3.2) with connectivity κ and scaled hopping t, it has been shown [87] that the effective field $g^{\text{lat}}(z)$ interacting with a site o in the lattice is related to the Green's functions $G^{(o)}_{ii}(z)$ as,

$$g^{\text{lat}}(z)^{-1} = z + \mu - \frac{t^2}{\kappa} \sum_{\langle i,o \rangle} G^{(o)}_{ii}(z) = z + \mu - t^2 G^{(o)}_{ii}(z) \tag{3.16}$$

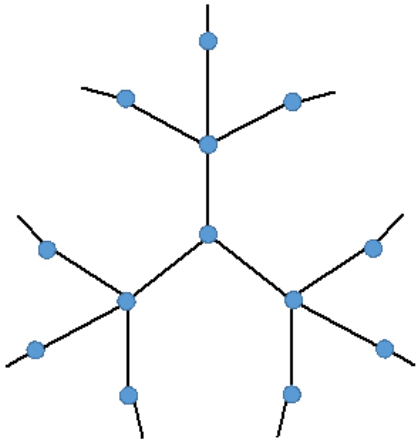

Figure 3.2: An illustration of the tree-like Bethe lattice with connectivity three. Each site is symmetrically connected to three other sites, rendering the overall geometry unphysical and impossible to illustrate with accurate angles.

where $\langle i, o\rangle$ indicates hopping of electrons only between the impurity site and its nearest-neighbours in the Bethe lattice. For a Bethe lattice with limited connectivity the removal of site o has a significant effect on the local topology, since the connectivity of its neighbouring sites is fundamentally altered. For increasing connectivity, however, the removal of site o has a diminishing effect on the local dynamics since $z \approx z-1$, so that $G_{ii}^{(o)}(z) \approx G_{ii}(z)$, the latter Green's function being identified with a complete lattice without a cavity. Henceforth we will denote the onsite lattice Green's function $G_{ii}(z)$ as $G^{\mathrm{lat}}(z)$, which will clarify the notation in the multiorbital configuration.

According to the discussion in section 3.2, in the limit of infinite bath pseudo-sites, (3.15) becomes exactly equivalent to expression (3.16), for an appropriate finite number and choice of bath parameters, ε_l and V_l. Arriving at the proper values of these parameters for the specific Hubbard model under consideration is the ultimate goal of the DMFT method and is accomplished by enforcing the equivalence of these mean field functions:

$$g^{\mathrm{imp}}(z) = g^{\mathrm{lat}}(z)\,. \tag{3.17}$$

Because the dynamical field (3.15) describes the non-interacting mean-field environment of the impurity, it can be related to the interacting SIAM Green's function $G^{\mathrm{imp}}(z)$ through a Dyson equation,

$$g^{\mathrm{imp}}(z)^{-1} = G^{\mathrm{imp}}(z)^{-1} + \Sigma^{\mathrm{imp}}(z). \tag{3.18}$$

where $\Sigma^{\mathrm{imp}}(z)$ is the momentum-independent local self energy. The self energy is therefore

accessible given a solution of the SIAM Green's function $G^{\rm imp}(z)$.[4] Provided with defined values of the bath parameters in the impurity Hamiltonian (3.14), there are a variety of strategies available to find $G^{\rm imp}(z)$. These methods of solving the Hamiltonian are referred to as "impurity solvers" and will be discussed in section 3.5.

At the same time, the effective field $g^{\rm lat}(z)$, arising from the cavity picture of the lattice, can also be related to a Dyson equation involving the local lattice Green's function $G^{\rm lat}(z)$, and associated self energy $\Sigma^{\rm lat}(z)$:

$$g^{\rm lat}(z)^{-1} = G^{\rm lat}(z)^{-1} + \Sigma^{\rm lat}(z)\,. \tag{3.19}$$

In the DMFT problem, then, there are two parallel scenarios, the impurity model and lattice picture, equivalent in the limit of infinite dimensionality. The mean field parameters, ε_l and V_l, are the link mapping one model to the other.

This equivalence applies not only to (3.17), but to all elements in the two Dyson equations, (3.18) and (3.19). Thus, the Green's function $G^{\rm imp}(z)$, arrived at by application of an impurity solver on (3.14), will provide a good approximation of the local Green's function $G^{\rm lat}(z)$ of the Bethe lattice. As well, the SIAM self energy determined by (3.18) can be considered identical to the lattice self energy so that,

$$\Sigma^{\rm imp}(z) = \Sigma^{\rm lat}(z) \equiv \Sigma(z)\,. \tag{3.20}$$

The onsite Green's function is generally defined, for electrons with dispersion ϵ_k, as,

$$G^{\rm lat}(z) = \frac{1}{N}\sum_k \frac{1}{z - (\epsilon_k - \mu) - \Sigma(k,z)}\,, \tag{3.21}$$

and is related to the probability of an electron, with some frequency z, leaving site i and traveling through the lattice before again returning. Some simple limits illustrate its character. For an insulating material, where electron-electron Coulomb interactions dominate the dynamics of the Hubbard model (1.4), the real part of the complex self energy, $\Sigma(k,z)$, will be large and dominate the denominator of (3.21) for relatively low energy electron excitations, $z - \epsilon_k + \mu$. In this scenario the probability expressed by the local Green's function will be small. In the opposite limit, where Coulomb interactions between electrons are tending toward zero, the probability will reflect a k-dependent delta

[4] Another method to find the self-energy is through the ratio of the two-particle and one-particle Green's functions, $F^{\rm imp}(z)$ and $G^{\rm imp}(z)$ respectively, so that $\Sigma^{\rm imp}(z) = U\frac{F^{\rm imp}(z)}{G^{\rm imp}(z)}$, which provides a more accurate solution of the spectral density for the DMFT problem when numerical renormalization group methods are employed as an impurity solver (*q.v.* section 3.5) [98].

function centered around the Fermi energy of the material, where $z = \epsilon_k - \mu$.

Accounting for the momentum-independence of the self energy, from (3.11), k is restricted to the dispersion, ϵ_k. Then the sum over k can be replaced by the non-interacting electron density of states $D^{(0)}(\epsilon)$ particular to the (infinite) lattice geometry, according to,

$$D^{(0)}(\epsilon) = \frac{1}{N} \sum_k \delta(\epsilon - \epsilon_k) \,. \tag{3.22}$$

Thus, (3.21) can be expressed as,

$$G^{\text{lat}}(z) = \int \frac{D^{(0)}(\epsilon)}{z - (\epsilon - \mu) - \Sigma(z)} d\epsilon \tag{3.23}$$

which, as mentioned, is equivalent to the SIAM Green's function for a proper choice of mean field bath parameters. It should be noted that the choice of density of states in (3.23) is the only place in the DMFT method where the lattice geometry explicitly enters.

The appropriate values of these bath parameters are arrived at through an iterative self-consistency algorithm, wherein the *impurity* Dyson equation (3.18) is used to find the self energy, which can be employed in the *lattice* Dyson equation to arrive at the mean field function $g^{\text{lat}}(z)$. This function can then be compared with the effective field value from the impurity model $g^{\text{imp}}(z)$, according to some distance function χ^2. If the comparison shows equivalence within some tolerance ζ, then the mean field parameter values, ε_l and V_l, can be considered correct for the lattice under consideration. If the effective field functions do not agree then they must be adjusted by minimizing the distance function,

$$\chi^2 = \int dz f(z) \left| g^{\text{lat}}(z) - g^{\text{imp}}(z) \right|^2 \tag{3.24}$$

where $f(z)$ is a possible weighting factor that biases the minimization toward agreement at some region of the frequency domain.

The adjusted bath parameter values that minimize (3.24) are now taken as input for a new, refined SIAM Hamiltonian (3.14), which is submitted to the impurity solver, and the analysis continues as before until convergence, where (3.24) is within ζ. At convergence, these values should describe a mean field that—for the chosen number of bath sites—most closely models the physics of a lattice model with the same system parameters of electron hopping, Coulomb repulsion and chemical potential.

The lattice picture mean field contribution $g^{\text{lat}}(z)$ is only determined after the value of the lattice interacting Green's function $G^{\text{lat}}(z)$ has been established. In general, these are related through (3.19) which requires an explicit solution of the integral in (3.23). In

special cases of infinite dimensionality the relationship is simplified. For the Bethe lattice with infinite coordination number, the lattice mean field function is directly related to the impurity interacting Green's function $G^{\text{imp}}(z)$ via,

$$g^{\text{lat}}(z)^{-1} = z + \mu - t^2 G^{\text{imp}}(z) \tag{3.25}$$

by exchanging $G^{\text{imp}}(z)$ for $G^{\text{lat}}(z)$ (which are equivalent for the proper selection of bath parameters) in (3.16) [87]. Under this formulation, the explicit determination of the self energy becomes irrelevant to achieving a converged solution of the DMFT problem. Of course, $\Sigma(z)$ can be calculated after the fact using a Dyson equation.

In this simple case of a single-orbital Hubbard model, an analytical solution of the integral can be evaluated exactly for the Bethe lattice density of states (3.10) with scaled hopping t^* [51]:

$$\begin{aligned} G_\sigma^{\text{lat}}(z) &= \int \frac{d\epsilon}{\pi t^*} \left(\frac{1}{z - (\epsilon - \mu) - \Sigma_\sigma(z)} \right) \sqrt{1 - \frac{\epsilon^2}{4t^{*2}}} \\ &= \frac{1}{2t^{*2}} \Bigg(z + \mu - \Sigma(z) \\ &\quad - \operatorname{sgn}\left\{ \Re\left[z + \mu - \Sigma(z) \right] \right\} \sqrt{\left[z + \mu - \Sigma(z) \right]^2 - 4t^{*2}} \Bigg) . \end{aligned} \tag{3.26}$$

The usefulness of the form provided by (3.25) becomes apparent in the multiorbital DMFT solution presented in the following chapter, where the integration in (3.23) may become analytically challenging and numerically time-consuming.

3.5 Impurity Solvers

The appropriate choice of an impurity solver is often cited as the most challenging step in a reliable DMFT solution (see, for example, [20, 80, 84]). Both approximate and numerically exact impurity solvers have been employed in DMFT studies, with each method providing advantages and suffering from limitations. There is, therefore, no universal strategy that can be employed to determine the appropriate system Green's functions without the involvement of approximations or assumptions. In selecting an appropriate impurity solver the central conflict is between accuracy, efficiency and flexibility in the scope of the parameter space available for analysis.

Approximate methods include iterated perturbation theory [87, 88, 95], non-crossing approximation [87,99,100] and the fluctuation exchange approximation [80,101,102]. These

impurity solvers are useful for the efficient insight they provide into the SIAM Hamiltonian dynamics within certain parameter constraints. For instance, in the case of the non-crossing approximation the Coulomb repulsion is large compared to the bandwidth W [99]; for fluctuation exchange, $U < \frac{W}{2}$ [80]. The flexibility to solve the Hamiltonian for any choice of system parameters is sacrificed in favour of computational speed.

Numerically exact impurity solvers can be grouped into four computational strategies: numerical renormalization group (NRG) [103–105], density matrix renormalization group (DMRG) [106–108], and more commonly, quantum Monte Carlo (QMC) [87, 88, 109–111] and exact diagonalization (ED) [51, 112–114].

NRG methods map a discretized model of the electron conduction band onto a semi-infinite chain linked to the impurity site, where the adjusted hopping parameter falls off exponentially away from the impurity along the one-dimensional chain [105]. NRG offers good resolution of low energy spectral details (including the metal-insulator transition), but not in high energy regions such as the edges of the Hubbard bands. It is also unable to solve a multiorbital DMFT problem in a robust way (such as, where the orbital energies are dissimilar) [105, 115], a requirement for the present study.

DMRG works similarly, mapping the interacting lattice of interest to a one-dimensional model, but is less suited to resolving detailed spectral function structure, especially at low energies, or the excited states of the Hamiltonian, which are important for determining the Green's function [108].

QMC methods are widely used as DMFT impurity solvers, employing either the Hirsch-Fye [116] or continuous-time [109] methods. QMC is able to explore a very large Hilbert space for the impurity model, thus employing an excellent mapping of the physical lattice, but the accuracy of the method's results grows with the square root of the simulation time. As well, access to real-frequency results, as required for spectral properties, involves analytic continuation via the maximum entropy method [117], a difficult problem especially where the statistical errors associated with QMC are sizable [87].

Most importantly, for a multiorbital problem, the well-known QMC fermion sign-problem becomes increasingly intense as the system moves away from particle-hole symmetry. This is particularly relevant to any study where the Coulomb repulsion between electrons is not restricted to twice the chemical potential of the system, or the electrons are in a superposition of states across non-symmetric orbitals [118].

Exact diagonalization produces a numerically exact Green's function through the solution of the Anderson model Hamiltonian (3.14), and compared to QMC allows for a relatively simple extension of results to real frequencies through analytic continuation and rational function extrapolation methods (*q.v.* section 5.1). It is also reliable for both fi-

nite and zero temperature, and is unconstrained with respect to the parameters of the system. In contrast to renormalization methods, ED can, in principle, handle multiorbital Hamiltonians in a natural and simple way, and is free from the sign problem and statistical uncertainties of QMC.

The main drawback of the ED method is that it becomes computationally intensive as the Hilbert space of the largest Hamiltonian block increases, corresponding to an increase in mean field bath sites. For a large number of sites one must rely on the Lanczos [119,120] or Arnoldi [121] algorithms for an approximate solution that restricts the Hilbert space to a manageable size by keeping temperature near zero [112, 113]. A smaller number of bath sites, while computationally tractable, introduces disagreement at low energies in the convergence of (3.24) [87], although this is somewhat alleviated in a multiorbital scenario (*q.v.* section 6.2).

In this work, which focuses on a multiorbital model of strongly correlated electrons, ED is a natural choice for the impurity solver for the reasons given. As well, the existence of an early published FORTRAN implementation of the DMFT algorithm, the *local impurity self-consistent approximation* (LISA) [87,122] for the single-orbital Hubbard model provides a reliable ED comparison for results from new implementations of the DMFT problem (*q.v.* section 3.6).

Under ED DMFT, the Anderson Hamiltonian (3.14) is diagonalized to give the exact eigenstates $|j\rangle$ and eigenvalues λ_j of the system. For our work a reliable and efficient algorithm, `SelfAdjointEigenSolver.h`, from the C++ *Eigen* library [123] is used to perform the numerical diagonalization.

As discussed in section 3.1, the Hamiltonian is solved block-wise, to reduce the computational time required for the diagonalization by taking advantage of symmetries in the system. Each block is a matrix of size $N \times N$, whose N-dimensional Hilbert space is spanned by N eigenpairs.

For an impurity model of n_s total sites ($n_b = n_s - 1$ bath sites) coupled to a single impurity site as depicted in figure 3.1, the collection of states from all the blocks of H_{SIAM} are given by

$$| j\rangle = | n_{1\uparrow} n_{2\uparrow} \dots n_{n_s\uparrow}\rangle \otimes | n_{1\downarrow} n_{2\downarrow} \dots n_{n_s\downarrow}\rangle \,, \tag{3.27}$$

where $n_{i\sigma}$ is 1 if that eigenstate includes an electron of spin σ at site i and 0 if not.

At finite temperature T, the Green's function of the system can be evaluated directly from the collection of these eigenstates and their eigenvalues, along the Matsubara frequency axis — the discretized imaginary axis of the complex frequency z [30]. For fermions, the Matsubara frequency ω_n is defined as a function of integer n and the inverse tempera-

ture β as,

$$\omega_n = (2n+1)\frac{\pi}{\beta}\,. \tag{3.28}$$

The collection of eigenstates $|j\rangle$ (with eigenvalues λ_j) found from diagonalizing all the Hamiltonian blocks contributes to finding the Green's function associated with the impurity problem, $G_\sigma^{\text{imp}}(i\omega_n)$, which is [30],

$$G_\sigma^{\text{imp}}(i\omega_n) = \frac{1}{Z}\sum_{j,k}\frac{\left|\langle k|\, c_\sigma^\dagger\, |j\rangle\right|^2 (e^{-\beta\lambda_j} + e^{-\beta\lambda_k})}{i\omega_n - (\lambda_j - \lambda_k)}\,, \tag{3.29}$$

where the summations are over all eigenstates. Z is the partition function for inverse temperature β.

This method of finding the impurity Green's function shifts the DMFT solution to the imaginary frequency axis, where the self-consistency routine described in section 3.4 remains unchanged except discretization of the complex frequency variable $z = i\omega_n$. Real frequency properties of the system, such as the spectral function $A(\omega)$ or optical conductivity $\sigma(\omega)$, can be recovered through analytic continuation using the substitution $i\omega \to \omega + i\eta$, or a numerical rational function extrapolation technique relying on the analyticity of (3.29) throughout the domain covered by the Matsubara points which ensures that as a function of z, it is uniquely defined throughout the entire complex plane when locally well-defined on the imaginary axis [124] (*q.v.* section 5.1).

The discrete nature of the Matsubara frequency finite-temperature solution requires some care in the choice of the inverse temperature parameter β, to minimize finite-size effects. Matsubara points are spaced as $[2(n+1)+1]\frac{\pi}{\beta} - (2n+1)\frac{\pi}{\beta} = \frac{2\pi}{\beta}$, which must be considered in reference to the energy level spacing of the eigenstates found by diagonalization. This spacing is affected by the discretization of the bath.

Continuation and extrapolation of the imaginary frequency results to real frequency observables are sensitive to the fine structure afforded by a sufficiently large number of bath levels. A small number of bath levels will result in non-physical gaps in the density of states evidenced by kinks in the low energy portion of $g^{\text{imp}}(i\omega_n)$, which can be especially disruptive in the Fermi liquid regime resulting in a poor low-frequency fit between the lattice and impurity functions in equation (3.24) [113]. This finite-size effect is somewhat mitigated by restricting solutions to not-too-large β and through an appropriate weight, $f(z)$ in (3.24), that encourages proper fitting at low frequency.

3.6 Single Band LISA Implementation

The inaugural DMFT computational algorithm was developed in FORTRAN by Werner Krauth [122] and initial results focusing on the metal-insulator transition were published in 1994 by Si *et al.* [111], with a more extensive set of results and a widely-cited general review following two years later [87]. This algorithm, called "LISA" (Local Impurity Self-consistent Approximation), is available online as open source software [122] and has been used as the core of several DMFT studies on strongly correlated electron systems.[5]

The available LISA code is designed to solve a single-band Hubbard model using either ED or Hirsch-Fye QMC as the impurity solver. The ED version of LISA includes a distribution employing a finite-temperature implementation as well as one utilizing the Lanczos algorithm which approximately solves the single-band problem at zero-temperature for a larger number of mean field bath sites, but may offer unreliable information about excitations [119, 120].

In this thesis, a DMFT solver has been independently developed in the C++ programming language. As mentioned in section 3.5, it employs an exact diagonalization routine from the *Eigen* C++ libraries [123] as the impurity solver. The LISA algorithm provides a reference for assessing the reliability of our new C++ code, especially given numerous demonstrations of LISA's agreement with experimental observations of real systems (see, for example, [80, 128]). The conjugate gradient minimization sub-routine, `minimize` [129], employed in the FORTRAN code was borrowed in our implementation and translated to C++, as the detailed structure of that algorithm provides very reliable[6] results as a method in finding global minima in the functional landscape of the DMFT self-consistency condition (3.24).

As described previously, the principal goal of the DMFT self-consistency algorithm is to find a set of parameters for the Anderson model bath in (3.14) which best approximates the full lattice system, in order to derive the lattice Green's function, self energy, or other desired outputs. The self-consistency loop begins with an initial guess or more sophisticated estimate (for example, see [62] and [130], respectively) at the value of these parameters, and through successive minimizations convergence to a unique set of final values is expected.

Ideally, this convergence is robust—that is, there should exist a global minimum in

[5] For example, early DMFT results obtained with LISA include [87, 112, 125]. More recent research groups continue to explicitly acknowledge their use of the algorithm, including [114, 126, 127].

[6] While of remarkable reliability, the sub-routine `minimize` is an arcane construction of about 300 lines of interwoven `GO TO` statements. Curiously, Krauth comments in the code's header, "This is a most reliable conjugent [*sic*] gradient routine! It has served us well for many years, and is capable to cope with a very large number of variables. Unfortunately, we don't know who wrote this routine (original name: 'va10a'), and we find it very obscure. Don't worry, it works just fine." [129]

the functional landscape of the self-consistency method such that the particular values of the starting parameters should be irrelevant to the "correct" result of the mapping from the continuous system to the discrete Anderson model.[7] A comparison of sample results (table 3.1) between our C++ code and those from LISA illustrates our ability to find a set of converged bath parameters with perhaps greater robustness than the original FORTRAN implementation. The system parameters are kept constant for all cases. The Coulomb repulsion of this single-band Hamiltonian is $U = 1.0$ and the chemical potential is $\mu = 0.5$, ensuring a metallic physical state where the Green's function (3.29) should properly diverge to negative infinity.

Figure 3.3 shows the low-frequency spectrum for the imaginary part of the self-consistent Green's function in Matsubara frequency for the illustrative sets of starting bath parameters in table 3.1. The low-frequency region is of particular relevance as it is most sensitive to perturbations in the conjugate gradient minimization and to numerical inaccuracies. Results for the LISA and C++ code are compared, demonstrating the convergence of our results along a consistent curve. In contrast the LISA results are somewhat sensitive to the choice of initial parameters. This sensitivity is found to depend as well on the choice of optimization flags employed in executing the FORTRAN compiler (the results shown are for the non-optimized FORTRAN compilation of LISA), and appears in the output of two different machine architectures on which the code was compiled.

	Initial parameters		**Self-consistent final bath parameters**			
			LISA		**C++**	
Set	**V**	ε	**V**	ε	**V**	ε
1	0.20000	0.10000	0.167581	0.042032	0.192225	0.051220
	0.30000	0.20000	0.419902	0.448987	0.414271	0.498435
	0.20000	-0.10000	0.169194	-0.043284	0.191536	-0.050683
	0.30000	-0.20000	0.420228	-0.454990	0.413722	-0.495746
2	0.10000	1.00000	0.191090	0.049528	0.194250	0.051481
	0.20000	2.00000	-0.421647	0.510805	0.422266	0.524235
	0.10000	-1.00000	0.196718	-0.053710	0.419528	-0.052171
	0.20000	-2.00000	-0.420995	-0.525202	-0.417396	-0.518024
3	20.00000	7.00000	5.900908	41.881046	0.195649	0.051510
	30.00000	10.00000	0.450311	0.001506	-0.426948	0.541305
	20.00000	-7.00000	5.168741	-32.059884	0.198597	-0.053669
	30.00000	-10.00000	-0.015162	-17.882145	0.425515	-0.548340

Table 3.1: Initial bath parameters used in self-consistency algorithm to compare our C++ code's convergence with that of LISA. Ideally, the converged values should agree across all three sets.

[7] This is not universally seen in all DMFT studies; for example, [130].

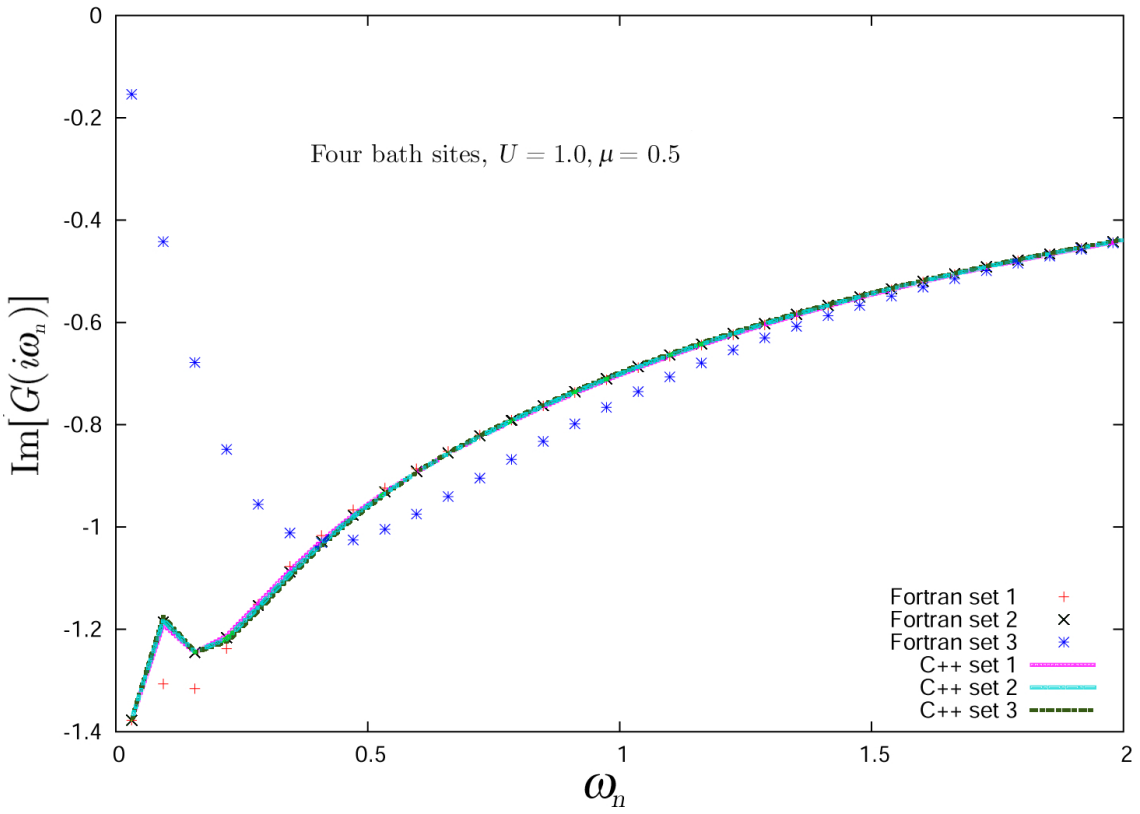

Figure 3.3: A comparison of the self-consistently converged Green's functions (3.29) for a single-band Hubbard model from our C++ algorithm (lines) with the LISA Fortran algorithm (points). Shown are results for three sets of initial bath parameters (*q.v.* table 3.1) which illustrate the variance in convergence, at fixed system parameters ($U = 1.0$, $\mu = 0.5$) and four bath sites. With these parameters, the system is properly metallic and a negative divergence is expected at zero Matsubara frequency, $i\omega_n$. All three C++ lines overlap with Fortran set 2, which appears to be the proper result (for different starting parameters similar to set 2, the Fortran code also converges to this line). The C++ results therefore appear to be robust regardless of the initial parameter choices, whereas the LISA code wanders into different global minima in the conjugate gradient routine, resulting in unexpectedly different apparent physics.

The self-consistent Green's function is the main quantity of ultimate interest in the DMFT problem, and it is derived from the appropriate set of bath parameters. The proper convergence of this quantity is therefore an important indicator of the DMFT algorithm's proper functioning and in this case is a helpful test of the reliability of our multiorbital C++ DMFT implementation (chapter 4) applied in the limiting case of a single-band model.

3.7 MIT in Single Band DMFT

One definitive achievement [112] of the DMFT method was the visualization of the metal-insulator transition at half-filling, emerging from the competition between electron kinetic energy-driven hopping between sites and the Mott insulator state that arises from strong on-site Coulomb repulsion (*q.v.* section 1.2). DMFT provided the first view of the MIT without the need to restrict analysis to one of the transition's two limits [131].

Varying the parameters of the Hubbard model under consideration, DMFT yields the impurity density of states $\rho(\omega)$ defined for the analytically continued impurity Green's function $G^{\text{imp}}(\omega)$ as,

$$\rho(\omega) = -\frac{1}{\pi}\Im G^{\text{imp}}(\omega), \tag{3.30}$$

which can show the opening of a Mott-insulator gap in the Hubbard model at half filling around a critical value of the Coulomb repulsion, U_c. The shoulder Hubbard bands are spaced symmetrically around the Fermi energy, as illustrated in figure 1.1.

The insulating phase is characterized by the complete lack of electron occupation at the Fermi level, with a gap of non-occupied states between two separated Hubbard bands. The metallic state shows a non-zero density of states at zero frequency (the Fermi energy) along with the Hubbard bands, and thus a "three-peak" structure which becomes increasingly distinct as Coulomb repulsion increases. The height of the central peak is the quasiparticle weight and is an order parameter for metallicity [87]. (The evolution of these features can be seen in figure 3.5 for the case of a finite temperature DMFT solution with four bath sites.)

For zero temperature, as the Coulomb repulsion between electrons is gradually increased, the metallic quasi-particle peak of constant height narrows in width until disappearing abruptly at $U = U_c$, associated with a diverging electron effective mass [and thus a vanishing quasiparticle weight (*q.v.* section 5.3)]. As the peak narrows, a finite insulating gap appears in anticipation of the final disappearance of the peak. This sharp MIT was observed by an early application of the LISA code [132] and visualized via an ED impurity solver [112] using the zero-temperature Lanczos method on a paramagnetic system. In

both studies a metal-insulator "co-existence region" appeared near the MIT. In the ED study this was found in the region where $1.11W \leq U \leq 1.15W$ (for a free electron density of states bandwidth $W = 4$). In this region LISA returned converged DMFT results for both metallic and insulating behaviours. The rough consensus of various DMFT studies of the MIT at zero temperature suggests a value of U_c between W and $1.5W$ [133].

At finite temperature the metallic and insulating definitions are less precise. The central quasiparticle peak is gradually suppressed in height as weight is redistributed to the Hubbard shoulders. A coexistence region is found up to a critical end point temperature above which there is a gradual suppression of metallicity as the Coulomb repulsion is changed, and the phase of the material shows a gradual crossover between a state dominated by a strong quasiparticle peak to that with a small central peak and dominant gapped Hubbard bands [87]. Below this temperature, as the Coulomb repulsion is decreased from a large insulating value, the phase becomes metallic at a critical value $U = U_{c1}(T)$. Similarly, as U is increased from the metallic side of the transition there is a value $U = U_{c2}(T) > U_{c1}(T)$ at which the phase becomes insulating. A typical phase diagram for the finite-temperature MIT is shown in figure 3.4.

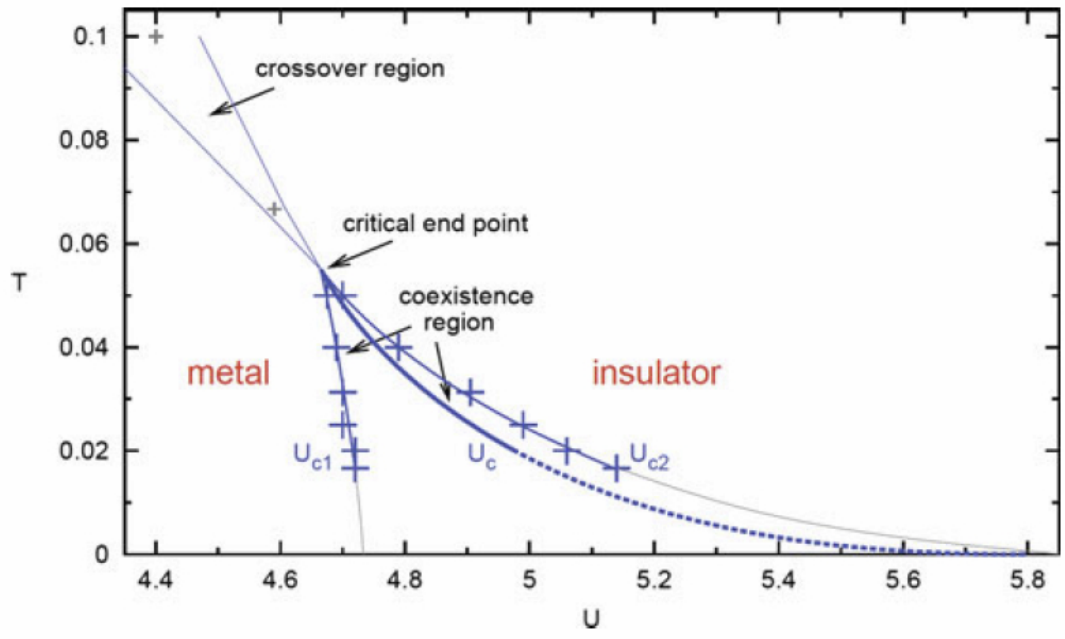

Figure 3.4: Finite temperature phase diagram for the MIT. A coexistence region is bounded by the $U_{c1}(T)$ and $U_{c2}(T)$ curves. $U_{c1}(T)$ marks the transition to metallicity as U is decreased from a high, insulating value, while $U_{c2}(T)$ marks the onset of insulating behaviour when U is increased from a low, metallic value. The actual transition point, $U_c(T)$, is calculated from (3.31). From [20].

The coexistence region has been thought of as a region of hysteresis, arising near the MIT by increasing or decreasing the Coulomb repulsion toward $U_c(T)$, and is indicative of a first-order transition. The actual transition point is found by examining the lower free energy state of the two phases. This free energy $F(U,T)$, at temperature T for some Coulomb repulsion U, can be calculated [134] by an integration,

$$F(U,T) = F(0,T) + \int_0^U D(U',T)dU' \,, \tag{3.31}$$

where $D(U',T)$ is the average double occupancy defined by,

$$D = \langle n_\uparrow n_\downarrow \rangle \,. \tag{3.32}$$

In the practical context of the DMFT algorithm, the coexistence region appears to arise as a discrepancy in the converged values of the bath parameters owing to the minimization technique finding different stable solutions for differing input parameter regimes. With all elements of the lattice Hubbard Hamiltonian held constant, one might expect a unique physical solution for a set of bath parameters corresponding to the best fit between the SIAM and the lattice system. In the coexistence region, however, this ideal case is not actualized, and the existence of more than one stable solution must result from the minimization routine settling on well-separated local minima in the bath parameter functional landscape. These minima may correspond to equally low ground state energies, although a transparent test along these lines does not appear to have been published. It is also unclear whether the many studies on DMFT hysteresis have all employed the `minimize` conjugate gradient method subroutine [129] packaged in the LISA code, or another method. Such details are almost never indicated in the publications.

There has been some controversy regarding both the quantitative value of $U_c(T)$ as a function of temperature, as well as the qualitative nature of the transition, whether an abrupt first-order transition or a continuous change [131]. Many early finite-temperature DMFT studies found an abrupt transition (characterized by the disappearance of the quasiparticle weight) accompanied by a hysteresis region [87, 104], reminiscent of experimental expectations from studying the MIT in V_2O_2 [19]. This was disputed by other non-DMFT methods based on similar infinite-dimensionality assumptions [135, 136] which found continuous transitions at different values of $U_c(T)$. In an attempt at resolving the confusion, Schlipf *et al.* [131] performed a careful finite-temperature QMC DMFT study (using two different code implementations to identify and eliminate code-specific biases or errors) on the Bethe lattice, finding a continuous MIT with no hysteresis region. This result was

challenged by Krauth [137] as an error in methodology. Shortly thereafter, a (mean-field) self-energy functional analysis by Potthoff [133] again found a first-order transition along with a hysteresis region.

Figure 3.5 illustrates the spectral density evolution of the single-band system as the MIT crossover develops with increasing U. In this plot the temperature is above the maximum critical temperature T_c for the first-order transition. The electron quasiparticle weight transfer from the metallic to the insulating regime is clearly seen as the central coherent peak decreases in height until disappearing entirely.

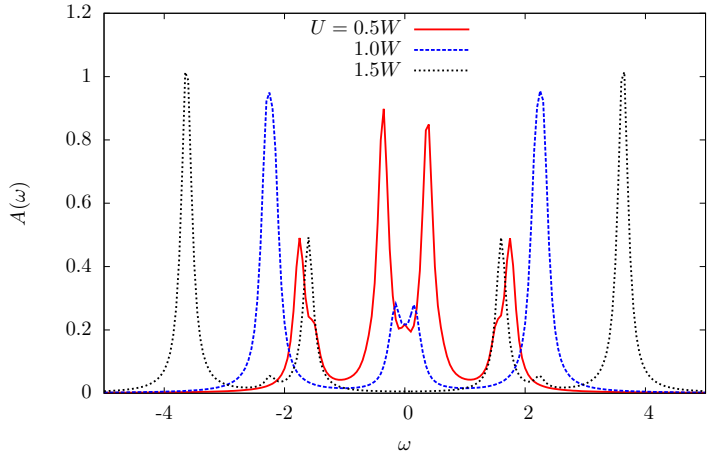

Figure 3.5: The evolution of the Mott metal-insulator transition (MIT) in the single-band Hubbard model at half-filling, derived from our DMFT code with four bath sites ($\beta = 100$; $W = 4.0$ is the bandwidth) for changing electron interaction potential. The actual numerical quantities are delta functions, but are broadened as Lorentzians ($\eta = 0.1$) for clarity. A central, non-zero quasi-particle peak at $\omega = 0.0$ indicates metallic behaviour. The collections of side peaks are Hubbard bands, which grow and separate with increasing Coulomb repulsion opening up an insulating gap as the quasi-particle peak falls away. Note that once the insulating phase is attained, the separation of the shoulder Hubbard peak centres is approximately U as expected [26, 87] (*c.f.* figure 1.1). (Apparent asymmetry in the central peak for $U = 0.5W$ case is an artifact of the real frequency sampling resolution.)

It should be noted that the discretization of the Anderson model bath generates discrete delta functions in all DMFT real frequency quantities. Thus, the fine details of the spectral density (for example) are poor, while the clustering of delta peaks provides a very accurate "coarse-grained" insight into the actual electron states [87]. This is evident in figure 3.5 in the structure which forms the normally continuous shoulders of the Hubbard bands, and the "spikey" appearance of the coherent central peak that dominates for small U.

Corresponding to the change in the density of states that occurs around the MIT, another indicator of the transition is an abrupt change in the slope of the self energy

around the Fermi energy. In particular, the imaginary part of $\Sigma(i\omega_n)$ changes from a ω_n dependency near $\omega_n = 0$ to a negative divergence, as shown in figure 3.6 as the Coulomb repulsion at half filling passes through the critical value for the MIT shown in figure 3.5.

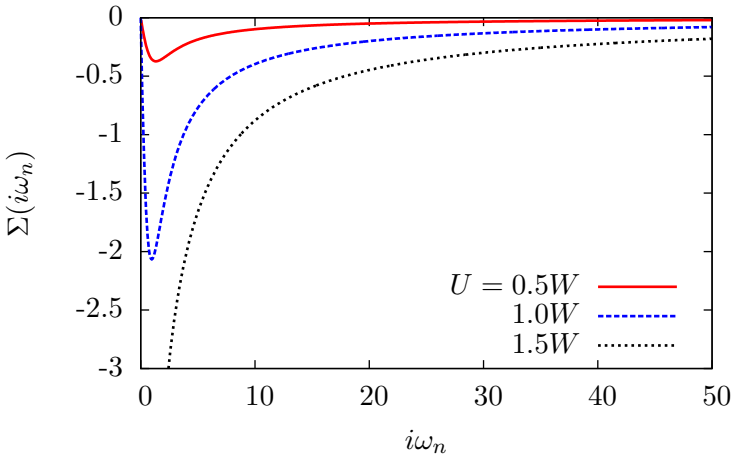

Figure 3.6: In addition to the elimination of the quasiparticle peak at the Fermi energy shown in figure 3.5, the MIT is also signaled (perhaps more clearly) by an abrupt change in the self energy as the Coulomb repulsion crosses the critical value. On the metallic side of the transition, the slope of $\Im\Sigma(i\omega_n)$ goes to zero as $\omega_n \to 0$, while for the insulating case it has a negative divergence.

Chapter 4

Dynamic Hubbard Model in Dynamical Mean Field Theory

4.1 A Short History of Multiorbital DMFT

Multiorbital models were implemented very early in the history of DMFT in an attempt to explore electron transport in the copper-oxide planes of high temperature superconductors. Already in 1993, Si and Kotliar [138, 139] studied a very general two-orbital model with local hybridization and a dispersionless upper orbital using a matrix representation of Green's functions which defined the formalism of later multiorbital DMFT (MODMFT) studies, including our work.

Georges *et al.* [61] employed a bipartite lattice with strongly correlated copper d orbitals and uncorrelated higher energy p orbitals, which they solved on the Bethe lattice with a Monte Carlo impurity solver. In 1994, Cafarrel and Krauth [112] developed the exact diagonalization DMFT impurity solver and immediately applied it to a similar Hubbard model, exploring superconducting order through the inclusion of an explicit pairing term. Concurrently, Si *et al.* [62] included onsite hybridization between a half-filled lower orbital coupled to the bath and a dispersionless upper orbital, observing a phase diagram exhibiting non-Fermi liquid metallicity ascribed to the presence of the hybridization parameter. Pruschke and Bulla [115] employed a numerical renormalization group solver on a non-hybridized two-orbital system with Hund's coupling, exploring novel MIT behaviour. Koga *et al.* [60] evaluated a degenerate two-orbital model with local hybridization using QMC DMFT, examining the role of t' in enhancing the MIT and "orbital selective" Mott transition (OSMT) behaviour (see section 7.6).

An important benchmark study of exact diagonalization MODMFT was performed by

Liebsch and Ishida [113], evaluating the importance of Matsubara frequency resolution and the accuracy of using a limited number of bath sites per orbital. They employed a matrix formalism similar to Si and Kotliar [139], and studied non-hybridized degenerate three-band models and various lattice geometries realized through symmetries applied to the Green's functions of the different orbitals.

Winograd and DeMedici [65] have analyzed the OSMT with a two-orbital locally hybridized model including Hund's coupling at zero temperature with the Lanczos approximation.

Recently, a few DMFT studies have incorporated the intersite hybridization, t_{01}, into their multiband Hubbard Hamiltonians.

Poteryaev *et al.* [140] focused on the quarter-filling state of a non-degenerate two-orbital model with both exact diagonalization and continuous time Monte Carlo DMFT impurity solvers, enforcing a hypercubic lattice geometry on the DMFT solution through the dispersion which incorporated a finite non-local momentum dependent hybridization, $t_{01}(k)$, which drives the MIT at a different electron filling value than expected from the non-hybridized case.

Song and Zou [63] and Song [64] have studied a two-orbital system with two-site DMFT [141] including the nonlocal hybridization, but in the absence of local t'. They examined the effects of the energy gap $(\epsilon_1 - \epsilon_0)$ and hybridization on optical conductivity and orbital-selective Mott transitions.

4.2 MODMFT Formalism and Workflow

The formalism and algorithm of MODMFT are a generalization of that set out in chapter 3 for the single orbital case. The critical difference, which leads to a significant increase in complexity, is the introduction of matrices to represent the Green's functions and self energy of the impurity and lattice models, coupled with the hybridization parameters, which mix the electron states between the lower energy and higher energy orbitals, and are necessary to capture DHM physics. These are the parameters introduced in chapter 2: t', the local (onsite) hybridization, and t_{01}, the nonlocal (intersite) hybridization which is a hopping parameter.

Figure 4.1 shows the workflow of the MODMFT algorithm we employ in solving the electronic DHM for a particular system parameter set, involving a unique choice for each of the following variables:

ϵ_0 lower orbital energy (in general set to zero)

ϵ_1 upper orbital energy

t_0 lower band hopping

t_1 upper band hopping

t_{01} nonlocal hybridization (interband hopping)

t' local hybridization

U_0 lower orbital Coulomb repulsion

U_1 upper orbital Coulomb repulsion

U_{01} interorbital Coulomb repulsion

μ chemical potential

As with the single band Hubbard model (1.4), the full Hamiltonian for the electronic dynamic Hubbard model (2.15) is mapped to an impurity model, where the impurity site is defined with a lower and upper orbital energy state. Each energy level is represented in the impurity model by its own site. Electrons are locally hybridized between orbitals by a non-zero value of t', which is not a spatial hopping, thus retaining the local character of DMFT and the momentum-independence of the self energy and Green's function. Two electrons with opposite spin can occupy each orbital site of the impurity, in keeping with Pauli exclusion.

The non-interacting bath is composed of n_l pseudosites, with energies ε_l, representing the surrounding lattice environment of the impurity orbitals. The bath sites are coupled to the impurity lower (0) and upper (1) impurity sites via hopping/hybridization parameters V_{0l} and V_{1l}, respectively. Two coupling geometries [113] are possible to connect the multiorbital impurity to the bath, as shown in figure 4.2. One geometry identifies each bath site with a particular orbital, while the other more generally shares every bath site between the orbitals. The impurity orbitals interact directly with one another through the local hybridization t' and Coulomb term U_{01}.

The more general bath hybridization/hopping geometry, allowing electron transitions from both orbitals to all bath sites, better reflects the character of finite cross-orbital intersite hopping in the electronic DHM. As well, connecting two impurity orbitals to n_l bath sites allows for $2n_l$ adjustable hopping hybridization terms, instead of n_l such terms if each orbital is restricted to its own bath. The larger space of parameters in which to

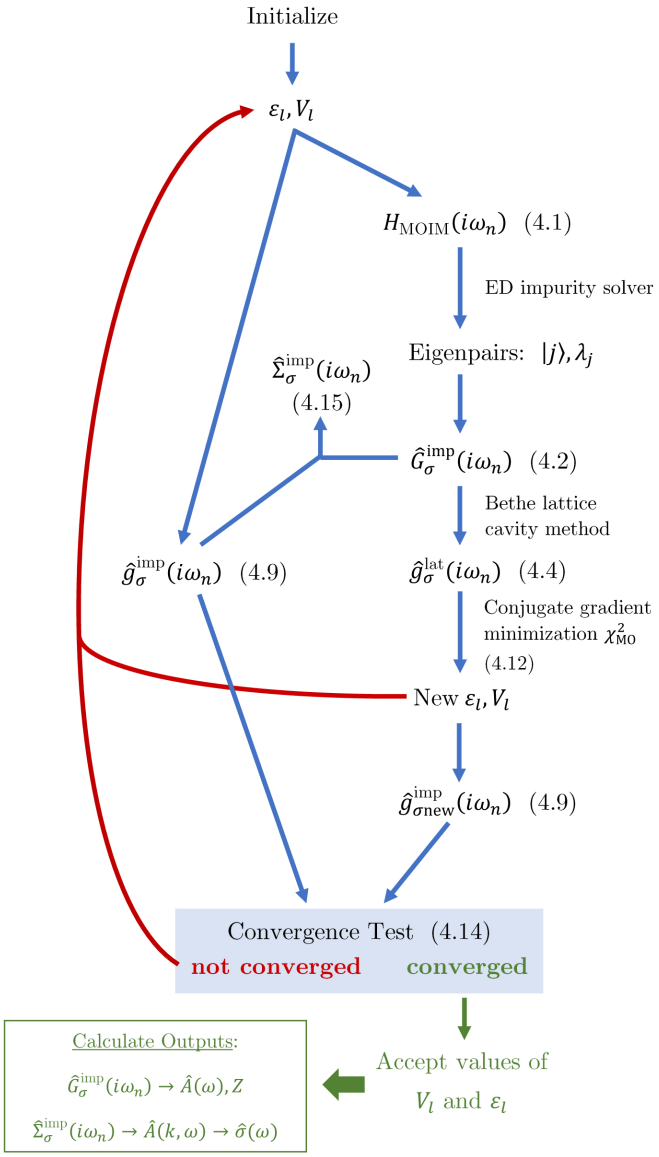

Figure 4.1: Workflow in MODMFT solution, illustrating the steps described in section 4.2. The logic describes a self-consistency routine terminating with a convergence condition on the mean field functions.

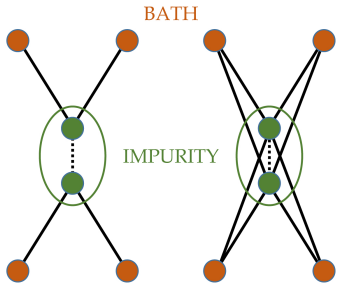

Figure 4.2: Two possible geometries for electronic transitions between the two-orbital DMFT impurity (green circles) and the bath pseudo-sites (orange circles). On the left, each orbital is connected to its own bath, while on the right electrons from either orbital are allowed transitions to all the bath sites. The solid lines indicate electron hopping between the impurity and bath, while the dotted lines represent the local hybridization t'.

map the lattice problem to the impurity model allows for a better fit in the minimization routine, and we take advantage of this by selecting the more general geometry.[1]

The multiorbital impurity model (MOIM), a generalization of (3.14), is,

$$\begin{aligned} H_{\mathrm{MOIM}} \;=\; & (\epsilon_0-\mu)\sum_{\sigma} c^{\dagger}_{0\sigma}c_{0\sigma} + (\epsilon_1-\mu)\sum_{\sigma} c^{\dagger}_{1\sigma}c_{1\sigma} + \sum_{l\sigma}(\varepsilon_l-\mu)b^{\dagger}_{l\sigma}b_{l\sigma} \\ & + U_0 c^{\dagger}_{0\uparrow}c_{0\uparrow}c^{\dagger}_{0\downarrow}c_{0\downarrow} + U_1 c^{\dagger}_{1\uparrow}c_{1\uparrow}c^{\dagger}_{1\downarrow}c_{1\downarrow} + U_{01}\sum_{\sigma\sigma'} c^{\dagger}_{0\sigma}c_{0\sigma}c^{\dagger}_{1\sigma'}c_{1\sigma'} \\ & + \sum_{l\sigma} V_{0l}(b^{\dagger}_{l\sigma}c_{0\sigma} + c^{\dagger}_{0\sigma}b_{l\sigma}) + \sum_{l\sigma} V_{1l}(b^{\dagger}_{l\sigma}c_{1\sigma} + c^{\dagger}_{1\sigma}b_{l\sigma}) + t'\sum_{\sigma}(c^{\dagger}_{0\sigma}c_{1\sigma} + c^{\dagger}_{1\sigma}c_{0\sigma}), \end{aligned} \tag{4.1}$$

where the operators $c^{\dagger}_0$ and c_0 create and annihilate electrons on the impurity lower orbital, $c^{\dagger}_1$ and c_1 on the upper orbital, and $b^{\dagger}_l$ and b_l on bath pseudo-site l.

The MODMFT workflow illustrated in figure 4.1 begins with an initialization of the bath parameters in the impurity Hamiltonian (4.1).

The extra orbital associated with the impurity increases the Hilbert space of the Hamiltonian for a fixed number of bath pseudosites. As discussed in section 3.5, an exact diagonalization solver is used in our implementation to find the eigensolution of (4.1), with eigenvalues λ_j and eigenvectors $\mid j\rangle$. These eigenpairs are used to find the finite temperature Matsubara Green's function defined in the multiorbital case as,

$$\hat{G}^{\mathrm{imp}}_{\sigma}(i\omega_n) = \frac{1}{Z}\sum_{j,k}\frac{\hat{\Phi}_{jk}(e^{-\beta\lambda_j}+e^{-\beta\lambda_k})}{i\omega_n-(\lambda_j-\lambda_k)} \tag{4.2}$$

[1] Our reasoning follows a similar line as that taken in cluster DMFT studies, where one chooses the most general bath parameterization possible for the self-consistency condition to be fulfilled [118].

where,

$$\hat{\Phi}_{jk} = \begin{pmatrix} \left|\langle k|\, c^{\dagger}_{0\sigma}\, |j\rangle\right|^2 & \langle j|\, c_{1\sigma}\, |k\rangle\, \langle k|\, c^{\dagger}_{0\sigma}\, |j\rangle \\ \langle j|\, c_{0\sigma}\, |k\rangle\, \langle k|\, c^{\dagger}_{1\sigma}\, |j\rangle & \left|\langle k|\, c^{\dagger}_{1\sigma}\, |j\rangle\right|^2 \end{pmatrix} . \tag{4.3}$$

The impurity Green's function is applied to the multiband matrix equivalent of the self-consistency condition, (3.16), derived by the cavity method [87]. Borrowing from and generalizing the usage in CDMFT [139, 142], we have for the multiband case on the Bethe lattice an expression for the lattice mean field function,

$$\left[\hat{g}^{\mathrm{lat}}_{\sigma}(i\omega_n)\right]^{-1} = (i\omega_n + \mu)\,\hat{\mathbb{1}} - \hat{\epsilon} - \hat{t}' - \hat{t}\,\hat{G}^{\mathrm{imp}}_{\sigma}(i\omega_n)\,\hat{t}\,, \tag{4.4}$$

where $\hat{\mathbb{1}}$ is the 2×2 identity matrix. The energy matrix $\hat{\epsilon}$ and hybridization matrix $\hat{t}'$ are,

$$\hat{\epsilon} = \begin{pmatrix} \epsilon_0 & 0 \\ 0 & \epsilon_1 \end{pmatrix} \tag{4.5}$$

$$\hat{t}' = \begin{pmatrix} 0 & t' \\ t' & 0 \end{pmatrix} . \tag{4.6}$$

The hopping matrix $\hat{t}$ is,

$$\hat{t} = \begin{pmatrix} t_0 & t_{01} \\ t_{01} & t_1 \end{pmatrix} . \tag{4.7}$$

With $t_{01} = 0$ it reduces to the form used in reference [65].

The use of (4.4) is specific to the Bethe lattice, and is the step in which the density of states of its specialized "geometry", reflected in its derivation [87], enters into the MODMFT procedure. This avoids the necessity of solving, at each iteration of the MODMFT self-consistency routine, the multiorbital integral defining the lattice Green's function:

$$\hat{G}^{\mathrm{lat}}_{\sigma}(z) = \int D^{(0)}(\epsilon)\left[(z + \mu - \epsilon)\,\hat{\mathbb{1}} - \hat{\epsilon} - \hat{t}' - \hat{\Sigma}_{\sigma}(z)\right]^{-1} d\epsilon, \tag{4.8}$$

where $D^{(0)}(\epsilon)$ is the non-interacting density of states of the multiorbital system, which has no simple analytical form (see section 4.3 below).

At convergence, the lattice mean field function resulting from (4.4) is expected to be equal to the mean field function $\hat{g}^{\mathrm{imp}}_{\sigma}(i\omega_n)$ defined from the impurity bath as,

$$\hat{g}^{\mathrm{imp}}_{\sigma}(i\omega_n) = \left[(i\omega_n + \mu)\hat{\mathbb{1}} - \hat{\epsilon} - \hat{t}' - \hat{\Delta}_{\sigma}(\varepsilon_l, V_{0l}, V_{1l})\right]^{-1} \tag{4.9}$$

where $\hat{\Delta}_\sigma(\varepsilon_l, V_{0l}, V_{1l})$ is the bath hybridization function,

$$\hat{\Delta}(\varepsilon_l, V_{0l}, V_{1l}) = \sum_{l=0}^{n_b} \begin{pmatrix} \frac{V_{0l}^2}{i\omega_n - \varepsilon_l} & \frac{V_{0l}V_{1l}}{i\omega_n - \varepsilon_l} \\ \frac{V_{1l}V_{0l}}{i\omega_n - \varepsilon_l} & \frac{V_{1l}^2}{i\omega_n - \varepsilon_l} \end{pmatrix} . \tag{4.10}$$

(In the paramagnetic case a spin index is superfluous and suppressed on the bath parameters.)

Expression (4.10) is not the most general form which could be employed for this multiorbital function. Rather, for a construction with the number of orbitals, n_x, it could be defined in terms of n_x independent bath parameters $\hat{V}_x$ and $\hat{\varepsilon}_x$ of size $n_l \times n_l$ [142]. The computational expense required for this general configuration has motivated us to follow the approximate form of the bath parameterization function employed by Bolech *et al.* [142] as well as Ishida and Liebsch [143] for the cluster DMFT formulation, which has essential similarities to MODMFT.

The equivalence of the lattice and impurity mean field functions,

$$\hat{g}_\sigma^{\text{lat}}(i\omega_n) = \hat{g}_\sigma^{\text{imp}}(i\omega_n) \,, \tag{4.11}$$

is sought by mapping the value of $\hat{g}_\sigma^{\text{lat}}(i\omega_n)$ at each frequency onto the functional form of $\hat{g}_\sigma^{\text{imp}}(i\omega_n)$, which is defined in terms of the bath parameters through (4.10). This is accomplished by characterizing a distance function χ^2, similar to (3.24), over the multiorbital matrix components,

$$\chi^2_{\text{MO}} = \frac{1}{N+1} \sum_{\sigma xy} \sum_{n=0}^{N} f(\omega_n) \left| g_{\sigma xy}^{\text{lat}}(i\omega_n) - g_{\sigma xy}^{\text{imp}}(i\omega_n) \right|^2 , \tag{4.12}$$

where N is the number of Matsubara frequencies employed in the solution. The subscripts x, y denote the orbitals and the sum is a single sum over each unique pairing. $f(\omega_n)$ is a weighting factor which can take a range of forms in order to ensure better convergence relative to some part of the energy spectrum.

As discussed in section 3.6, the efficient conjugate gradient minimization routine, `minimize` [129], is employed to traverse the functional landscape of $\hat{g}_\sigma^{\text{imp}}(i\omega_n)$ until it achieves a minimal value for the distance function (4.12).

With respect to the form of the weight function $f(\omega_n)$, we choose to emphasize the bath parameters fitting the high structure lower frequency region through,

$$f(\omega_n) = \frac{1}{\omega_n}, \tag{4.13}$$

since the Green's function smoothly approaches zero for $\omega_n \to \infty$. Other forms of $f(\omega_n)$ such as 1 and $\frac{1}{\omega_n^2}$ have been tested for MODMFT [113] and agree with our experience that (4.13) provides a reliable and efficient result.[2]

An ideal mapping of the lattice Hubbard model to the impurity model will result in the functions being strictly equal in (4.11). In practice, with a finite-sized bath the equivalence condition (4.12) will remain approximate, and the minimization routine [129] will find as close a fit as possible with the size of the parameter space available.

The minimization routine returns a set of bath parameters from the functional fit, which are fed back into the impurity mean field function (4.9) and the components of this new matrix $\hat{g}^{\mathrm{imp}}_{\mathrm{new}}(i\omega_n)$ are compared to those of the old function defined by the bath parameters in use prior to the fit, testing for convergence between the two functions. The convergence condition,

$$\frac{1}{N+1}\left|\hat{g}^{\mathrm{imp}}_{\sigma xy\,\mathrm{new}}(i\omega_n) - \hat{g}^{\mathrm{imp}}_{\sigma xy\,\mathrm{old}}(i\omega_n)\right|^2 < \eta \tag{4.14}$$

tests whether the appropriate set of bath parameters for the mapping have been found within some tolerance η. Having begun by inserting guessed parameters into the Anderson impurity Hamiltonian (4.1), it is unlikely that on the first iteration the condition (4.14) will be satisfied for a reasonably constrained η.

We take $(N+1)\eta \approx 10^{-6}$-$10^{-7}$, which in general seems to ensure an efficient arrival at a converged solution while maintaining an apparently identical visual correspondence between the ultimate and penultimate functions within the resolution of useful output plots. We have found the results of increasing this value to the range of 10^{-8} and 10^{-9} to be a case of diminishing returns.

Agreement in (4.14) signals a converged solution and the end of the MODMFT routine at which point the converged impurity Green's function and mean field function can be used to determine the orbital self energy matrix $\hat{\Sigma}_\sigma(i\omega_n)$ through a multidimensional Dyson equation,

$$\hat{\Sigma}^{\mathrm{imp}}_\sigma(i\omega_n) = \left[\hat{g}^{\mathrm{imp}}_\sigma(i\omega_n)\right]^{-1} - \left[\hat{G}^{\mathrm{imp}}_\sigma(i\omega_n)\right]^{-1} . \tag{4.15}$$

The self energy of the impurity model is considered equivalent to that of the lattice at convergence of the bath parameters, so that,

$$\hat{\Sigma}^{\mathrm{imp}}_\sigma(i\omega_n) = \hat{\Sigma}^{\mathrm{lat}}_\sigma(i\omega_n) = \hat{\Sigma}_\sigma(i\omega_n)\,. \tag{4.16}$$

While the self energy plays no role in solving for the bath parameters in the MODMFT

[2] In contrast, the self energy functional approach of CDMFT [144] favours a weight of the squared self energy, with $f(\omega_n) = \frac{1}{\omega_n}$ providing a less adequate result in weakly metallic or insulating phases [145].

algorithm, it is important for understanding and calculating the physical properties of the system, including the tools of our DHM study defined in chapter 5, some of which are also dependent on the converged value of the impurity Green's function $\hat{G}^{\mathrm{imp}}_{\sigma}(i\omega_n)$.

If the convergence check in (4.14) does not produce sufficient agreement between the current and previous values of the impurity mean field function, the new bath parameters obtained from the minimization fit of (4.12) are taken as the initialization parameters for a new (improved) instantiation of the MODMFT workflow, returning to the top of figure 4.1. The impurity Hamiltonian (4.1) is redefined and the procedure is restarted and repeated until the convergence condition is met.

The problem of finding proper bath parameters to map the lattice model to an impurity model, from which Green's functions and self energies can be evaluated, is therefore a complex problem in self-consistency. The value of the converged bath parameters are defined in terms of the impurity Green's function through the self-consistency condition (4.4) and its use in the minimization algorithm applied to (4.12). In turn, they define the impurity Green's function through the impurity Hamiltonian solution, and the impurity mean field function $\hat{g}^{\mathrm{imp}}(i\omega_n)$.

4.3 Multiorbital Bethe Lattice Density of States

The Bethe lattice depicted in figure 3.2, in the limit of infinite connectivity, is widely used in DMFT studies to simplify the self-consistency procedure through expressions (3.16) and (4.4).

The free electron density of states (DOS) for the infinitely-connected Bethe lattice (4.22) is strictly applicable to the single band Hubbard Hamiltonian (1.4). While the explicit form of the Bethe lattice DOS is not required for the simplification of the DMFT or MODMFT routine itself, it is an explicit component in evaluating the optical conductivity (5.30) discussed at length in section 5.4.

The single band Bethe lattice DOS has the semi-circular form depicted in figure 4.3, centered at the orbital energy of the DMFT impurity, and dependent on the band hopping, t, relevant to that orbital, with bandwidth $W = 4t$. Strictly speaking, it represents the energies of electrons which begin at some site o, propagate away through the lattice, and return to site o [93, 94]. In the multiorbital case, we expect the DOS to depend in a non-trivial way on all three intersite hoppings, t_0, t_1 and t_{01}, as well as the onsite hybridization t' and the orbital energy gap ϵ_1. In the non-hybridized single band limit it will reduce to two semicircular forms with bandwidth $W_0 = 4t_0$ and $W_1 = 4t_1$.

To our knowledge, a derivation of the multiorbital density of states for the infinitely

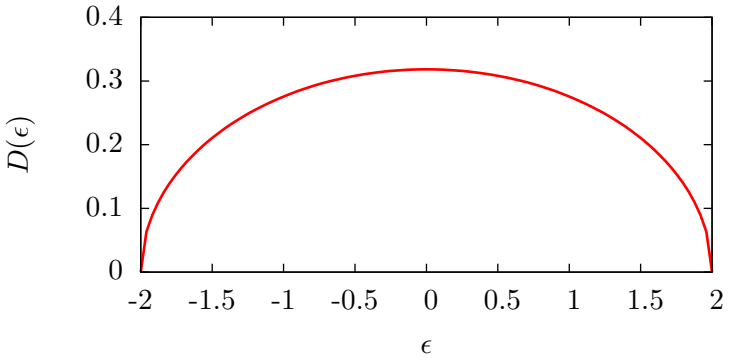

Figure 4.3: Semi-circular Bethe lattice density of states, $D(\epsilon)$, for infinite connectivity, with $t = 1.0$. The bandwidth is $W = 4t$.

connected Bethe lattice including intersite/interband hopping has not yet been achieved, and in principle would require an analytical diagonalization of a infinite-dimensional pentatriangular matrix [94].

Here we generalize Mahan's intuitive derivation [94] of the single orbital Bethe lattice DOS to the two-orbital case and derive the Hamiltonian matrix for the z-connected Bethe lattice geometry, which will provide the eigenspectrum necessary to numerically determine the multiorbital DOS which will depend on the specific inputs of the hopping and hybridization parameters. These results will be used to provide a more reliable estimate of the optical conductivity calculations in section 7.5.

We begin by defining eigenstates of the DHM Hamiltonian (2.15) for a Bethe lattice geometry of connectivity z and two orbitals per site, focusing on the number of hops an electron takes away from a site j without backtracking. The null ket is defined as $|\emptyset\rangle$, the vacuum state with no electrons occupying the lattice. A particle in the lower orbital on site j will be identified as the state $|0_0\rangle$, and in the upper orbital as $|0_1\rangle$. Electron hopping to any of the z nearest-neighbour sites is defined to be symmetric, and results in states designated $|1_0\rangle$ and $|1_1\rangle$, corresponding to the lower and upper orbitals respectively. From this site, a second hop is allowed to any of $z-1$ nearest neighbours (a backwards hop is not allowed) denoted by $|2_0\rangle$ and $|2_1\rangle$. All further states are defined by additional hops to $z-1$ nearest neighbours in the lattice.

These states are explicitly defined in terms of the null ket as,

$$|0_0\rangle = c_0^\dagger |\emptyset\rangle \tag{4.17a}$$
$$|0_1\rangle = c_1^\dagger |\emptyset\rangle \tag{4.17b}$$
$$|1_0\rangle = \frac{1}{\sqrt{z}} \sum_\delta c_{0,\delta}^\dagger |\emptyset\rangle \tag{4.17c}$$
$$|1_1\rangle = \frac{1}{\sqrt{z}} \sum_\delta c_{1,\delta}^\dagger |\emptyset\rangle \tag{4.17d}$$
$$|2_0\rangle = \frac{1}{\sqrt{z(z-1)}} \sum_\delta \sum_{\delta' \neq -\delta} c_{0,\delta+\delta'}^\dagger |\emptyset\rangle \tag{4.17e}$$
$$|2_1\rangle = \frac{1}{\sqrt{z(z-1)}} \sum_\delta \sum_{\delta' \neq -\delta} c_{1,\delta+\delta'}^\dagger |\emptyset\rangle \tag{4.17f}$$

where the sum over δ and δ' is over the nearest neighbour sites.

Hamiltonian matrix elements are determined by applying the non-interacting part of Hamiltonian (2.15) on these states:

$$H_{\mathrm{DHM}} |0_0\rangle = \epsilon_0 |0_0\rangle + t' |0_1\rangle + t_0\sqrt{z} |1_0\rangle + t_{01}\sqrt{z} |1_1\rangle \tag{4.18a}$$
$$H_{\mathrm{DHM}} |0_1\rangle = t' |0_0\rangle + \epsilon_1 |0_1\rangle + t_{01}\sqrt{z} |1_0\rangle + t_1\sqrt{z} |1_1\rangle \tag{4.18b}$$
$$\begin{aligned} H_{\mathrm{DHM}} |1_0\rangle = {} & t_0\sqrt{z} |0_0\rangle + t_{01}\sqrt{z} |0_1\rangle + \epsilon_0 |1_0\rangle + t'\sqrt{z} |1_1\rangle \\ & + t_0\sqrt{z-1} |2_0\rangle + t_{01}\sqrt{z-1} |2_1\rangle \end{aligned} \tag{4.18c}$$
$$\begin{aligned} H_{\mathrm{DHM}} |1_1\rangle = {} & t_{01}\sqrt{z} |0_0\rangle + t_1\sqrt{z} |0_1\rangle + t'\sqrt{z} |1_0\rangle + \epsilon_1 |1_1\rangle \\ & + t_{01}\sqrt{z-1} |2_0\rangle + t_1\sqrt{z-1} |2_1\rangle \end{aligned} \tag{4.18d}$$
$$\begin{aligned} H_{\mathrm{DHM}} |2_0\rangle = {} & t_0\sqrt{z-1} |1_0\rangle + t_{01}\sqrt{z-1} |1_1\rangle + \epsilon_0 |2_0\rangle + t'\sqrt{z(z-1)} |2_1\rangle \\ & + t_0\sqrt{z-1} |3_0\rangle + t_{01}\sqrt{z-1} |3_1\rangle \end{aligned} \tag{4.18e}$$
$$\begin{aligned} H_{\mathrm{DHM}} |2_1\rangle = {} & t_{01}\sqrt{z-1} |1_0\rangle + t_1\sqrt{z-1} |1_1\rangle + t'\sqrt{z(z-1)} |2_0\rangle + \epsilon_1 |2_1\rangle \\ & + t_{01}\sqrt{z-1} |3_0\rangle + t_1\sqrt{z-1} |3_1\rangle \end{aligned} \tag{4.18f}$$

and for states corresponding to a larger number of hops, l,

$$H_{\mathrm{DHM}}\,|l_0\rangle = t_0\sqrt{z-1}\,|(l-1)_0\rangle + t_{01}\sqrt{z-1}\,|(l-1)_1\rangle + \epsilon_0\,|l_0\rangle + t'\sqrt{z(z-1)}\,|l_1\rangle + t_0\sqrt{z-1}\,|(l+1)_0\rangle + t_{01}\sqrt{z-1}\,|(l+1)_1\rangle \tag{4.18g}$$

$$H_{\mathrm{DHM}}\,|l_1\rangle = t_{01}\sqrt{z-1}\,|(l-1)_0\rangle + t_1\sqrt{z-1}\,|(l-1)_1\rangle + t'\sqrt{z(z-1)}\,|l_0\rangle + \epsilon_1\,|l_1\rangle + t_{01}\sqrt{z-1}\,|(l+1)_0\rangle + t_1\sqrt{z-1}\,|(l+1)_1\rangle\,. \tag{4.18h}$$

The resultant Hamiltonian matrix is then,

$$H = \begin{pmatrix} \epsilon_0 & t' & t_0\sqrt{z} & t_{01}\sqrt{z} & 0 & 0 & \cdots \\ t' & \epsilon_1 & t_{01}\sqrt{z} & t_1\sqrt{z} & 0 & 0 & \cdots \\ t_0\sqrt{z} & t_{01}\sqrt{z} & \epsilon_0 & t' & t_0\sqrt{z-1} & t_{01}\sqrt{z-1} & \cdots \\ t_{01}\sqrt{z} & t_1\sqrt{z} & t' & \epsilon_1 & t_{01}\sqrt{z-1} & t_1\sqrt{z-1} & \cdots \\ 0 & 0 & t_0\sqrt{z-1} & t_{01}\sqrt{z-1} & \epsilon_0 & t' & \cdots \\ 0 & 0 & t_{01}\sqrt{z-1} & t_1\sqrt{z-1} & t' & \epsilon_1 & \cdots \\ \vdots & \vdots & \vdots & \vdots & \vdots & \vdots & \ddots \end{pmatrix}. \tag{4.19}$$

The equivalent Hamiltonian for the single band Hubbard model has eigenvalues [94]

$$E_\theta = 2t\sqrt{z-1}\cos(\theta)\,. \tag{4.20}$$

The hopping is rescaled in the limit of large $z \approx z-1$ as,

$$t^* = t\sqrt{z}\,, \tag{4.21}$$

and the bandwidth is $W = 4t^*$, as expected. The semi-circular DOS $D(\epsilon)$ then arises from $G^{00}(\epsilon)$, the probability of an electron starting at site j propagating into the lattice and returning to its starting position, and is dependent on the first component of all the eigenvectors $\phi_0(k)$ of the infinitely-connected Bethe lattice:

$$\begin{aligned} D(\epsilon) &= -\frac{1}{\pi}\Im G^{00}(\epsilon) \\ &= \int_0^\pi dk\,|\phi_0(k)|^2\,\delta\left[\epsilon-\epsilon_k\right] \\ &= \frac{\sqrt{4t^{*2}-\epsilon^2}}{2\pi t^{*2}}\,. \end{aligned} \tag{4.22}$$

In the multiorbital case, the eigenvectors follow from the exact diagonalization of the

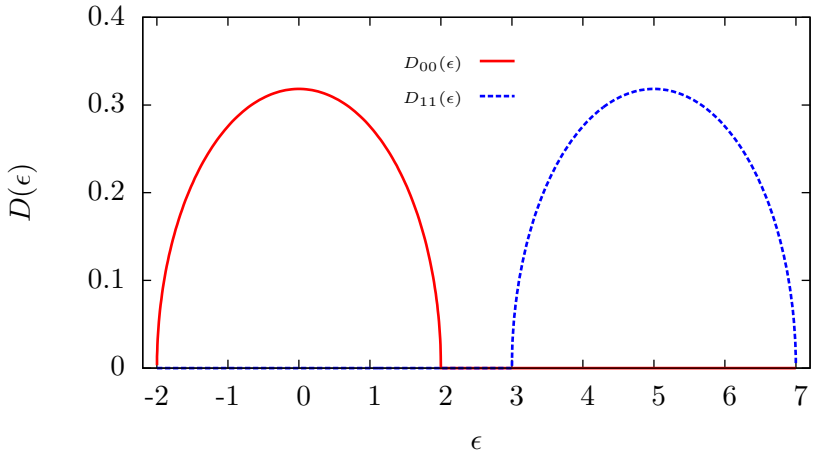

Figure 4.4: DOS for a non-hybridized two-orbital Hubbard system with $t_0 = t_1 = 1.0$ and band gap $\epsilon_1 = 5.0$. As expected, the DOS for the lower and upper orbitals are the semi-circular form with bandwidth $4t$. The plot is numerically produced approximating the infinitely-connected Bethe lattice with a 300×300 matrix.

Hamiltonian (4.19), and in principle could be used in a similar way to the single band case to derive an analytical form of the non-interacting multiorbital Bethe lattice DOS. We leave this involved task for future work and for the present purposes have employed a numerical solution which is incorporated into the optical conductivity results in section 7.5 through a matrix form of the DOS,

$$\hat{D}(\epsilon) = \begin{pmatrix} D_{00}(\epsilon) & D_{01}(\epsilon) \\ D_{10}(\epsilon) & D_{11}(\epsilon) \end{pmatrix} . \tag{4.23}$$

Each of the DOS parameters in (4.23) follow from a construction identical to (4.22), with $D_{xy}(\epsilon)$ dependent on the product of the x and y elements, $\phi_x(k)$ and $\phi_y(k)$, associated with each eigenvector of (4.19).

Figure 4.4 provides an example of the multiorbital DOS for a non-hybridized two-orbital Hubbard system with intraband hopping $t_0 = t_1 = 1.0$ separated by an energy gap $\epsilon_1 = 5.0$. Figure 4.5 demonstrates the effects of hybridization $t' = 0.2$ and $t_{01} = 1.0$ on the same set of orbitals.

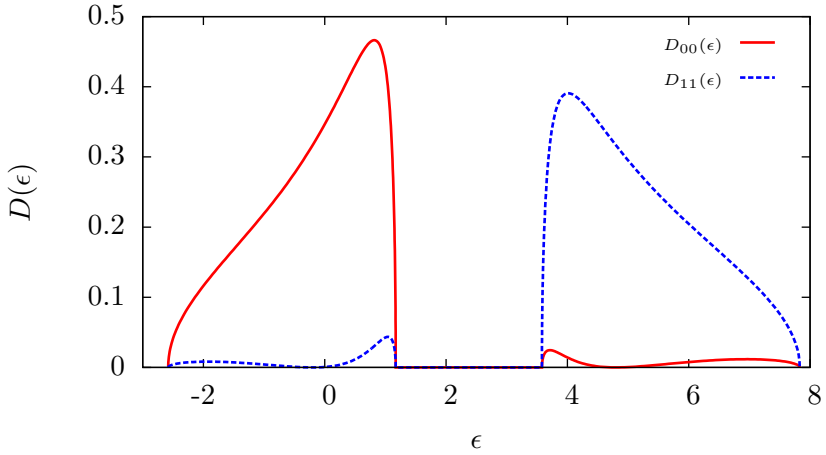

Figure 4.5: DOS for the two-orbital Hubbard system in figure 4.4 with hybridization $t' = 0.2$ and $t_{01} = 1.0$. $t_0 = t_1 = 1.0$ and band gap $\epsilon_1 = 5.0$. Finite hybridization has warped the DOS for both the lower and upper bands from their semi-circular form, and slightly affected the bandwidths as well. The plot is numerically produced approximating the infinitely-connected Bethe lattice with a 300×300 matrix.

Chapter 5

Analysis Tools

5.1 Spectral Densities

In the limit of infinite connectivity, the DMFT and MODMFT methods map the physical lattice problem onto a discretized impurity/mean field solution as described in chapters 2 and 3. The impurity solution provides a momentum-independent approximation of the lattice Green's function and self energy. At convergence, the impurity Green's function $\hat{G}^{\rm imp}_{\sigma}(i\omega_n)$ (4.2) is considered equivalent to the momentum-integrated on-site lattice Green's function $\hat{G}^{\rm lat}_{\sigma}(i\omega_n)$ (4.8), and thus the spectral density $\hat{A}(\omega)$ of the impurity problem provides an important real frequency output of the DMFT method. Using the analytic continuation of the imaginary frequency to the real frequency axis,

$$i\omega_n \rightarrow \omega + i\eta^+ \,, \tag{5.1}$$

where η^+ is some small shift above the real axis, the Matsubara Green's function form of $\hat{G}^{\rm imp}_{\sigma}(i\omega_n)$ uniquely provides the real frequency function $\hat{G}^{\rm imp}_{\sigma}(\omega)$, whose x, y matrix component is [113],

$$G^{\rm imp}_{\sigma xy}(\omega) = \frac{1}{Z}\sum_{j,k}\frac{\langle k|\, c^{\dagger}_{y\sigma}\,|j\rangle\,\langle j\,|c_{x\sigma}|\,k\rangle(e^{-\beta\lambda_j}+e^{-\beta\lambda_k})}{\omega + i\eta^+ - (\lambda_j - \lambda_k)}, \tag{5.2}$$

where $x, y = 0, 1$ for the lower and upper orbitals respectively.

The impurity single-particle spectral density for either orbital $x = 0, 1$ can then be found from,

$$A_{xx}(\omega) = -\frac{1}{\pi}\Im G^{\rm imp}_{xx}(\omega)\,, \tag{5.3}$$

and will be formed from a series of delta functions (broadened into Lorentzians by the finite contribution of η), corresponding to the allowed single particle transitions between the eigenstates of the impurity model (4.1). Only those transitions with a finite overlap of the eigenvectors $\langle j|$ and $|k\rangle$ in (5.2) will contribute, and a larger bath will provide more structure in the spectrum. In the limit of infinite bath sites, the spectrum will appear to be smoothly continuous. For a small number of bath sites, however, the artificial broadening from η will tend to capture some of the main features of the true continuous spectrum.

The impurity spectral density is useful for visualizing the quasiparticle weight, which is defined as the spectral weight at the Fermi energy ($\omega = 0$). The peak formed by this weight is not singular, but has finite width that is dependent on the temperature ($\frac{1}{\beta}$), bandwidth and Coulomb repulsion, but in particular acquires its structure from the low energy limit of the effective impurity model bath density of states, contained in the bath hybridization function $\Delta(i\omega_n)$ (4.10), in $g_\sigma^{\mathrm{imp}}(i\omega_n)$ (4.9) [87].

Figure 5.1 shows the evolution of the spectral weight as a function of inverse temperature β for four bath sites and a non-interacting system. The three central features of the discretized non-interacting quasiparticle peak are centered on the Fermi energy and provide an important reference for the spectral density of interacting systems. For finite onsite Coulomb repulsions U_0, U_1 and U_{01}, the Hubbard bands will acquire weight at the expense of the central structure, which will also narrow in width as Coulomb repulsion increases, as shown in figure 5.2. The non-singularity of the quasiparticle peak along with this dynamic narrowing makes it difficult to evaluate the quasiparticle residue by integrating over the spectral weight at or near $\omega = 0$, and other methods are necessary as discussed in section 5.3.

The impurity densities of states (5.3) are equivalent at convergence to the momentum-integrated local spectral function of the lattice problem, related by analytic continuation to $G_{\sigma xx}^{\mathrm{lat}}(i\omega_n)$ (4.8). This quantity provides insight into the energetics of the quasiparticle residue (section 7.3), and is essential to determining the optical conductivity (section 7.5).

The momentum-resolved spectral functions $\hat{A}_{\sigma xx}(k,\omega)$ (for orbitals $x = 0,\ 1$) can be reconstructed from the local Green's function expressed as a function of the non-interacting dispersion, $\epsilon(k)$, recalling that the converged self energy matrix $\hat{\Sigma}_\sigma(i\omega_n)$ remains momentum-independent. If it is assumed that this momentum-independent value (appropriate in the infinite-dimensional system) derived from the DMFT problem provides a reliable self energy for all momentum states of the electronic system, then the local k-dependent Green's function is,

$$\hat{G}_\sigma^{\mathrm{lat}}(k, i\omega_n) = \int \left\{ [i\omega_n + \mu - \epsilon(k)]\, \mathbb{1} - \hat{\epsilon} - \hat{t}' - \hat{\Sigma}_\sigma(i\omega_n) \right\}^{-1} \mathrm{d}k \tag{5.4}$$

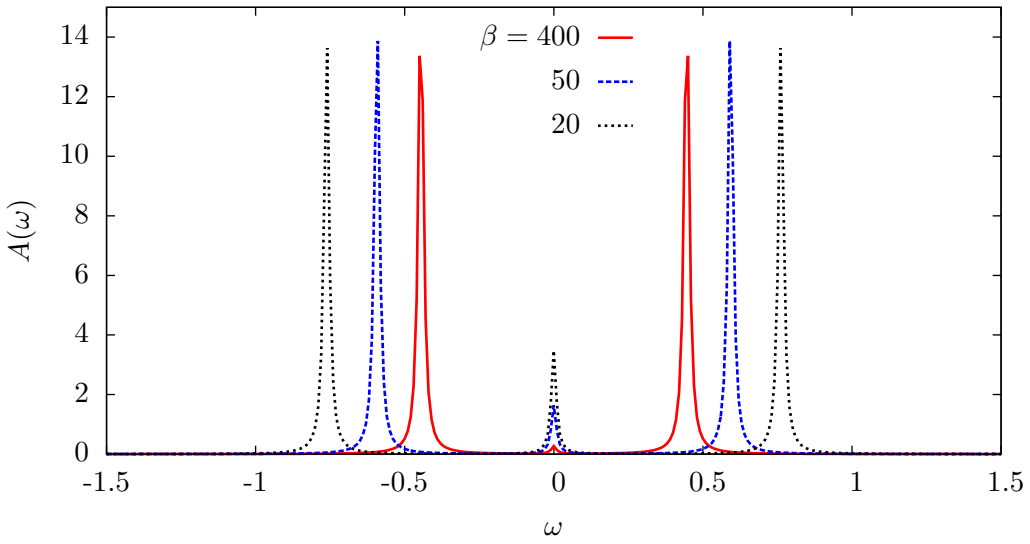

Figure 5.1: Spectral density for the non-interacting four bath site system showing dependence on inverse temperature, β, of the metallic quasiparticle peak. With increasing bath size, the delta functions (broadened into Lorentzians by $\eta = 0.01$) would "fill out" to a more continuous form centered at the Fermi energy, $\omega = 0$. This central peak widens as temperature is increased (*i.e.* β is decreased).

where $\epsilon(k)$ is necessarily restricted to values within the free particle bandwidth. The matrices $\hat{\epsilon}$ and $\hat{t}'$ are defined in (4.5) and (4.6), respectively.

In principle, the momentum-resolved spectral functions $A_x(k, \omega)$ can be determined through (5.1) applied to (5.4), if the self energy values have also been accurately defined near the real frequency axis.

One apparent strategy to evaluate these real frequency self energies is through the analytic continuation of the multiorbital Dyson equation (4.15). Here, $\hat{\Sigma}_\sigma(z)$ is an analytic function defined in terms of the converged impurity mean field and Green's functions, each analytically defined as well. This technique, however well-defined, is very sensitive to imprecise convergence of the Green's function at small imaginary frequencies. An appropriate set of converged bath parameters will, in principle, result in an exact match between the lattice mean field functions $\hat{g}^{\text{lat}}_\sigma(i\omega_n)$ and Anderson impurity mean field function $\hat{g}^{\text{imp}}_\sigma(i\omega_n)$. However, this is compromised at low energy by the finite structure of the impurity DOS contained in $\hat{\Delta}(i\omega_n)$.

The effect of mismatch in the low imaginary frequency scale is carried over across the entire real frequency domain of the self energy, and is especially pronounced near the poles of $\hat{\Delta}(\omega + i\eta^+)$, which are pinned by the bath energies. Since these bath energies tend to

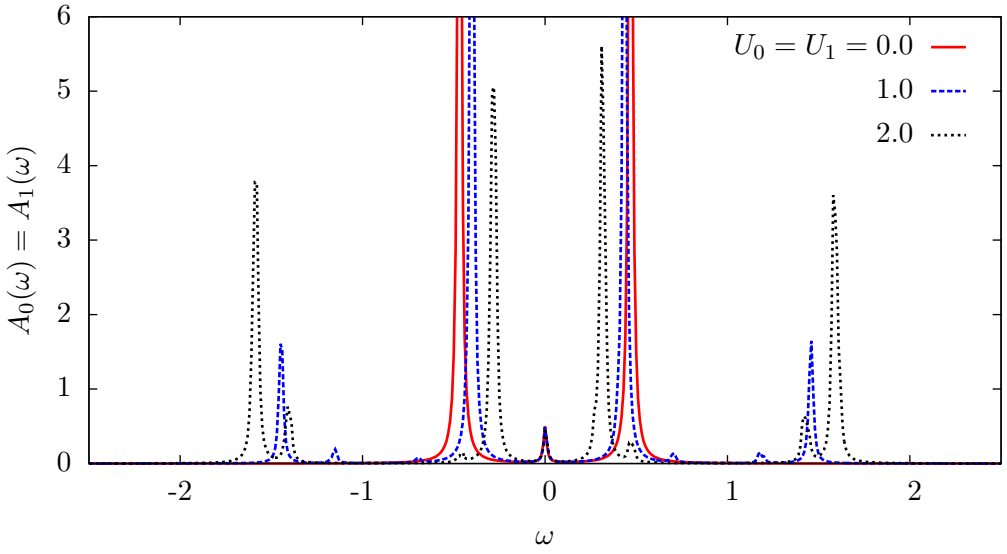

Figure 5.2: Spectral density for the interacting four bath site system for different values of Coulomb repulsion, $U_0 = U_1$ ($U_{01} = 0.0$ for clarity), at half-filling. $\beta = 200$ with Lorentzian broadening of $\eta = 0.01$. As Coulomb repulsion increases, quasiparticle weight is transferred from the central quasiparticle peak (defined in figure 5.1 for the non-interacting case) to the Hubbard bands, and there is a simultaneous narrowing of the peak centered at the Fermi level, $\omega = 0.0$. This dynamic narrowing makes it difficult to systematically determine the quasiparticle residue by integrating over the central metallic peak.

resolve at low frequency, in the analytic continuation the effects of the mismatch become pronounced at small real frequencies in the self energy. This leads to negative values of the (necessarily positive-definite) spectral function, especially near the Fermi energy, which is an area of special interest in the energy scale of the problem. For a small number of bath sites, including up to six, this technique of analytic continuation to find real frequency properties provides a decidedly poor result, and is even avoided in zero-temperature DMFT studies employing a much larger bath through Lanczos-type approximation schemes [113].

An example of the anomalous negative spectral weight for six bath sites is shown in figure 5.3a, along with the positive definite impurity spectral density. The mismatch between the lower orbital mean field Green's functions, $g^{\text{lat}}_{\sigma 00}(i\omega_n)$ and $g^{\text{imp}}_{\sigma 00}(i\omega_n)$, is shown in figure 5.3b.

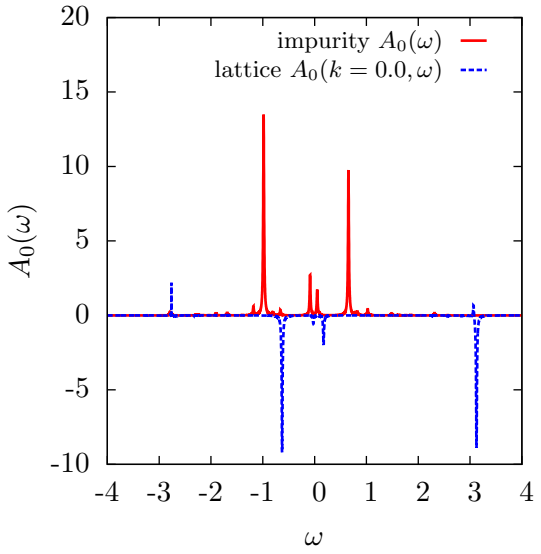

(a) Anomalous negative values in the momentum-resolved lattice spectral function component $A_0(k = 0.0, \omega)$ for a six bath site problem. For comparison, the positive definite spectral density of the impurity solution $A_0(\omega)$ is also shown. $\beta = 200$, $U_0 = 0.8$, $U_1 = 0.1$, $U_{01} = 0.0$, $\epsilon_1 = 1.0$, $t_{01} = 0.0$, $t' = 0.1$, $\mu = 0.75$. (The apparent asymmetry in the impurity plot is a numerical artifact of the sampling resolution.)

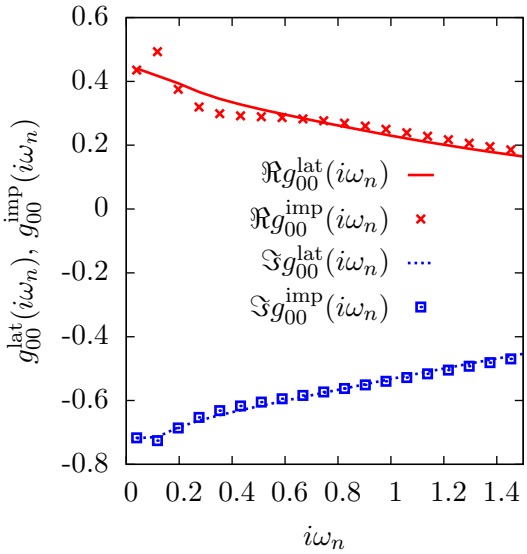

(b) The negative spectral weight in 5.3a is caused by the low energy mismatching of the mean field Green's functions, even in this six-site MODMFT implementation. Parameters are the same as in 5.3a.

Figure 5.3: Problematic analytic continuation of imaginary frequency multiorbital self energy to real frequency.

An alternative method to find real frequency momentum-resolved spectral functions

is to numerically extrapolate the imaginary frequency values to the real axis through a rational function approximation, as in [113]. We have generalized an algorithm, `Rat_interp`, from the Numerical Recipes library [82], to the complex plane so that the real frequency self energy is taken as a function of the complex variable z. Through a local fit to the Matsubara data points, the algorithm determines an expression of the form $\frac{p(z)}{q(z)}$ where $p(z)$ and $q(z)$ are polynomials with the order $\mathcal{O}(z)$ of the numerator less than that of the denominator. Since z is a complex variable of general form, $z = \omega + i\omega_n$, and because the functions in question are analytic in the neighbourhood of the fit, the functional form at the imaginary axis uniquely determines the value of the function even at the real axis. The quality of fit is somewhat improved for lower temperatures which provide a finer resolution on the Matsubara axis, and thus more data points from which to fit the function elsewhere on the complex plane.

Two checks are made on the quality of the rational function fit. First, the algorithm should be able to produce the impurity density of states (5.3) from a fit to the imaginary frequency impurity Green's function (5.2), which is known exactly from the direct analytic continuation of the Matsubara sums. Figure 5.4 shows an example of this check for a system with non-trivial correlations. The extrapolation method captures the main features of the impurity spectrum, and provides an especially good reconstruction near the Fermi energy, which is a region of particular interest. (It should be noted that the real frequency extrapolation is computationally time-intensive, necessitating a lower energy resolution which is partly responsible for the non-matching details in [5.4].)

A second check is the Kramers-Kronig relation between the real and imaginary parts of the extrapolated self energy. For a complex function $F(x) = F_r(x) + iF_i(x)$, the Kramers-Kronig relation relates the real and imaginary parts, $F_r(x)$ and $F_i(x)$ respectively, to one another as,

$$F_r(x) - F_r(\infty) = \frac{1}{\pi}\mathcal{P}\int dx' \frac{F_i(x')}{x' - x} \tag{5.5}$$

The rational function extrapolation method can find the real and imaginary parts of the real frequency self energies. Properly determined, these values should be related according to (5.5).

In the single orbital DMFT problem, $\Re\Sigma_{\sigma xx}(z)$ converges to its high frequency limit, $\Re\Sigma_{\sigma xx}(\infty)$, according to,

$$\Re\Sigma_{\sigma xx}(z \to \infty) \to \mu - \epsilon_x + \frac{\sum_{\mu\nu} \left|\langle \mu \left| d_x^\dagger \right| \nu \rangle\right|^2 \left(e^{-\beta\lambda_\mu} + e^{-\beta\lambda_\nu}\right)(\lambda_\mu - \lambda_\nu)}{\sum_\mu e^{-\beta\lambda_\mu}} \tag{5.6}$$

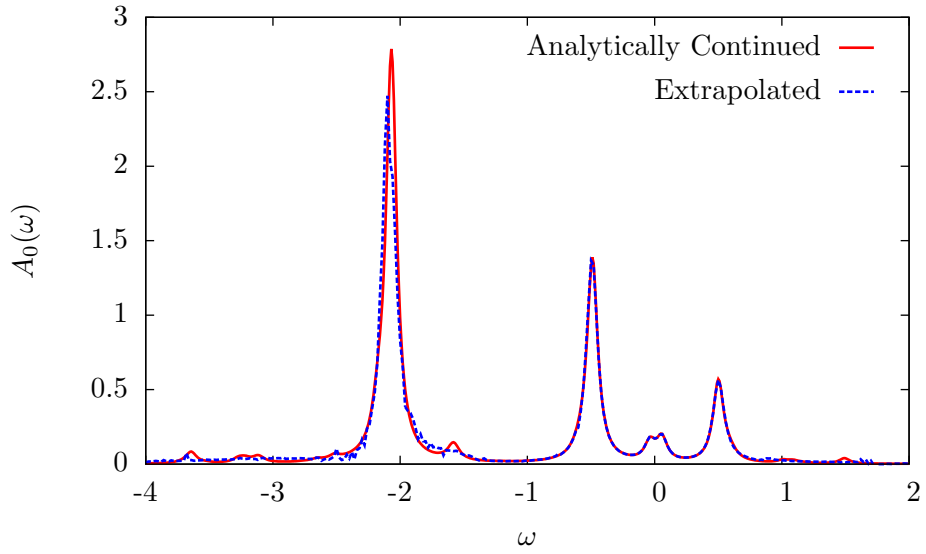

Figure 5.4: Comparison of lower orbital spectral density $A_0(\omega)$ for the impurity system determined by a rational function extrapolation from imaginary to real frequencies, and the analytic continuation of the imaginary frequency impurity Green's function. The extrapolation method captures the main details of the analytically continued curve, and they are indistinguishable near the Fermi energy. Four bath sites, $U_0 = 6.0$, $U_1 = 2.0$, $U_{01} = 4.0$, $\epsilon_1 = t_{01} = 1.0$, $t' = 0.2$, $\mu = 15.0$.

where μ and ν denote the eigenstates of the Anderson impurity Hamiltonian. The last term in this expression is the shift in energy due to the Hartree-Fock mean field [146]. It is an asymptotic value equivalently expressed by the leading term of the self energy perturbation theory expansion on the imaginary frequency axis [147],

$$\lim_{i\omega_n \to \infty} \Sigma_{\sigma x x}(k, i\omega_n) \approx U_x n_{-\sigma x} + \frac{U_x^2 n_{-\sigma x}(1 - n_{-\sigma x})}{i\omega_n}, \tag{5.7}$$

which constant value is readily available from the converged DMFT and MODMFT imaginary frequency results for substitution into (5.5), to recover $\Re\Sigma_{\sigma x x}(\omega)$.

Figure 5.5 shows the agreement of $\Re\Sigma_{\sigma x x}(\omega)$ values directly extrapolated to the real axis and those determined from the extrapolated $\Im\Sigma_{\sigma x x}(\omega)$ using (5.5), which relies on a numerical integration over ω.

5.2 Filling

The average electron occupation, or electron "filling" $\langle n_\sigma \rangle$, is an important observable of the converged DMFT system. In the MODMFT problem it provides critical information

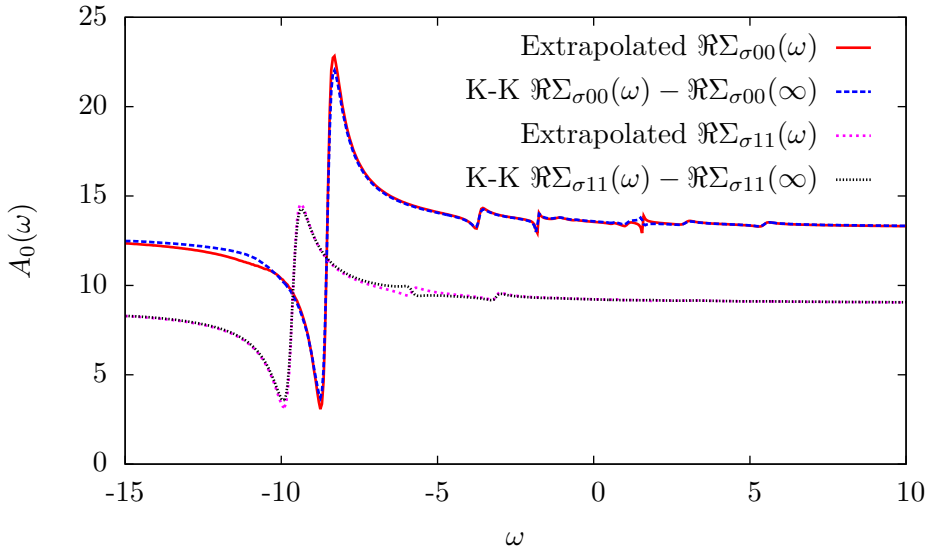

Figure 5.5: Comparison of $\Re\Sigma_{\sigma 00}(\omega)$ and $\Re\Sigma_{\sigma 11}(\omega)$ directly extrapolated to the real frequency axis from a complex rational function fit to the Matsubara frequency self energy data, versus the values obtained from the Kramers-Kronig (K-K) relation (5.5), utilizing the extrapolated imaginary frequency self energies. The K-K curves have been adjusted by the Hartree-Fock high frequency limit, $\Re\Sigma_{\sigma xx}(\infty)$, taken from the imaginary frequency self energy data. Four bath sites, $U_0 = 6.0$, $U_1 = 2.0$, $U_{01} = 4.0$, $\epsilon_1 = t_{01} = 1.0$, $t' = 0.2$, $\mu = 15.0$.

about the response of electrons to the relative energies and Coulomb repulsions of the two orbitals. For simplicity we will hereafter denote the filling without chevrons.

At convergence, the filling is determined most easily from the impurity solutions. By definition, the Fermi energy, corresponding to $\omega = 0$, is the upper limit of electronic occupation, allowing the determination n_σ to be calculated by integrating over the negative frequency spectral weight,

$$n_\sigma = \int_{-\infty}^{\infty} \frac{A_\sigma(\omega)}{e^{\beta\omega} + 1} \mathrm{d}\omega \tag{5.8}$$

where the energies, ω, are defined relative to the Fermi energy. For temperatures on the order of $\beta = 100$ or higher, the Fermi factor $\frac{1}{e^{\beta\omega}+1}$ is essentially a step function.

The denominator of the impurity Green's function $\hat{G}_\sigma^{\mathrm{imp}}(i\omega_n)$ locates the poles of the function at the eigenenergy differences $\lambda_\nu - \lambda_\mu$, weighted in the numerator by the eigenstates' Boltzmann factors as $e^{-\beta\lambda_\nu} + e^{-\beta\lambda_\mu}$. For $\beta \sim 200$, only terms that include a transition to or from a ground state have significant weight in this expression. Of these terms, the gap between the first excited state and the ground state is already usually too large to significantly affect the filling (5.8) through the Fermi factor.

Noting the dominance of the ground state, an alternative and computationally simpler

approach to determining the electronic occupation is through the ground state eigenvector $|\text{g.s.}\rangle$, itself, along with the first excited state vector. The ground state is a superposition of different basis states $|\phi\rangle$, so that

$$|\text{g.s.}\rangle = \sum_{\phi} \alpha_{\phi} |\phi\rangle \,, \tag{5.9}$$

each basis state contributing a weight α_ϕ to the total eigenstate character. The second and higher excited levels near the ground state are easily checked to evaluate their contribution to the total filling through their Boltzmann weight in the partition function, and we truncate for values of less than 0.01. However, we automatically include the contribution of the first excited state, regardless of its weight. We determine the overall filling of the ground state vector (plus contributions from other low-lying states) by counting the electron occupation on the impurity site lower orbital n_0, and upper orbital n_1, through the operation,

$$\langle \text{g.s.}| \left(\hat{n}_0 + \hat{n}_1\right) |\text{g.s.}\rangle = \sum_{\phi,\rho} \alpha_\phi \alpha_\rho \langle \rho| \left(\hat{n}_0 + \hat{n}_1\right) |\phi\rangle \,. \tag{5.10}$$

Figure 5.6 shows the Boltzmann weight of the first twenty excited states for a typical set of interacting parameters.

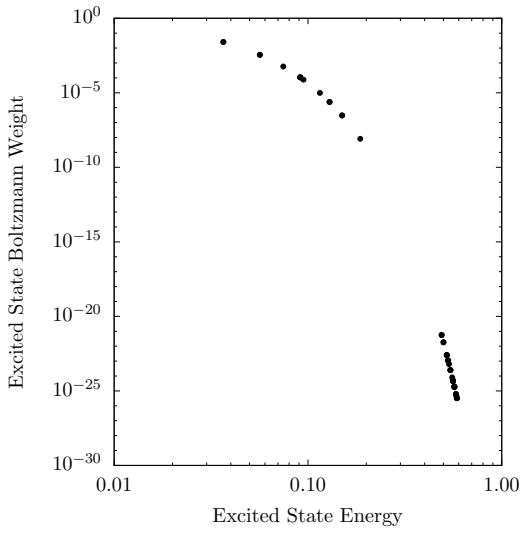

Figure 5.6: Boltzmann factors for the twenty lowest excited states of the impurity system, demonstrating their minimal contribution to the overall state of the electrons. Note the log-log scale. Data is for four bath sites, $U_0 = 6.0$, $U_1 = 2.0$, $U_{01} = 4.0$, $\epsilon_1 = t_{01} = 1.0$, $t' = 0.2$, $\mu = 15.0$.

The filling results from these two methods have been found to have very good agreement

across a variety of test cases at the temperatures used in our study ($\beta \sim 100 - 200$).

5.3 Quasiparticle Weight

The quasiparticle concept of Fermi liquid theory (*q.v.* section 1.3) is crucial to our understanding of many-particle electronic systems. In an interacting lattice environment electrons lose, to some extent, their identity and behaviour as individual particles and assume a more corporate form in keeping with their wave-like properties, "dressed" up as they move about the lattice with a "cloud" of interaction effects following them [148].

With the loss of free-particle identity, particle electrons are replaced by quasiparticle excitations, characterized by an increased effective mass m^*, and a finite lifetime. The density of states of the quasiparticle excitations is contained in the Green's function, which is divided by interactions into a coherent part $G_{\mathrm{coh}}(k,\omega)$, and an incoherent part $G_{\mathrm{inc}}(k,\omega)$, written as

$$G(k,\omega) = G_{\mathrm{coh}}(k,\omega) + G_{\mathrm{inc}}(k,\omega)\,. \tag{5.11}$$

For a lightly dressed quasiparticle with a long lifetime, behaving very much as a free electron, the incoherent part of the Green's function will be small and the spectral density will be dominated by a peak at the Fermi energy. As dressing is increased, this weight will transfer to higher energies, as occurs in the MIT (*q.v.* section 3.7).

The weight of the peak at the Fermi energy is therefore a measure of quasiparticle undressing and is denoted by Z.

For a single band system of interacting electrons, the quasiparticle weight can be derived from the Green's function,

$$G(z,k) = \frac{1}{z - \epsilon(k) + \mu - \Sigma(z)} \tag{5.12}$$

(where the self energy is momentum independent, as in DMFT). If the system is in a Fermi liquid state, the self energy is continuous in the limit of $z \to 0$ and can be expanded as,

$$\Sigma(z) \overset{z\to 0}{\approx} \Sigma(0) + z\,\frac{\mathrm{d}\Sigma(z)}{\mathrm{d}z}\bigg|_{z=0}\,, \tag{5.13}$$

so that (5.12) becomes,

$$G(k,z) \approx \frac{1}{z-\epsilon(k)+\mu-\Sigma(0)-z\left.\frac{\mathrm{d}\Sigma(z)}{\mathrm{d}z}\right|_{z=0}} = \left(\frac{1}{1-\left.\frac{\mathrm{d}\Sigma(z)}{\mathrm{d}z}\right|_{z=0}}\right)\frac{1}{z+\frac{\mu-\epsilon(k)-\Sigma(0)}{1-\left.\frac{\mathrm{d}\Sigma(z)}{\mathrm{d}z}\right|_{z=0}}}\,. \tag{5.14}$$

With non-zero interactions, the Fermi momentum is renormalized as $k = \tilde{k}_F$, corresponding to a Fermi energy defined where the real part of the self energy vanishes as [23],

$$\epsilon(\tilde{k}_F) - \mu + \Re\Sigma(0) = 0\,. \tag{5.15}$$

This condition gives rise to a coherent part of the Green's function, a delta function at $z = 0$, so that,

$$G_{\mathrm{coh}}(k,z) = \left(\frac{1}{1-\left.\frac{\mathrm{d}\Sigma(z)}{\mathrm{d}z}\right|_{z=0}}\right)\delta\left[\mu-\epsilon(k)-\Im\Sigma(0)\right]\,. \tag{5.16}$$

The renormalization factor in parenthesis is the weight of the quasiparticle peak, located at the renormalized Fermi energy when,

$$\Im\Sigma(z) = 0\,. \tag{5.17}$$

This is a condition for Fermi liquidity, under which the quasiparticle weight is related to the slope of the self energy near the Fermi level, $\omega = 0$, through,

$$Z = \frac{1}{1-\left.\frac{\partial\Re\Sigma(\omega)}{\partial\omega}\right|_{\omega=0}}\,, \tag{5.18}$$

where $\Re\Sigma(\omega)$ approaches zero as ω^2. In the case where the system is an insulator, the quasiparticles have lost all of their free-particle like quality and the self energy diverges at the Fermi level, so definition (5.18) does not apply. The single particle Green's function behaves in an opposite way to the self energy, diverging for undressed quasiparticles and going to zero for insulating behaviour.

In the language of Matsubara frequencies, on the imaginary axis the quasiparticle weight

can be estimated [149] as,

$$Z = \frac{1}{1 - \frac{\Im\Sigma(i\omega_0)}{\omega_0}}\,, \tag{5.19}$$

where ω_0 is the lowest Matsubara frequency,

$$\omega_0 = \frac{\pi}{\beta}\,. \tag{5.20}$$

In general, near the renormalized Fermi level $k = \tilde{k}_F$, $\omega = 0$, the quasiparticle effective mass is inversely related to Z through,

$$\begin{aligned}\frac{m}{m^*} &= \frac{1 + \frac{m}{\epsilon(k)}\frac{\partial}{\partial k}\Re\Sigma(k,0)\Big|_{k=\tilde{k}_F}}{1 - \frac{\partial}{\partial\omega}\Re\Sigma(k,0)\big|_{k=\tilde{k}_F}} \\ &= Z\left(1 + \frac{m}{\epsilon(k)}\frac{\partial}{\partial k}\Re\Sigma(k,0)\Big|_{k=\tilde{k}_F}\right)\end{aligned} \tag{5.21}$$

and to the energy band curvature through,

$$\frac{m}{m^*} = \frac{\partial^2 E(k,\omega)}{\partial k^2}\Big|_{k=\tilde{k}_F,\,\omega=0} \tag{5.22}$$

which follows from a series expansion of $E(k,\omega)$ around $k = \tilde{k}_F$, $\omega = 0$.

Together, (5.21) and (5.22) connect the local curvature of the energy versus momentum graph with quasiparticle coherence. The relationship is indicative of the effective mass of quasiparticles occupying energy levels in a certain region of the dispersion. A slowly varying topology of the interacting dispersion indicates carriers having a high effective mass and conversely a sharp change in curvature suggests undressed quasiparticles of lower effective mass.

The multiorbital lattice with hybridization between bands complicates the form of the quasiparticle weight, as the Green's function takes a matrix form. The diagonal elements of the matrix no longer permit a form of the quasiparticle residue (5.18) as a renormalization factor defined simply in terms of the diagonals of the matrix self energy $\hat{\Sigma}(z)$. For non-zero hybridization the matrix form of the Dyson equation (4.15) ensures that the diagonal elements of the lattice Green's function depend on all four elements of the two-by-two self energy matrix,

$$\hat{\Sigma}(z) = \begin{pmatrix}\Sigma_{00}(z) & \Sigma_{01}(z)\\ \Sigma_{10}(z) & \Sigma_{11}(z)\end{pmatrix}\,. \tag{5.23}$$

The simple diagonal form of (5.16) is approximately correct only in the limit of small hybridization and very weak interactions. Nonetheless, this single band form has been explicitly used for the hybridized multiorbital case in the literature, for example in [65,140].

More appropriately, the diagonal lattice Green's function elements are decomposed into a sum of terms relating to hybridized energy orbitals (we neglect the spin index, assuming the paramagnetic case),

$$G^{\text{lat}}_{00}(k,z) = G^{\text{lat}}_{0-}(k,z) + G^{\text{lat}}_{0+}(k,z) \tag{5.24a}$$

$$G^{\text{lat}}_{11}(k,z) = G^{\text{lat}}_{1-}(k,z) + G^{\text{lat}}_{1+}(k,z) \tag{5.24b}$$

where (for $x = 0$ or 1 denoting the orbitals),

$$G^{\text{lat}}_{x-}(k,z) = \frac{u^2(z)}{z - \epsilon(k) - \zeta_-(z)} \tag{5.25a}$$

$$G^{\text{lat}}_{x+}(k,z) = \frac{v^2(z)}{z - \epsilon(k) - \zeta_+(z)}\,. \tag{5.25b}$$

The poles of the Green's function now take the form of effective self energies, $\zeta_-(z)$ and $\zeta_+(z)$, of hybridized energy orbitals. The contribution of each pole, $\zeta_\pm(z)$, to the full quasiparticle residue Z_x is weighted by the numerators, $u^2(z)$ and $v^2(z)$. The factors $\zeta_\pm(z)$, $u^2(z)$ and $v^2(z)$ are functions of the self energy matrix elements:

$$\zeta_\pm(z) = \frac{1}{2}\left[\epsilon_0 + \epsilon_1 + \Sigma_{00}(z) + \Sigma_{11}(z)\right] \pm \kappa(z) \tag{5.26a}$$

$$u^2(z) = \frac{1}{2}\left[1 - \frac{\epsilon_0 - \epsilon_1 + \Sigma_{00}(z) - \Sigma_{11}(z)}{\kappa(z)}\right] \tag{5.26b}$$

$$v^2(z) = \frac{1}{2}\left[1 + \frac{\epsilon_0 - \epsilon_1 + \Sigma_{00}(z) - \Sigma_{11}(z)}{\kappa(z)}\right] \tag{5.26c}$$

where

$$\kappa(z) = \sqrt{\left[\epsilon_0 - \epsilon_1 + \Sigma_{00}(z) - \Sigma_{11}(z)\right]^2 + 4\left[t' - \Sigma_{01}(z)\right]\left[t' - \Sigma_{10}(z)\right]}\,. \tag{5.27}$$

Clearly, $u^2(z) + v^2(z) = 1$.

In contrast to the single band case where a single quasiparticle peak forms at the Fermi energy for an electron of momentum $\epsilon(k)$, the two terms of (5.24) form two quasiparticle peaks located at the Fermi energy when $z = \zeta_\pm(z) - \epsilon(k)$, for some momentum k specific to each peak.

The single band conditions for coherent quasiparticle formation, (5.15) and (5.17), find

their multiorbital expression as,

$$\epsilon(\tilde{k}_F) - \mu + \Re\zeta_{\pm}(z) = 0 \tag{5.28a}$$

$$\Im\zeta_{\pm}(z) = 0\,, \tag{5.28b}$$

where $\epsilon(\tilde{k}_F)$ is the free particle energy dependent on the bandwidths, $4t_0$ and $4t_1$, as well as the hybridization parameters.

Under these conditions (5.28), four definitions of the multiorbital quasiparticle weight suggest themselves as usefully constructed from the components of (5.26): Z_0 the quasiparticle weight contribution for charge carriers in the lower orbital; Z_1 for the upper orbital; and $Z_{\pm}$ giving the weight associated with one of the two hybridized energy orbitals, constructed by linear combination from the physical upper and lower orbitals. These are defined in terms of the Matsubara frequency from the slopes of $\zeta_{\pm}(i\omega_n)$ near zero frequency as,

$$Z_0 = \frac{\Re u^2(0)}{1 - \frac{\partial\Im\zeta_-(i\omega_0)}{\omega_0}} + \frac{\Re v^2(0)}{1 - \frac{\partial\Im\zeta_+(i\omega_0)}{\omega_0}} \tag{5.29a}$$

$$Z_1 = \frac{\Re u^2(0)}{1 - \frac{\partial\Im\zeta_+(i\omega_0)}{0}} + \frac{\Re v^2(0)}{1 - \frac{\partial\Im\zeta_-(i\omega_0)}{\omega_0}} \tag{5.29b}$$

$$Z_{\pm} = \frac{\Re u^2(0) + \Re v^2(0)}{1 - \frac{\partial\Im\zeta_{\pm}(i\omega_0)}{\omega_0}}\,. \tag{5.29c}$$

In the case of a large band gap ϵ_1, the dominant quasiparticle expression is Z_0, as most of the electron identity is located in the lower orbital, and in this limit $Z_- \approx Z_0$. As will be found in chapter 7, the key physics of the DHM becomes evident even in this regime, emphasized as the gap narrows. The concept of orbital relaxation for electrons in the lower energy state, which is the key paradigm of the DHM, suggests a focus on the quasiparticle behaviour for electrons in this lower physical orbital, and thus we are particularly interested in the behaviour of Z_0 throughout this study and in our comparisons of the results from [31].

As a final note of contrast, in a regime of system parameters where electron-hole asymmetry is particularly evident, figure 5.7 demonstrates the difference in quasiparticle weight between definitions (5.29a) and (5.29b), and the single-band self energy definition commonly found in the multiorbital literature [65, 140]. There are clearly qualitative distinctions.

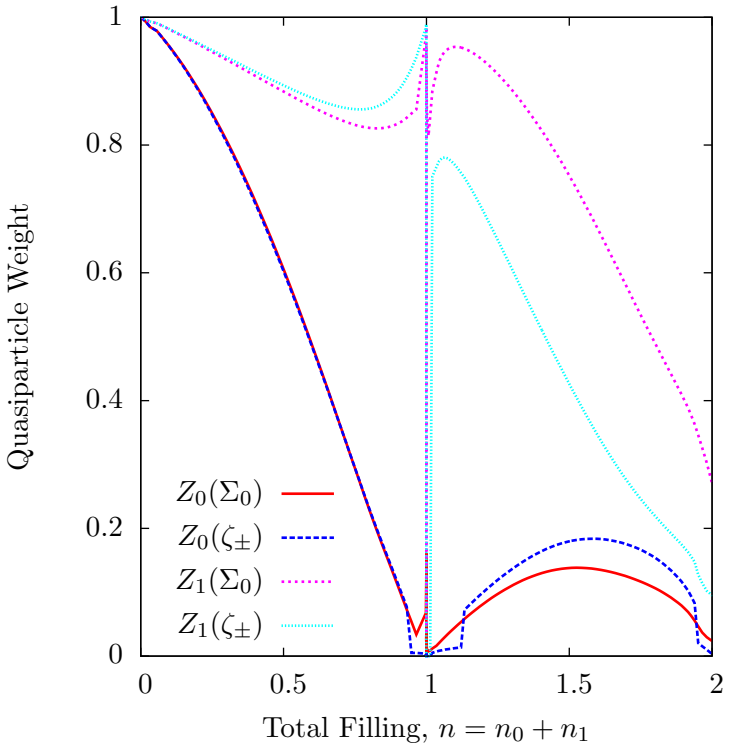

Figure 5.7: Upper and lower orbital quasiparticle weights, Z_1 and Z_0, versus total band filling, up to the half-filled lattice (for clarity), for a system of strong electron-hole asymmetry. Above quarter filling there is a qualitative difference between the quasiparticle weights $Z(\Sigma)$ estimated from the orbital self energies as in (5.19), and the values $Z(\zeta_\pm)$ derived more appropriately from effective self energies (5.29), especially in the upper orbital case (Z_1).

5.4 Optical Conductivity

Spectroscopic methods provide experimental probes of material electronic structure. Optical spectroscopy evaluates a material's response to incident electromagnetic radiation across some spectrum of frequency correlated to an appropriate energy scale for phenomena of interest. In particular, the optical conductivity $\sigma(\omega)$ is a response function accounting for electronic transitions in a material between occupied and unoccupied energy states, and a measure of electron transport in a lattice.

The low frequency component of $\sigma(\omega)$, called the "Drude weight", corresponds to the DC response of a material in the presence of an external electric field $\mathbb{E}(\omega)$. For a small perturbation there is a linear response. In an isotropic system it is captured by the con-

ductivity relating the field to the induced current density $\mathbb{J}(\omega)$ by,

$$\mathbb{J}(\omega) = \sigma(\omega)\mathbb{E}(\omega)\,. \tag{5.30}$$

The optical conductivity is sensitive to changing material phase with, for instance, a MIT at half filling in a band corresponding to a complete suppression of the Drude weight. In the case of the DHM, as discussed in section 2.5, orbital relaxation as a band is filled with electrons should be signaled by a decrease in low frequency optical spectral weight, transferred to higher frequency. This result was confirmed for a finite-chain QMC study of the DHM in [48], where Hirsch used an optical conductivity expression for the one-dimensional single band Hubbard model derived by Maldague [150].

The general form of the optical conductivity on an infinitely-connected lattice was derived by Pruschke *et al.* [100] as,

$$\sigma(i\nu) = \frac{1}{N\nu\beta}\sum_{\mathbf{k}s\omega_n}\sum_{l} v_{\mathbf{k}_l}^2 G_{\mathbf{k}s}(i\omega_n)G_{\mathbf{k}s}(i\omega_n + i\nu)\,. \tag{5.31}$$

N is the number of lattice sites and $v_{\mathbf{k}_l}$ is the lth component of the charge carrier Fermi velocity,

$$\mathbf{v}_{\mathbf{k}} = \nabla\epsilon_{\mathbf{k}} = -2t\nabla\left[\sum_l \cos(k_l a)\right]\,. \tag{5.32}$$

For the case of an isotropic hypercubic geometry the sum over the Fermi velocity can be expressed as an energy integral over the non-interacting density of states $D(\epsilon)$ [100, 151], resulting in the expression,

$$\sigma_{\mathrm{HC}}(\omega) = \frac{\sigma_{\mathrm{pre}}}{\omega}\sum_s \int_{-\infty}^{\infty} d\epsilon D(\epsilon)\int_{-\infty}^{\infty} d\omega'\left[f(\omega') - f(\omega+\omega')\right]\left[A_s(\epsilon,\omega')A_s(\epsilon,\omega+\omega')\right], \tag{5.33}$$

where charge carriers have spin s. $f(\omega)$ denotes the Fermi function,

$$f(\omega) = \frac{1}{e^{(\omega-\mu)\beta}+1}\,. \tag{5.34}$$

The prefactor, σ_{pre}, is given by,

$$\sigma_{\mathrm{pre}} = \frac{e^2a^2t^{*2}}{\pi\hbar^2 V} \tag{5.35}$$

with e the electric charge, a the lattice spacing, and $V = a^d$ the unit cell volume for dimensionality. In our analysis we will in general be concerned with the values $\sigma(\omega)/\sigma_{\mathrm{pre}}$.

On the Bethe lattice, determining the optical conductivity is an ill-posed problem.

The lattice geometry is normally ambiguous, defined not in terms of spatial direction or bond angles and lattice spacings, but only in terms of topological connectivity: a constant number of nearest neighbours relative to each site (*q.v.* figure 3.2). Defining transport properties is therefore a difficult problem, and several methods have been proposed for calculating $\sigma(\omega)$.

Most simply, and commonly used in early DMFT work, one can adopt the assumptions proper for the hypercubic lattice, as given by σ_{HC} in equation (5.33), assuming the translational invariance carries over equally well in the case of the Bethe lattice's tree-like structure. This expression has been used for the DMFT Bethe lattice in references [51, 87, 152, 153], presumably as an approximation.

Chattopadhyay *et al.* [154] derived a more nuanced correction to (5.33) using the optical sum rule for systems dominated by cubic nearest-neighbour hopping,

$$\int_0^\infty \frac{2}{\pi}\,\mathrm{d}\omega\sigma(\omega) = \frac{e^2}{a^{d-2}}K \tag{5.36}$$

where K is the kinetic energy. Requiring K to be consistent with the general kinetic energy expression,

$$K = \frac{1}{\pi}\int \mathrm{d}\epsilon_k D(\epsilon_k)\int \mathrm{d}\omega f(\omega)\Im G(\epsilon_k,\omega), \tag{5.37}$$

as well as that for the optical conductivity, they defined what we denote as a "Chattopadhyay" optical conductivity for the Bethe lattice, $\sigma_{\mathrm{Chat}}(\omega)$,

$$\begin{aligned}\sigma_{\mathrm{Chat}}(\omega) =& \frac{\sigma_{\mathrm{pre}}}{3\omega}\sum_s \int_{-\infty}^{\infty} d\epsilon \left(4t^2-\epsilon^2\right) D(\epsilon) \\ &\times \int_{-\infty}^{\infty} d\omega' \left[f(\omega')-f(\omega+\omega')\right]\left[A_s(\epsilon,\omega')A_s(\epsilon,\omega+\omega')\right].\end{aligned} \tag{5.38}$$

Blümer [155] was critical of the underlying assumption behind (5.38), that the infinite-dimensional Bethe lattice will approximately obey the hypercubic lattice sum rule (5.36), showing that this leads to results which are characteristic of geometric anisotropy. Instead, he derived a robustly isotropic density of states for the Bethe lattice, employing a redefined dispersion,

$$\epsilon_{\mathbf{k}} = \sum_{d=1}^{\infty} \mathrm{He}_d\left(\epsilon_{\mathbf{k}}^{\mathrm{hc}} t_d^*/\sqrt{d!}\right), \tag{5.39}$$

where d is the electron hopping "Manhattan" distance (*i.e.* the path taken by charge carriers in the lattice as measured along the lattice bonds, reminiscent of measuring the distance walked along rectangular city blocks). $\mathrm{He}_d(x)$ is the Hermite polynomial of order

d, and $\epsilon_{\mathbf{k}}^{\mathrm{hc}}$ is the dispersion of the hypercubic lattice with nearest-neighbour hopping only.

For this Bethe lattice definition, with the usual semi-elliptic density of states, the "Blümer" optical conductivity $\sigma_B(\omega)$ takes the form,

$$\sigma_{\mathrm{B}}(\omega) = \frac{\sigma_{\mathrm{pre}}}{\omega} \sum_s \int_{-\infty}^{\infty} d\epsilon \tilde{D}(\epsilon) \int_{-\infty}^{\infty} d\omega' \left[f(\omega') - f(\omega + \omega') \right] \left[A_s(\epsilon, \omega') A_s(\epsilon, \omega + \omega') \right], \tag{5.40}$$

The energy parameter $\tilde{D}(\epsilon)$ is given by,

$$\tilde{D}(\epsilon) = \frac{1}{\sqrt{4t^{*2} - \epsilon^2}} \exp\left(-2 \left\{ \mathrm{erf}^{-1} \left[\frac{\epsilon \sqrt{4t^{*2} - \epsilon^2} + 4t^{*2} \sin^{-1}\left(\frac{\epsilon}{2t^*}\right)}{\pi t^{*2}} \right] \right\}^2 \right), \tag{5.41}$$

where t^* is the renormalized Bethe lattice hopping parameter.

In this thesis we are under the constraint that a proper, generalized multiorbital Bethe lattice formulation of transport properties, including the conductivity, appears not yet to have been derived beyond an involved numerical solution in the context of a linear muffin-tin orbital [28] band structure approximation [156], and a Peierls substitution approach which couples the electromagnetic field to a physical lattice geometry with translational symmetry [157]. Blümer's derivation (5.40) is also specific to a single band system, dependent on a careful evaluation of the hopping behaviour in that context [155] and not generalizable to the multiorbital case. In each of these cases there is no apparent generalization applicable to our scenario.

As a result, we adopt the assumption that the single band formulations (5.33) and (5.38) can be appropriately generalized for the multiorbital case by recasting them into matrix form; we rely on this as an effective avenue toward insight into the multiorbital conductivity. The orbital-specific conductivities, $\sigma_0(\omega)$ and $\sigma_1(\omega)$, are dependent on the diagonal elements of the matrix convolution of spectral function operators, $\hat{A}_0(\epsilon, \omega')$ and $\hat{A}_1(\epsilon, \omega + \omega')$. Ideally, the density of states should be recast in a proper multiorbital expression not only including a dependence on the intra-orbital hopping parameters, t_0 and t_1, but also the interorbital nonlocal hybridization t_{01}. As discussed in section 4.3, we lack a rigorous analytical derivation for the multiorbital Bethe lattice DOS, but are able to perform a numerical calculation in the context of the optical conductivity algorithm.

We thus proceed to estimate the optical conductivity aware of the limitations of the hypercubic assumption and the lack of a proper multiorbital derivation for this property of the system. Nonetheless, our multiorbital realization should provide insight into the impact of interband transition absorption effects that are expected to reduce the orbital-specific conductivity spectral weight.

Under these assumptions our multiorbital optical conductivity $\sigma_{\rm MO}(\omega)$ becomes (for orbital α),

$$\sigma_{{\rm MO},\alpha}(\omega) = \frac{\sigma_{\rm pre}}{\omega}\sum_s \left[\int_{-\infty}^{\infty} d\epsilon \hat{\tilde{D}}(\epsilon)\int_{-\infty}^{\infty} d\omega' \left[f(\omega') - f(\omega+\omega')\right] \hat{A}_s(\epsilon,\omega')\hat{A}_s(\epsilon,\omega+\omega')\right]_\alpha \tag{5.42}$$

where $\hat{\tilde{D}}(\epsilon)$ is a modified matrix DOS whose components are chosen appropriate to (5.33) or (5.38) so that,

$$\hat{\tilde{D}}_{\rm Prus} = \begin{pmatrix} D_{00}(\epsilon) & D_{01}(\epsilon) \\ D_{01}(\epsilon) & D_{11}(\epsilon)\end{pmatrix} \tag{5.43}$$

$$\hat{\tilde{D}}_{\rm Chat} = \frac{1}{3}\begin{pmatrix} \left[4t_0^2 - (\epsilon+\epsilon_0)^2\right] D_{00}(\epsilon) & \left[4t_{01}^2 - (\epsilon+t')^2\right] D_{01}(\epsilon) \\ \left[4t_{01}^2 - (\epsilon+t')^2\right] D_{01}(\epsilon) & \left[4t_1^2 - (\epsilon+\epsilon_1)^2\right] D_{11}(\epsilon)\end{pmatrix}. \tag{5.44}$$

We will use (5.42) in our analysis of the DHM in section 7.5 where we identify the affects of hybridization on the transfer of spectral weight between low and high frequencies.

Chapter 6

Checks and Limits

6.1 Parameter Scales

In the single band case, the lattice DOS (4.22) in the limit of infinite connectivity has allowed values of ϵ under the square root in the range of $-2t \leq \epsilon \leq 2t$ with a bandwidth of $W = 4t$. In the multiorbital case, the non-hybridized bands are similarly characterized by bandwidths $W_0 = 4t_0$ and $W_1 = 4t_1$. The system parameters used throughout our DHM analysis are scaled relative to the lower orbital nearest-neighbour hopping parameter, $t_0 = 1.0$, which serves as a reference value for all other parameters including the Coulomb repulsions. Thus the lower orbital bandwidth is maintained at a value of $W_0 = 4.0$. Realistic units for the energy scale are on the order of eV, although the *relative* (unitless) specification of Coulomb repulsions with respect to bandwidth is the critical issue in the physics of the DHM.

6.2 Bath Size

As discussed in chapter 3, the DMFT method is grounded in a mapping of an infinite lattice onto a finite single impurity Anderson model (3.14). The effects of the whole lattice environment on the local dynamics of an individual lattice site are captured by a small set of non-interacting pseudo-sites representing the energetics of a mean-field "bath". The overall picture is illustrated in figure 3.1.

In principle, utilizing a larger bath should result in a more accurate parameterization, as the conjugate gradient minimization routine [129] is able to explore a more nuanced landscape in search of a function of finite dimension that best satisfies the distance relationship (4.12). An increasingly large bath, however, begets the same computational

problems discussed in section 3.1 that prohibit exact diagonalization of a large system: a larger number of bath sites increases the Hilbert space of the problem, requiring significant resources of time and computational memory. One of the critical challenges of DMFT calculations is to find the best bath parameterization at the least cost [113].

The Lanczos method [119, 158] has been used (for example, [87, 112, 159, 160]) in the history of DMFT to solve systems with larger baths at zero temperature. The Lanczos algorithm accurately returns the ground state of the system, but suffers from a limitation in handling degeneracies without additional time-consuming strategies [120,160]. As well, our experience has shown that obtaining converged hybridized multi-orbital Green's functions in an efficient manner is also challenging under Lanczos. The Arnoldi algorithm [121] alleviates the first of the problems, by reliably returning the full eigenspectrum of the Hamiltonian, but the second difficulty remains. It has, however, been successfully applied to multiorbital DMFT in the absence of orbital hybridization [114].

Figure 6.1 shows the effect of bath size on agreement between the single band mean field Green's functions, $g^{\mathrm{lat}}(i\omega_n)$ and $g^{\mathrm{imp}}(i\omega_n)$, which should become identical in the limit of infinite bath site number. Figure 6.2 shows, as a function of bath size, the maximum absolute difference separating the data sets, evaluated at the Matsubara frequency where agreement is poorest. The data in the figures is calculated at half-filling near the metal-insulator transition, where convergence is most difficult to obtain, especially at low frequency. It is clear from the scale of the plots that even with three bath sites the maximum *disagreement* between the functions is only a small fraction of their absolute value. This contrasts sharply with results found in the original paper [87] on the single-orbital LISA implementation where the same maximum relative disagreement for three bath sites was much larger.

It is also important to note the consistency among all four size examples at $\omega_n = 0$. This agreement at very low energy is significant since the self energy behaviour at the real axis is employed in determining the quasiparticle weight of the system.

In our exploration of the multiorbital electronic DHM (2.15), we have chosen to employ a full finite-temperature exact diagonalization for ease and reliability of implementation. The bulk of our calculations are performed with a four-site bath in addition to the two impurity sites (one for each orbital). This choice provides sufficient parameterization of the mean field to allow adequate agreement between the mean field functions, while limiting the time required for the algorithm to be run to self-consistency and swept across incrementally changing values of the parameters of interest in order to identify relevant trends such as band filling or quasiparticle weight as a function of chemical potential.

Similar to figure 6.1 for the single band case, the agreement between mean field Green's functions for the multiorbital implementation is shown in figures 6.3 and 6.4 for the real

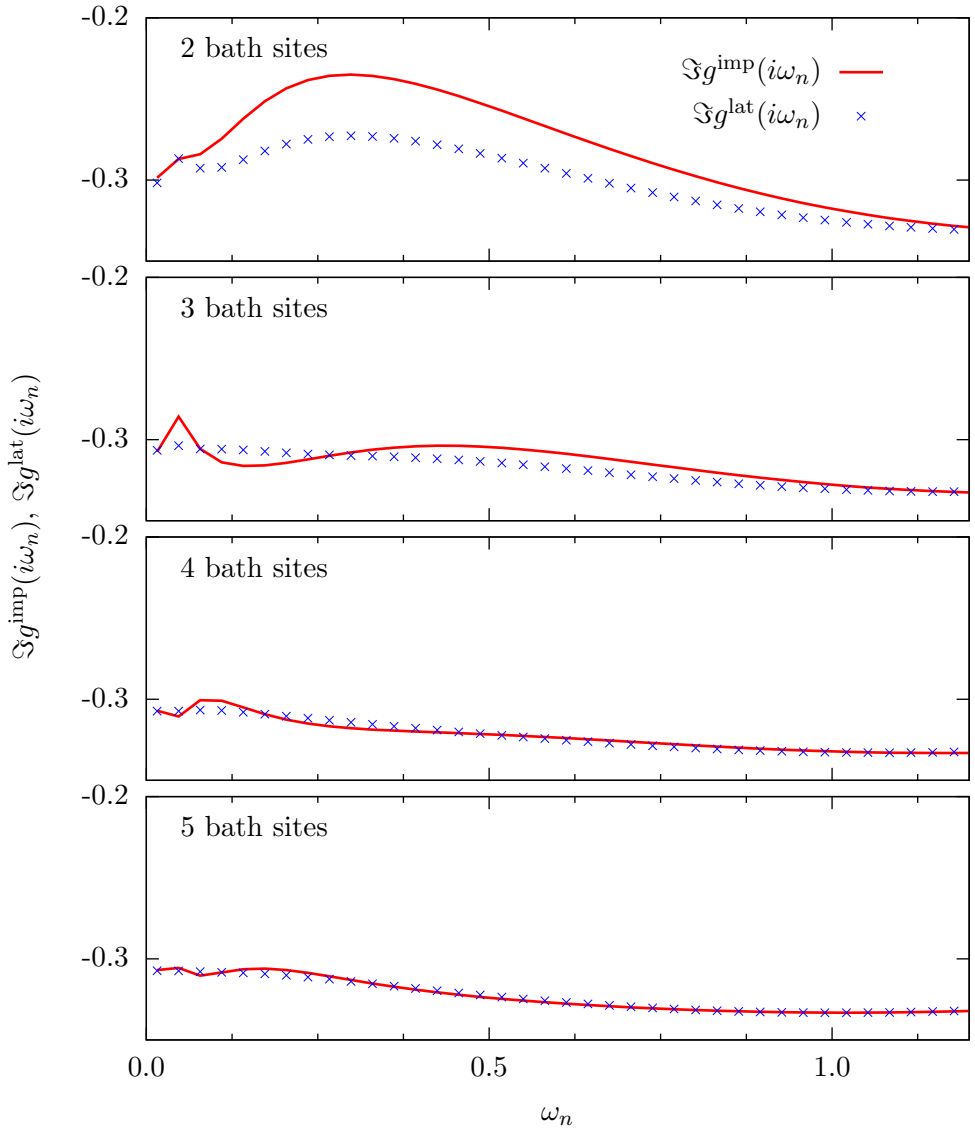

Figure 6.1: Comparison of the converged single band mean field Green's functions for the lattice, $g^{\mathrm{lat}}(i\omega_n)$, and SIAM, $g^{\mathrm{imp}}(i\omega_n)$, for different impurity bath sizes. Data is for $U = 3$, $\beta = 200$ at half filling near the MIT where convergence is most difficult. Note the narrow scale of the y-axis, demonstrating that even with three bath sites, the maximum discrepancy is a small fraction of the absolute functional values. Also note the robust agreement among all cases at ω_0, the data point nearest the real axis, where the value and slope of the self energy determines the quasiparticle weight.

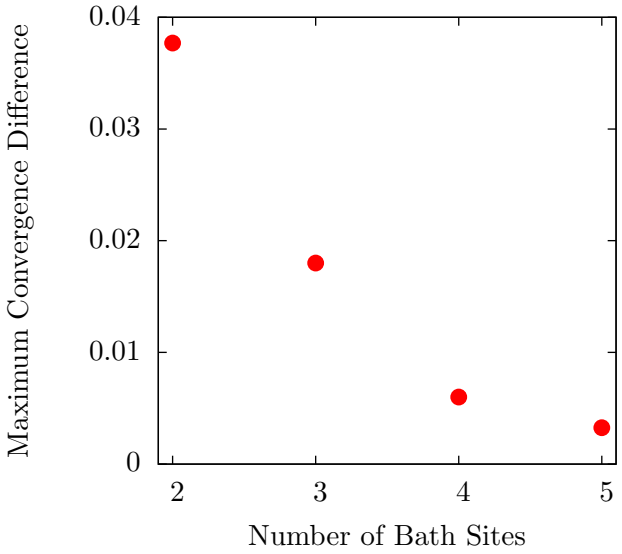

Figure 6.2: Maximum disagreement between single band mean field Green's functions, $\Im g^{\text{lat}}(i\omega_n)$ and $\Im g^{\text{imp}}(i\omega_n)$, from data plotted in figure 6.1. The value indicates the separation value at the Matsubara frequency with the worst agreement between the data sets.

and imaginary parts, respectively. The system parameters are comparable to the single orbital case above, with symmetric half-filled orbitals ($\epsilon_0 = \epsilon_1 = 0$), Coulomb repulsions near the metal insulator transition ($U_0 = U_1 = 3.0$, $\mu = 1.5$), and coupling between the orbitals ($t_{01} = 1.0$, $t' = 0.2$ and $U_{01} = 1.5$). The agreement between the imaginary values is excellent for all cases, whereas convergence of the real part of the Green's functions appears to be systematically more difficult in the multi-orbital realization and so is a better measure of the appropriate size of the bath. The maximum disagreement of these functions in figure 6.3 is shown in figure 6.5.

Our usual choice of four bath sites, or two per impurity orbital, is consistent with findings in [113], where it was concluded (for non-hybridized orbitals) that this size of bath provides reliable information so long as the inverse temperature, T, is not "too low" (roughly $\frac{T}{t} > 0.005$). It is important to note that those results pertained to a larger number of impurities embedded in the bath (a minimum three, as opposed to our two), but the extra hybridization parameter accompanying an additional orbital in their case is off-set by the inclusion of off-diagonal hybridization terms, V_{0l} and V_{1l}, in ours. This concurs with the findings of reference [161] for the reliability of a two-orbital system with four bath sites.

Having said this, for certain instances where greater resolution or better convergence is required, we can employ five or even six bath sites (seven or eight total sites). This level of resolution can be useful, for example, in examining changes in the slope of the self energy

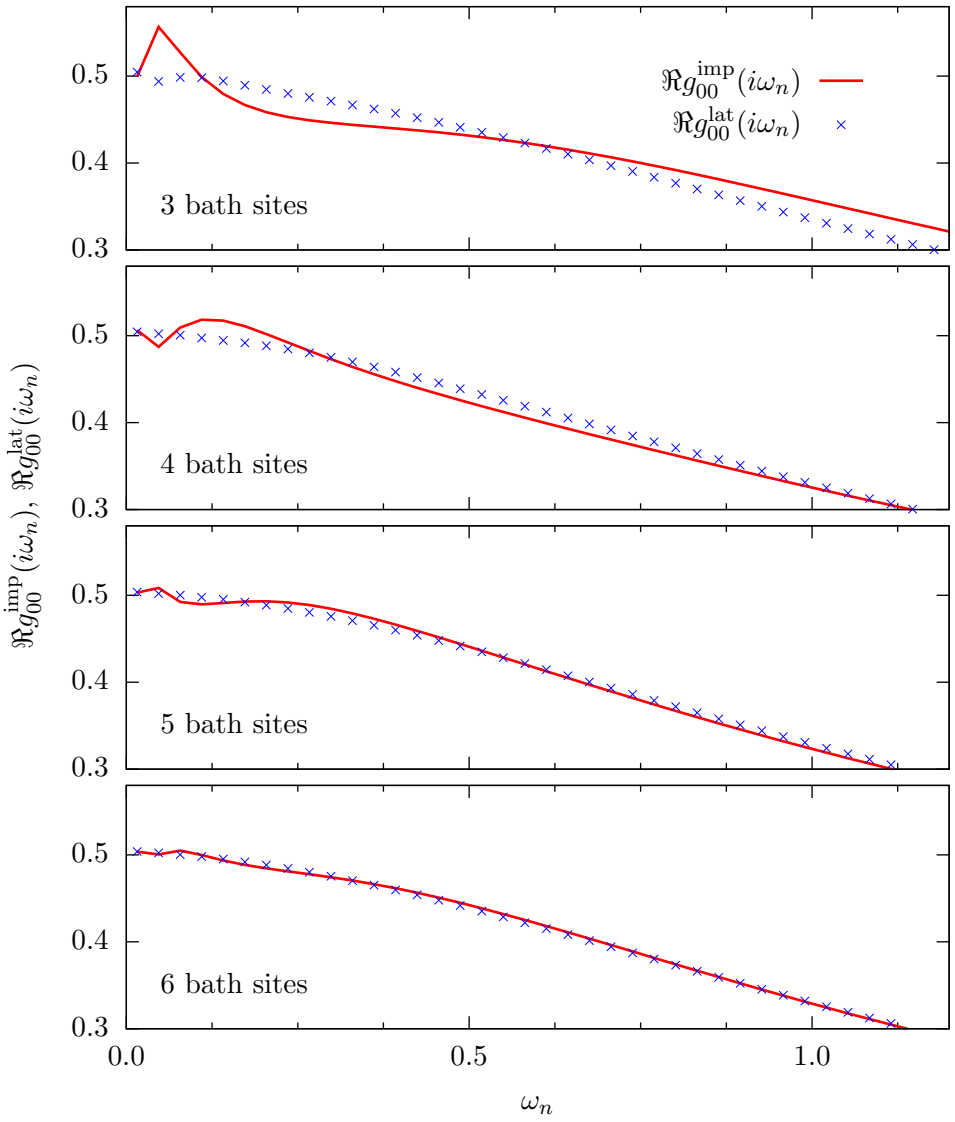

Figure 6.3: Comparison of real parts of the converged mean field Green's functions for the lattice, $\Re g_{00}^{\rm lat}(i\omega_n)$, and SIAM, $\Re g_{00}^{\rm imp}(i\omega_n)$, for different impurity bath sizes. Data is for $U_0 = U_1 = 3.0$, $\mu = 1.5$, $\beta = 200$ at half filling near the MIT where convergence is more difficult than in the metallic or insulating phases. Coupling between the orbitals is $t_{01} = 1.0$, $t' = 0.2$ and $U_{01} = 1.5$.

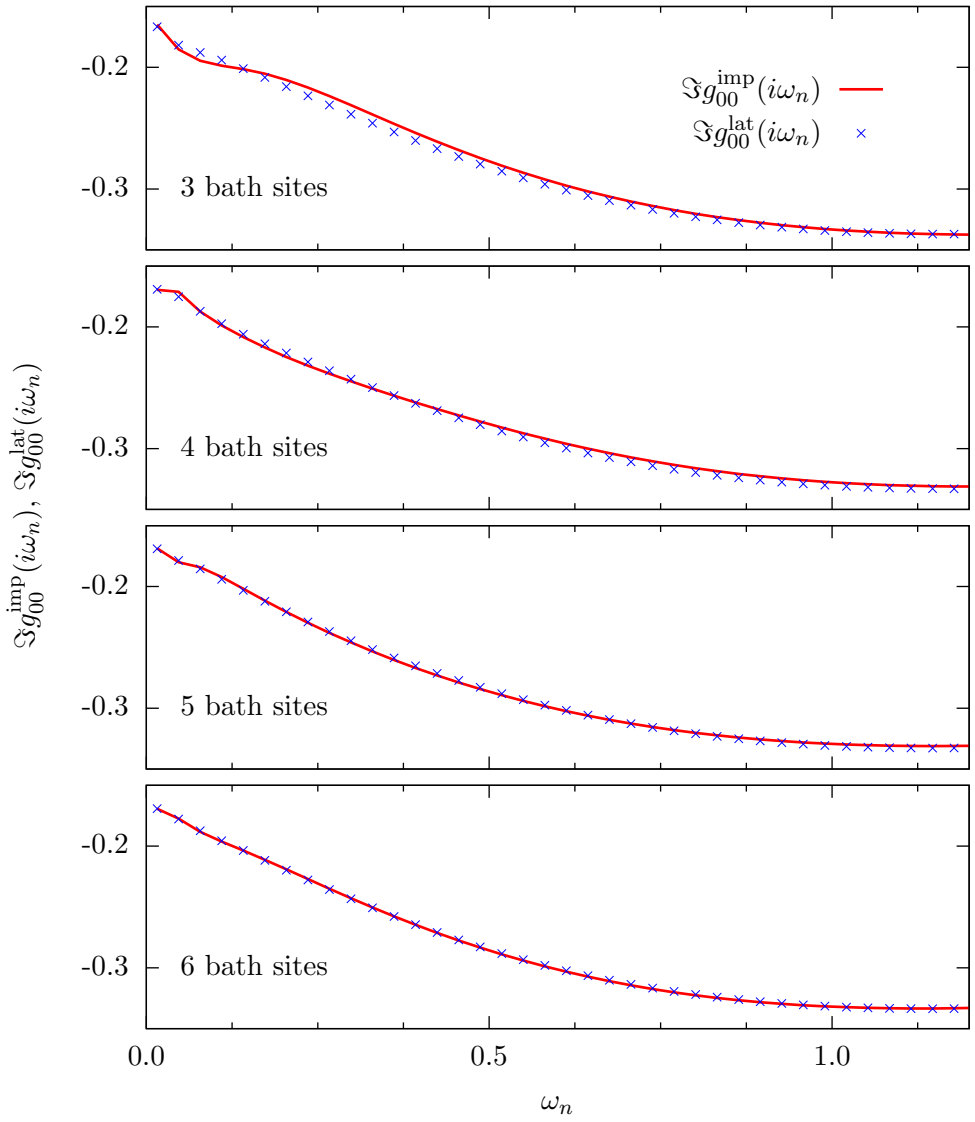

Figure 6.4: Comparison of imaginary parts of the converged multiorbital mean field Green's functions. Parameters are the same as in figure 6.3.

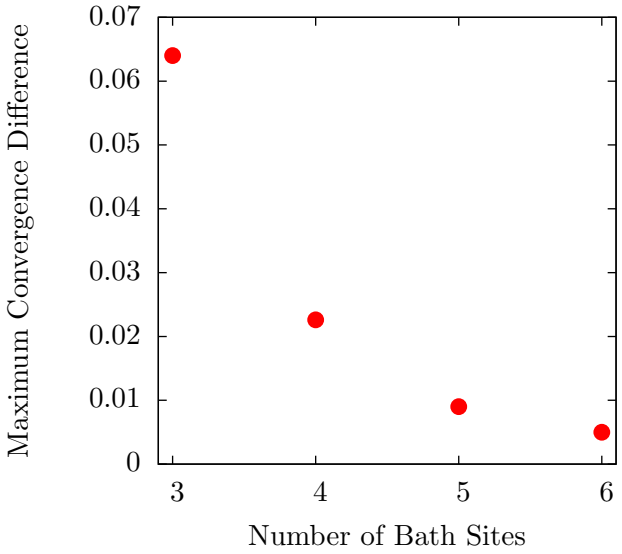

Figure 6.5: Maximum disagreement between real parts of the double band mean field Green's functions, $\Re g_{00}^{\mathrm{lat}}(i\omega_n)$ and $\Re g_{00}^{\mathrm{imp}}(i\omega_n)$, from data plotted in figure 6.3.

(or functions derived therefrom) at the Fermi energy, or evaluating the real frequency spectral functions, where an increase in multi-site correlations tends to add detail to the overall structure of the spectrum. There is, however, a high cost in computational time related to the exact diagonalization of a much larger Hamiltonian matrix.

The distance functions (3.24) in the single orbital case, and (4.12) in our two-orbital implementation, provide a measure of how well the chosen number of bath sites approximate the lattice solution. As discussed in section 3.6, the output of this function is determined through our C++ translation of the conjugate gradient minimization routine, `minimize` [129]. The actual convergence of the MODMFT algorithm (figure 4.1) is based on the norm of the agreement between the matrix components of the impurity mean field Green's functions $\hat{g}^{\mathrm{imp}}(i\omega_n)$ at two subsequent iterations of the algorithm. The level of agreement is measured across all frequencies and compared to some arbitrarily small tolerance η in (4.14), as discussed in section 4.2.

6.3 Nonlocal Hybridization and Convergence

The hybridization of electrons between orbitals and between sites through t_{01} is important to the physical motivation of the DHM (2.15). It is of value to consider the effect of this parameter on low-frequency convergence of the MODMFT solution.

The strength of t_{01} is expected to govern the emphasis placed on the off-diagonal impurity-bath hopping parameters V_{0l} and V_{1l}, which, as mentioned above, expand the functional landscape for our multiorbital problem as compared to that of a non-hybridizing multiorbital implementation of equivalent size. Figure 6.6 shows the change in the difference, $\left|\Re g_{00}^{\text{imp}}(i\omega_n) - \Re g_{00}^{\text{lat}}(i\omega_n)\right|$, for the low energy region of the Matsubara spectrum. An increase in t_{01} strongly corresponds with an increase in agreement between the converged functions. The parameters are the same as in figure 6.3, with four bath sites and $t' = 0$[1] to clarify the role of t_{01}.

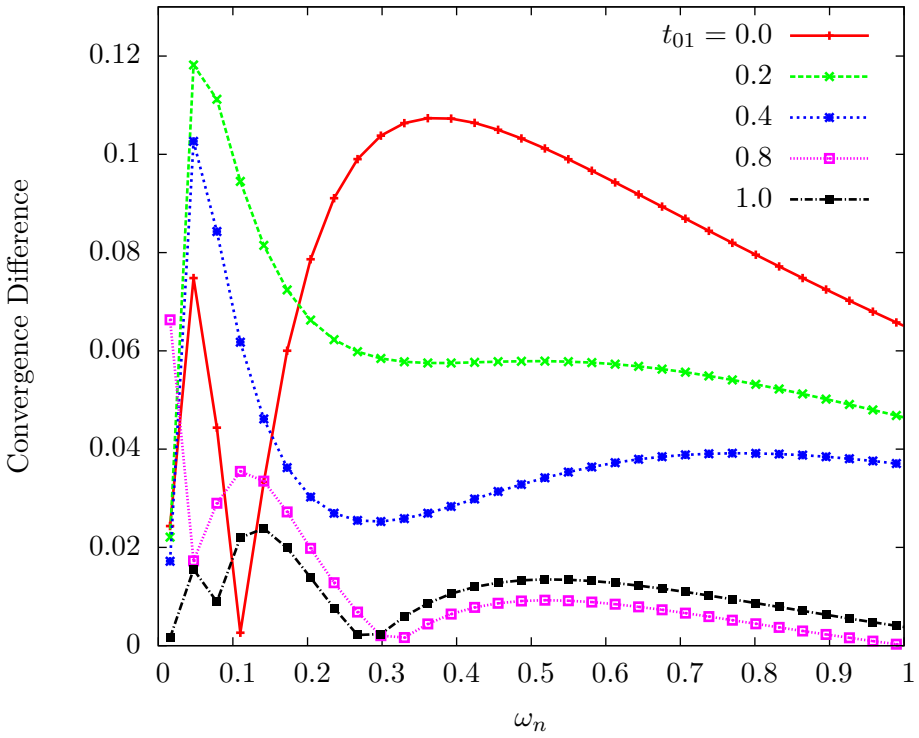

Figure 6.6: Disagreement between real parts of the double band mean field Green's functions, $g_{00}^{\text{imp}}(i\omega_n)$ and $g_{00}^{\text{lat}}(i\omega_n)$, for low frequency region of Matsubara spectrum, with varying nonlocal hybridization t_{01}. Four bath sites are used, with system parameters as in figure 6.3 and $t' = 0$. It is clear that a larger value of t_{01} corresponds to a better parameterization of the impurity model, because of the greater emphasis on additional bath hybridization parameters .

Figure 6.7 shows the maximum disagreement between the mean field Green's functions from the data in figure 6.6. A model which includes a non-zero t_{01} will tend to be more reliable in a MODMFT application with fewer bath sites than a model without this pa-

[1] $t' = 0$ out of an abundance of caution, since it has been found to have no effect on the question at hand, which is not surprising given its entirely local contribution to the impurity problem.

rameter. Thus, this hybridization has a stabilizing effect on the DHM solution across a larger set of system parameters which affects that logistics of modeling these systems.

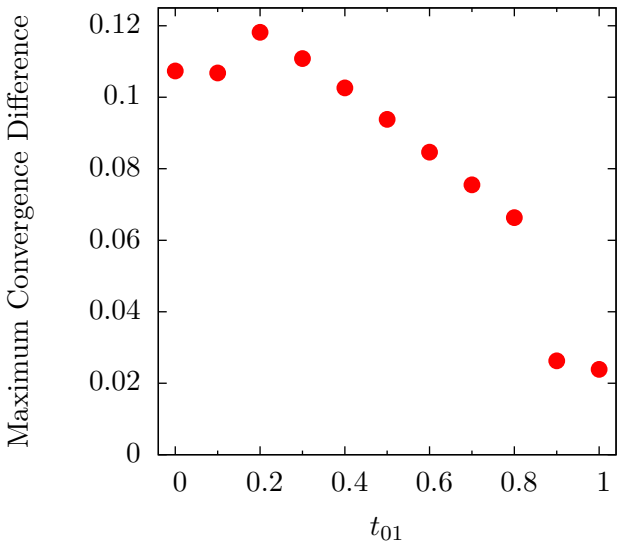

Figure 6.7: Effect of t_{01} on maximum disagreement between real parts of the two-orbital mean field Green's functions, $g_{00}^{\text{lat}}(i\omega_n)$ and $g_{00}^{\text{imp}}(i\omega_n)$. Using data plotted in figure 6.6.

Additionally, we have found t_{01} to provide a helpful degree of freedom in converging an otherwise difficult MODMFT solution. In certain parameter regions, usually in the vicinity of a hysteresis region (see section 6.5), the MODMFT routine will fail to converge within several hundred iterations. An increased value of t_{01} will often provide robust convergence, following which the hybridization value can be scaled down to its original value in a stepwise continuous way to arrive back at the original desired parameter definitions and convergence results.

6.4 Single Band Limit

The single band exact diagonalization implementation of DMFT has been well tested and well understood since its development in 1994 by Caffarel and Krauth [112], and a benchmark algorithm has been freely distributed in the LISA Fortran program [87,122] discussed in section 3.6.

The single band limit provides an important reliability test for our MODMFT implementation. The matrix construction of the Green's functions and self energy are structurally different from the single-orbital form, and this slightly complicates the search for

equivalence between the two cases. Naturally, electronic occupation of the upper orbital must be made energetically unfavourable by setting $(\epsilon_1 - \epsilon_0) \to \infty$. This ensures that in the impurity Green's function $\hat{G}^{\text{imp}}(i\omega_n)$ the only finite component is G^{imp}_{00}. Figure 6.8 provides a comparison of the self energy and lattice mean field Green's function in this limit, for $\epsilon_1 = 1000$ and the metallic half-filling system parameters $U_0 = 2$, $\mu = 1$, and $\beta = 100$.

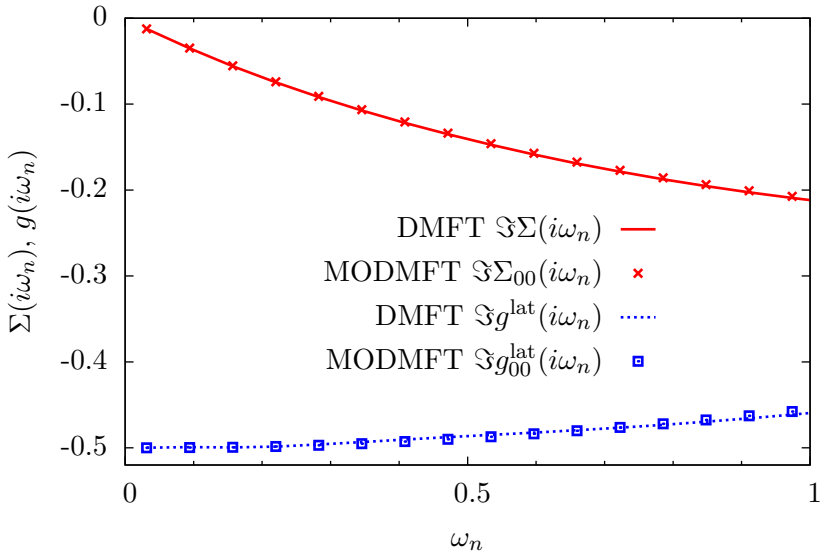

Figure 6.8: A test of the multiorbital DMFT code in the single orbital limit with the upper energy level gapped out at $\epsilon_1 = 1000$. There is good agreement at low energy between the self energies and lattice mean field Green's functions for the single orbital case (solid lines) and multiorbital lower band result (points) $U_0 = 2$, $\mu = 1$ and $\beta = 100$.

Figure 6.9 provides a comparison of the converged bath parameters corresponding to the data in figure 6.8, from the single orbital DMFT solution and the lower energy orbital of the MODMFT solution. The hybridization values V_l and V_{0l}, for bath sites l, show very good agreement as do the bath energies ε_l, demonstrating the proper convergence of the multiorbital code in the large ϵ_1 limit. Test cases on other parameter sets provide equally good results.

6.5 Hysteresis

As discussed in section 3.7, a hysteretic region has been observed in the MIT phase diagram of strongly correlated electron systems examined under DMFT, and is understood as evidence of a first-order transition. The existence of actual hysteresis has been challenged,

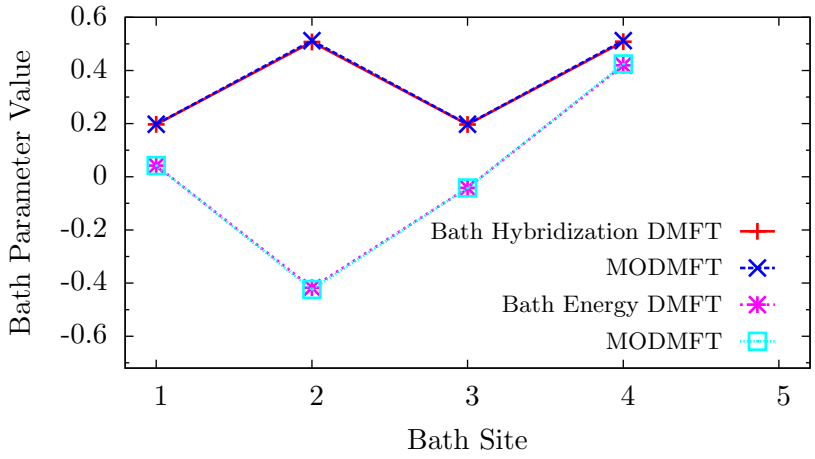

Figure 6.9: Comparison of converged bath parameters for data shown in figure 6.8. The top line shows agreement between hybridization parameters V_l and V_{0l}; the lower set of data shows agreement between the bath energies ε_l.

however, as a numerical deficiency [131].

In our two-orbital model of DMFT, it is unambiguous that hysteresis regions appear, especially in diagrams showing the fillings and quasiparticle weights of the system. This phenomenon arises when the MODMFT code is employed in subsequent cases to sweep a system parameter across a discretized spectrum of increasing or decreasing values. At certain regions of a phase diagram related to that parameter, there is disagreement between the converged solutions from sweeping up and sweeping down, and one might say the hysteretic path that results is "connected" to the extremal phase which formed the starting point of a high value or low value of the parameter. For example, hysteresis observed in the MIT region arising from subsequent iterations of the code where U_0 is adjusted up or down will provide two converged solutions: one connected to the insulating region (sweeping down from high U_0) and the other connected to the metallic limit (sweeping up from low or zero U_0). Various incarnations of hysteresis have been identified in MODMFT studies including plots of band filling [161], double occupancy [162], spectral weight [163] and quasiparticle weight [164]. A qualitative difference has also been observed between the hysteresis regions found with QMC and ED DMFT impurity solvers [165].

In agreement with previous multiorbital results (*e.g.*, [113,161,164]) we have found quite generally that the hysteresis regions correspond to parameter spaces where the convergence of the bath parameters is especially difficult, normally (but not exclusively) in the vicinity of a MIT (as well as insulator to metal transitions [IMT]) in one of the two bands (or the region where a MIT *would* occur except for the enhancement of the quasiparticle weight

by the intersite hybridization t_{01}). In the four-site MODMFT problem a converged set of bath parameters can normally be arrived at with only 2-6 iterations of the MODMFT loop. In a hysteresis region, this may take upwards of 100-200 iterations depending on the specific conditions, and convergence will not occur at all in some instances after several hundred iterations, especially for systems with large Coulomb repulsions relative to the bandwidths.

A very typical example of the type of hysteresis encountered is shown in figure 6.10, where the chemical potential μ is swept up and down across the same parameter space to plot the total filling n of the two bands. The plateau region at half filling ($n = 2$) is bounded by two hysteretic features at the MIT and the IMT. The total electronic filling is expected to increase (decrease) monotonically with increasing (decreasing) chemical potential, as it does in the case of increasing μ where each MODMFT run is initialized by the converged bath parameters of the preceding converged solution at lower μ. In the case where chemical potential is swept down, it is clear from the figure that the filling violates the physical expectation of monotonical decrease across the entire insulating plateau and especially in the left-hand hysteresis region.

Another example, not connected to Mott physics, is seen in figure 6.11. Here, hysteretic behaviour arises in connection with an abrupt onset of energetics favourable for filling the upper band, where before the value of the chemical potential had favoured filling of the lower band. Again, this figure presents a choice between physical and non-physical solutions evaluated on the monotonic change in the total filling of the combined bands.

The examples in figures 6.10 and 6.11 are for four bath sites, but our observations are fairly consistent with tests made on five bath site systems. However, while still present, both the hysteresis and the non-monotonic behaviour of the total filling are obviously suppressed with the extra pseudosite. This suggests the hysteretic behaviour in our DMFT algorithm is related to the computational method and may not reflect actual physics of the system.

We are unaware of any other MODMFT studies which indicate the same physical defect in a hysteresis region, perhaps due in part to the fact that hybridization between bands is often neglected whereas we do find it plays a role in moderating hysteresis (as do changes in spin flip and pair exchange and temperature [164]), although not altogether eliminating it. It is also critical to evaluate the effect of hysteresis on the monotonic change in *total* band filling of a multiorbital system, and our review of the MODMFT literature has found an understandable emphasis on hysteresis in the context of individual band filling alone (where monotonic change is not necessarily expected) with no apparent examples of the close-up total filling in the hysteresis regions, as in figure 6.11.

We have found these unidirectional violations of the anticipated relationship between

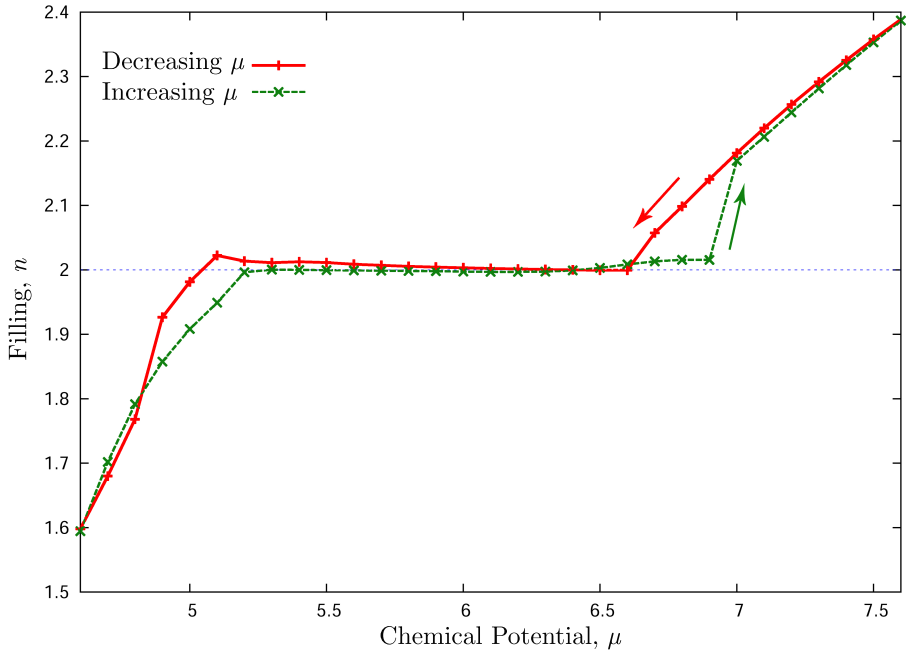

Figure 6.10: Hysteresis in the total electron filling at the MIT and IMT in the converged MODFMT solution, as chemical potential is swept up or down (direction of sweep indicated by arrows). At each new data point calculation, the bath parameters are initialized with the converged parameters of the previous solution in the sweep. The total electron filling should change monotonically in the same direction as increasing or decreasing chemical potential — a physical expectation violated in the case of decreasing μ, especially at the left-most transition. Four bath sites, $\beta = 100, U_0 = 6.0, U_{01} = 4.0, U_1 = 2.0, t_{01} = 1.0, t' = 0.2, \epsilon_1 = 1.0$.

total filling and chemical potential to be typical of our MODMFT hysteresis regions, and indicative that one of the two convergence paths should not be considered physical. As a rule, throughout this thesis we only present the converged result that agrees with the physical expectations of monotonic changes in the total electron filling of a hysteresis region.

6.6 Non-Interacting Limit

6.6.1 Overview

We conclude this chapter by examining the non-interacting limit ($U_0 = U_1 = U_{01} = 0$) of the electronic DHM Hamiltonian (2.15) and the ability of our MODMFT code to produce the results expected in this limit.

In subsection 6.6.2 we will explore the analytical expression for the dispersion of the one-dimensional tight-binding DHM lattice, evaluating the effects of hybridization on this

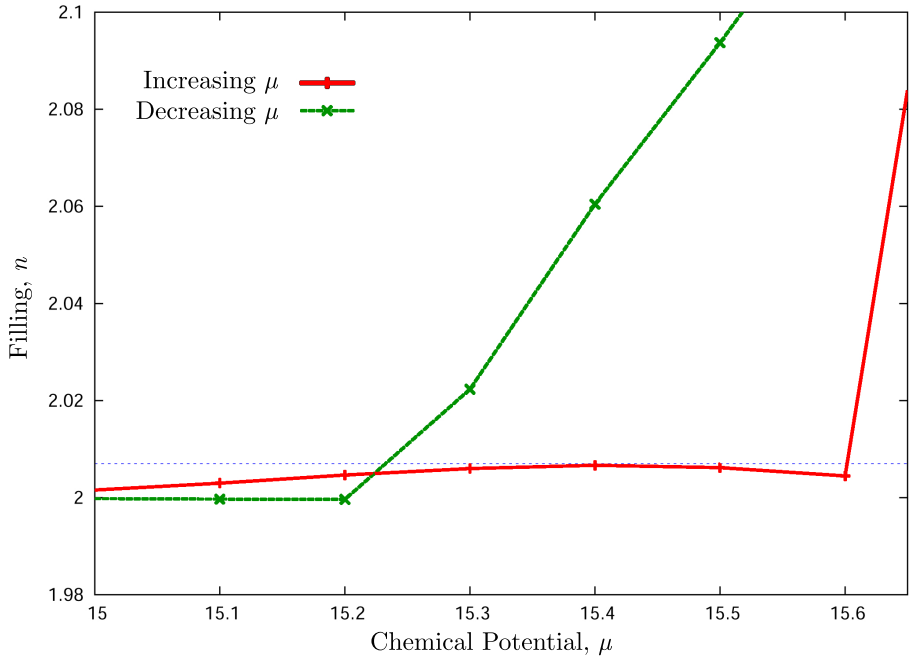

Figure 6.11: A close-up example of a hysteresis region that arises from sweeping the chemical potential up and down to change the electron occupation of the orbitals. In this region, the curve corresponding to increasing μ (red with data points indicated by + markers) violates the expectation of an associated monotonic increase in the total electron filling. Instead, the curve approaches and then drops away from the blue horizontal reference line. The green curve ($\times$ symbols), corresponding to a decreasing sweep in the chemical potential, levels off in the plateau region (below $\mu = 15.6$) without similar unphysical behaviour. The underlying dynamic creating this region of hysteresis is the abrupt onset of favourable energetics for filling the upper orbital and is not associated with an orbital MIT or IMT. Four sites $\beta = 120, U_0 = 10.0, U_{01} = 6.0, U_1 = 4.0, t_{01} = 1.0, t' = 0.2, \epsilon_1 = 5.0$.

system before Coulomb repulsion is included in its dynamics. This analysis is not directly comparable to the Bethe lattice geometry employed in the DMFT method. However, it is relevant to the linear chain of four sites employed in Hirsch's study [31], to which our results in chapter 7 are otherwise compared. It is intended to provide insight into the behaviour of the general model under hybridization.

In subsection 6.6.3, we turn to the multiorbital Bethe lattice and explore the non-interacting limit as an additional simple check on the behaviour of our MODMFT code. We examine the output of the algorithm with respect to the expected Drude peak in the non-interacting spectral density and optical conductivity.

6.6.2 Effect of Hybridization on Non-Interacting Bands

The energy bands of the non-interacting DHM Hamiltonian can be calculated analytically through a Fourier transform to k-space. Taking the lower orbital energy centered at $\epsilon_0 = 0$, the Hamiltonian matrix for a one-dimensional system becomes,

$$H_k = \begin{pmatrix} c_{0k}^\dagger & c_{1k}^\dagger \end{pmatrix} \begin{pmatrix} -2t_0\cos(k) & -2t_{01}\cos(k) - t' \\ -2t_{01}\cos(k) - t' & -2t_1\cos(k) + \epsilon_1 \end{pmatrix} \begin{pmatrix} c_{0k} \\ c_{1k} \end{pmatrix}, \tag{6.1}$$

with eigenvalues,

$$\lambda_\pm = \frac{1}{2}\left[\varepsilon_0(k) + \varepsilon_1(k) + \epsilon_1\right] \pm \frac{1}{2}\sqrt{\left[\varepsilon_0(k) - \varepsilon_1(k) - \epsilon_1\right]^2 + 4\left[\varepsilon_{01}(k) - t'\right]^2} \tag{6.2}$$

where,

$$\varepsilon_0(k) = -2t_0\cos(k) \tag{6.3}$$

$$\varepsilon_1(k) = -2t_1\cos(k) \tag{6.4}$$

$$\varepsilon_{01}(k) = -2t_{01}\cos(k). \tag{6.5}$$

The solutions of (6.2) are the energies of the electron bands which, for non-zero hybridization, are occupied by linear combinations of electrons in the physical bands centered at ϵ_0 and ϵ_1.

The indirect energy gap between non-interacting (NIN) upper and lower bands is defined by

$$\Delta_{\text{NIN}}(k) = \lambda_+ - \lambda_- = \sqrt{\left[\varepsilon_0(k) - \varepsilon_1(k) - \epsilon_1\right]^2 + 4\left[\varepsilon_{01}(k) - t'\right]^2}. \tag{6.6}$$

For $t_0 = t_1$, $\Delta_{\text{NIN}}(k) \neq 0\ \forall k$ under either of two conditions:

1. $\epsilon_1 > 0$.
2. $\left|\frac{t'}{t_{01}}\right| > 2$.

Under either condition, the energy dispersion will be gapped. The presence of hybridization therefore introduces another means—besides the usual $\epsilon_1 - \epsilon_0$—of separating the energy bands of the system.

Figure 6.12 compares the response of the non-interacting band structure to the opening of a gap by changes in the values of ϵ_1 and the onsite hybridization t', where $t_{01} = 0$. These illustrations of (6.6) make it clear that both parameters can play an equivalent role in tending to separate the energy bands of the system, although the effect of t' is more

dramatic in that it affects the lower band as well as the upper. In the case of increasing ϵ_1 [figure 6.12 a)], the lower band position remains fixed for all values of the upper orbital energy. Similar observations were made in a study of the two-orbital periodic Anderson model by Continentino *et al.* [57].

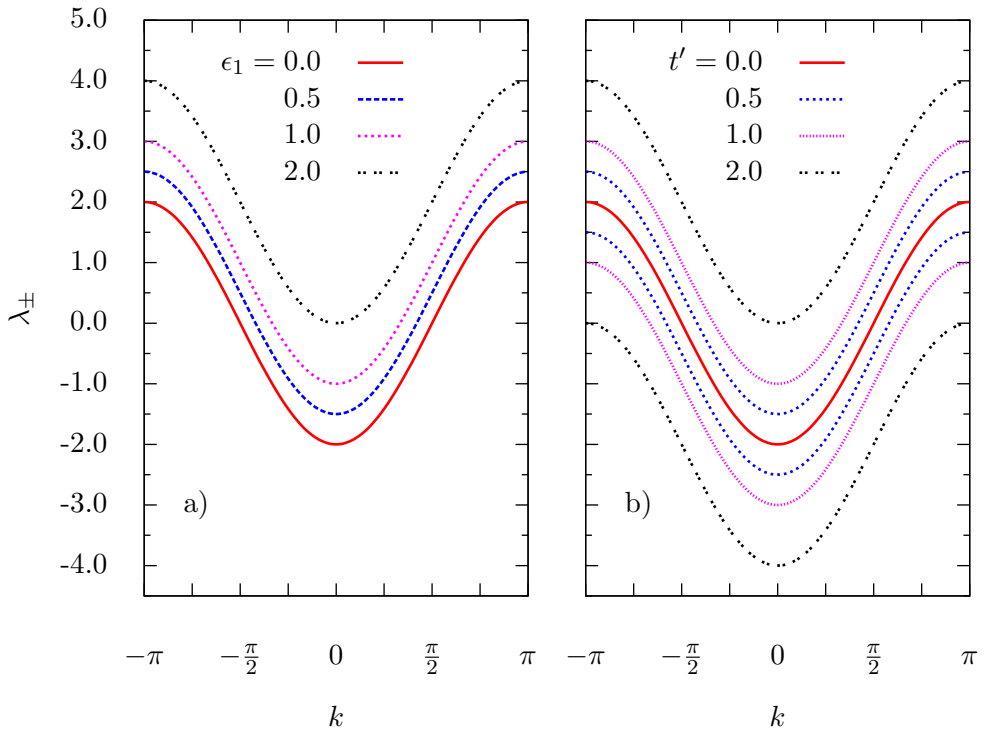

Figure 6.12: A gap is opened in the non-interacting 1D dispersion of the electronic DHM through either a) ϵ_1 or b) the local hybridization t'. $t_0 = t_1 = 1$. All other system parameter are zero including t_{01}. For the $\epsilon_1 = 0.0$ case in a) and $t' = 0.0$ in b), the upper and lower bands are degenerate ($\lambda_+ = \lambda_-$). In a), as ϵ_1 is increased, the lower band (energies λ_-) remains fixed (at the $\epsilon_1 = 0.0$ position) while the upper band (λ_+) moves up opening the gap. In b), increasing the local hybridization t' causes both the upper band to move up and the lower band to descend. It is therefore clear that t' produces a similar but enhanced effect on the non-interacting band structure as ϵ_1 (when the condition $\left|\frac{t'}{t_{01}}\right| > 2$ is met). Also of note, in b), the band-widths are unaffected by changes in t'.

The effect of t_{01} on the non-interacting band structure is shown in figure 6.13. With $t' < t_{01}$, this intersite/interorbital hybridization does not open a gap in the band structure, unlike the local hybridization t' acting by itself.

The impact on the energy gap (6.6) for various parameter combinations is shown in figure 6.14, demonstrating their relative importance in the spacing between the lower and upper bands.

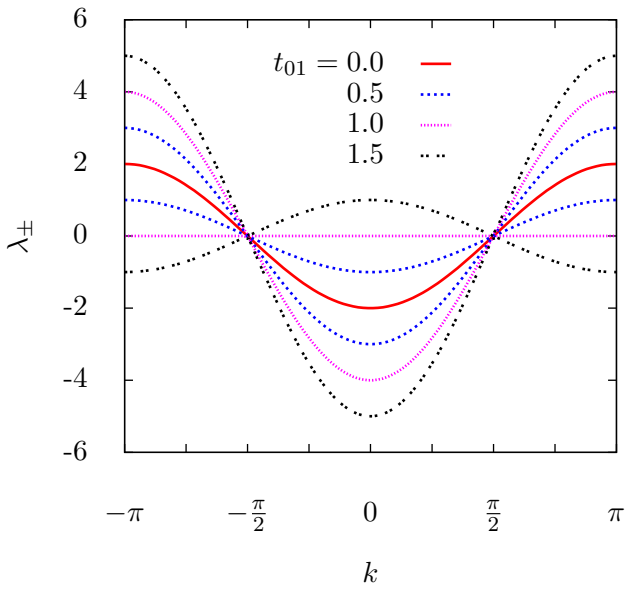

Figure 6.13: The effect on the non-interacting linear chain from increasing t_{01}, with $t_0 = t_1 = 1$ and $t' = \epsilon_1 = 0$. The upper and lower bands are degenerate for $t_{01} = 0.0$. A flattening of the bands becomes evident for $t_{01} \approx t_0 = t_1 = 1.0$.

The particular case where $t_{01} = 1.0$ leads to complete band flattening, as shown in figure 6.13 for $t_{01} = t_0 = t_1 = 1.0$, is worth further consideration. Figure 6.15 shows the evolution of this phenomenon around this value of the hybridization, for t' turned off. The equal values of the interorbital hopping with the intraorbital hoppings t_0 and t_1 is critical for the onset of flatness as seen in the figure.

Figure 6.16 shows the effect of the onsite hybridization near this regime where $t_{01} = 0.8$ is close to $t_0 = t_1 = 1.0$. The upper orbital energy is fixed at $\epsilon_1 = 1.5$. Increasing t' tends to change the free electron bandwidths, widening the lower band and narrowing the upper and causing a mild moderating effect on the overall curvature effect of t_{01}.

6.6.3 Non-Interacting Limit of the MODMFT Implementation

We conclude by examining the results of our MODMFT implementation for the non-interacting case where all Coulomb repulsion input parameters are set to zero. In this regime we examine the spectral densities and optical conductivity to establish the kind of output generated by our code in this regime where analytical results are well established.

The structure of the non-interacting impurity spectral density generated by our MODMFT

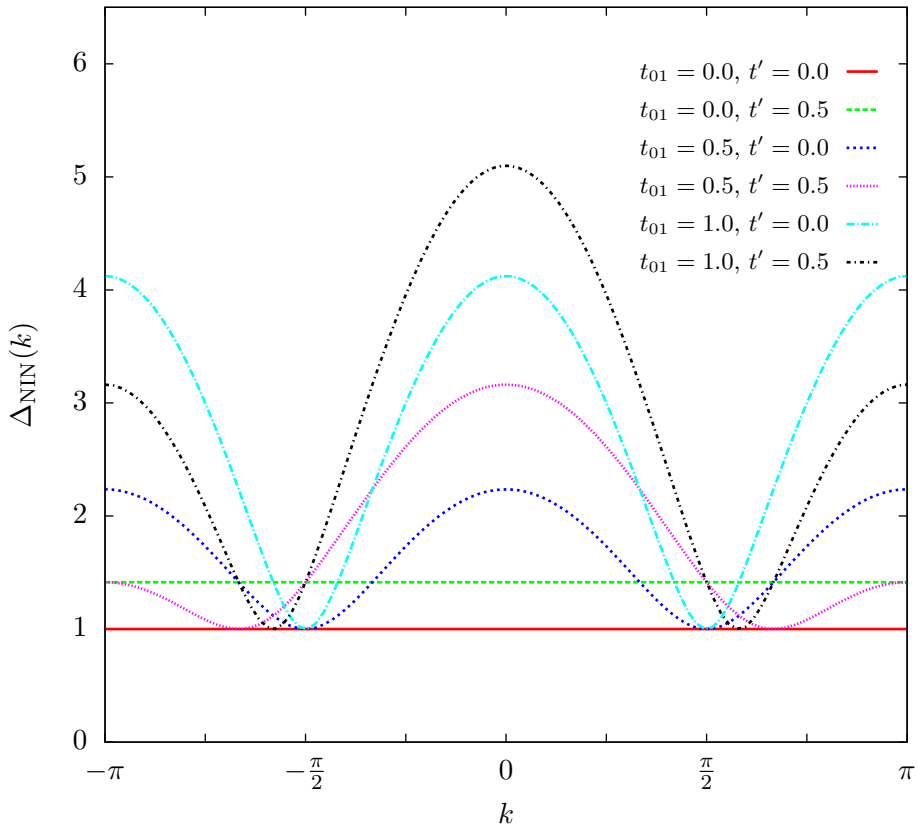

Figure 6.14: Change in the energy band gap (6.6) for various parameter values t_{01}, t' and ϵ_1 in the 1D electronic DHM.

routine is shown in figure 6.17, comparing the quasiparticle features of the four and five bath site systems at half filling in the lower orbital for bandwidth $W = 4$. As discussed in section 5.1, the structure around the Fermi energy, $\omega = 0.0$, is formed by delta functions artificially broadened into Lorentzians, arising due to the contribution (and limitations) of the discrete bath density of states.

The densities of states of figure 6.17 are approximations to the exact semi-circular density of states for the non-interacting Bethe lattice in infinite dimensions (4.22). This is plotted for bandwidth $W = 4t^* = 4$ in figure 6.18, in comparison to the four-site result of figure 6.17 broadened to a Lorentzian with $\eta = 0.05$.

It is clear that many more bath sites are required to achieve visual congruence between the finite DMFT structure and the exact solution in figure 6.18.

Finally, we show the lower orbital optical conductivity $\sigma_0(\omega)$ for the non-interacting system with four bath sites in figure 6.19. We compare the MODMFT output for both the

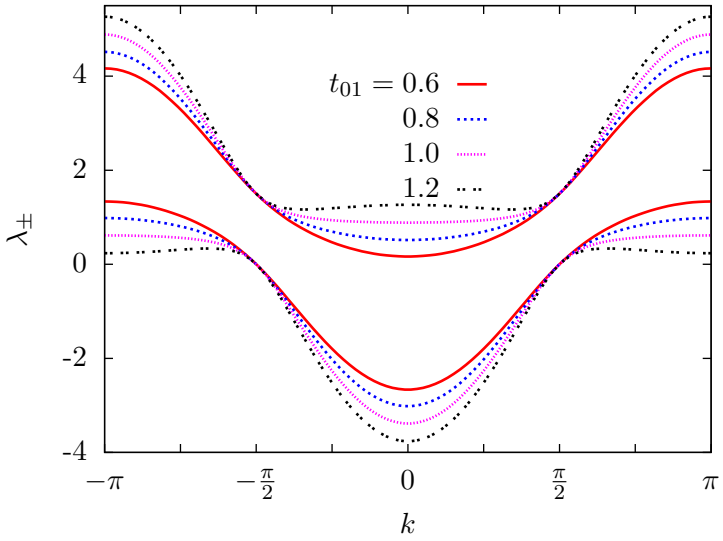

Figure 6.15: Effect of changing t_{01} on flattening of the energy bands in the 1D non-interacting DHM system with onsite hybridization $t' = 0$ and upper orbital energy $\epsilon_1 = 1.5$. The difference in curvature between the $k = 0$ electron quasiparticles and hole carriers at the band edges signals a difference in their effective masses and thus clear electron/hole asymmetry even in the non-interacting case.

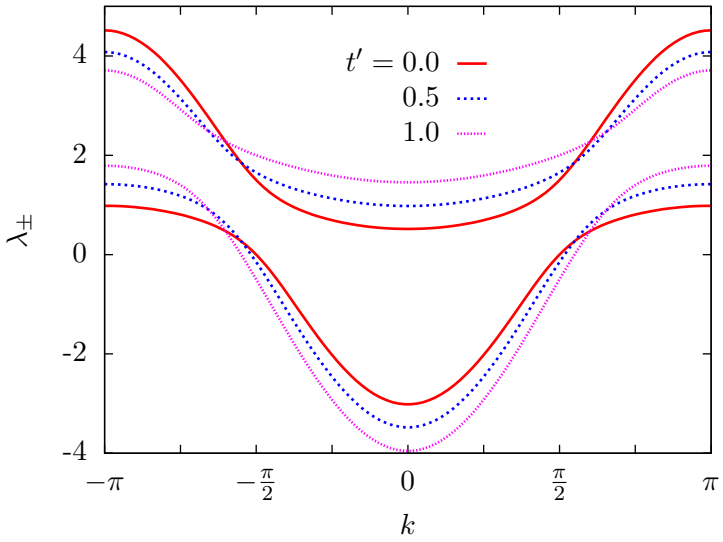

Figure 6.16: Change in the 1D non-interacting DHM band structure for finite $\epsilon_1 = 1.5$ and $t_{01} = 0.8$, where the latter parameter provides a flattening effect on the bands. Increasing t' tends to widen the lower bandwidth and narrow the upper.

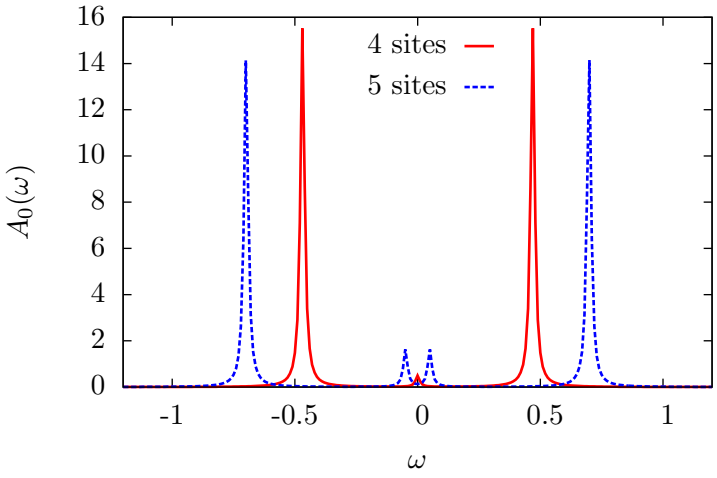

Figure 6.17: Lower orbital impurity spectral density for non-interacting MODMFT at half filling, comparing the four bath site result to that of five bath sites in the fully metallic system. The structure of this quasiparticle peak is determined by the bath discretization of the Anderson impurity model. This observation is important when discerning the quasiparticle peak at the Fermi energy in cases with non-zero interactions. The delta functions are artificially broadened by $\eta = 0.01$, for $\beta = 200$.

hypercubic form (5.33) and the Chattopadhyay definition (5.38) at half filling ($n = 2$) with degenerate orbitals, alongside the analytically exact results which match the MODMFT data very well. The extension of the low frequency Drude peak which is determined by the Lorentzian broadening ($\eta = 0.05$ in the figure) is an important reference for identifying the same contribution in interacting systems.

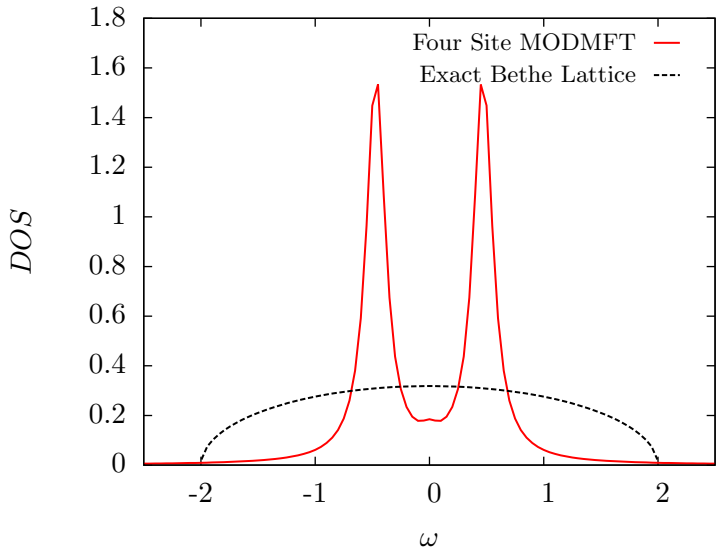

Figure 6.18: Lower orbital impurity DOS for non-interacting four bath site MODMFT at half filling, artificially broadened into a Lorentzian with $\eta = 0.05$, compared with the analytically exact non-interacting DOS for the infinitely connected Bethe lattice given by (4.22), with bandwidth $W = 4t^* = 4$.

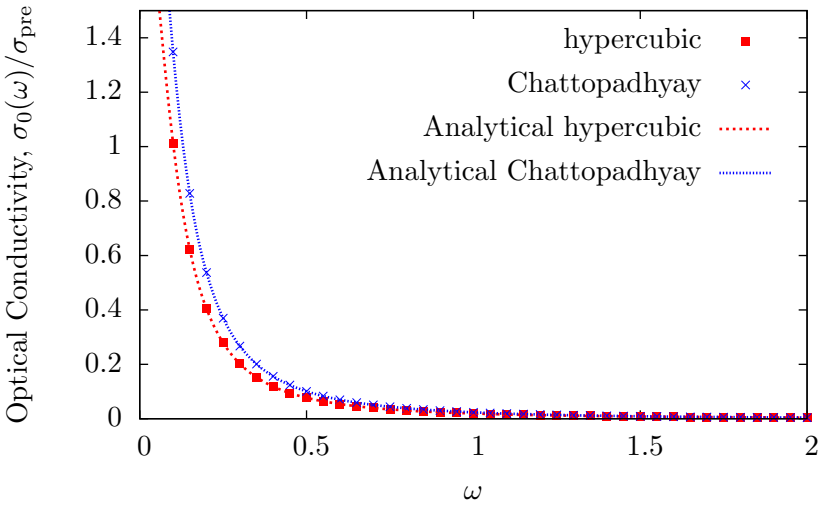

Figure 6.19: Lower orbital optical conductivity for the non-interacting four-site system, comparing results from the hypercubic approximation, $\sigma_{\text{HC},0}(\omega)$, and the Chattopadhyay improvement, $\sigma_{\text{Chat},0}(\omega)$ (see section 5.4), alongside analytically exact results. The non-interacting conductivity defines the extension of the low-frequency Drude peak due to artificial Lorentzian broadening of $\eta = 0.05$. The lower orbital is at half filling.

Chapter 7

Results

7.1 Overview

In this chapter we provide comparative results of our MODMFT Bethe lattice analysis of the electronic DHM (2.15) and those of Hirsch in his 2003 four-site exact diagonalization study of the same model [31]. The critical observation of electron-hole asymmetry related to orbital relaxation is analyzed in the subsections that follow, each focusing on a particular evidence for the phenomenon.

In section 7.2 we evaluate Hirsch's observation of asymmetry in the quasiparticle eigenvalue spectrum. Section 7.3 provides an analysis of the quasiparticle weight reduction in the regime of clear orbital relaxation, a primary outcome of Hirsch's paper. In section 7.5 we evaluate the optical conductivity spectral weight transfer from low to high energies that is associated with asymmetry between electron and hole quasiparticles.

In our analysis of the electronic DHM system, we focus on the influence of two aspects of the model that have not been previously investigated to any great extent: the importance of the intersite-interorbital hybridization t_{01} and the influence of the metal-insulator transition on this two-orbital system. We find a complex relationship in the system dynamics arising from the interplay between hybridization, Mott physics and orbital relaxation.

We conclude in section 7.6 with a brief observation of the orbital selective Mott transition in the electronic DHM. This phenomenon, while not directly related to our primary interest in studying orbital relaxation, is nonetheless an interesting physical result and a noteworthy consequence of the conditions which support orbital relaxation in this model.

7.2 Quasiparticle Bands

In the single band Hubbard model an essential symmetry between holes and electrons is built into the bands and is evidenced by the $-2t\cos(k)$ dispersion of the non-interacting system. As discussed in chapter 2, it is observed in the four-site electronic DHM study [31] that electron orbital relaxation in response to local *non-zero* Coulomb repulsions gives rise to asymmetry between electrons and holes in strongly correlated electron systems. Despite the energy cost, charge carriers in the lower orbital access the higher energy orbital as an alternative quantum state in which to escape the penalty of double-occupancy.

The electron-hole asymmetry is evidenced by a reduced quasiparticle weight near the top of the lower band (the hole-carrier regime) compared with that at very low filling (the electron-carrier regime). This is a consequence of the orbital relaxation physics. For the proper tuning of system parameters, in particular non-zero t' and sufficiently large $\frac{U_0}{\epsilon_1}$ and $\frac{U_0}{U_1}$, Hirsch showed the onset of an effective attractive interaction (2.21) between quasiparticles indicative of hole pairing, as well as a lower effective hopping for holes than for electrons (*q.v.* figure 2.6).

Throughout Hirsch's study the nonlocal hybridization was fixed at the value of the intraband hoppings so that,

$$t_{01} = t_0 = t_1 \,. \tag{7.1}$$

As well, the Hilbert space was truncated to remove the contribution of states with greater than two electrons or net spin polarization on any lattice site.

While the balance of non-zero Coulomb repulsion plays a significant role in the asymmetry between hole and electron states (examined below), we emphasize (in contrast to [31]) that the essential differences are already present *in potentia* in the non-interacting band structure of the model. The asymmetry arises first of all from the effects of a non-zero t_{01}, and then secondarily through the contribution of finite onsite-hybridization t' and Coulomb repulsions. The electron-hole asymmetry in the DHM is therefore not only a local relaxation response of double-occupied electrons but is also a *nonlocal* effect: a bias present throughout the arguments of [31] due to (7.1).

In keeping with the results shown in figure 6.15, the hybridization assumption (7.1) is exactly the condition for maximum flattening in the hole regime of the band structure even in the non-interacting case, when ϵ_1 is sufficiently large to open a gap at half-filling. The curvature of the band energy ϵ_k is related to the effective mass m^* of the charge carriers in a metal by the relation,

$$m^* \propto \left[\frac{\partial^2 \epsilon_k}{\partial k^2}\right]^{-1} . \tag{7.2}$$

Effective mass differences are present in the one-dimensional chain for all values of ϵ_1, including zero, so long as t_{01} is non-zero, as seen in figure 7.1, comparing values of $t_{01} = 0.8$ and 1.0. The difference in curvature between the low-energy $k = 0$ point and the high-energy band edges is therefore strongly indicative of a latent electron-hole asymmetry in any two-orbital Hubbard model with non-zero intersite interorbital hybridization. The greatest amount of flattening is present, in fact, for a degenerate two-orbital model with $t_{01} = t_0 = t_1$. This is exactly the parameter set used by Hirsch in [31].

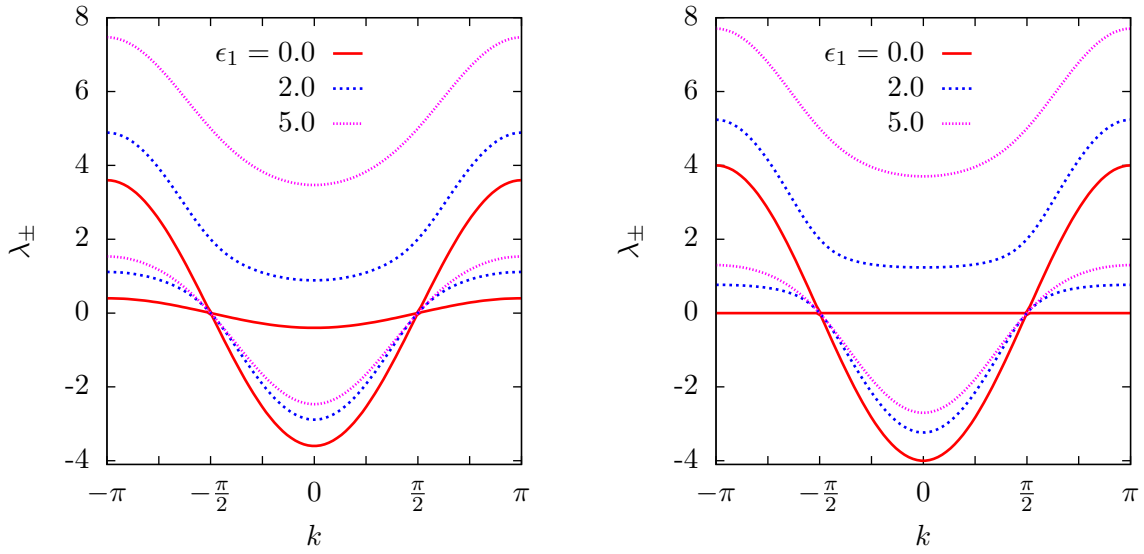

(a) $t_{01} = 0.8$ **(b)** $t_{01} = 1.0$

Figure 7.1: Dispersion of non-interacting DHM linear chain for different values of t_{01} and varying upper orbital energy ϵ_1. The effective mass asymmetry between electrons and holes is evident in the curvature difference at the centre (electrons) and edges (holes) of the lower band for all values of ϵ_1, so long as t_{01} is non-zero. As t_{01} is increased toward equality with the intra-orbital hopping values, $t_0 = t_1 = 1.0$, the asymmetry between electrons and holes increases. Four bath sites, $U_0 = U_1 = U_{01} = t' = 0.0$.

The electron-hole asymmetry can also be seen from the impurity model eigenvalue spectra of the non-interacting MODMFT Bethe lattice results, found by diagonalizing the Anderson impurity Hamiltonian (4.1).

Figure 7.2 shows the impurity site bands as a function of electron filling. The bands in the figure are hybridized only by $t' = 0.2$, with $t_{01} = 0.0$. The large interorbital energy gap, $\epsilon_1 = 12.0$, ensures that as chemical potential increases, lattice filling is predominantly in the lower orbitals. Total filling occurs exclusively in the lower quasiparticle band all the way up to $n = 2.0$, and in the upper band from $n = 2.0$ to 4.0. The eigenstate energy

spectrum is symmetrical about the half-filling of the lower band ($n = 1.0$). Where total filling is close to zero and quasiparticles are electron-like, the eigenvalue spectrum is the same as near the top of lower band filling (filling near 2.0), where charge carriers are holes.

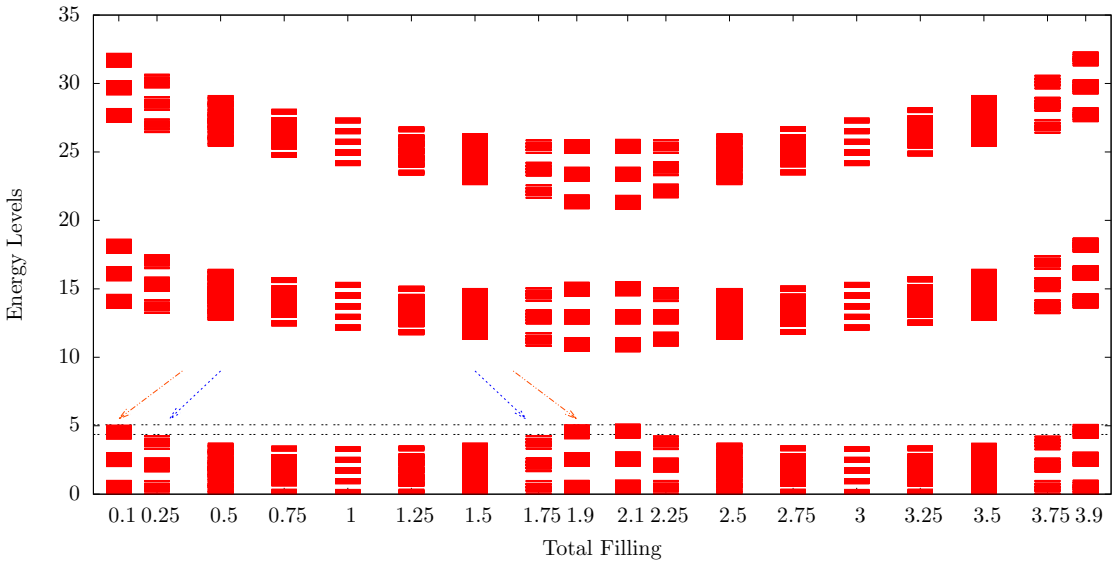

Figure 7.2: $t_{01} = 0.0$, $t' = 0.2$ impurity model eigenvalues for the non-interacting Bethe lattice solution, for various electron fillings of the impurity site. The horizontal lines and arrows are a guide to the eye, showing the symmetry of the lower band between electron filling 0.0 (empty lattice) and 2.0 (half-filled lattice, filled lower band). This symmetry demonstrates that in the absence of nonlocal hybridization t_{01}, even with non-zero onsite hybridization t', the non-interacting DHM treats electron and hole carriers on an equal footing. $\epsilon_1 = 12.0$, an extreme value, to provide a clear separation of the hybridized eigenvalue bands. The detailed structure is also dependent on the bath pseudosite energies.

For the same system with $t_{01} = 1.0$, figure 7.3, electron-hole asymmetry sets in, as seen in the difference in lower width of the lower impurity model eigenvalue band at fillings 0.1 and 1.9, or between fillings 0.25 and 1.75.

Figure 7.4(a) shows a similar eigenvalue spectrum from reference [31] for the four-site electronic DHM. While the parameter relationships are similar to those in figure 7.3 (including $t_{01} = 1.0$), figure 7.4(a) exhibits an apparent electron-hole *symmetry* around half-filling in the lower eigenvalue band. The difference in results is due to Hirsch's truncation of the Hilbert space. The impact of slightly weighted eigenstates of high electron filling is therefore of some consequence to the physics of the DHM.

Recalling that $U_0 = U_1 = U_{01} = 0.0$, and all other parameters are unchanged, it is clear that electron-hole asymmetry is already latent in the DHM before the dynamics of

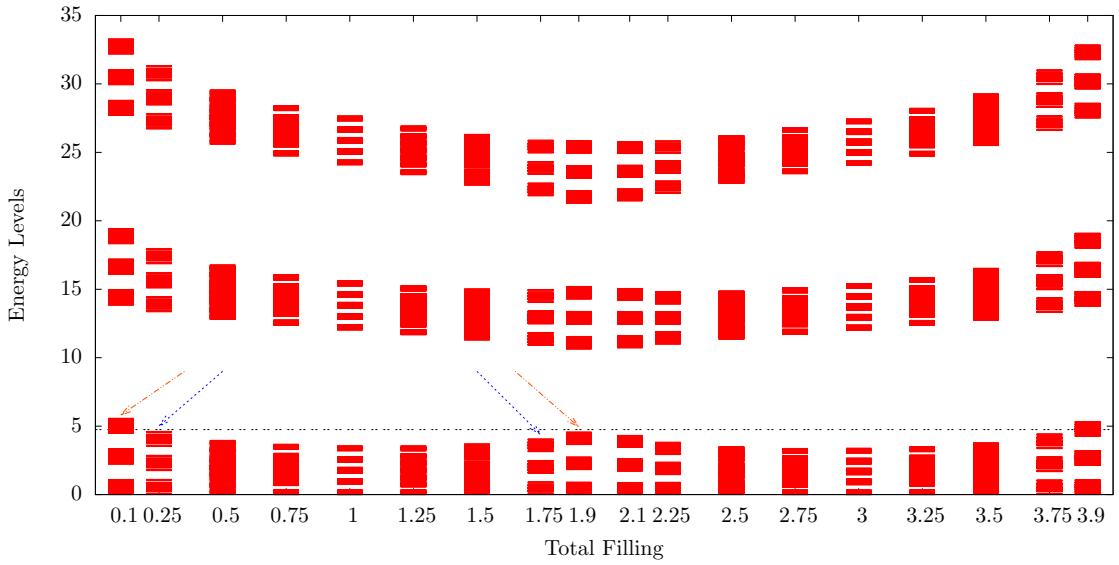

Figure 7.3: $t_{01} = 1.0$, $t' = 0.2$ impurity model eigenvalues for the non-interacting Bethe lattice MODMFT solution, for various electron fillings of the impurity site. Compare with figure 7.2. Arrows and reference line indicate the asymmetry between the electron-carrier region near the bottom of the band (total filling near zero), and the hole-carrier region at the top of the lower quasiparticle band (filling near 2.0).

orbital relaxation are introduced. This asymmetry should be present in any two-orbital Hubbard-like system where quasiparticles hybridize nonlocally between lattice sites, including systems with degenerate orbitals.

The interaction-driven orbital relaxation should serve to enhance the electron-hole asymmetry of the non-interacting DHM. Figure 7.4(b) illustrates this expectation through exaggerated values of the Coulomb repulsion and a large energy band gap $\epsilon_1 = 6.0$. The hybridization parameters are the same as in 7.4(a), $t_{01} = 1.0$ and $t' = 0.2$. The states in the band below the gap are those in which the Coulomb repulsion does not contribute significantly, and are therefore approximate solutions to the non-interacting electronic DHM Hamiltonian. As a comparison to this, and to better understand the important role of interactions, figure 7.5 shows the Bethe lattice MODMFT eigenvalue bands for a less extreme set of Coulomb repulsions (those chosen by Hirsch are ill-suited to MODMFT convergence due to very sharp filling transitions and extended insulating behaviour as a function of chemical potential). It is plotted against impurity site total filling with $t_{01} = 0.0$ thus showing the effect of strong Coulomb interactions on generating particle-hole asymmetry.

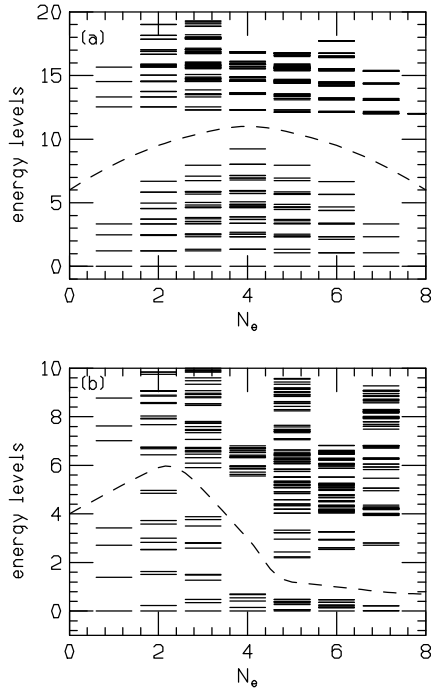

Figure 7.4: Energy eigenvalue spectra at various fillings from exact diagonalization of the four-site linear chain electronic DHM [31]. $t_{01} = 1.0$ and $t' = 0.2$. Eigenenergies are plotted according to the countable number of electrons N_e in the state, with $N_e = 8$ indicating a full four-site lattice, since the Hilbert space is truncated to eliminate states where any site holds more than two electrons. In (a) the system is non-interacting and the apparent electron-hole symmetry is artificially due to the Hilbert space truncation. In (b) the system is strongly interacting with $U_0 = 20.0$, $U_1 = 2.0$, $U_{01} = 12.0$ and $\epsilon_1 = 6.0$, introducing a clear asymmetry between one-electron ($N_\mathrm{e} = 1$) and one-hole ($N_\mathrm{e} = 7$) states. The lower band is comprised of states dominated by singly-occupied lattice sites, described approximately by the non-interacting DHM Hamiltonian. From [31] figure 4.

7.3 Quasiparticle Weight

An analysis of the quasiparticle weight provides particularly good insight into the claim of orbital relaxation in the DHM. For the four-site exact diagonalization, with a countable number of electrons on the lattice, Hirsch [31] defines the quasiparticle weight as a sum over the lattice sites, i,

$$Z_{\mathrm{H}\sigma}(N) = \sum_i \left(|\langle 0_{N-1} \, |c_{0i\sigma}| \, 0_N \rangle|^2 + |\langle 0_{N-1} \, |c_{1i\sigma}| \, 0_N \rangle|^2 \right) \tag{7.3}$$

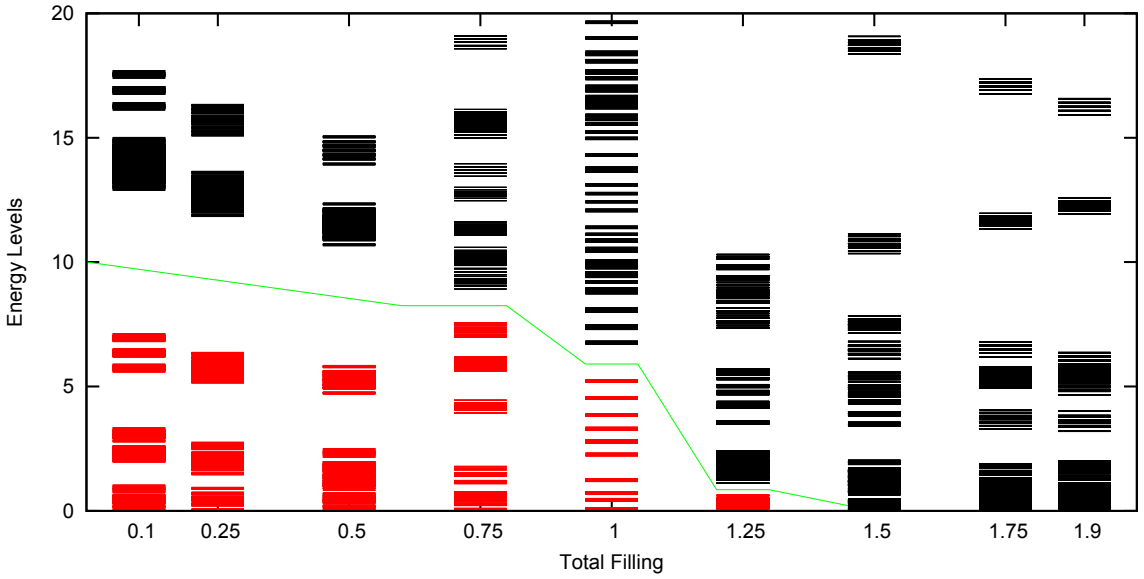

Figure 7.5: Energy eigenvalue spectra at various fillings from the MODMFT Bethe lattice solution, for comparison with figures 7.4(b) and 7.3. Here, the interaction parameters are less severe than in figure 7.4(b) by necessity, with $U_0 = 10.0$, $U_1 = 5.0$, $U_{01} = 6.0$ and $\epsilon_1 = 4.0$. $t_{01} = 0.0$ and $t' = 0.2$. Eigenenergies are plotted according to the average filling of the impurity. This graph shows the effect of Coulomb repulsion, without the presence of t_{01}, on the lower eigenvalue band which is comprised mainly of eigenstates with a small Coulomb contribution to the energy. The gap (shown with a line) signals the beginning of moderately interacting higher energy states. The band below the line has a narrowing trend from low to high filling, in agreement with figure 7.4(b). The Hilbert space used by Hirsch to produce figure 7.4(b) is truncated, as described in section 2.4, whereas here it is not. The larger Hilbert space and contribution of bath pseudosite energies to the eigenvalues complicate the plot considerably. Higher energy states are not shown, for clarity.

where $|0_N\rangle$ is the ground state eigenvector for the four site system with N electrons. The fraction of quasiparticle weight in lower and upper bands is given, respectively, by,

$$u_\sigma^2 = \frac{\sum_i |\langle 0_{N-1}\ |c_{0i\sigma}|\ 0_N\rangle|^2}{Z_{\mathrm{H}\sigma}(N)} \tag{7.4a}$$

$$v_\sigma^2 = \frac{\sum_i |\langle 0_{N-1}\ |c_{1i\sigma}|\ 0_N\rangle|^2}{Z_{\mathrm{H}\sigma}(N)}. \tag{7.4b}$$

In the single band limit, $v_\sigma^2 = 0$.

For ϵ_1 large, the bands are well-separated and the quasiparticle weight evolution can be clearly seen with respect to increasing interactions, which drive orbital relaxation in the hole-pairing interpretation of the DHM. In this limit, we expect the quasiparticle weight of the lower band to resemble that of the single band Hubbard model such that increasing the Coulomb repulsion, U_0, will produce a MIT at half-filling ($n_0 = 1$), and show electron-

hole symmetry between the empty and filled band states. At all Coulomb repulsions, the bottom of the lower band, $n_0 = 0$, and top, $n_0 = 2$, should have $Z_0 = 1$ as a small number of electron or hole carriers are lightly dressed and behave as nearly free particles. At intermediate fillings, interactions depress the quasiparticle weight toward zero due to Mott physics.

Hirsch considered this case of a large energy gap with $\epsilon_1 = 10.0$, reproduced in figure 7.6. For the non-interacting case, $U_0 = 0.0$, $Z = 1$ at all fillings, as expected. Due to the truncated Hilbert space, Mott physics does not drive the quasiparticle weight to zero at half-filling for the highest Coulomb repulsions, but close inspection suggests electron-hole asymmetry for all non-zero U_0, even for a large penalty on upper orbital occupation. For Hirsch's finite lattice, the asymmetry around half-filling in the lower orbital can be defined generally by the rule,

$$Z_{\mathrm{H}}(N_e) > Z_{\mathrm{H}}(2 - N_e) \tag{7.5}$$

where N_e is the band filling, determined by a countable number of electrons in the four-site lattice with maximum occupation $N_e = 8$. Hirsch provides the rule (7.5) as a consequence of the DHM having a higher energy orbital, believing it to describe "the physics of all electronic energy bands" so that "holes are *always* more dressed than electrons" (emphasis in original) [31].

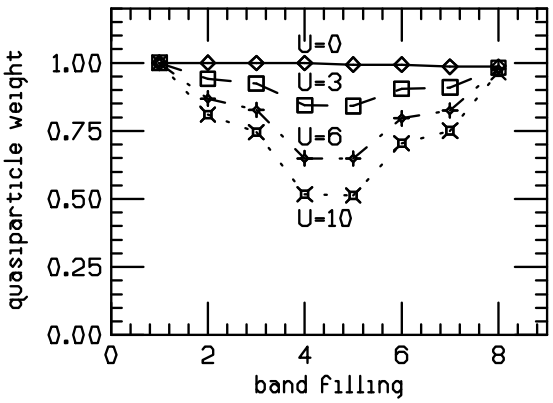

Figure 7.6: Quasiparticle weight versus band filling for the four-site DHM solution with truncated Hilbert space. Even for this large band gap, the asymmetry (7.5) in Z_{H} (7.3) between electron and hole states is small but noticeable. The variable U denotes our U_0. Solid line: $U_0 = U_{01} = U_1 = 0.0$. Dashed line: $U_0 = 3.0$, $U_{01} = 2.0$, $U_1 = 1.0$. Dash-dotted line: $U_0 = 6.0$, $U_{01} = 4.0$, $U_1 = 3.0$. Dotted line: $U_0 = 10.0$, $U_{01} = 6.0$, $U_1 = 5.0$. For all cases, $\epsilon_1 = 10.0$, $t' = 0.2$, $t_{01} = 1.0$. From [31], figure 5(a).

With the same parameter scale, our MODMFT study also demonstrates somewhat more clearly the onset of the electron-hole asymmetry on either side of the half-filled lower

band, in support of Hirsch's results. The asymmetry rule (7.5) can be stated more generally for the continuous filling spectrum of MODMFT as,

$$Z(n) > Z(2-n) \text{ for } n < 1 \tag{7.6}$$

where n is the total electron filling of the MODMFT impurity site.

In what follows it is important to note the full Hilbert space of our study allows for total filling up to $n = 4$, and the proper area of comparison to Hirsch's work is between the empty lattice at $n = 0$ and $n = 2$, the half-filled lattice. The asymmetry condition (7.5) is therefore relevant to the quasiparticle spectrum below and above quarter total filling, $n = 1$, or approximate half-filling in a dominant lower band.

We find that orbital relaxation is already creating asymmetry even for large ϵ_1, where it is driven by the presence of finite t_{01}, and is largely absent for $t_{01} = 0$ even when local hybridization t' persists. Recalling that in [31] $t_{01} = 1.0$ and $t' = 0.2$ in all cases, figure 7.7a shows the total electronic filling of the impurity site for the same parameters as in figure 7.6. As expected, the band gap at $n = 2$ from the large value of $\epsilon_1 = 10.0$ is common to all graphs. Increasing the lower orbital Coulomb repulsion leads to greater definition in the insulating Hubbard gap at $n = 1$, which should resolve into a definite MIT at this quarter filling value. The Mott physics evident in this figure is in contrast to its absence in Hirsch's work [31]. Due to the large interorbital energy gap, below half-filling of the impurity ($n = 2$) the upper orbital remains largely empty and the lower orbital increasingly fills and provides the dominant quasiparticle residue, Z_0. Above a critical chemical potential the upper orbital begins to fill and contributes to the quasiparticle identity of the system through Z_1.

We compare figure 7.7a with the case where $t_{01} = 0.0$ in figure 7.7b, finding very little difference due to the nonlocal hybridization. By contrast, in what follows the quasiparticle weight will be seen to be particularly responsive to t_{01}. We will focus our analysis on the lower orbital physics, which is of primary interest in the DHM as the dominant orbital normally favoured in electron occupation up to double occupancy.

It must first be remembered that the quasiparticle residue is appropriately defined under conditions (5.28), whereas the system can be characterized as non-Fermi liquid (NFL) [161] exhibiting what has been termed "bad metallic behaviour" [65] (also called a

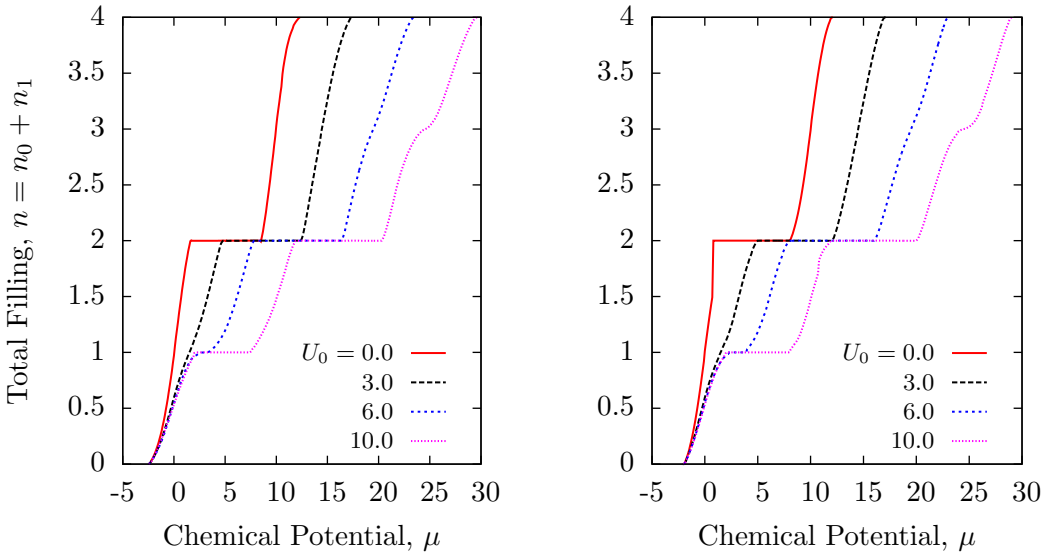

(a) $t_{01} = 1.0$ **(b)** $t_{01} = 0.0$

Figure 7.7: Impurity orbital filling versus chemical potential for MODMFT Bethe lattice DHM solution with full Hilbert space. System parameters are the same as figure 7.6, showing minimal effect of nonlocal hybridization t_{01}.

"quasi-insulator" [140])[1] where condition (5.28b) is violated as,

$$\Im\zeta_{\pm}(i\omega_n) < 0,\ \Im\zeta_{\pm}(i\omega_n) \text{ finite} \tag{7.7}$$

and thus is not yet diverging as in the insulating case. NFL behaviour in multiorbital systems is associated with non-zero local hybridization [62, 65, 139] and Hund's Coupling [161].

This NFL state will be associated with some finite quasiparticle weight at the Fermi energy in the band spectral density. In practice, in order to distinguish NFL behaviour from an insulating system where we cannot see a rapid divergence of the effective self energy at very low energy below the Matsubara resolution,

$$\Im\zeta_{\pm}(i\omega_n) \to \infty \text{ for } \omega_n < \omega_0 \tag{7.8}$$

[1]The distinction should be made that in these references the notion of NFL behaviour is ascribed to a finite value of the orbital self energies, $\Im\Sigma$, which we regard as only an approximate measure of the proper state of the hybridized system. It may be, then, that NFL phases identified in the literature through the self energy, itself, will appear to be FL or insulating if our "effective self energy" parameters $\zeta_{\pm}(i\omega_n)$ are employed instead.

we employ an approximate cutoff value where $|\Im\zeta_{\pm}(i\omega_n)| \approx 0.5\Re\zeta_{\pm}(i\omega_n)$, thus recognizing the (poor) metallic behaviour remaining for a potentially ambiguous, very small quasiparticle peak. This scenario, while subjective, is necessary for efficient large scale data analysis and occurs mainly in the presence of Mott physics.

A final caution is due with respect to an insulating band gap, where the self energy from a full band will be returned as uniformly zero, and thus its derivative at the Fermi energy will show, deceptively, a quasiparticle weight in keeping with free electrons. A plateau in the filling will provide evidence that the system is, in fact, insulating by virtue of a filled band and the quasiparticle weight, while apparently unity, is actually not defined in this region.

In comparison to the four-site DHM system of figure 7.6, the lower orbital quasiparticle weight Z_0 (5.29a) is shown in figure 7.8 for the MODMFT model. This is the case for the large energy gap, $\epsilon_1 = 10.0$. The lower orbital develops through a MIT at half-filling (quarter-filling of the entire impurity), and is nearly filled above $n = 2$, but not quite, yielding Fermi liquid behaviour as the upper orbital begins to fill.

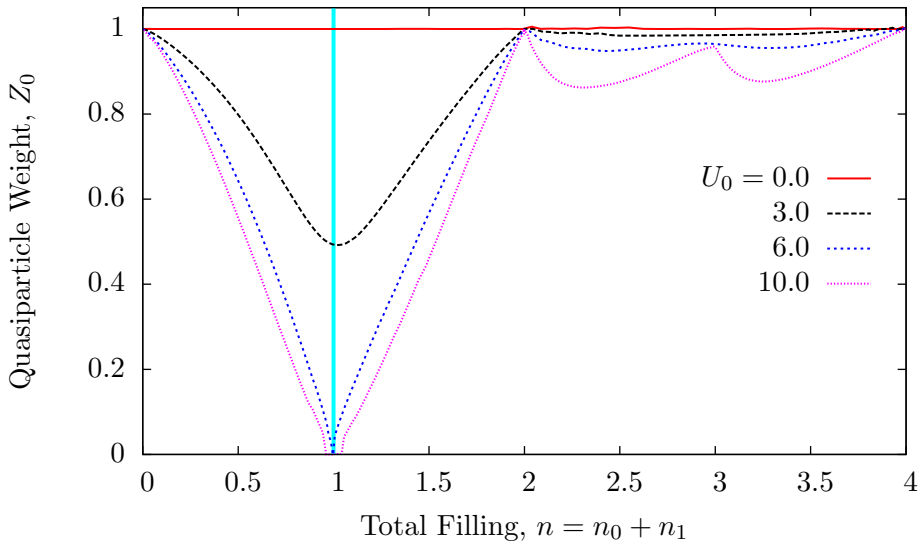

Figure 7.8: Lower orbital quasiparticle weight, Z_0, versus total band filling for the MODMFT Bethe lattice DHM solution. The lower orbital develops a Mott MIT at $n = 1$ for large U_0, and for all cases is nearly filled above $n = 2$ where it remains metallic with hole carriers. System parameters are the same as in figure 7.6, including nonlocal hybridization $t_{01} = 1.0$. The vertical line at $n = 1.0$ is the reference for electron-hole asymmetry in the lower band, using (7.6). The asymmetry is shown in a more obvious way for the case of $U_0 = 3.0$ in figure 7.9.

The electron-hole asymmetry in the lower orbital, defined by (7.6), can be evaluated

with respect to vertical reference line at $n = 1$, where even for this large energy gap there is asymmetry in the quasiparticle weight for $U_0 > 0.0$. The effect is more obvious than in the four-site result, figure 7.6.

The asymmetry is noticeable even for the smaller case of $U_0 = 3.0$, where the double occupancy penalty is less and thus the orbital relaxation effect is expected to be less obvious. Figure 7.9 shows the hole carrier side ($n > 1$) of the Z_0 curve reflected back across the half-filling line for the lower band.

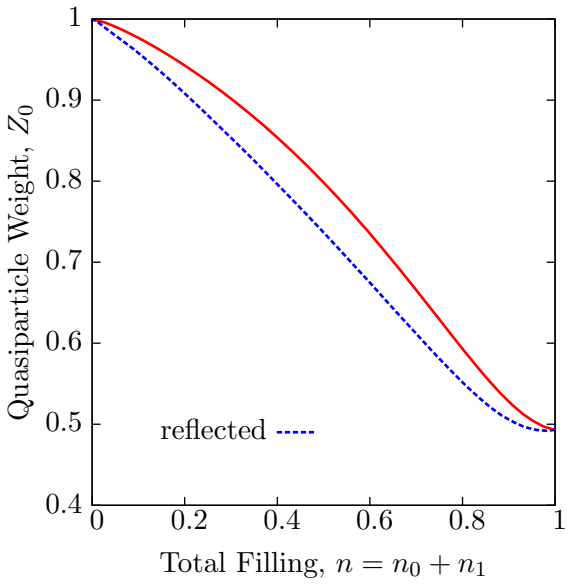

Figure 7.9: Lower orbital quasiparticle weight Z_0 for the $U_0 = 3.0$ case of figure 7.8. The quasiparticle weight for the filling range $1 < n < 2$ is reflected back across $n = 1$ to evaluate the electron-hole asymmetry arising from orbital relaxation when U_0 is small with hybridizations $t_{01} = 1.0$ and $t' = 0.2$.

The asymmetry in figure 7.9 is the combined effect of non-zero nonlocal and local hybridization values, $t_{01} = 1.0$ and $t' = 0.2$, respectively. The qualitative difference observed in the non-interacting system from these parameters (see section 6.6) prompts an investigation into their influence on this asymmetry in the interacting case, in order to identify what role they play in orbital relaxation.

Turning off the nonlocal hybridization t_{01}, and setting t' to a large value, $t' = 1.0$, for an otherwise identical system to that in figure 7.9, figure 7.10b demonstrates the lack of impact on the asymmetry from the local hybridization t', even for a large value of that parameter. By contrast, figure 7.10a reveals that t_{01} continues to produce an obvious asymmetry when it is the only hybridization acting on the system.

Increasing the local hybridization t' has a more complex effect on the asymmetry when

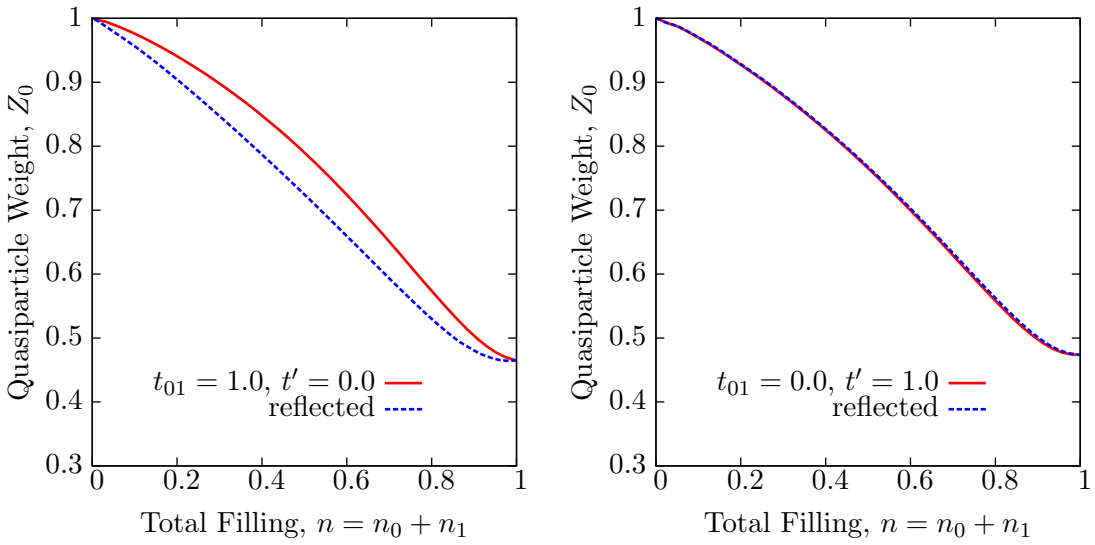

(a) Nonlocal hybridization. **(b)** Local hybridization.

Figure 7.10: A comparison of the effects of local and nonlocal hybridizations on the electron-hole asymmetry of the system in figure 7.8 where $U_0 = 3.0$. The plots show the lower orbital quasiparticle weight, with the states for filling $1 < n < 2$ reflected back over the quarter filling line, $n = 1$. (a) $t_{01} = 1.0$, $t' = 0.0$: the local hybridization has almost no effect on the electron-hole asymmetry, even for this large value. (b) $t_{01} = 0.0$, $t' = 1.0$: a noticeable asymmetry is present due to the nonlocal hybridization alone.

the lower orbital Coulomb repulsion and upper orbital energy are kept high ($U_0 = \epsilon_1 = 10.0$). In this case, the asymmetry is small and we see in figure 7.11 that large $t_{01} = 1.0$ yields a lowering of the quasiparticle weight on the hole side of $n = 1$, whereas a large value of the local hybridization, $t' = 1.0$, leads to a violation of the asymmetry rule (7.6). The quasiparticle weight on the hole side of a half-filled lower orbital is actually increased by the presence of substantial onsite hybridization, before the quasiparticles are again dressed as the band becomes full.

From figures 7.10 and 7.11 we make two observations about the role played by the hybridization parameters in the DHM.

First, in [31], Hirsch's assumption that "we do not expect the qualitative physics of the [DHM] model to depend on the particular choice for [t_{01}]" is a statement more readily applicable to the value of t'. The local hybridization value, $t' = 0.2$, used throughout [31] plays a secondary and small role in the asymmetry, while the nonlocal hybridization, $t_{01} = 1.0$, is predominantly and strongly responsible for orbital relaxation in conjunction with the Coulomb repulsions and orbital energy gap. This is not surprising, given the impact of t_{01} as the hybridization parameter responsible for altering the curvature of the

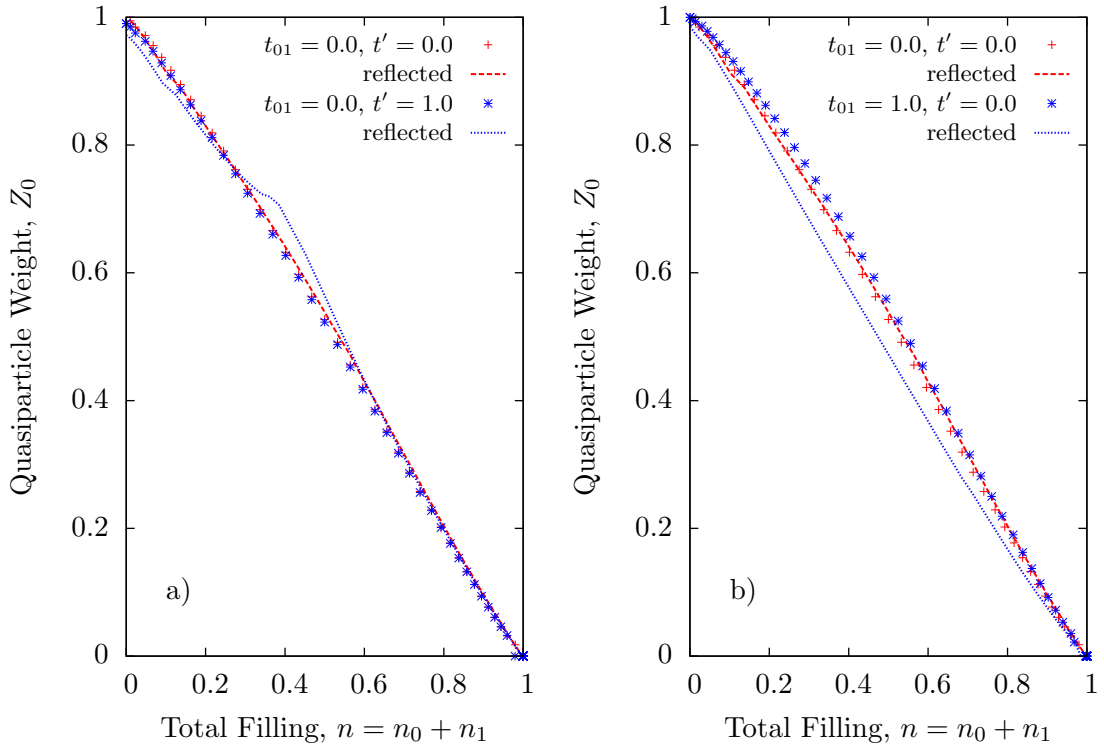

Figure 7.11: Reflection of Z_0 around $n = 1$, for the $U_0 = 10.0$ case in figure 7.8, comparing the non-hybridized case ($t_{01} = t' = 0.0$) with a) hybridization exclusively local (and large), and b) exclusively nonlocal hybridization of the usual size. The local hybridization case violates the general asymmetry rule (7.6), as the reflected Z_0 line is larger than the non-reflected line in the intermediate filling region.

non-interacting dispersion in figure 7.1.

Second, a large onsite hybridization mixes the singly and doubly occupied states of the impurity site to such a strong degree as to initially cause *undressing* of the quasiparticles before the quasiparticle weight again drops near half-filling. That this phenomenon does not arise for the case of large t_{01} reinforces the secondary role played by the local hybridization in the orbital relaxation physics of the DHM. That such strong onsite mixing is to be avoided is a point touched upon briefly, as well, by Hirsch in [31], with the consequences clarified here in figure 7.11.

We now move beyond the limit of large band gap by lowering ϵ_1 so that the doubly-occupied states in the lower band become energetically less favourable in comparison to states with one or even two electrons in the upper orbital. As expected, the phenomenon of electron-hole asymmetry and orbital relaxation becomes more pronounced as the Coulomb

repulsion U_0 is maintained at a high value.

A choice of system parameters which emphasize this physics, $U_0 = 10.0$, $U_{01} = 6.0$ and $U_1 = 5.0$, is used in figure 7.12 to show the change in quasiparticle weight $Z_{\rm H}$ as ϵ_1 is progressively lowered for Hirsch's four-site lattice problem [31]. The high energy case, $\epsilon_1 = 10.0$, is somewhat equivalent to a single band Hubbard model result, where the upper orbital is gapped out for low chemical potential, and the lower orbital has electron-hole symmetry. As the upper orbital energy decreases, it becomes energetically competitive. Double occupancy is avoided and quasiparticle holes are clearly dressed.

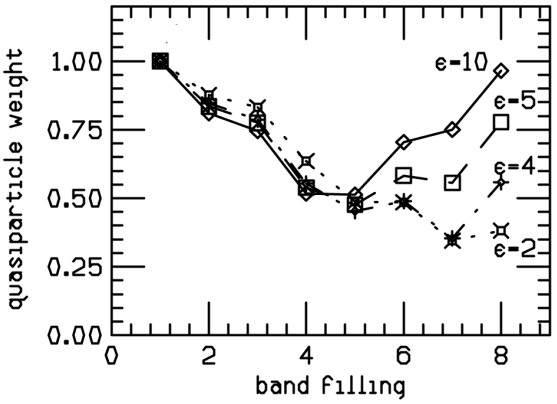

Figure 7.12: Quasiparticle weight $Z_{\rm H}$ versus band filling for the four-site ED DHM solution with truncated Hilbert space, as the orbital energy gap ϵ_1 (ϵ in the figure) is lowered. The lowering of $Z_{\rm H}$ as ϵ_1 increases demonstrates dressing of the quasiparticles, and clear electron-hole asymmetry between the left and right of band filling 4 (half-filling of the lower band). $U_0 = 10.0$, $U_{01} = 6.0$, $U_1 = 5.0$, $t_0 = t_1 = t_{01} = 1.0$, $t' = 0.2$. From [31], figure 6(a).

This effect of lowering ϵ_1 on Z_0 in our MODMFT Bethe lattice results is shown in figure 7.13 for the same set of parameters across the same region of filling. As the upper orbital becomes energetically more favourable for occupation towards impurity half-filling, there is dramatic dressing of the quasiparticles and strong electron-hole asymmetry. The strong competition between orbitals for the $\epsilon_1 = 2.0$ case leads to a second MIT at $n \approx 1.85$.

The individual orbital fillings, shown in figure 7.14, elucidate the mechanics of orbital relaxation shown in figure 7.13. As the upper orbital energy is reduced, electron occupation transfers from the lower to the increasingly competitive upper band. The dressing of quasiparticles (indicated by lowering of Z_0) is associated with this reduction in the lower orbital filling, n_0. For a nearly full band, $n_0 \approx 2$, the quasiparticles experience Fermi liquid renormalization. They become increasingly heavy, or dressed, as the filling drops toward $n_0 = 1$, where the conditions for Mott physics take over near $\epsilon_1 = 2.0$. The transfer of

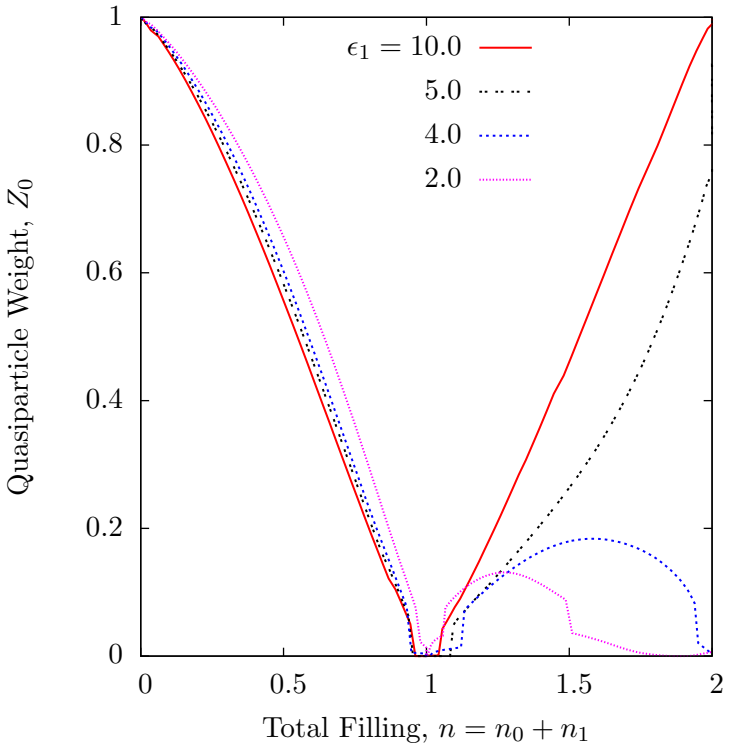

Figure 7.13: Lower orbital quasiparticle weight Z_0 versus total band filling for the MODMFT Bethe lattice DHM solution, in comparison to the four-site lattice results of figure 7.12. Electron-hole asymmetry is clear, with quasiparticle dressing on the hole side (near half-filling of the impurity orbital, $n = 2$) as the upper orbital energy ϵ_1 is lowered. The effects of orbital competition are readily apparent in the lowest energy case, $\epsilon_1 = 2.0$, where the lower orbital experiences a second MIT at $n \approx 1.85$. $U_0 = 10.0$, $U_{01} = 6.0$, $U_1 = 5.0$, $t_0 = t_1 = t_{01} = 1.0$, $t' = 0.2$.

charge density from lower to upper orbital in the presence of appropriate Coulomb penalties drives the quasiparticle dressing.

The particular case of $\epsilon_1 = 5.0$ in figure 7.13 involves an obvious dressing of holes, while the energy gap is large enough to maintain a dominant lower band at half-filling above the MIT range of $n_0 = 1.0$. Attending to this case, we can examine the role of hybridization as a critical element in the orbital relaxation physics of the DHM. The relative effects of the local (t') and nonlocal (t_{01}) hybridizations on Z_0 are mapped out in figure 7.15. The total electron filling is fixed at $n = 1.990$, very near to the right edges of figure 7.14, where in the single band limit it is expected that $Z_0 \approx 1.0$. It is notable that t_{01} has a greater influence on the quasiparticle weight than the local hybridization t', and for all values of t' increasing the nonlocal hybridization leads to dressing of the holes (lowering of Z_0). In contrast, the onsite hybridization tends to lower the quasiparticle weight up to some minimum around

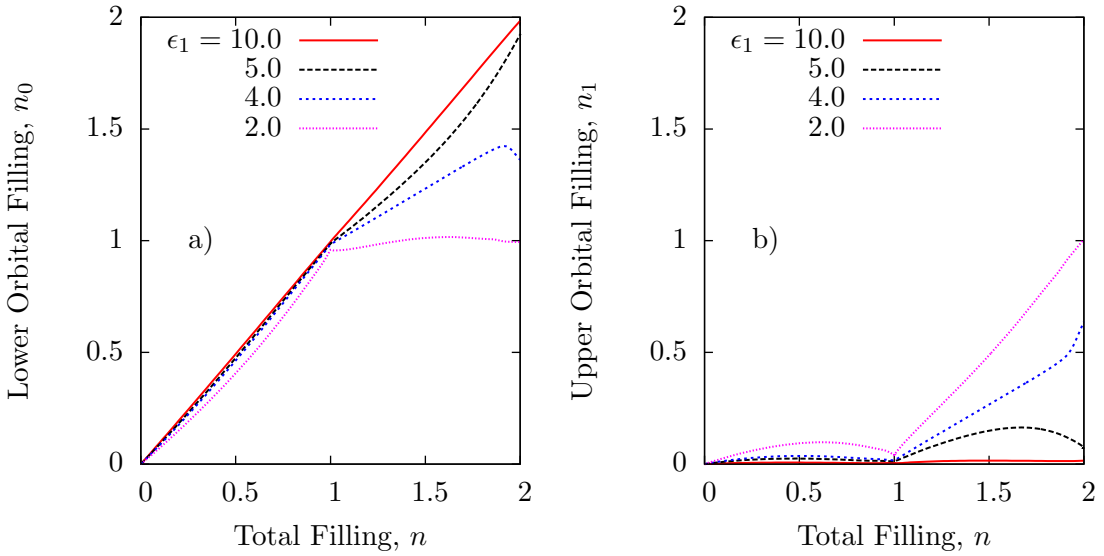

Figure 7.14: a) Lower orbital filling, n_0, and b) upper orbital filling, n_1, plotted against total filling of the impurity up to $n = 2$ for changing upper orbital energy, ϵ_1, for the same cases as in figure 7.13. The MIT at $n = 1$ corresponds to the lower orbital filling passing through $n_0 = 1$. At half-filling in the impurity, $n = 2$, a lowering of ϵ_1 is correlated with electrons occupying the upper rather than lower orbital. This reduces n_0 in a) from the Fermi liquid regime near the top of the band toward the Mott insulating region at half-filling ($n_0 = 1$, which occurs here for $\epsilon_1 = 2.0$).

$t' = 0.5$, and then cause mild undressing again toward $t' = 1.0$.

The influence of local hybridization affords the electrons the opportunity to avoid double occupancy without undergoing intraband transport, which would constitute the only energy-reducing degree of freedom available in the single band Hubbard model. In this two-band case of $\epsilon_1 = 5.0$, local hybridization immediately relieves the Coulomb repulsion through charge transfer to the upper orbital. Figure 7.16 shows the filling of the lower orbital for different values of hybridization. Lacking local hybridization, the electrons are predominantly doubly-occupying this orbital, but as t' increases, they lower their energy by charge density transfer to the upper orbital (rather than by hopping to the same orbital on neighbouring sites) and n_0 falls. This situation obtains across all values of t_{01}, since filling is a local measurement responsive to local hybridization. Comparing with the quasiparticle weight in figure 7.15, as n_0 falls in the direction of half-filling, Mott physics brings down Z_0 toward an insulating state.

The role of the nonlocal hybridization t_{01} in figure 7.15 is even more dramatic than that of t'. This is emphasized by its lack of impact on the lower orbital filling in figure 7.16. In that case, there is only a very small (though nonzero) response to increasing t_{01} as a limited

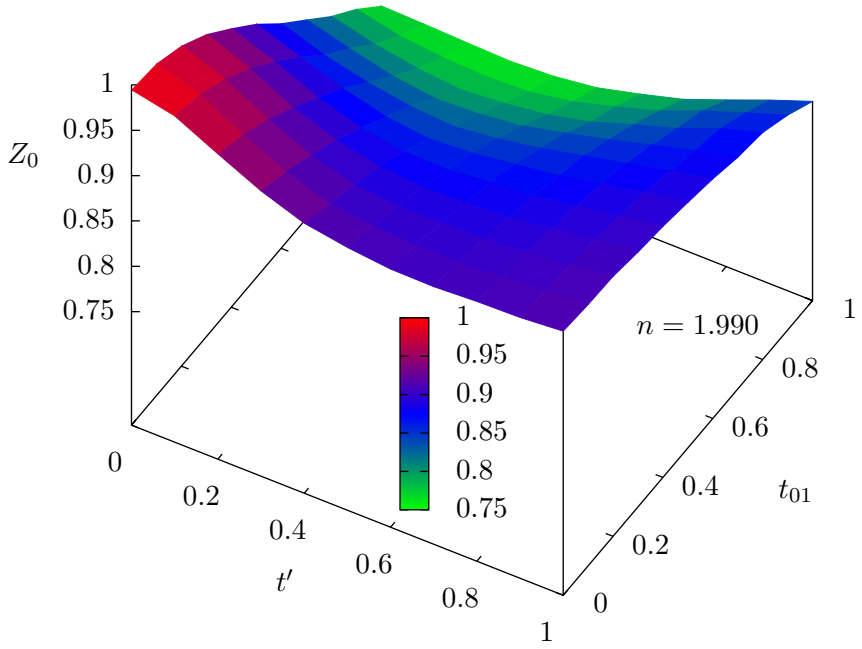

Figure 7.15: Lower orbital quasiparticle weight Z_0 at orbital filling $n = 1.990$ for the case of $\epsilon_1 = 5.0$ in figure 7.13, as a function of changing hybridization. For all values of the onsite hybridization t' held constant, increasing the nonlocal hybridization t_{01} leads to dressing of quasiparticles. This is especially obvious at low t', but is still apparent even at $t' = 1.0$. As t' increases it diminishes the dressing effect, and for all constant values of t_{01}, Z_0 has a minimum at roughly $t' = 0.5$, above which the increasing value of the local hybridization correlates with increased undressing of the quasiparticles.

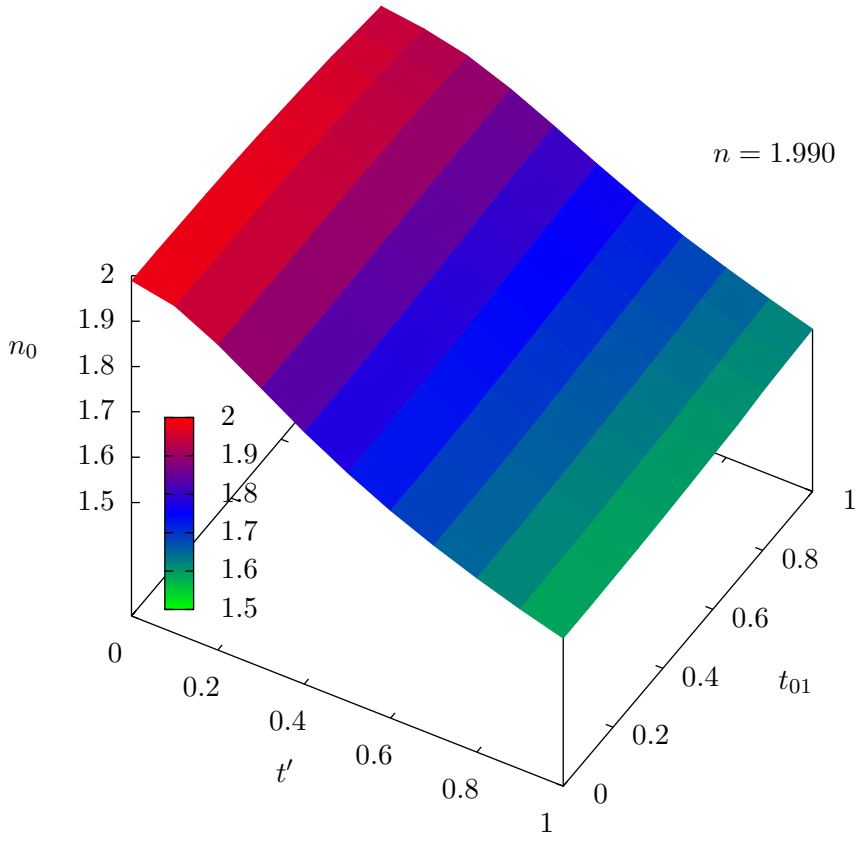

Figure 7.16: Lower orbital filling n_0 at orbital filling $n = 1.990$ for the case of $\epsilon_1 = 5.0$ in figure 7.13, as a function of changing hybridization. An increase in t' allows the orbital energy to drop via charge density transfer to the upper orbital, resulting in a reduction in n_0. The simple behaviour of the filling is in contrast to the more complex dependence of Z_0 on both hybridization parameters shown in figure 7.15.

concentration of electrons escape the Coulomb repulsion on the lower orbital by occupying the upper orbital via translation through the lattice. The effect of this small amount of intersite/interorbital charge transfer is too limited to have any significant impact on the Mott physics of the system, but is nonetheless more influential on the quasiparticle weight in figure 7.15 than that of the local hybridization.

The reason for this acute difference is that charge transfer through t_{01}, while slight, provides a finite secondary channel for electronic transport off the lower orbital which does not contribute to an increase in Z_0. Z_0 is related directly to the coherent part of the lower orbital Green's function $G_{00}^{\text{imp}}(z)$, which is a measure of the probability of electrons leaving the lower orbital, entering the bath, and returning to the lower orbital with frequency z. With a large value of cross-orbital hopping (t_{01}), electrons at the Fermi level may be energetically more likely to leave the lower band and not return, thus reducing Z_0 through the off-diagonal contribution of the Green's function matrix, $\hat{G}^{\text{imp}}(z)$.

However, any increase in electronic transport in the lattice should be reflected by a corresponding change in the kinetic energy. The lower orbital kinetic energy (K_0) map for the situation under consideration is shown in figure 7.17. In our model, K_0 is a measure of electrons traveling between the MODMFT lower orbital impurity site and the bath pseudosites as represented by the converged expectation value of the applicable term in the impurity Hamiltonian, equation (4.1),

$$\sum_{l\sigma} V_{0l}(b_{l\sigma}^{\dagger} c_{0\sigma} + c_{0\sigma}^{\dagger} b_{l\sigma}) \tag{7.9}$$

acting on the ground state eigenvector. It captures electron transport via both t_0 and t_{01}. For small onsite hybridization, a large value of t_{01} clearly decreases the lower orbital kinetic energy (*i.e.* increases the magnitude of the kinetic energy). Examining figure 7.15, this behaviour corresponds to an obvious reduction in Z_0. Note that this is the hybridization range employed in Hirsch's study, $t' = 0.2$ and $t_{01} = 1.0$.

For small t_{01}, the kinetic energy is virtually unaffected by changes in local hybridization, as expected, and where both are large it appears the impact of cross-orbital hopping is much reduced as the local hybridization is already transferring charge carrier density into the upper band (as seen in figure 7.16), making it less attractive as a destination for "off-diagonal" electron translation.

In summary, for the parameters of the DHM system currently under consideration, the effect of the local hybridization on quasiparticle dressing is closely tied to Mott physics as the lower orbital filling responds to charge transfer. The influence of the nonlocal hybridization, however, is even greater and tends to lower the quasiparticle weight not

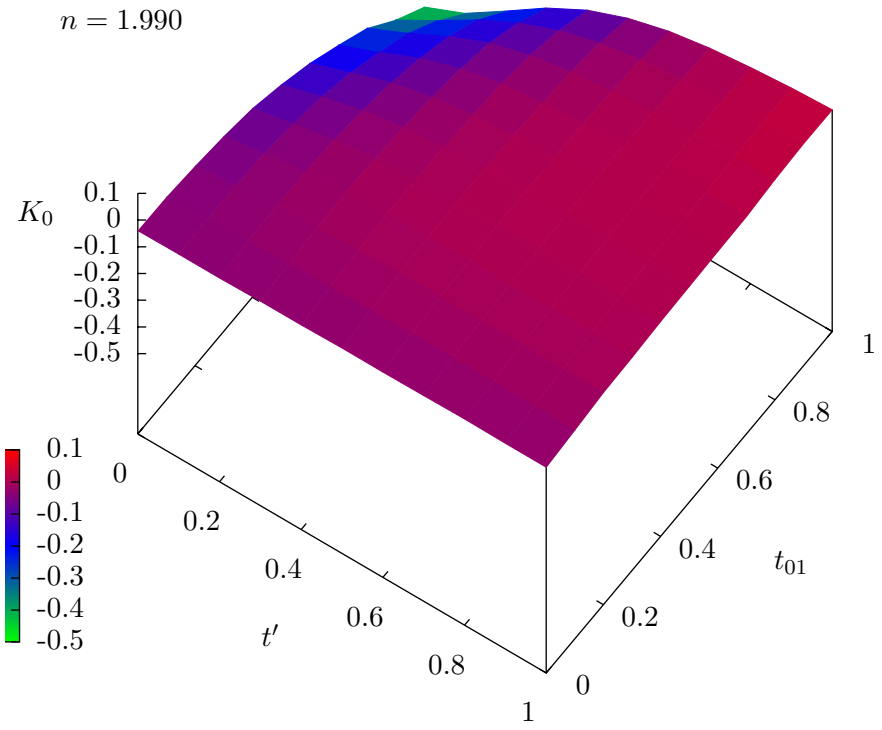

Figure 7.17: Lower orbital kinetic energy K_0 at orbital filling $n = 1.990$ for $\epsilon_1 = 5.0$ case of figure 7.13, as a function of changing hybridization.

through Mott physics but rather by providing an interband channel for electron transport off the lower orbital. For this set of parameters, therefore, the two hybridizations cause quasiparticle dressing in the lower energy band for very different reasons.

With respect to the quasiparticle weight, therefore, there is a somewhat complicated interplay in this system between three factors: 1) local hybridization which dresses the quasiparticles through non-kinetic charge density transfer between orbitals; 2) the lowering of Z_0 that arises from increased nonlocal hybridization, where the kinetic energy is simultaneously enhanced; and 3) Mott physics which tends to lower Z_0 as $n_0 \to 1.0$, arising under certain conditions as an indirect consequence of the interorbital charge density transfer of the hybridization, especially when the impurity orbitals are energetically similar (*i.e.* $\epsilon_1 \approx \epsilon_0$).

The importance of Mott physics in the behaviour of the quasiparticle weight can be seen from a different perspective for a lower range of Coulomb repulsions. In contrast to figure 7.14, in a regime with $U_0 = 3.0$, $U_{01} = 2.0$ and $U_1 = 1.0$, quasiparticle dressing appears not to persist in the hole regime for decreasing ϵ_1. Rather, as seen in figure 7.18, the holes become undressed as the upper orbital becomes increasingly energetically favourable.[2]

We explain the undressing behaviour in figure 7.18 as arising from the same tendency toward Mott physics as in the case of the larger Coulomb repulsion—but with the reverse effect. In the presence of the small, roughly comparable intra-orbital Coulomb repulsions, as ϵ_1 falls the system increasingly resembles the limit of two energetically degenerate single band orbitals. Normally, a filled single band where $n = 2$ would have fully undressed quasiparticle holes, but in this double orbital case the filling near $n = 2$ is more equally shared between orbitals.

Figure 7.19 shows that the suppressed value of Z_0 for $\epsilon_1 = 0.8$ and 1.0 in figure 7.18 is a consequence of the lower orbital sitting at about half-filling, $n_0 = 1$, and approaching a Mott insulating transition. As the energy gap is lowered, the electrons increasingly favour the upper orbital and the lower band moves away from half-filling to become more metallic: the quasiparticles undress as upper orbital energy decreases.

The hybridization effects on this system are shown in figure 7.20 for the case of $\epsilon_1 = 0.4$. The asymmetry caused by the difference in the Coulomb repulsions is present in the non-

[2]The parameters for this system satisfy the energy ordering requirement of (2.17), so long as $\epsilon_1 < 1.0$, which causes double occupancy of the lower orbital to be the energetically least favourable state, and double occupancy of the upper orbital the most favourable. However, the scale ordering, (2.18), where $t_0 << \epsilon_1$ is not observed in this case, thus violating the physical dynamics proposed by Hirsch for the DHM which ensure that electronic reorganization of the local orbital occupation proceeds on a shorter timescale than electronic delocalization via intersite hopping [40]

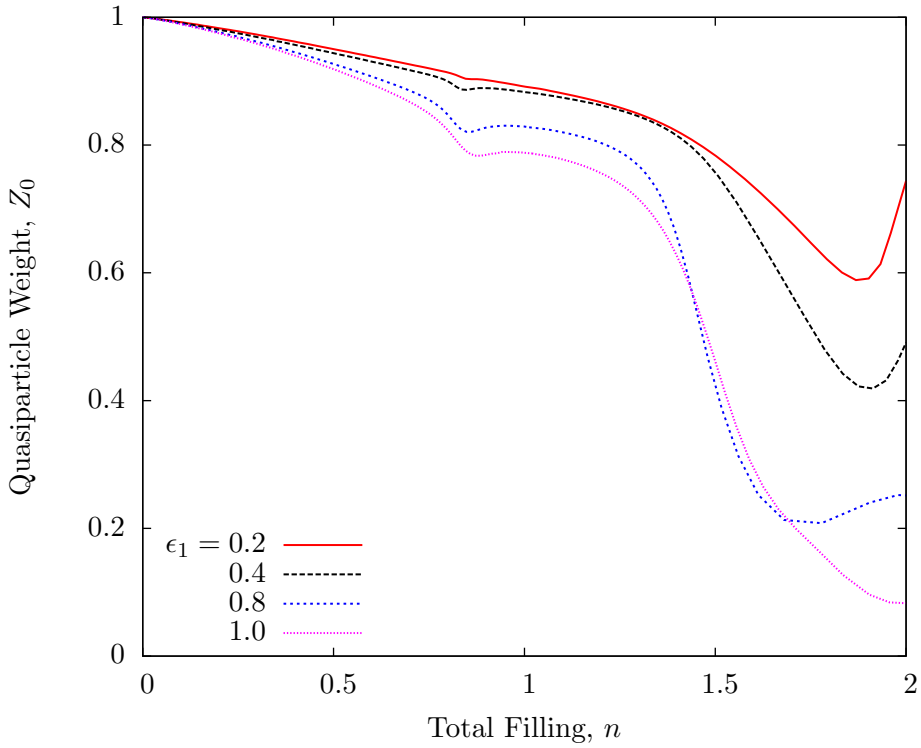

Figure 7.18: Lower orbital quasiparticle weight Z_0 plotted up to half-filling in the impurity site, for changing upper orbital energy ϵ_1 with reduced Coulomb interaction values: $U_0 = 3.0$, $U_{01} = 2.0$, $U_1 = 1.0$. In contrast to the case of figure 7.13 where $U_0 = 10.0$, here the quasiparticles experience *undressing* as the energy gap between the orbitals narrows. $t_{01} = 1.0$, $t' = 0.2$.

hybridized system, and a non-zero value of the local hybridization t', alone, tends to override this, moving the quasiparticle weight up. From the non-interacting results of section 6.6, we know that t' accentuates the band gap while mixing the orbital identity of the electrons. Here, they are promoted out of the lower orbital, driving n_0 away from orbital half-filling and the MIT, increasing Z_0. The figure also shows, however, that an increase in the nonlocal hybridization t_{01} dresses the holes thus enhancing the asymmetry. In fact, it is redirecting electron tunneling from the intraband channel (from which Z_0 acquires its definition), to the interband hybridization/hopping channel thus reducing the quasiparticle weight in the lower band.

The opposite trends in quasiparticle weight exhibited in these two cases (with $U_0 = 10.0$ and $U_0 = 3.0$) demonstrates the critical importance of Mott physics on the electronic DHM system. Charge density transfer from the lower to upper orbital with decreasing ϵ_1 can promote quasiparticle dressing in the case where the lower orbital is already energetically

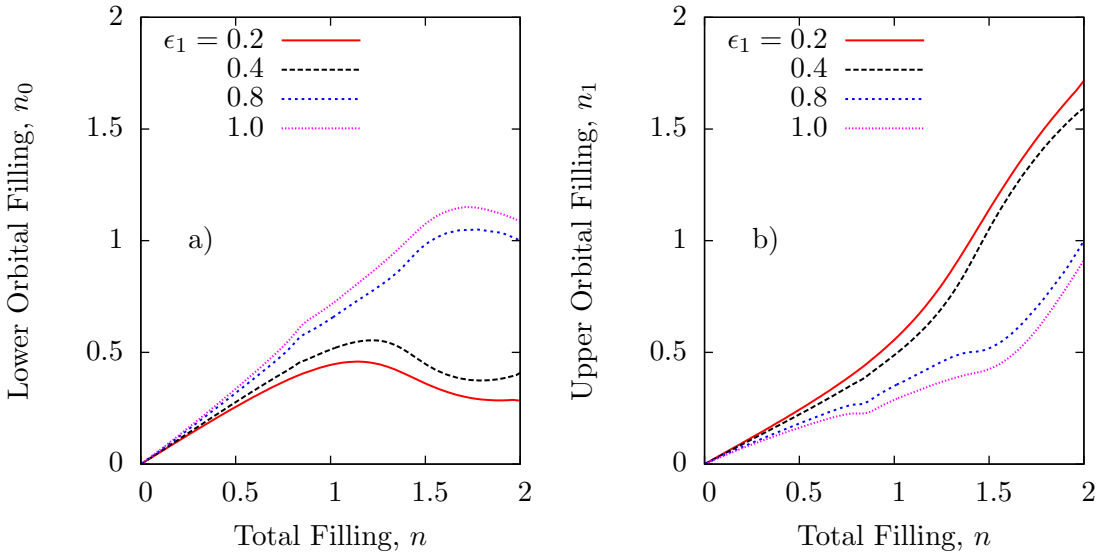

Figure 7.19: a) Lower orbital filling, n_0, and b) upper orbital filling, n_1, plotted against total filling of the impurity up to $n = 2$ for changing upper orbital energy, ϵ_1. The cases with a larger energy gap are near half-filled in the lower orbital, driving the band toward a Mott insulating state and thus low quasiparticle weight, Z_0, in figure 7.18. $U_0 = 3.0$, $U_{01} = 2.0$, $U_1 = 1.0$, $t_{01} = 1.0$, $t' = 0.2$.

dominant (and $n_0 > 1$), or undressing where the orbitals are more similar and $n_0 < 1$. The phenomenon of orbital relaxation therefore leads to very different consequences for the coherence of hole carriers depending on this condition.

In summary, we have found that the physics of orbital relaxation in the DHM is present even in the case of large orbital separation, where it is primarily caused by the nonlocal hybridization t_{01}. Two mechanisms drive quasiparticle dressing as they relax to escape the penalty of Coulomb repulsion. The first is the nonlocal hybridization t_{01} offering an intersite/interorbital channel for charge transfer off the lower orbital, which simultaneously increases the magnitude of kinetic energy and decreases the lower orbital quasiparticle weight Z_0. The second is the local hybridization t' driving charge transfer to the upper orbital, thereby depleting the lower orbital toward half-filling. This invokes Mott physics which dresses the quasiparticles as the lower orbital moves toward an insulating state. For large enough Coulomb repulsion, the system may even experience a MIT caused by hybridization, strictly a multiorbital phenomenon. We have also shown, however, that t' may lead to undressing of holes for a system where the orbital energies are close in value or where t' is very large. In this case, quasiparticle undressing occurs only through the mechanism of t_{01}. This contrasts with Hirsch's expectations for the general behaviour of the

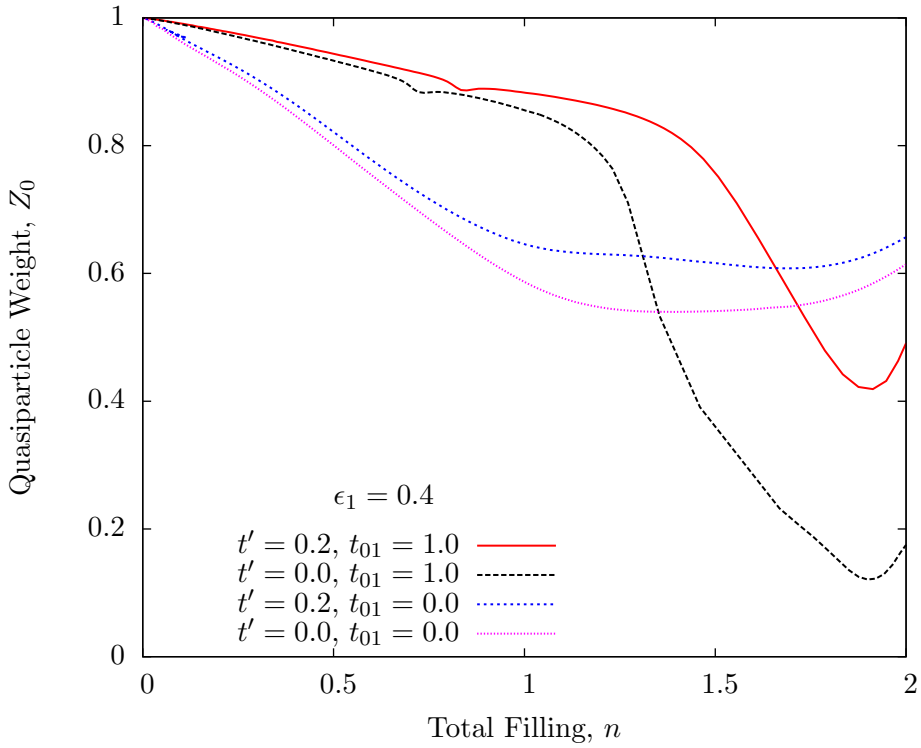

Figure 7.20: For the system in figure 7.18 with $\epsilon_1 = 0.4$, the quasiparticle dressing of the lower orbital weight, Z_0, is strongly dependent on the hybridization strengths. Although the system is tending toward the single band limit, the non-hybridized case exhibits some inherent asymmetry at half-filling ($n = 2$) due to the uneven Coulomb repulsions between orbitals. With only $t_{01} = 1.0$, the quasiparticles are strongly dressed compared to this non-hybridized case, whereas the effect of local hybridization alone t', tends to mix the electron identity between orbitals, strongly opposing this effect. The nonlocal hybridization, t_{01}, seems to do the opposite, suppressing hole mobility. In fact, it provides an alternative channel for quasiparticle tunneling between sites, which the holes take advantage of when the orbital energies are small enough. This effectively reduces the quasiparticle weight of the lower orbital, which measures intraband transport.

DHM, that the local hybridization is the most important parameter in orbital relaxation physics, and that holes should always be more dressed than electrons according to (7.5).

7.4 Band Flattening and the Hirsch Model

A note is due on the dispersion-flattening effect of the nonlocal hybridization t_{01}, observed clearly in the non-interacting solution to the DHM Hamiltonian illustrated in figures 6.15, 6.16 and 7.1.

Experimental evidence from cuprates [166, 167] suggests a correlation between high-T_c superconductivity and band flattening from Van Hove singularities in the DOS near the Fermi energy [168,169]. Theoretical work on extended-hopping Hubbard models [168,169], the periodic Anderson model [170], as well as sub-lattice graphene geometries [171], have suggested a connection between Van Hove singularities and band flattening attributable to secondary hopping parameters which affect the non-interacting dispersion in a way very similar to the influence of nonlocal hybridization.

We have shown that the nonlocal hybridization parameter in the electronic DHM (2.15) serves both as a generator of band flattening in the non-interacting dispersion, and in the preceding section 7.3 that non-zero t_{01} has a significant influence on quasiparticle dressing and undressing in conjunction with Coulomb repulsion. Thus, an emphasis on nonlocal hybridization in the electronic DHM should be an important consideration in the phenomenon of orbital relaxation as it relates to the Hirsch model of hole-pairing driven superconductivity (*q.v.* section 2.5).

7.5 Optical Conductivity

The optical conductivity provides another window on the physics of orbital relaxation, as the dressing of quasiparticles with increased electron filling prompts the transfer of spectral weight from the low frequency Drude peak to higher frequencies in the spectrum. Here we demonstrate that this phenomenon, which is observed by Hirsch in his DHM exact diagonalization study [31] and by Bach *et al.* in a two-site DMFT study [51] of the auxiliary spin dynamic Hubbard model (*q.v.* section 2.3), also appears within the framework of our MODMFT study. We also examine the influence of the hybridization parameters on the optical conductivity within a parameter set that is conducive to orbital relaxation.

In section 5.4 we described the challenge of defining the optical conductivity (5.42) for the multiorbital infinitely-connected Bethe lattice, and in section 5.1 we demonstrated our technique for determining the real frequency momentum-resolved spectral function, a

necessary step in determining conductivity. Keeping in mind the difficulties and *caveats* involved in those discussions, we have employed the simpler hypercubic form (5.33) of the optical conductivity in the following analysis, since it is both qualitatively and quantitatively very similar to the results from the Chattopadhyay form (5.38).

For reference, the optical conductivity of the non-interacting system is shown in figure 7.21 for various hybridization values. The two curves in each plot are for quasiparticle filling $n = 0.1$ (the electron case) and $n = 1.9$ (the hole carrier case). The upper orbital energy is $\epsilon_1 = 4.0$ and five bath sites are employed.[3] The plot is a set of Lorentzian-broadened delta functions with $\eta = 0.1$, and the extent of the low frequency Drude peak can be clearly seen. The effect of different hybridizations is very small, but nonetheless noticeable for non-zero t_{01}.

In figure 7.22 we introduce finite Coulomb repulsion values of $U_0 = 10.0$, $U_{01} = 5.0$ and $U_1 = 0.5$ which privilege double occupancy in the upper orbital with $\epsilon_1 = 4.0$. We compare the conductivity for different hybridization values between the electron-carrier ($n = 0.1$) and hole-carrier ($n = 1.9$) regimes, as electron occupation becomes somewhat more inclined toward the upper orbital near overall electron half-filling ($n = 2$). There is a clear transfer of spectral weight from the low energy Drude peak to higher frequencies for increased n. This agrees with the results of Hirsch's study [31] (as well as two-site DMFT applied to auxiliary spin DHM [51]), where it is further determined (using a countable number of electrons and holes) that the advent of hole-pairing near $n = 2$ will reverse this trend, as paired quasiparticles undress (*q.v.* section 2.5). Since we employ an impurity model where the bath does not represent physical lattice sites, we are unable to verify this observation which relies on a finite lattice model with a countable number of electrons distributed on the lattice sites.

The low energy Drude weight in figure 7.22 is reduced not only by transfer to higher energies, but also by the Mott physics associated with half-filling in the dominant lower orbital. The value of n_0 approaches or retreats from unity under the influence of the hybridizations parameters, t' and t_{01}, as illustrated and discussed in section 7.3, thus affecting the conductivity spectral weight near $\omega = 0$. The behaviour of this response function is in agreement with the complicated quasiparticle weight response to the local and nonlocal hybridizations.

The transfer of spectral weight from low to high energy is suppressed as the upper orbital energy increases and its contribution through orbital relaxation is effectively removed.

[3] The non-interacting optical conductivity can be determined analytically without recourse to the DMFT procedure. We have employed MODMFT and the impurity model with five bath sites here for the purpose of direct comparison to the interacting results in figures 7.22 and 7.23. In figure 6.19 we demonstrated the agreement between the analytical and MODMFT optical conductivity results in the non-interacting limit.

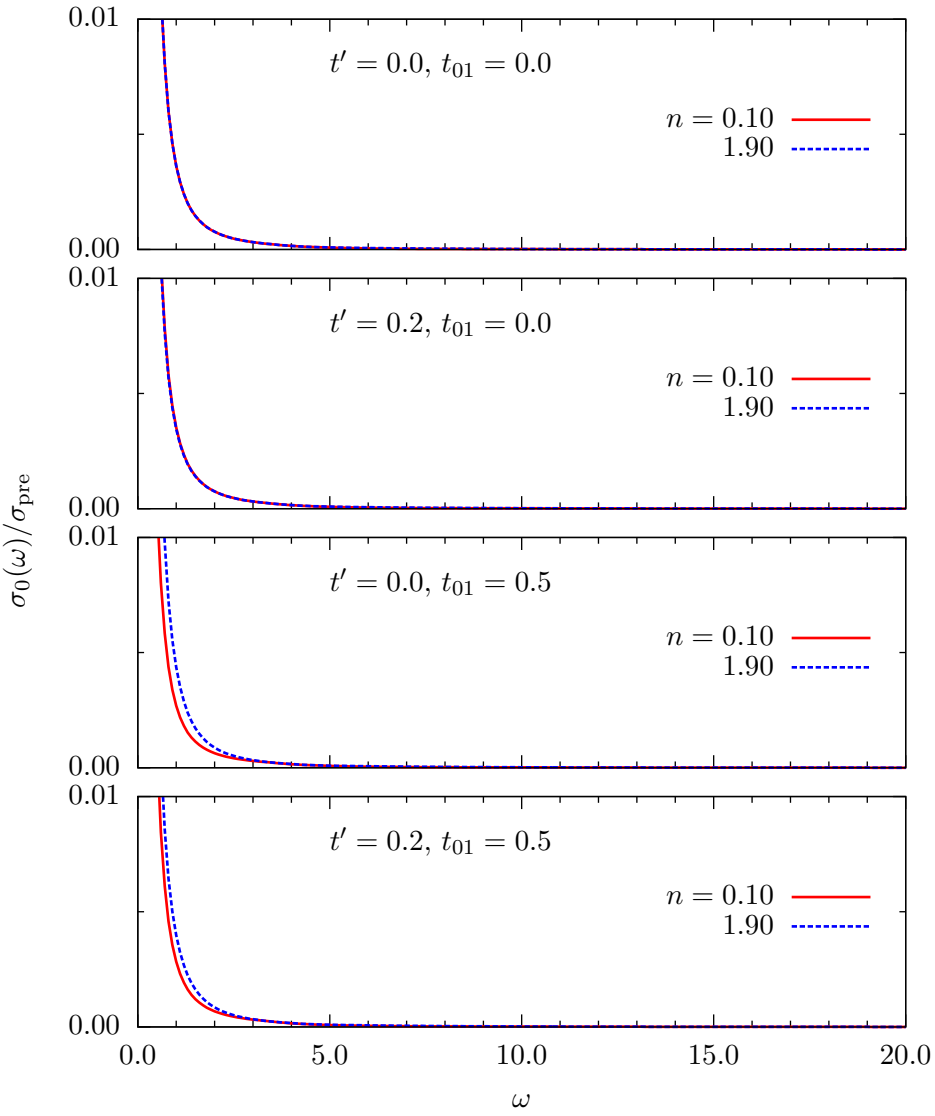

Figure 7.21: Optical conductivity $\sigma(\omega)$ for the non-interacting impurity ($U_0 = U_{01} = U_1 = 0.0$) with $\epsilon_1 = 4.0$, comparing the electron quasiparticle regime ($n = 0.10$) and hole-carrier regime ($n = 1.90$) for different hybridization values. The shape of the low frequency Drude peak is only slightly affected by the hybridization parameters. There is a stronger response to the nonlocal hybridization t_{01}. Lorentzian broadening of $\eta = 0.1$; an impurity model with five bath sites is used for consistency with the interacting results. $\sigma_{\rm pre}$ is the prefactor (5.35).

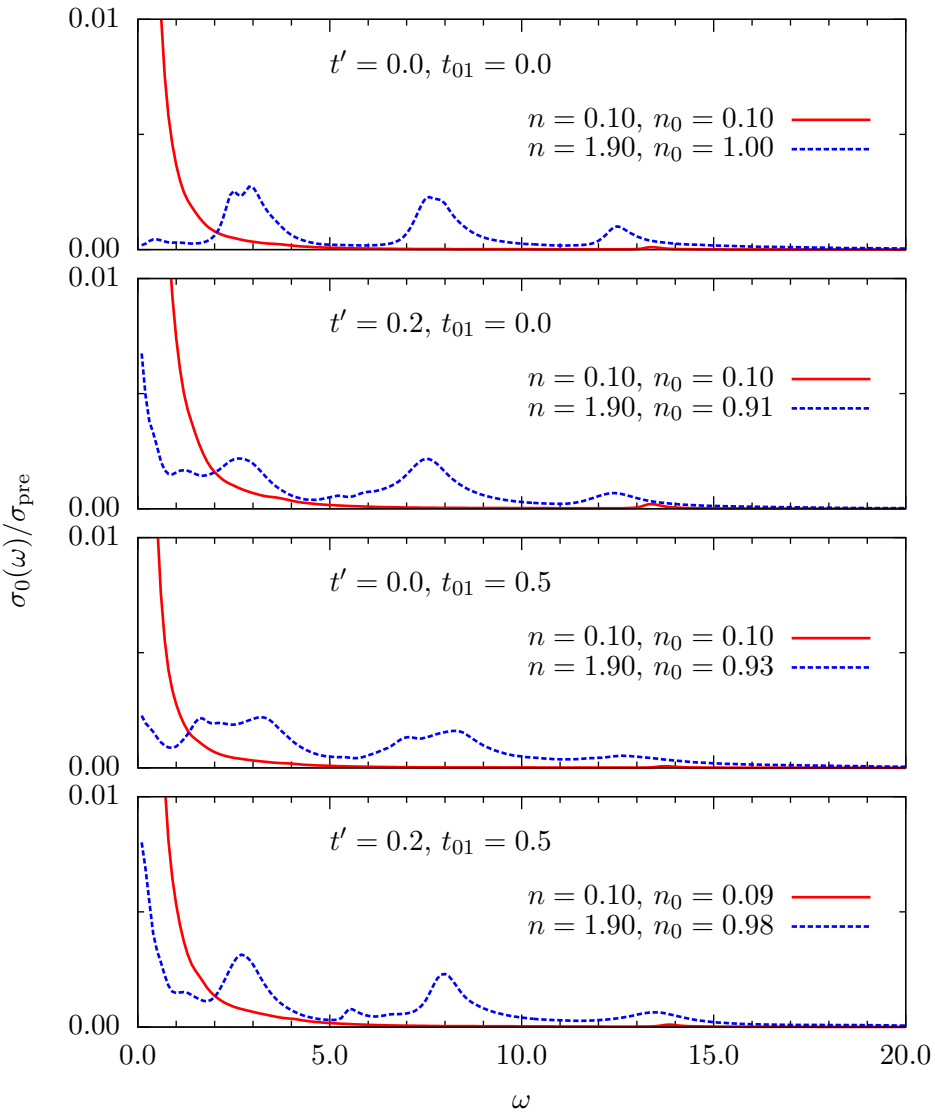

Figure 7.22: Transfer of optical conductivity $\sigma(\omega)$ spectral weight from low to high frequency, comparing the electron quasiparticle regime ($n = 0.10$) and hole-carrier regime ($n = 1.90$), for different hybridization values. Much of the low frequency Drude weight (*c.f.* figure 7.21) is transferred to higher energy structure in the hole regime. The remainder of the Drude peak is affected by Mott physics as the dominant lower orbital weight is adjusted relative to $n_0 = 1.0$ by the hybridization parameters. The parameters are chosen to fall withing the DHM ordering criteria for orbital relaxation (2.17) so that, $U_0 = 10.0$, $U_{01} = 5.0$, $U_1 = 0.5$, $\epsilon_1 = 4.0$. Lorentzian broadening of $\eta = 0.1$, five bath sites.

Under these circumstances we expect the higher energy features at filling $n = 1.9$ in figure 7.22 to be absent, but also that the hybridization will have almost no influence on the conductivity since electrons will prefer to remain in the lower orbital even at high filling. Quasiparticles should have metallic character at fillings $n = 0.1$ and $n = 1.9$, being well-separated in the lattice and behaving like free particles. In figure 7.23, both of these expectations are met. In this plot all the Coulomb repulsion values are the same as in figure 7.22 but the upper orbital energy has been doubled to $\epsilon_1 = 8.0$, creating an effective single band system. The contrast demonstrates that dramatic influence on the conductivity under positive conditions for orbital relaxation.

7.6 Orbital Selective Mott Transition

We conclude our results with a brief look at the development of orbital selective Mott transitions (OSMTs) in the electronic DHM. While OSMTs are not directly related to our comparison of orbital relaxation results in Hirsch's study[4], the system parameters which emphasize that physics in the DHM also provide a conducive environment to analyze OSMTs, where electrons undergo phase transitions between metallic and insulating states according to their occupation of inequivalent orbitals. Several studies [172–175] on multiorbital systems have shown that, not surprisingly, inequivalence between bands leads to orbital-specific behaviour at critical fillings. Theoretical work on OSMTs was stimulated by experimental observation [176] of a localized magnetic moment co-existing with a metallic system at a critical doping in the phase diagram of $Ca_{2-x}Sr_xRuO_4$, interpreted as a simultaneous existence of distinct phases in different electronic orbitals [177, 178].

Orbital inequivalence leading to OSMTs has most often been generated for locally hybridized degenerate two-orbital systems using different bandwidths along with Hund's exchange coupling [63, 65, 173, 175, 178–180]. With the addition of orbital hybridization, an orbital-selective phase persists throughout a range of small t', and is associated with non-Fermi liquid behaviour [65].

Nonlocal hybridization effects (for next-nearest neighbour hybridization of a particular lattice geometry, in the absence of local t') were studied in the two-orbital system with small band gap in [140], showing the disappearance of spin-polarized phases which occur in the otherwise non-hybridized system.

As the characteristics of two-orbital systems with *both* local and nonlocal hybridization

[4]This is due, in particular, to the fact that Hirsch's truncated Hilbert space eliminates the possibility of MITs in his system. With a full Hilbert space, it is certainly true that the four site linear chain would also exhibit OSMT behaviour.

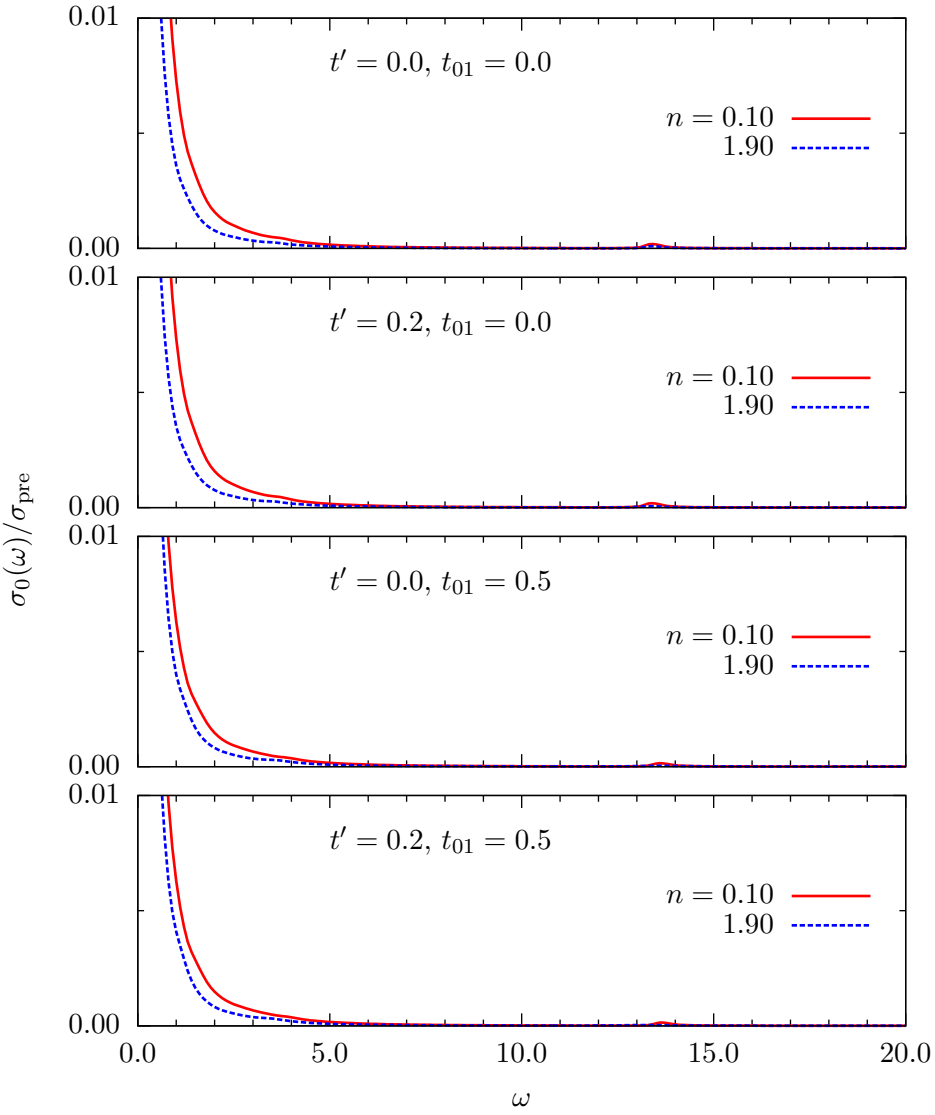

Figure 7.23: With the same Coulomb repulsions as figure 7.22, but $\epsilon_1 = 8.0$ (the upper orbital effectively gapped out), the transfer of optical conductivity $\sigma(\omega)$ spectral weight from low to high frequency is suppressed for all hybridization values. As well, hybridization has a minimal affect on the conductivity as expected when the upper orbital is not accessible. The system is effectively a single band. Lorentzian broadening of $\eta = 0.1$, five bath sites.

remain largely unexplored in the literature[5], here we briefly identify the OSMT behaviour for the DHM in response to both hybridization parameters, in the interesting regime of strong orbital relaxation. In this regime, the DHM appears to generate OSMT behaviour in response to appropriate tuning of the local and nonlocal hybridizations.

In the literature, the typical phase diagram for OSMT behaviour follows the pattern of earlier reports on the MIT presenting the change in quasiparticle weight as a function of changing Coulomb repulsion, usually with $U_0 = U_1$ maintained at half-filling, for example in references [65, 165, 178]. For $U_0 \neq U_1$ an OSMT arises quite generally [181].

We show this case in figure 7.24 where the chemical potential is maintained at $\mu = U_0/2.0$ which, in the single band realization, would ensure half-filling in the lower orbital. The other Coulomb repulsions are maintained at $U_{01} = U_0/2.0$ and $U_1 = U_0/4.0$ allowing for orbital relaxation of the electronic state at electron quarter filling (total filling $n = 1.0$), an effect that is amplified by a competitive value of the upper orbital energy, $\epsilon_1 = 3.0$. The influence of different hybridization parameters on the behaviour of the lower and upper orbital quasiparticle weights can be seen; these weights tend toward a MIT ($Z = 0$) for each orbital at distinct values of the chemical potential. For the case where both hybridizations are non-zero, the upper orbital approaches (but does not arrive at) a MIT in synchronization with the lower orbital, at $\mu \approx 4.5$, whereas in the other cases it remains reliably metallic until a higher value of the chemical potential is reached. At that point, the filled (and thus insulating) lower orbital loses charge to the upper orbital which fills to $n_1 = 1.0$, and the lower orbital returns to a metallic state with electrons as carriers.

The MODMFT routine does not converge reliably around $\mu = 12.0$ with either four or five bath sites, leading to an absence of data in that region of figure 7.24 where both orbitals experience an abrupt phase change. Nonetheless, the trend remains clear that, as expected, the upper orbital experiences its MIT at a higher value of chemical potential.

The influence of the hybridization on the OSMT behaviour is mainly restricted to the sharpness of the transitions. A finite nonlocal value, t_{01}, appears to "draw out" the final appearance of the insulating phase. This is especially evident in the lower orbital behaviour. The most obvious effect of the local hybridization t', is the early onset of the upper orbital transition in figure 7.24b, which appears to be correlated with the prevention of Z_1 from attaining perfect Fermi liquidity (*i.e.* $Z_1 = 1.0$) below its MIT.

As an alternative way of examining the DHM OSMT, we show in figure 7.25 the lower and upper orbital quasiparticle weights mapped as functions of the hybridizations (not the Coulomb repulsions), for a system with different parameters maintained around half-filling in the lower orbital, which in the single band case would again persist as a Mott insulator

[5] Reference [65] mentions investigation of this type of system but provides no results.

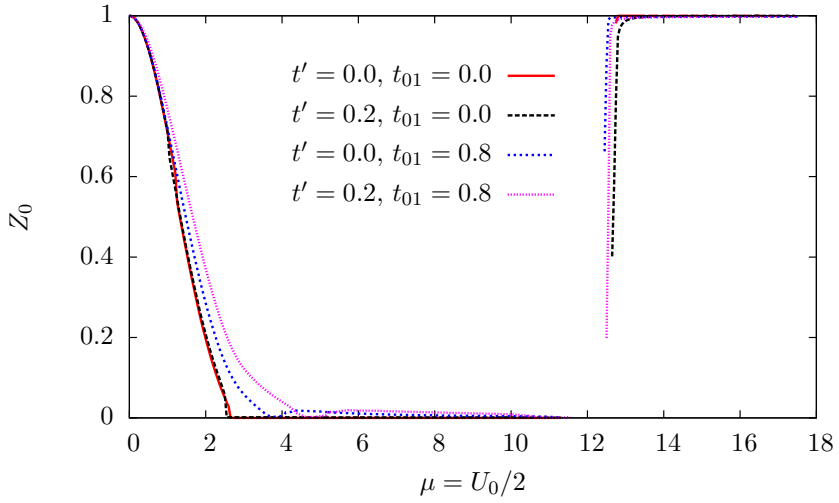

(a) Lower orbital

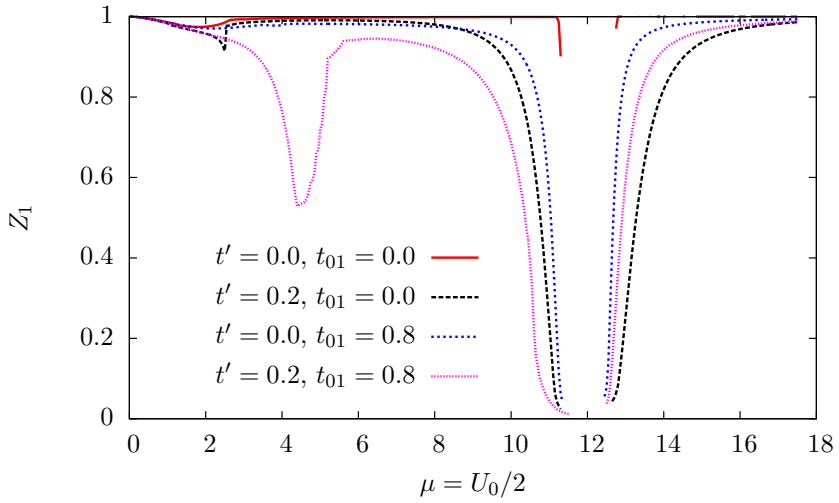

(b) Upper orbital

Figure 7.24: Response of the quasiparticle weight in the lower and upper orbitals to increasing lower Coulomb repulsion with dissimilar orbital energies ($\epsilon_1 = 3.0$). The chemical potential is fixed to $U_0/2$, which would pin a single band to half-filling. Any deviation from this condition is therefore due to the presence of the upper orbital and relaxation of the electron states. As U_0 increases, the orbitals exhibit distinct MITs. The effect of different hybridization values is demonstrated by the four cases of each curve. $U_{01} = U_0/2$ and $U_1 = U_0/4$, $\beta = 200$, and four bath sites are used except for some data near $\mu = 12.0$ where five sites were employed. The missing values in this region are the result of unreliable convergence as the state of both orbitals changes dramatically and simultaneously.

(MI) for the value of U_0 employed. With increased hybridization, the MI state moves through a non-Fermi liquid (NFL) phase into a Fermi liquid (FL) at large hybridization. The NFL phase is identifiable by a finite value in one of the effective self energies $\zeta_{\pm}$ (5.26).

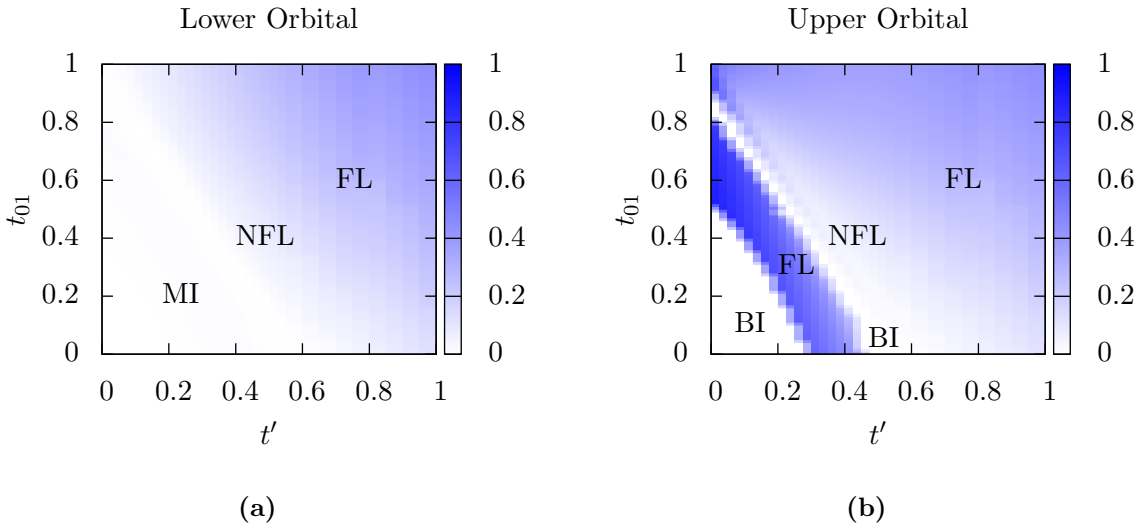

Figure 7.25: Quasiparticle weight phase diagrams for (a) lower orbital and (b) upper orbital, with respect to local (t') and nonlocal (t_{01}) hybridization for a system at half-filling in the lower orbital in which strong orbital relaxation occurs, but the orbital gap remains significantly larger than the hybridizations. The scale shows the value of the associated orbital quasiparticle weight, with $Z_x = 0.0$ insulating (uncoloured regions). Metallic regions may be Fermi liquid (FL) or non-Fermi liquid (NFL), depending on the low energy limit of the effective self-energies, $\zeta_{\pm}$. Near zero hybridization, the system is a Mott insulator (MI) in the lower orbital and a band insulator (BI) in the upper, as seen in the filling maps of figure 7.26. As the hybridizations increase, the upper orbital exhibits strong FL behaviour (the diagonal band) at very low filling, while the lower orbital remains a MI, signaling an OSMT. For both hybridizations large, the orbitals are FL. $U_0 = 10.0$, $U_{01} = 6.0$, $U_1 = 2.0$, $\epsilon_1 = 2.0$, $\mu = \frac{U_0}{2} = 5.0$.

The upper orbital phase is more complex (figure 7.25b). As the hybridizations are turned on, n_1 grows slowly (figure 7.26b), but the electrons abruptly transition from band insulating (BI) to FL, briefly back to BI, before returning to metallicity in NFL phase as electronic filling grows more rapidly. Finally, at large hybridizations, the FL electron density moves off the lower orbital to the upper clearly evidencing conditions for orbital relaxation.

Our main observation in this section is simply that the system parameters of the DHM, in particular those which lead to the phenomenon of orbital relaxation which we have

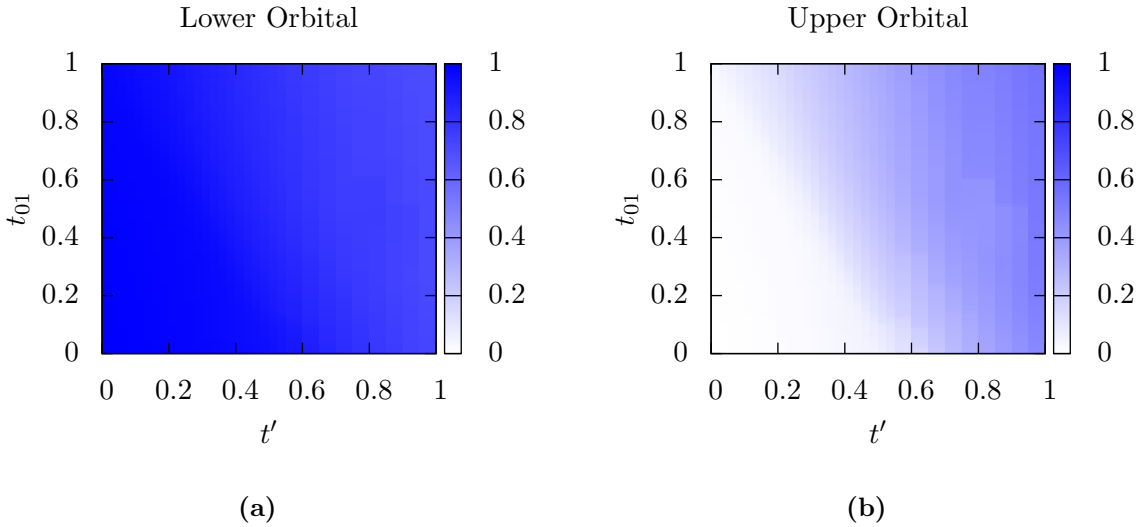

Figure 7.26: Filling map for (a) lower orbital and (b) upper orbital electron fillings, with respect to local (t') and nonlocal (t_{01}) hybridization for the system of figures 7.25. The filling of the lower orbital falls below $n_0 = 1.0$ with increasing hybridization, moving the orbital phase from a Mott insulator through a non-Fermi liquid to a metallic state.

been studying in comparison with Hirsch's four-site exact diagonalization [31], also appear to drive an OSMT. Since orbital relaxation depends on dissimilar orbital energies and Coulomb repulsions, this result is not surprising given the dependence between MITs and the value of the onsite Coulomb repulsion in the single band case. However, we have also addressed the additional dependence of the OSMT on the local and nonlocal hybridizations in the DHM. These brief results suggest that both hybridization parameters are influential in the appearance of OSMTs in this system. Since, as described above, OSMTs have proven to be of particular interest in multiorbital theoretical investigations, future examination of multiorbital DHM models may provide further insight into this ongoing area of research.

Chapter 8

Summary and Conclusion

The Coulomb interactions which repel electrons from one another as they occupy a condensed matter lattice system are known to be the source of a variety of interesting phenomena including superconductivity and both the Mott metal-insulator transition that arises in a single electron band, as well as orbital selective Mott transitions in multiband systems. The Hubbard model (1.4) has been an important theoretical tool for understanding the competition that exists in these systems between the strong onsite electron-electron repulsion and the charge carriers' propensity to move about the lattice.

While some of the important physics of real strongly interacting electron systems is captured by the Hubbard Hamiltonian, its nature as a single band description yields an inevitable limitation on other aspects of real-world lattice systems which arise only when multiorbital degrees of freedom are taken into account. The dynamic Hubbard model (DHM) provides an important improvement toward capturing the influence of higher energy orbitals that are known to affect the fundamental behaviour of electrons in strongly correlated systems. In particular, the electronic version of the DHM (2.15) is described by a Hamiltonian that includes two orbitals per lattice site which hybridize electron states both locally and nonlocally via hybridization parameters t' and t_{01}, respectively. Under a set of energy ordering rules (2.17) which determine the relative values of the orbital Coulomb repulsions and orbital energies, electron states will experience a relaxation from occupying only the lower orbital to a superposition state which also partially occupies the higher energy orbital as a means of escaping the high penalty of lower orbital Coulomb repulsion near the filling condition for double occupancy.

This orbital relaxation of the electronic ground state in the DHM has been extensively investigated in the exact diagonalization of a four site linear chain by Hirsch [31]. Hirsch has identified a link between the phenomenon of orbital relaxation in this model and

the pairing of holes, providing insight into a possible mechanism for high temperature superconductivity.

In our research project we have developed and applied a computational implementation of multiorbital dynamical mean field theory (MODMFT) to the problem of the DHM, in order to test the four-site results of Hirsch and more fully investigate the role played by the hybridization parameters, t' and t_{01}, in the dynamic Hubbard system. We designed and developed an original C++ algorithm generalizing the single band dynamical mean field problem to the context of two orbitals. After subjecting our implementation to a variety of checks, we employed it on various parameter sets of the DHM to evaluate Hirsch's conclusions about the nature of orbital relaxation.

Hirsch observed an essential asymmetry between the quasiparticles of the DHM at low filling (electrons) and high filling (holes) in the lower energy orbital. In the single band system, electron-like and hole-like quasiparticles have an identical effective mass, behaving as essentially free particles in the lattice. In the DHM two-orbital system, however, Hirsch found that holes become dressed as the electronic states relax into the upper orbital through the presence of interorbital hybridization. As well, he found that an increase in electron filling from the electron to the hole regime of charge carriers is accompanied by a transfer of optical conductivity spectral weight from low to high frequencies. We have found broad agreement with these observations in our MODMFT results, and have examined the mechanisms connecting the local and nonlocal hybridizations with these asymmetry effects. In particular, we have identified that the system parameters of the DHM are sensitive to a complex interplay between t_{01}, t' and Mott physics.

For a large energy gap $\epsilon_1 - \epsilon_0$, the local hybridization t' tends to drive quasiparticle dressing in the hole regime via charge density transfer, which causes a depletion in the otherwise nearly filled lower orbital toward half-filling. This initiates a drop in the quasiparticle weight as the lower orbital approaches the insulating regime of the MIT.

The nonlocal hybridization t_{01} appears to cause hole dressing as well, and thus electron-hole asymmetry, via a different mechanism that does not initiate Mott physics. Rather, the presence of the interband hopping creates an alternative channel for electrons to escape the lower orbital through transport, which diminishes the lower orbital quasiparticle weight without necessarily having a substantial impact on the lower orbital filling. We have found that the dynamics of orbital relaxation and hole dressing is more sensitive to this latter (nonlocal) mechanism.

Our analysis has also indicated that, under the right circumstances, the impact of the local hybridization t' can be toward hole undressing rather than dressing as the electron state relaxes to escape the lower orbital Coulomb repulsion. This scenario, unexplored in

Hirsch's study, obtains in the case of a small energy gap where a half-filled lattice already entails a sizable occupation of the upper orbital in the electron ground state. Under these circumstances, charge density transfer to the higher energy orbital through orbital relaxation accomplishes the task of lowering the overall energy of the system, but this is accompanied by a reduction in lower orbital filling *away from* the half-filling condition of the MIT and thus undressing of the quasiparticles. In this scenario, however, the nonlocal hybridization t_{01} continues to suppress the quasiparticle weight. There is, therefore, a regime of the DHM in which the two hybridization parameters work toward opposite ends with respect to electron-hole asymmetry, and the overall outcome is dependent on their comparative strengths in the system.

The response of the optical conductivity within the DHM serves as another indicator of electron-hole asymmetry in Hirsch's study. We have been clear that the calculation of the conductivity is something of an ill-posed problem in the infinitely-connected Bethe lattice of dynamical mean field theory, and that the multiorbital scenario creates further unsolved complications in the pursuit of a satisfying solution to this problem. With a few assumptions in mind, we have estimated the orbital-specific optical conductivities of the DHM and found agreement in our model with Hirsch's observation that conductivity spectral weight is transferred from low to high frequency as filling is increased from the electron regime to the hole regime. This also aligns with observations made by Bach *et al.* [51] using two-site DMFT on the auxiliary spin version of the DHM. While we did not explore the sensitivity of the conductivity to the different hybridization parameters in any great depth, it is nonetheless clear that some qualitative effects in the spectrum are dependent on the same mechanisms at play in the way these hybridizations drive the quasiparticle weight of the system. More work can be done in the future on this relationship.

In section 7.4 of our results we briefly touched on a qualitative connection between Hirsch's model of superconductivity through hole pairing and the flattening of the non-interacting energy bands of the DHM two-orbital system caused by the presence of nonlocal hybridization t_{01}. In connection with the dominant role this parameter plays in the dressing of holes through orbital relaxation, we believe there is further insight available in exploring its effects on hole pairing in the context of the Hirsch model.

Finally, we have observed the recently much-studied phenomenon of the orbital selective Mott transition (OSMT) in the DHM. While not directly related to our comparison with Hirsch's study of the four site linear chain, we have shown the appearance of OSMTs in the DHM as a result of the dissimilar orbital energies and Coulomb repulsion strengths. We also, briefly, examined the influence of the two different hybridization parameters, t' and t_{01}, on these OSMTs. The relative phases of electrons in the two bands—Fermi liquid,

non-Fermi liquid, Mott insulating and band insulating—are sensitive to the respective hybridization strengths of the system. We examined a system with parameters conducive to orbital relaxation with closely spaced energy levels, and found a complex response of transitions through the phases as the parameters were changed, especially within the higher energy band.

For clarity, we provide an itemization of these results of our research on the DHM using our MODMFT tool. We begin this summary of results by repeating that our research is grounded in our development of an original, reliable C++ application for studying strongly correlated two-orbital systems on the Bethe lattice with finite temperature using an exact diagonalization DMFT solver. Our implementation stands apart from many previous MODMFT studies in that we incorporate both local and nonlocal hybridization parameters.

Electron-Hole Asymmetry in the Quasiparticle Weight We have identified broad agreement with Hirsch's observation of quasiparticle asymmetry between electron and hole states.

The Role of Hybridizations in the Asymmetry We have demonstrated that the hybridization parameters t' and t_{01} play distinct roles in dressing holes near half-filling of the lattice.

Mott Physics and the Asymmetry We have identified the important connection of Mott physics to the asymmetry caused by the local hybridization t'.

Potential for Quasiparticle Undressing under Orbital Relaxation We have found that the presence of a local hybridization t' can, under certain parameter regimes, initiate an *undressing* of quasiparticle holes as electron states relax. This is in contrast to the emphasis of Hirsch's work.

Optical Conductivity Weight Transfer We have identified the same transfer of optical conductivity spectral weight observed by Hirsch in response to orbital relaxation.

Influence of Hybridizations on Optical Conductivity We have observed a dependence of the optical conductivity behaviour on the hybridizations consistent with their effects on the quasiparticle weight.

Greater Significance of the Nonlocal Hybridization We have observed that the quasiparticle weight is more sensitive to the nonlocal hybridization t_{01} than to t', which stands in contrast to an assumption made in Hirsch's work.

Band-Flattening and Nonlocal Hybridization We have noted the potentially significant connection between band-flattening in the non-interacting dispersion caused by t_{01} and its important role in orbital relaxation, which may be important to Hirsch's model of superconductivity.

Orbital Selective Mott Transition We observed the appearance of orbital selective MIT behaviour in the DHM within the parameter regime of orbital relaxation, and provided brief insight into the role played by the local and nonlocal hybridizations.

In light of these key results, we emphasize our discussion in section 4.1 where we surveyed the many multiorbital DMFT studies which have examined the role of local hybridization on strongly correlated electron systems. There, we also indicated the dearth of work that has been done with this computational tool on Hamiltonians incorporating nonlocal hybridization. This thesis has contributed some original and initial observations of the significance of this parameter in a system with two hybridized bands. This has been done while focusing on the specific physics of orbital relaxation and electron-hole asymmetry in the electronic DHM. There is a great deal of room for further investigation of the influence of t_{01} on multiorbital models, including those that do not obey the particular criteria to qualify as a dynamic Hubbard model.

Other interesting avenues of investigation were deliberately set aside in this research project, for simplicity, but beckon further study:

Hirsch has explored the influence of temperature on the optical conductivity response [48], which could be applied in a straightforward way in our finite temperature realization of the DHM in MODMFT. The role of temperature was not systematically explored in this thesis, but was rather kept within a range that did not substantially affect the qualitative results. Temperature sensitivity certainly provides an avenue for further study in relation to all the phenomena discussed, and has already been explored by Liebsch [165] for a non-hybridized system with Hund's exchange coupling between bands of different bandwidths.

Many other MODMFT studies have focused on the physics arising from additional terms in the multiorbital Hamiltonian which we have neglected for simplicity. In particular, a Hund's exchange term where electrons flip their spin as they hybridize between orbitals, and a pair-hybridization term where electrons transition in spin up-down pairs via some local parameter, might enhance the relevance of our multiorbital model with respect to real systems, providing comparisons to other multiorbital work and additional insight into orbital relaxation and the role of t_{01}.

The role of different bandwidths in the physics of the DHM was not explored in our study. Rather, we chose to maintain the intraband hoppings at $t_0 = t_1 = 1.0$, again for

simplicity and to properly compare with the same choice in Hirsch's study. This assumption of equal bandwidths is perhaps not ideal, since an intuitive understanding of orbital relaxation would imply that electrons escape the Coulomb repulsion of the lower orbital by relaxing their state to a higher energy orbital where a greater spatial range of occupation for the overlapping electron density reduces the Coulomb repulsion of double occupancy but in turn should result in a greater degree of overlap of the electronic wavefunction with neighbouring lattice sites. This implies the condition $t_1 > t_0$ between the intra-orbital hopping parameters. The influence of this scenario alongside an exploration of t_{01} values should provide new insights into different observables relevant to electron-hole asymmetry and the OSMT.

Finally, our choice to restrict our study to a small number of bath sites (four, five and very occasionally six) in the impurity model was motivated by computational efficiency and the difficulty of attaining reliable convergence in applying the Lanczos and Arnoldi algorithms to the multiorbital scenario. No doubt this is not an insurmountable problem, especially since Winograd and de' Medici [65] have recently published results employing the Lanczos method on a two-orbital Hamiltonian, where they have explicitly explored the influence of a local hybridization and made passing reference to results that included the nonlocal hybridization as well. A successful application of the Lanczos or Arnoldi algorithm in our MODMFT problem would allow the evaluation of a ground state solution at zero temperature using a large number of bath sites. This would improve the resolution of spectral density features and aid in convergence of the routine around abrupt phase transitions, such as that shown in figure 7.24.

We therefore conclude that our study of the dynamic Hubbard model through the computational tool of multiorbital dynamical mean field theory has shown significant and broad agreement with the four-site exact diagonalization study performed by Hirsch in support of his model of electron-hole asymmetry as a context for a hole-pairing mechanism in superconductivity. In particular, we have observed electron-hole asymmetry through the quasiparticle weight and optical conductivity results. We have evaluated the specific role played by the different hybridization parameters in creating the asymmetry, and have broken some new ground on the influence of nonlocal hybridization on the dynamics of multiorbital systems, including the identification of orbital selective metal-insulator transitions. Many of these results are first steps and suggest that a whole range of hybridized multiorbital scenarios can be explored in the future using these suggested improvements and extensions to this tool of doubly-hybridized multiorbital dynamical mean field theory.

Bibliography

[1] G. J. Stoney, Phil. Mag. **38**, 418 (1894).

[2] R. D. Tolman and T. D. Stewart, Phys. Rev. **8**, 97 (1916).

[3] R. D. Tolman and T. D. Stewart, Phys. Rev. **9**, 164 (1917).

[4] J. J. Thomson, Phil. Mag. **44**, 293 (1897).

[5] P. Drude, Ann. Phys. **1**, 566 (1900).

[6] P. Drude, Ann. Phys. (Leipzig) **3**, 369 (1900).

[7] H. A. Lorentz, *The Theory of Electrons and Its Applications to the Phenomena of Light and Radiant Heat*, B. G. Teubner, Leipzig, 1916.

[8] J. C. Slater, Rev. Mod. Phys. **6**, 209 (1934).

[9] A. Sommerfeld, W. V. Houston, and C. Eckart, Z. Phys. **47**, 1 (1928).

[10] F. Bloch, Z. Phys. **52**, 555 (1928).

[11] A. H. Wilson, Proc. R. Soc. London Ser. A **133**, 458 (1931).

[12] A. H. Wilson, Proc. R. Soc. London Ser. A **134**, 277 (1931).

[13] J. H. de Boer and E. J. W. Verwey, Proc. Phys. Soc. **49**, 59 (1937).

[14] N. F. Mott and R. Peierls, Proc. Phys. Soc. **49**, 72 (1937).

[15] N. F. Mott, Proc. Phys. Soc. A **62**, 416 (1949).

[16] N. F. Mott, Can. J. Phys. **34**, 1356 (1956).

[17] N. F. Mott, Phil. Mag. **6**, 287 (1961).

[18] G. Kotliar and D. Vollhardt, Phys. Today **57**, 53 (2004).

[19] M. Imada, A. Fujimori, and Y. Tokura, Rev. Mod. Phys. **70**, 1039 (1998).

[20] D. Vollhardt, K. Byczuk, and M. Kollar, Dynamical mean field theory, in *Strongly Correlated Systems*, edited by A. Avella and F. Mancini, pages 203–236, Springer-Verlag, Berlin, 2012.

[21] L. D. Landau, Sov. Phys. JETP **3**, 920 (1957).

[22] L. D. Landau, Sov. Phys. JETP **5**, 101 (1957).

[23] H. Bruus and K. Flensberg, *Many-Body Quantum Theory in Condensed Matter Physics*, Oxford University Press, Oxford, 2004.

[24] J. Hubbard, Proc. R. Soc. London Ser. A **276**, 238 (1963).

[25] J. Hubbard, Proc. R. Soc. London Ser. A **277**, 237 (1964).

[26] J. Hubbard, Proc. R. Soc. London Ser. A **281**, 401 (1964).

[27] J. Hubbard, Proc. R. Soc. London Ser. A **285**, 542 (1965).

[28] N. W. Ashcroft and N. D. Mermin, *Solid State Physics*, Brooks/Cole, Belmont, California, 1976.

[29] E. H. Lieb and F. Y. Wu, Phys. Rev. Lett. **20**, 1445 (1968).

[30] G. D. Mahan, *Many-Particle Physics*, Kluwer Academic/Plenum Publishers, New York, third edition, 2000.

[31] J. E. Hirsch, Phys. Rev. B **67**, 035103 (2003).

[32] J. E. Hirsch, Phys. Rev. Lett. **87**, 206402 (2001).

[33] Handbook of chemistry and physics (internet version), `http://www.hbcpnetbase.com`, 2012.

[34] A. Messiah, *Quantum Mechanics Vol. II*, Dover, Mineola, NY, 1999.

[35] J. Frenkel, *Einfuhrung in die Wellenmechanik*, J. Springer, Berlin, 1929.

[36] J. E. Hirsch, Phys. Rev. B **65**, 184502 (2002).

[37] C. Eckart, Phys. Rev. **36**, 878 (1930).

[38] E. A. Hylleraas, Z. Phys. **54**, 347 (1929).

[39] J. Hirsch, Int. J. Mod. Phys. B **23**, 3035 (2009).

[40] J. E. Hirsch, Phys. Rev. B **43**, 11400 (1991).

[41] C. Schwartz, Int. J. Mod. Phys. E **15**, 877 (2006).

[42] J. Hutchinson, M. Baker, and F. Marsiglio, Eur. J. Phys. **34**, 111 (2013).

[43] J. E. Hirsch, Physica C **201**, 347 (1992).

[44] T. Holstein, Ann. Phys. N. Y. **8**, 325 (1959).

[45] F. Marsiglio, R. Teshima, and J. E. Hirsch, Phys. Rev. B **68**, 224507 (2003).

[46] J. E. Hirsch, Phys. Rev. B **87**, 184506 (2013).

[47] J. E. Hirsch and S. Tang, Phys. Rev. B **40**, 2179 (1989).

[48] J. E. Hirsch, Phys. Rev. B **66**, 064507 (2002).

[49] J. E. Hirsch, Phys. Rev. B **65**, 214510 (2002).

[50] K. Bouadim, M. Enjalran, F. Hébert, G. G. Batrouni, and R. T. Scalettar, Phys. Rev. B **77**, 014516 (2008).

[51] G. H. Bach, J. E. Hirsch, and F. Marsiglio, Phys. Rev. B **82**, 155122 (2010).

[52] G. H. Bach and F. Marsiglio, Phys. Rev. B **85**, 155134 (2012).

[53] H. Tsunetsugu, M. Sigrist, and K. Ueda, Rev. Mod. Phys. **69**, 809 (1997).

[54] K. Held, C. Huscroft, R. T. Scalettar, and A. K. McMahan, Phys. Rev. Lett. **85**, 373 (2000).

[55] I. Kogoutiouk and H. Terletska, Int. J. Mod. Phys. B **20**, 3101 (2006).

[56] L. G. Sarasua and M. A. Continentino, Phys. Rev. B **65**, 184503 (2002).

[57] M. A. Continentino, G. M. Japiassú, and A. Troper, Phys. Rev. B **49**, 4432 (1994).

[58] M. V. Tovar Costa, A. Troper, N. A. de Oliveira, G. M. Japiassú, and M. A. Continentino, Phys. Rev. B **57**, 6943 (1998).

[59] M. T. Costa, N. de Oliveira, G. Japiassú, M. Continentino, and A. Troper, J. Magn. Magn. Mater. **177-181, Part 1**, 331 (1998), International Conference on Magnetism.

[60] A. Koga, N. Kawakami, T. M. Rice, and M. Sigrist, Phys. Rev. B **72**, 045128 (2005).

[61] A. Georges, G. Kotliar, and W. Krauth, Z. Phys. B **92**, 313 (1993).

[62] Q. Si, M. J. Rozenberg, G. Kotliar, and A. E. Ruckenstein, Phys. Rev. Lett. **72**, 2761 (1994).

[63] Y. Song and L.-J. Zou, Eur. Phys. J. B **72**, 59 (2009).

[64] Y. Song, Mod. Phys. Lett. B **23**, 2321 (2009).

[65] E. A. Winograd and L. de' Medici, Phys. Rev. B **89**, 085127 (2014).

[66] J. E. Hirsch, Phys. Lett. A **134**, 451 (1989).

[67] J. E. Hirsch and F. Marsiglio, Phys. Rev. B **39**, 11515 (1989).

[68] J. E. Hirsch, Phys. Rev. B **62**, 14487 (2000).

[69] J. Bardeen, L. N. Cooper, and J. R. Schrieffer, Phys. Rev. **108**, 1175 (1957).

[70] G. Rickaysen, *Theory of Superconductivity*, Interscience, New York, 1965.

[71] J. E. Hirsch and F. Marsiglio, Physica C **162-164**, 591 (1989).

[72] J. E. Hirsch, Int. J. Mod. Phys. B **17**, 3236 (2003).

[73] J. Hirsch, Physica C **364-365**, 37 (2001).

[74] J. Hirsch and F. Marsiglio, Phys. Rev. B **41**, 2049 (1990).

[75] J. E. Hirsch and F. Marsiglio, Phys. Rev. B **62**, 15131 (2000).

[76] J. E. Hirsch, Phys. Rev. B **68**, 012510 (2003).

[77] M. Tinkham, *Introduction to Superconductivity*, Dover, Mineola, NY, second edition, 1996.

[78] H. J. A. Molegraaf, C. Presura, D. van der Marel, P. H. Kes, and M. Li, Science **295**, 2239 (2002).

[79] D. N. Basov et al., Science **283**, 49 (1999).

[80] G. Kotliar et al., Rev. Mod. Phys. **78**, 865 (2006).

[81] E. H. Lieb and F. Y. Wu, Physica A **321**, 1 (2003).

[82] W. H. Press, S. A. Teukolsky, W. T. Vetterling, and B. P. Flannery, *Numerical Recipes: the Art of Scientific Computing*, Cambridge University Press, New York, third edition, 2007.

[83] `http://www.top500.org`, accessed April 5, 2014.

[84] T. Pruschke, Dynamical mean-field approximations and cluster methods for correlated electron systems, in *Computational Many-Particle Physics*, edited by H. Fehske, R. Schneider, and A. Weiße, pages 473–503, Springer-Verlag, Berlin, 2008.

[85] D. M. Edwards and A. C. Hewson, Rev. Mod. Phys. **40**, 810 (1968).

[86] W. F. Brinkman and T. M. Rice, Phys. Rev. B **2**, 4302 (1970).

[87] A. Georges, G. Kotliar, W. Krauth, and M. J. Rozenberg, Rev. Mod. Phys. **68**, 13 (1996).

[88] X. Y. Zhang, M. J. Rozenberg, and G. Kotliar, Phys. Rev. Lett. **70**, 1666 (1993).

[89] W. Metzner and D. Vollhardt, Phys. Rev. Lett. **62**, 324 (1989).

[90] E. Müller-Hartmann, Z. Phys. B **74**, 507 (1989), 10.1007/BF01311397.

[91] F. Reif, *Fundamentals of Statistical and Thermal Physics*, McGraw-Hill, New York, 1965.

[92] G. Santoro, M. Airoldi, S. Sorella, and E. Tosatti, Phys. Rev. B **47**, 16216 (1993).

[93] W. F. Brinkman and T. M. Rice, Phys. Rev. B **2**, 1324 (1970).

[94] G. D. Mahan, Phys. Rev. B **63**, 155110 (2001).

[95] A. Georges and G. Kotliar, Phys. Rev. B **45**, 6479 (1992).

[96] P. W. Anderson, Phys. Rev. **124**, 41 (1961).

[97] U. Fano, Phys. Rev. **124**, 1866 (1961).

[98] R. Bulla, A. C. Hewson, and T. Pruschke, J. Phys.-Condens. Mat. **10**, 8365 (1998).

[99] K. Held et al., Phys. Status Solidi B **243**, 2599 (2006).

[100] T. Pruschke, D. L. Cox, and M. Jarrell, Phys. Rev. B **47**, 3553 (1993).

[101] N. Bickers and D. Scalapino, Ann. Phys. N. Y. **193**, 206 (1989).

[102] M. I. Katsnelson and A. I. Lichtenstein, J. Phys.-Condens. Mat. **11**, 1037 (1999).

[103] R. Bulla, Phys. Rev. Lett. **83**, 136 (1999).

[104] R. Bulla, T. A. Costi, and D. Vollhardt, Phys. Rev. B **64**, 045103 (2001).

[105] R. Bulla, T. A. Costi, and T. Pruschke, Rev. Mod. Phys. **80**, 395 (2008).

[106] S. Nishimoto and E. Jeckelmann, J. Phys.-Condens. Mat. **16**, 613 (2004).

[107] D. J. García, K. Hallberg, and M. J. Rozenberg, Phys. Rev. Lett. **93**, 246403 (2004).

[108] R. Peters, Phys. Rev. B **84**, 075139 (2011).

[109] E. Gull et al., Rev. Mod. Phys. **83**, 349 (2011).

[110] M. Jarrell, Phys. Rev. Lett. **69**, 168 (1992).

[111] Q. Si, M. J. Rozenberg, G. Kotliar, and A. E. Ruckenstein, Phys. Rev. Lett. **72**, 2761 (1994).

[112] M. Caffarel and W. Krauth, Phys. Rev. Lett. **72**, 1545 (1994).

[113] A. Liebsch and H. Ishida, J. Phys.-Condens. Mat. **24**, 053201 (2012).

[114] C. A. Perroni, H. Ishida, and A. Liebsch, Phys. Rev. B **75**, 045125 (2007).

[115] T. Pruschke and R. Bulla, Eur. Phys. J. B **44**, 217 (2005).

[116] J. E. Hirsch and R. M. Fye, Phys. Rev. Lett. **56**, 2521 (1986).

[117] M. Jarrell and J. Gubernatis, Phys. Rep. **269**, 133 (1996).

[118] D. Senechal, Cluster dynamical mean field theory, in *Strongly Correlated Systems*, edited by A. Avella and F. Mancini, pages 341–370, Springer-Verlag, Berlin, 2012.

[119] H. Q. Lin and J. E. Gubernatis, Comp. Phys. **7**, 400 (1993).

[120] A. Weiße and H. Fehske, Exact diagonalization techniques, in *Computational Many-Particle Physics*, edited by H. Fehske, R. Schneider, and A. Weiße, pages 529–544, Springer-Verlag, Berlin, 2008.

[121] R. B. Lehoucq, D. C. Sorensen, and C. Yang, *ARPACK Users' Guide*, SIAM, Philadelphia, 1997.

[122] W. Krauth, *Georges Kotliar Krauth Rozenberg 1996*, `http://www.lps.ens.fr/~krauth/index.php/Georges_Kotliar_Krauth_Rozenberg_1996`, accessed online May 8, 2012.

[123] G. Gaël and J. Benoît, *Eigen v3*, `http://eigen.tuxfamily.org`, 2010.

[124] G. B. Arfken and H. J. Weber, *Mathematical Methods for Physicists*, Elsevier, Burlington, MA, sixth edition, 2005.

[125] M. J. Rozenberg, G. Moeller, and G. Kotliar, Phys. Rev. Lett. **70**, 12 (1994).

[126] V. Turkowski, A. Kabir, N. Nayyar, and T. S. Rahman, J. Phys.-Condens. Mat. **22**, 462202 (2010).

[127] R. Arita et al., Phys. Rev. B **69**, 195106 (2004).

[128] M. J. Rozenberg, I. H. Inoue, H. Makino, F. Iga, and Y. Nishihara, Phys. Rev. Lett. **76**, 4781 (1996).

[129] W. Krauth, `minimize` (version 30-sep-95) [FORTRAN computer software], 1995.

[130] D. Zgid and G. K.-L. Chan, J. Chem. Phys. **134**, 094115 (2011).

[131] J. Schlipf et al., Phys. Rev. Lett. **82**, 4890 (1999).

[132] A. Georges and W. Krauth, Phys. Rev. B **48**, 7167 (1993).

[133] M. Potthoff, Eur. Phys. J. B **36**, 335 (2003).

[134] N.-H. Tong, S.-Q. Shen, and F.-C. Pu, Phys. Rev. B **64**, 235109 (2001).

[135] C. Gros, W. Wenzel, R. Valentí, G. Hülsenbeck, and J. Stolze, Europhys. Lett. **27**, 299 (1994).

[136] R. M. Noack and F. Gebhard, Phys. Rev. Lett. **82**, 1915 (1999).

[137] W. Krauth, Phys. Rev. B **62**, 6860 (2000).

[138] Q. Si and G. Kotliar, Phys. Rev. Lett. **70**, 3143 (1993).

[139] Q. Si and G. Kotliar, Phys. Rev. B **48**, 13881 (1993).

[140] A. I. Poteryaev, M. Ferrero, A. Georges, and O. Parcollet, Phys. Rev. B **78**, 045115 (2008).

[141] M. Potthoff, Phys. Rev. B **64**, 165114 (2001).

[142] C. J. Bolech, S. S. Kancharla, and G. Kotliar, Phys. Rev. B **67**, 075110 (2003).

[143] H. Ishida and A. Liebsch, Phys. Rev. B **82**, 045107 (2010).

[144] M. Potthoff, Eur. Phys. J. B **36**, 335 (2003).

[145] D. Sénéchal, Phys. Rev. B **81**, 235125 (2010).

[146] J. W. Negele and H. Orland, *Quantum Many-Particle Systems*, Perseus Books, Reading, MA, 1998.

[147] Y. M. Vilk and A.-M. Tremblay, J. Phys. I Paris **7**, 1309 (1997).

[148] J. E. Hirsch, Phys. Rev. B **62**, 14131 (2000).

[149] E. Kuchinskii and M. Sadovskii, Sov. Phys. JETP **103**, 415 (2006).

[150] P. F. Maldague, Phys. Rev. B **16**, 2437 (1977).

[151] T. Pruschke, D. L. Cox, and M. Jarrell, Europhys. Lett. **21**, 593 (1993).

[152] M. J. Rozenberg et al., Phys. Rev. Lett. **75**, 105 (1995).

[153] J. Hong and H.-Y. Kee, EPL (Europhys. Lett.) **33**, 453 (1996).

[154] A. Chattopadhyay, A. J. Millis, and S. Das Sarma, Phys. Rev. B **61**, 10738 (2000).

[155] N. Blümer, *Mott-Hubbard metal-insulator transition and optical conductivity in high dimensions*, PhD thesis, Universität Augsburg, Germany, 2002.

[156] G. Pálsson, *Computational Studies of Thermoelectricity in Strongly Correlated Electron Systems*, PhD thesis, Rutgers University, New Brunswick, NJ, 2001.

[157] J. M. Thomczak, *Spectral and optical properties of correlated materials*, PhD thesis, Ecole Polytechnique, France, 2007.

[158] E. Dagotto, Rev. Mod. Phys. **66**, 763 (1994).

[159] E. Koch, G. Sangiovanni, and O. Gunnarsson, Phys. Rev. B **78**, 115102 (2008).

[160] M. Capone, L. de' Medici, and A. Georges, Phys. Rev. B **76**, 245116 (2007).

[161] A. Liebsch and T. A. Costi, Eur. Phys. J. B **51**, 523 (2006), 10.1140/epjb/e2006-00248-0.

[162] A. Liebsch and N.-H. Tong, Phys. Rev. B **80**, 165126 (2009).

[163] A. Liebsch, H. Ishida, and J. Merino, Phys. Rev. B **78**, 165123 (2008).

[164] A. Liebsch, Phys. Rev. B **70**, 165103 (2004).

[165] A. Liebsch, Phys. Rev. Lett. **95**, 116402 (2005).

[166] A. Abrikosov, J. Campuzano, and K. Gofron, Physica C **214**, 73 (1993).

[167] K. Gofron et al., Phys. Rev. Lett. **73**, 3302 (1994).

[168] J. Hirsch and D. Scalapino, Phys. Rev. Lett. **56**, 2732 (1986).

[169] M. Imada and M. Kohno, Phys. Rev. Lett. **84**, 143 (2000).

[170] A. Koitzsch et al., Phys. Rev. B **77**, 155128 (2008).

[171] E. S. Morell, J. Correa, P. Vargas, M. Pacheco, and Z. Barticevic, Phys. Rev. B **82**, 121407 (2010).

[172] S. Biermann, L. de' Medici, and A. Georges, Phys. Rev. Lett. **95**, 206401 (2005).

[173] T. A. Costi and A. Liebsch, Phys. Rev. Lett. **99**, 236404 (2007).

[174] A. Koga, N. Kawakami, T. Rice, and M. Sigrist, Physica B **359 - 361**, 1366 (2005), Proceedings of the International Conference on Strongly Correlated Electron Systems.

[175] A. Liebsch, Phys. Rev. Lett. **91**, 226401 (2003).

[176] S. Nakatsuji and Y. Maeno, Phys. Rev. Lett. **84**, 2666 (2000).

[177] V. Anisimov, I. Nekrasov, D. Kondakov, T. Rice, and M. Sigrist, Eur. J. Phys. B **25**, 191 (2002).

[178] P. G. J. van Dongen, C. Knecht, and N. Blümer, Phys. Status Solidi B **243**, 116 (2006).

[179] N. Blümer, C. Knecht, K. Požgajčić, and P. G. van Dongen, J. Magn. Magn. Mater. **310**, 922 (2007).

[180] E. Jakobi, N. Blümer, and P. van Dongen, Phys. Rev. B **80**, 115109 (2009).

[181] A. Koga, K. Inaba, and N. Kawakami, Prog. Theor. Phys. Supp. **160**, 253 (2005).